

New Insights into Water's Phase Diagram Using Ammonium Fluoride

Zainab Sharif

Thesis submitted in partial fulfilment of the
requirements for the degree of Doctor of
Philosophy

Department of Chemistry
University College London
July 2020

I, Zainab Sharif, confirm that the work presented in this thesis is my own.
Where information has been derived from other sources, I confirm that this
has been indicated in the thesis.

Signature:.....

Date:.....

Abstract

Ice is a complex, yet highly relevant material and has been a ripe area of research since the beginning of the 20th century.¹⁻⁵ Understanding ice is expected to have consequences not just for furthering our appreciation of the different states of water, but also general chemistry, physics and geology.^{2, 6, 7} It has often been found that properties first observed in ice (*e.g.* stacking disorder) are also present in other materials.^{2, 6, 8, 9} This thesis largely builds on work performed by Shephard *et al.* which explored the effect of 2.5 mol% NH₄F in ice, and astoundingly fully prevented ice II formation.¹⁰

Initially, the thesis focuses on the effect of adding NH₄F to ice at ambient pressure, which is demonstrated to produce a denser material than pure ice. At 0.5 GPa, NH₄F-ice solid solutions (≥ 12 mol%) surprisingly produce stable ice XII-type structures. Additionally, upon the mapping of the 2.5 mol% NH₄F phase diagram to 1.7 GPa, it was found that phase-pure ice XII could be quenched at 1.1 GPa. Both ice XII-type structures did not require an amorphous precursor.

The influence of NH₄F in ice is explored in mixtures that are subjected to the compression conditions that yield high-density amorphous ice ‘pressure-induced amorphised’ upon their compression to 1.4 GPa at 77 K. Unexpectedly, the crossover of PIA to recrystallisation is determined as beginning on the water-rich side (35 mol% NH₄F) of the solid solutions.

Stacking disorder from the heating of NH₄F II and III at ambient pressure is quantified. The materials reach a maximum cubicity of 77%, yet the stacking disorder obtained from each material is unique. Remarkably NH₄F III did not transform to an amorphous phase upon heating.

The final standalone chapter focuses on the ordering of ices V/XIII and IX with 0.01 M HCl doping.

298 / 300 words

1. P. W. Bridgman, *Proc. Am. Acad.*, 1912, **47**, 441-558.
2. C. G. Salzmann, P. G. Radaelli, B. Slater and J. L. Finney, *Phys. Chem. Chem. Phys.*, 2011, **13**, 18468-18480.
3. J. Finney, *Water: A Very Short Introduction*, OUP Oxford, 2015.
4. C. G. Salzmann, *J. Chem. Phys.*, 2019, **150**, 060901.

5. T. Loerting, K. Winkel, M. Seidl, M. Bauer, C. Mitterdorfer, P. H. Handle, C. G. Salzmann, E. Mayer, J. L. Finney and D. T. Bowron, *Phys. Chem. Chem. Phys.*, 2011, **13**, 8783-8794.
6. C. G. Salzmann, presented in part at the Water and Water Systems, Erice, Sicily, 2016.
7. V. F. Petrenko and R. W. Whitworth, *Physics of Ice*, OUP Oxford, 1999.
8. T. L. Malkin, B. J. Murray, C. G. Salzmann, V. Molinero, S. J. Pickering and T. F. Whale, *Phys. Chem. Chem. Phys.*, 2015, **17**, 60-76.
9. C. G. Salzmann, B. J. Murray and J. J. Shephard, *Diamond Relat. Mater.*, 2015, **59**, 69-72.
10. J. J. Shephard, B. Slater, P. Harvey, M. Hart, C. L. Bull, S. T. Bramwell and C. G. Salzmann, *Nat. Phys.*, 2018, **14**, 569-572.

Impact statement

This thesis explores the effect of the addition of NH_4F to the dynamics and thermodynamics of processes that occur in ice, as well as drawing on observations in pure NH_4F for phenomena also known to occur in pure ice.

Although we encounter ice regularly without much thought, it is a truly unusual material – for instance in its increase in density on melting.^{1, 2} On a fundamental level, the study of pure ice has qualified it as a model material for the discovery of phenomena, such as stacking disorder^{3, 4} and pressure-induced amorphisation,⁵ which have since been observed in a host of other materials and provide the potential for tuning material properties.⁶

Recent research has seen a shift towards the study of ice with mixed species and the attempt to delve into the chemical dimension.⁶ This provides for the more realistic study of ice which is relevant to, but not limited to, astronomical,⁷ meteorological,⁸ and chemical contexts^{9, 10} which often observe mixed-ice species. In addition to many naturally occurring mixed-ice species, the opportunity to utilise guest species in crystal engineering allows for the tailoring of many of the undesirable properties of ice.⁶ For instance, caged-ice structures called clathrate hydrates which frequently block gas pipelines¹² can be inhibited from forming in the presence of NH_4F .¹³

Turning to the specific results showcased in this thesis, there are wider consequences for the community's understanding of ice and its cornucopia of states which arise from its 'pseudo'-crystalline nature.⁶ The presence of NH_4F in ice provides a unique opportunity to disturb the pure ice phase diagram, and 'switch off' properties otherwise observed.¹⁴

The discovery of pressure-induced amorphisation of ice *Ih* by Mishima *et al.*⁵ gave rise to the theory that the two amorphous forms of ice could have a structural link with two proposed liquid states.¹⁵ However, these two hypothetical liquids have not been observed experimentally – they are only ever studied computationally.¹⁶ In this thesis, the study of pressure-induced amorphisation and its crossover to recrystallisation for solid solutions of NH_4F -ice have provided strong evidence to disprove the link between amorphous ices and the proposed high- and low-density liquids.

As NH_4F III and ice VII/VIII share the same structure,¹⁷ further potential structural links between crystalline and amorphous ice can also be inferred from the behaviour exhibited on the heating of NH_4F III at ambient pressure. This has presented an analogous structural relaxation route to what is observed with the heating of ice VII/VIII at ambient pressure. Notably, the heating of ice VII/VIII at ambient pressure leads to the formation of low-density amorphous ice,¹⁸ whereas it has now been clearly demonstrated in this thesis that the heating of NH_4F III leads instead to the formation of an ill-crystalline structure which has several broad features that coincide with features seen for low-density amorphous ice.

Many of the findings presented have the potential to correctly define the nature of the many forms of ice as well as liquid water.

489 / 500 words

1. J. Finney, *Water: A Very Short Introduction*, OUP Oxford, 2015.
2. J. L. Finney, *Philos. Trans. R. Soc. B*, 2004, **359**, 1145-1165.
3. W. F. Kuhs, C. Sippel, A. Falenty and T. C. Hansen, *PNAS*, 2012, **109**, 21259-21264.
4. T. L. Malkin, B. J. Murray, C. G. Salzmann, V. Molinero, S. J. Pickering and T. F. Whale, *Phys. Chem. Chem. Phys.*, 2015, **17**, 60-76.
5. O. Mishima, L. D. Calvert and E. Whalley, *Nature*, 1984, **310**, 393-395.
6. C. G. Salzmann, *J. Chem. Phys.*, 2019, **150**, 060901.
7. S. O. Halukeerthi, J. J. Shephard, S. K. Talewar, J. S. O. Evans, A. Rosu-Finsen and C. G. Salzmann, *J. Phys. Chem. A*, 2020, **124**, 5015-5022.
8. B. J. Murray, T. L. Malkin and C. G. Salzmann, *J. Atmos. Sol.-Terr. Phys.*, 2015, **127**, 78-82.
9. S. Klotz, K. Komatsu, F. Pietrucci, H. Kagi, A. A. Ludl, S. Machida, T. Hattori, A. Sano-Furukawa and L. E. Bove, *Sci. Rep.*, 2016, **6**, 32040.
10. S. Klotz, L. E. Bove, T. Strassle, T. C. Hansen and A. M. Saitta, *Nat. Mater.*, 2009, **8**, 405-409.
11. L. E. Bove and U. Ranieri, *Philos. Trans. R. Soc. A*, 2019, **377**, 20180262.
12. A. Perrin, O. M. Musa and J. W. Steed, *Chem. Soc. Rev.*, 2013, **42**, 1996-2015.
13. S. Park, D. Lim, Y. Seo and H. Lee, *Chem. Commun.*, 2015, **51**, 8761-8764.
14. J. J. Shephard, B. Slater, P. Harvey, M. Hart, C. L. Bull, S. T. Bramwell and C. G. Salzmann, *Nat. Phys.*, 2018, **14**, 569-572.
15. O. Mishima, *Nature*, 1996, **384**, 546-549.
16. A. K. Soper, *J. Chem. Phys.*, 2019, **150**, 234503.
17. C. G. Salzmann, Z. Sharif, C. L. Bull, S. T. Bramwell, A. Rosu-Finsen and N. P. Funnell, *J. Phys. Chem. C*, 2019, **123**, 16486-16492.
18. J. J. Shephard, S. Klotz, M. Vickers and C. G. Salzmann, *J. Chem. Phys.*, 2016, **144**, 204502.

Acknowledgements

The work carried out in this thesis was only possible with the help of many different people. Firstly, I would like to acknowledge Martin Vickers and Dr. Jeremy Cockcroft at UCL Chemistry who allowed for the collection of low-temperature XRD measurements using the Cryojet. Additionally, low-temperature Raman was conducted using Dr. Steve Firth's Ramascope at UCL Chemistry.

I would also like to thank the instrument scientists on the PEARL beamline at ISIS, namely Dr. Craig Bull, Dr. Nick Funnell and Dr. Chris Ridley, as well as the many pressure engineers who facilitated the collection of the gas cell neutron data.

Data was also collected on the VESUVIO beamline alongside Dr. Giovanni Romanelli and Pierfrancesco Ulpiani. Although the findings from the beamtime are not presented here, I hope that Pier can make good use of the data. Nevertheless, I had a good laugh with you both and learnt some Italian!

I am also indebted to the people that I have received much support from in the Salzmänn Research group. Christoph, you have been a truly exceptional supervisor. I have benefitted immensely from your unrivalled knowledge of all things ice, as well as of general chemistry and physics, all of which has helped me make sense of my experimental findings. Your infectious love for the subject has kept me afloat in some of my most testing times where it felt like my chances of succeeding were slipping away.

Dr. Alexander Rosu-Finsen, thank you for providing me with much support and familiarising me with a great deal of experimental techniques which I was reliant upon. Dr. Martin Rosillo-Lopez and Dr. Martin Hart, even though you are no longer in the group, you both helped me find my footing at the start of the PhD and were always approachable even when I asked the most basic of questions.

Sukhpreet Talewar and Siriney Halukeerthi, I am so glad that you both are in our group. You have been there for me when I've needed to collect XRD data well after everyone else had already left the Chemistry Department. Also, at ISIS you guys brought a layer of craziness to an otherwise extremely gruelling experience! Rachael Smith, thanks for enlightening me about stacking disorder, the antics of the fourth-floor office and for the support you have also given me over the many years we have both been in this group.

Acknowledgements

Dr. Alfred Amon and Bharvi Chikani, even though you are both relatively new members to our group, your help has not gone unnoticed. Divya Amin, you are an honorary member of our group so of course I also need to mention you – you have genuinely gone out of your way with the support you have provided me, I truly appreciate it.

I have also been blessed with the support of several of my close friends Mina Nikitovič, Lisa Sharma, Kate Sanders and Catherine Spencer all of whom have listened to my complaints when things were going wrong and also provided me with encouragement when experiments did take a good turn.

I would also like to mention Prof. Robert Palgrave at UCL Chemistry and Dr. Andy Wain at NPL, both of whom gave me the opportunity to experience a ‘real’ lab during two of my summers in undergraduate study. Without your encouragement and backing, I wouldn’t have had the courage to start (and thankfully complete!) this PhD project.

Last but not least are the (many) members of my family, in particular my aunts and Nani – you have all bolstered me with support and du’as throughout the duration of the PhD. Ammu, thank you for showing your full support in my decision to complete this PhD; you and Tahir have been especially patient with me in this final year. Ammu, thank you also for your final proofread of this. Nafisa, thank you also for all your support and encouragement!

| | |
|---|-----------|
| Table of Contents | |
| Abstract | 3 |
| Impact statement | 5 |
| Acknowledgements | 7 |
| List of symbols | 13 |
| List of abbreviations | 14 |
| List of tables | 15 |
| 1 Introduction | 17 |
| 1.1 Water and ice | 17 |
| 1.2 Crystalline ice | 20 |
| 1.2.1 Bernal-Fowler rules | 22 |
| 1.2.2 Defining ices crystallographically | 22 |
| 1.2.3 Pauling entropy | 24 |
| 1.2.4 Ordering parameters | 25 |
| 1.2.5 Defects in ice | 28 |
| 1.2.6 Doped ice | 29 |
| 1.2.6.1 Hydrogen-ordering agents | 30 |
| 1.2.6.2 Hydrogen-disordering agents | 31 |
| 1.2.7 Hydrogen order from an enthalpy standpoint | 32 |
| 1.3 Amorphous ices | 37 |
| 1.4 Ices with other species | 40 |
| 1.4.1 Ice and ammonium fluoride mixtures | 40 |
| 1.4.2 Clathrate hydrates and filled ices | 52 |
| 1.4.3 Salty ices | 54 |
| 1.5 Ammonium fluoride | 60 |
| 1.5.1 NH_4F I | 65 |
| 1.5.2 NH_4F II | 65 |
| 1.5.2.1 Stacking faulted NH_4F V | 65 |
| 1.5.3 NH_4F III | 66 |
| 1.5.3.1 Stacking faulted NH_4F VI and NH_4F VII | 68 |
| 1.5.4 NH_4F IV | 69 |
| 1.5.5 Liquid NH_4F | 70 |
| 1.6 Aims of this thesis | 71 |
| 1.7 References | 72 |

| | | |
|----------|---|------------|
| 2 | Experimental methods and characterisation techniques | 79 |
| 2.1 | Purity of materials used | 79 |
| 2.2 | Handling of NH_4F | 79 |
| 2.3 | Preparation of mixtures and solutions | 79 |
| 2.3.1 | NH_4F -based solutions and mixtures | 79 |
| 2.3.2 | ND_4F -based solutions and mixtures | 80 |
| 2.4 | Sample preparation techniques | 81 |
| 2.4.1 | Splat-quenching | 81 |
| 2.4.2 | High-pressure samples | 81 |
| 2.4.2.1 | Frimo HyPress 30 tonne hydraulic press | 81 |
| 2.4.2.2 | Zwick Roell Universal Testing Machine | 81 |
| 2.4.3 | PEARL, ISIS experiments | 84 |
| 2.4.3.1 | TiZr and CuBe gas cells on PEARL | 86 |
| 2.5 | Diffraction | 87 |
| 2.5.1 | Crystallinity | 87 |
| 2.5.2 | Diffraction | 88 |
| 2.5.2.1 | Bragg's Law | 88 |
| 2.5.3 | Intensity | 89 |
| 2.5.4 | Atomic structure factors and scattering length | 90 |
| 2.5.5 | X-ray diffraction | 92 |
| 2.5.5.1 | Low temperature XRD | 93 |
| 2.5.6 | Neutron diffraction | 94 |
| 2.5.6.1 | Low temperature ND | 95 |
| 2.6 | Differential scanning calorimetry (DSC) | 95 |
| 2.6.1 | Low temperature DSC | 96 |
| 2.7 | Raman spectroscopy | 97 |
| 2.7.1 | Low temperature Raman | 98 |
| 2.8 | Software | 100 |
| 2.8.1 | MCDIFFaX | 100 |
| 2.8.2 | General Structure Analysis System – GSAS | 103 |
| 2.9 | References | 104 |
| 3 | Mapping the phase diagram of H_2O-NH_4F mixtures | 107 |
| 3.1 | Ambient pressure NH_4F - H_2O ices | 107 |
| 3.1.1 | X-ray investigations into ice-ammonium fluoride mixtures | 107 |
| 3.1.2 | Calorimetric investigations into ice-ammonium fluoride mixtures | 111 |

| | | |
|------------|--|------------|
| 3.1.3 | Conclusions..... | 113 |
| 3.2 | Mixtures of ice and ammonium fluoride at 0.5 GPa..... | 114 |
| 3.2.1 | From 0 to 2.5 mol% NH ₄ F | 114 |
| 3.2.2 | Beyond 2.5 mol% NH ₄ F | 116 |
| 3.2.2.1 | Up to 10 mol% NH ₄ F, holding onto ice V character..... | 119 |
| 3.2.2.2 | 12 mol% to 50 mol% NH ₄ F, the unexpected dominance of ice XII-type structures | 120 |
| 3.2.2.3 | 60 mol% to 90 mol% NH ₄ F, the eventual separation of mixtures..... | 124 |
| 3.2.3 | Conclusions..... | 126 |
| 3.3 | References | 128 |
| 4 | Mapping the 2.5 mol% NH₄F ice phase diagram up to 1.7 GPa..... | 130 |
| 4.1 | Isobaric ice IX↔III heat cycling at 0.3 GPa on PEARL | 130 |
| 4.1.1 | Introduction..... | 130 |
| 4.1.2 | Aims..... | 131 |
| 4.1.3 | Outline of ISIS experiment | 131 |
| 4.1.4 | First observation of the reversible conversion between ices III ↔ IX at 0.3 GPa | 133 |
| 4.1.5 | Conclusions..... | 137 |
| 4.2 | Mapping of phases in the 0.3 to 0.8 GPa region on PEARL | 138 |
| 4.2.1 | Conclusions..... | 140 |
| 4.3 | Volume-change mapping of the 2.5 mol% NH₄F-ice phase diagram up to 1.7 GPa | 141 |
| 4.3.1 | Aims..... | 141 |
| 4.3.2 | Volume change plots from 0.5 to 1.7 GPa..... | 141 |
| 4.3.3 | The unusual competition between ices IV, XII and VI | 143 |
| 4.3.4 | The formation of pure 2.5 mol% NH ₄ F-ice XII..... | 144 |
| 4.3.5 | The final 2.5 mol% NH ₄ F-ice phase diagram..... | 147 |
| 4.3.6 | Conclusions..... | 149 |
| 4.4 | References | 151 |
| 5 | Pressure-induced amorphisation of NH₄F-H₂O mixtures | 153 |
| 5.1 | Introduction | 153 |
| 5.2 | Aims | 159 |
| 5.3 | Pressure collapses of 0 to 100 mol% NH₄F-ice mixtures..... | 159 |
| 5.4 | Assessing the cross-over to PIA to crystallisation | 161 |
| 5.4.1 | XRD determination of amorphous character | 161 |

| | | |
|------------|--|------------|
| 5.4.2 | Calorimetric insights into the character of the compressed solid solutions..... | 167 |
| 5.5 | Conclusions | 169 |
| 5.6 | References | 171 |
| 6 | Phase behaviour of high-pressure NH₄F II and III at ambient pressure.... | 173 |
| 6.1 | Aims | 173 |
| 6.2 | Preparation of NH ₄ F II and NH ₄ F III | 173 |
| 6.3 | Observation of stacking disorder from heating NH ₄ F II..... | 175 |
| 6.4 | Observation of stacking disorder from heating NH ₄ F III | 178 |
| 6.5 | A comparison of cubicities of heated NH ₄ F II and NH ₄ F III | 182 |
| 6.6 | Calorimetric trends on heating the high-pressure phases of NH ₄ F | 183 |
| 6.7 | Conclusions | 186 |
| 6.8 | References | 188 |
| 7 | HCl-doped ices | 190 |
| 7.1 | The removal of residual disorder within ice IX..... | 190 |
| 7.1.1 | Introduction..... | 190 |
| 7.1.2 | Aims..... | 193 |
| 7.1.3 | Calorimetric detection of hydrogen disorder | 194 |
| 7.1.4 | Kinetic/thermal control of order | 196 |
| 7.1.5 | Acid-doping with 0.01 M HCl | 198 |
| 7.1.6 | Spectroscopic consideration of inherent hydrogen disorder..... | 202 |
| 7.1.7 | Conclusions..... | 204 |
| 7.2 | The metastability region of ice V/XIII..... | 206 |
| 7.2.1 | Introduction..... | 206 |
| 7.2.2 | Aims..... | 211 |
| 7.2.3 | Determining the metastability region of ice V/XIII..... | 211 |
| 7.2.4 | The effect of pressure and cooling rate of sample preparation | 214 |
| 7.2.5 | Conclusions..... | 221 |
| 7.3 | References | 222 |
| 8 | Final conclusions and outlook | 225 |
| 8.1 | References | 228 |
| | Appendix..... | 229 |

List of symbols

| | | Units |
|--------------------|---------------------------------|-----------------------------------|
| \AA | Angstrom | \AA or 10^{-10} m |
| θ | angle | $^{\circ}$ |
| $^{\circ}\text{C}$ | Celsius | $^{\circ}\text{C}$ |
| Φ_c | Cubicity | - |
| μ | Decoupled wavenumber shift | cm^{-1} |
| ρ | Density | g cm^{-3} |
| H | Enthalpy | J mol^{-1} |
| T_g | Glass transition temperature | K |
| C_p | Isobaric specific heat capacity | $\text{J mol}^{-1} \text{K}^{-1}$ |
| K | Kelvin | K |
| M | Molar concentration | mol dm^{-3} |
| T_{om} | Onset melting temperature | K |
| α | Ordering parameter α | - |
| β | Ordering parameter β | - |
| T_q | Quenching temperature | K |
| ν | Wavenumber shift | cm^{-1} |

List of abbreviations

| | |
|------------|-----------------------------------|
| 3D | Three dimensional |
| ΔV | Change in volume |
| <i>c</i> | Cubic |
| CS | Cubic structure |
| DFT | Density functional theory |
| DSC | Differential scanning calorimetry |
| FWHM | Full-width half-maximum |
| <i>h</i> | Hexagonal |
| HDA | High-density amorphous ice |
| HDL | High-density liquid |
| HS | Hexagonal structure |
| LDA | Low-density amorphous ice |
| LDL | Low-density liquid |
| ND | Neutron diffraction |
| PIA | Pressure-induced amorphisation |
| <i>p-T</i> | Pressure-temperature |
| <i>sd</i> | Stacking disordered |
| w% | Weight percent |
| XRD | X-ray diffraction |

List of tables

| | |
|---|----|
| <i>Table 1.1: Phases of ice which achieve ordering with the introduction of either an acid or base dopant as listed. Where several acid dopants are included for one phase ordering process, they are listed in order of decreasing efficacy.</i> | 30 |
|---|----|

| | |
|--|----|
| <i>Table 1.2: Bulk amorphous solid ice forms categorised with respect to density and preparation method.</i> | 38 |
|--|----|

| | |
|--|----|
| <i>Table 1.3: Crystal structures of the polymorphs of NH₄F reported with their space groups. Nitrogen, fluorine and hydrogen atoms are shown by blue, green and white spheres respectively. Hydrogen bonds between fluorine atoms and hydrogen atoms are shown by black dotted lines. The hydrogen positions are not shown in NH₄F IV and NH₄F Isd, as they are unknown for the former, and do not affect the structure for the latter.</i> | 61 |
|--|----|

| | |
|--|----|
| <i>Table 1.4: Simulated XRD patterns using Cu Kα radiation of the known polymorphs of NH₄F shown with their Miller indices. Prepared by the author.</i> | 63 |
|--|----|

| | |
|---|----|
| <i>Table 1.5: Calculated unit cell data for NH₄F III with space group symmetry P4₃m and lattice parameter $a = (3.284192 \pm 0.000112) \text{ \AA}$. The values were calculated from reducing the symmetry of an ice VII cell and then performing a Rietveld refinement of a sample of NH₄F III at ambient pressure and 95 K.</i> | 67 |
|---|----|

| | |
|--|----|
| <i>Table 1.6: Structural data for NH₄F IV with the cubic space group Fm3m which has the lattice parameter $a = (5.77 \pm 0.04) \text{ \AA}$, as determined from Calvert et al.'s suggestion that the material is isostructural with NaCl. The positions of the hydrogen atoms are unknown.</i> | 70 |
|--|----|

| | |
|---|----|
| <i>Table 2.1: Range of p-Ts recorded of powdered 2.5 mol% ND₄F in D₂O in a CuBe/TiZr can.</i> | 86 |
|---|----|

| | |
|--|------------|
| <i>Table 2.2: Range of p-Ts recorded of powdered 2.5 mol% ND₄F in D₂O in a TiZr can.....</i> | <i>86</i> |
| <i>Table 2.3: X-ray structure factors and neutron scattering lengths for a variety of species.....</i> | <i>92</i> |
| <i>Table 3.1: Lattice constants of solid solutions of NH₄F-ice calculated from the XRD patterns shown in Figure 3.1. The values at 0 mol% NH₄F are the literature values given by Fortes⁵ which were used to ‘calibrate’ the rest of the measurements.....</i> | <i>109</i> |
| <i>Table 4.1: Fractional coordinates, atomic displacement parameters and occupancies for 2.5 mol% ND₄F ice III at 210 K and 0.3 GPa. The associated lattice constants are $a = 6.66444 \text{ \AA}$, $c = 6.878615 \text{ \AA}$</i> | <i>134</i> |
| <i>Table 4.2: Fractional coordinates, atomic displacement parameters and occupancies for 2.5 mol% ND₄F ice IX at 150 K and 0.3 GPa. The associated lattice constants are $a = 6.669404 \text{ \AA}$, $c = 6.797101 \text{ \AA}$</i> | <i>134</i> |
| <i>Table 7.1: Ice III fractional occupancies of atoms within the unit cell as defined by their ordering parameters.</i> | <i>191</i> |
| <i>Table 7.2: Spread of enthalpies relating to ice IX samples from scans (1a), (1b) and (2a) in Figure 7.4. Percentages of Pauling entropy are also shown bearing in mind the caveat mentioned in the text. The heating rate of the DSC in all cases was 10 K min^{-1}. The protiated ice IX appears to retain disorder on sample preparation with more ease than the other samples.</i> | <i>197</i> |
| <i>Table 7.3: Ice V fractional occupancies of atoms within the unit cell as defined by their ordering parameters.</i> | <i>207</i> |

1 Introduction

This chapter firstly considers the relevance of liquid and solid H₂O before delving into the entire family of crystalline and amorphous forms of ice. Following this, ices co-existing with other species are discussed, and lastly focus is placed on the states of pure NH₄F.

1.1 Water and ice I

Water is required for many physical, chemical and biological processes, and its abundance on Earth, distinguishes it from other planets in the Solar System.^{1, 2} The water molecule is composed of only three atoms and assumes a bent configuration as shown in Figure 1.1 where the angle between the oxygen atom and hydrogen atoms is 104.5°.²

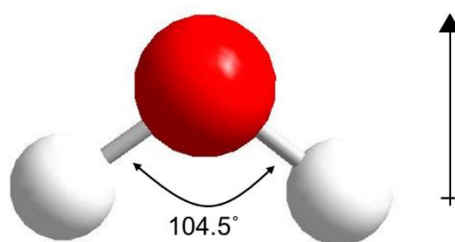


Figure 1.1: A water molecule, composed of an oxygen atom (red) and two hydrogen atoms (white). A dipole moment exists due to the large differences in electronegativity between the oxygen and hydrogens.

As oxygen is electronegative, it is able to ‘pull’ electrons that exist along the O–H bond towards itself, leading to the formation of δ^+ on the hydrogen and δ^- on the oxygen.^{3, 4} The asymmetric charge distribution over the molecule creates a permanent dipole moment.⁴ Hence when water molecules interact with one another they do so using dipole-dipole interactions (along with other higher and lower order interactions); they also interact *via* hydrogen bonds.⁴ Positive and negative charge is oriented along a central water molecule in a tetrahedral conformation (Figure 1.2), meaning that four water molecules interact with the one central water molecule.⁴ In such a case the lone pairs of electrons on the oxygen are hydrogen-bond donors to the hydrogen atoms which act as hydrogen bond acceptors.⁴

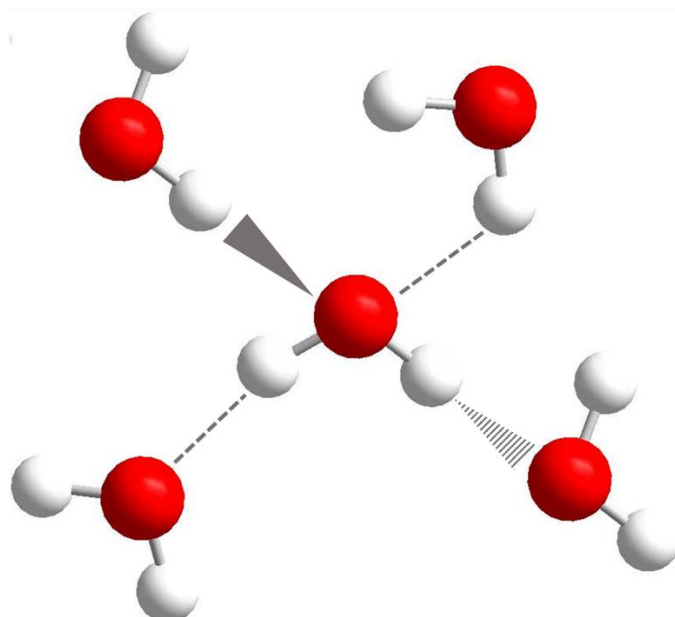


Figure 1.2: An ensemble of water molecules interacting via hydrogen bonding shown by grey lines in the known tetrahedral arrangement of water. This tetrahedral configuration is adopted on cooling water to form ice.

Hydrogen bonding within a water pentamer (Figure 1.2) can explain its many unusual and extraordinary properties.^{5, 6} The boiling point of water, for instance, is far higher than would be expected with respect to trends followed by other group 6 dihydrides.⁵ Water is known to have a range of unusual thermodynamic and kinetic properties such as its density maximum at 4°C, expansion upon freezing and high heat capacity.⁷ Without these anomalous properties, it seems fair to say that life on Earth would not exist as it does today.

The freezing of water at 0°C leads to the formation of an equally intriguing species – ice. When water freezes to form ice, it takes on the tetrahedral conformation referred to previously in Figure 1.2. Ice, in similarity to water, also covers swathes of the planet, for example in the form of icebergs, however, unlike other solids, it does not sink in water.⁸ This is due to the lower density of ice ($0.91668 \text{ Mg m}^{-3}$ at 0°C) to water (0.9998 Mg m^{-3} at 0°C), which is a consequence of the open-channel structure adopted by ice.^{3, 8}

Layers of ice molecules can stack in different arrangements giving rise to different polytypes of ice. Figure 1.3 depicts the different polytypes of ice I with respect to the layers of oxygens that build up its framework. The type of stacking present is

denoted by an italicised initialisation after ice I; other authors also use the subscript of the initialised letter.

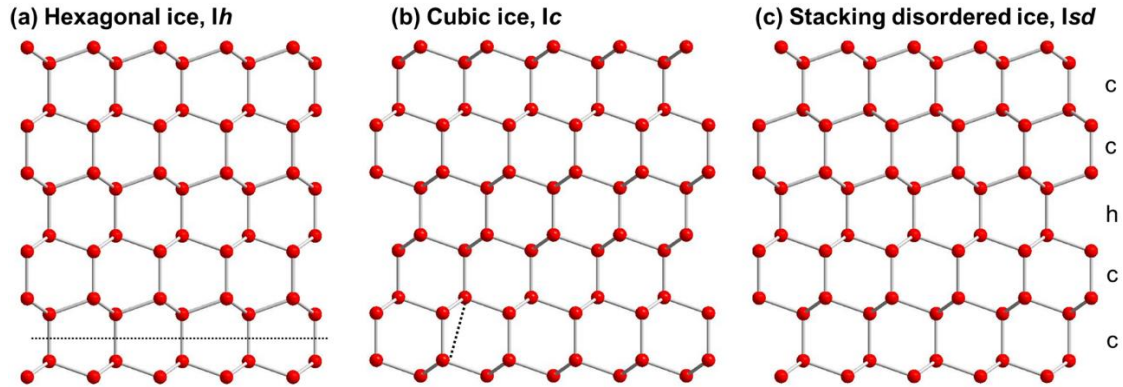


Figure 1.3: Representation of different structures of ice I based on stacking of layers of water molecules. The hydrogens are omitted for simplicity. (a) shows hexagonally stacked ice, each chair layer conformation of oxygen atoms contains mirror image stacking. (b) demonstrates cubically stacked ice that contains layers which are shifted halfway across the six-membered rings. (c) shows an example of stacking disordered ice, which contains a combination of hexagonal and cubically stacked ice indicated by the letters h and c respectively.

The ice that we are familiar with, hexagonal ice (or ice *I_h*) comprises hexagonally stacked layers of water molecules as shown in Figure 1.3(a). In nature, another common form of stacking of layers of atoms is referred to as cubic (Figure 1.3(b)). Cubic ice (ice *I_c*) was prepared for the first time concurrently in 2020 by del Rosso *et al.*⁹ and by Komatsu *et al.*¹⁰ and is depicted in Figure 1.3(b). Prior to this milestone, there has been mention of cubic ice, however this was actually another metastable phase which should be referred to as stacking disordered ice (*I_{sd}*); an example structure of this is shown in Figure 1.3(c). Kuhs *et al.*^{11, 12} and Malkin *et al.*¹³ are among researchers who are proponents of the correct naming of stacking disordered ice, which in fact ice is made up of a mixture of hexagonally and cubically stacked layers. Stacking disordered ice can be defined with respect to the percentage of cubic stacking it possesses¹⁴ – this is termed as its cubicity (Φ_c)¹⁵ – and it can be determined quantitatively from diffraction data.¹⁶

Depending on the polytype, ice I is formed of either chair- or boat-type ring conformations of interconnected oxygen atoms between layers. Cubic ice is composed solely of chair-type linking between layers, while hexagonal ice contains a 50:50 mixture of armchair and boat conformations.¹⁵

1.2 Crystalline ice

An entire family of 18 experimentally known ice modifications exist over a large p - T (pressure-temperature) range as shown in the phase diagram of ice.¹⁷ They are numbered with Roman numerals in order of their discovery.¹⁶ Deuterated analogues can be obtained for each phase and they are known to be structurally similar to their protiated counterparts,¹⁸ whose melting temperatures at triple points differ slightly from their protiated forms.⁸ The development of high pressure apparatus, such as Bridgman's seal,¹⁹ allowed for the discovery of the first few phases of ice by pioneers such as Tammann and Bridgman.^{20, 21} The further development of apparatus and analysis techniques laid the groundwork for the increasing number of modifications to be found. The most recently discovered phase of ice, superionic ice XVIII, was prepared by Millot and co-workers after the shockwave compression of water, which concurrently heated and compressed water to a maximum of 3000 K and 400 GPa.¹⁷

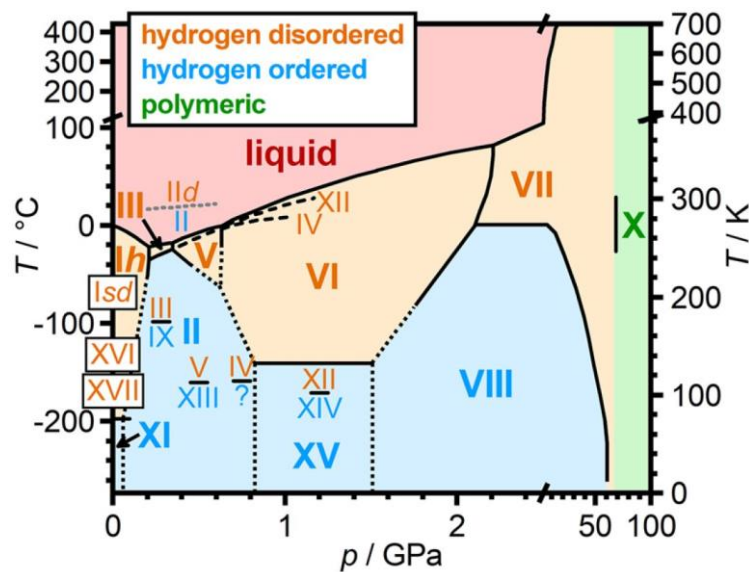
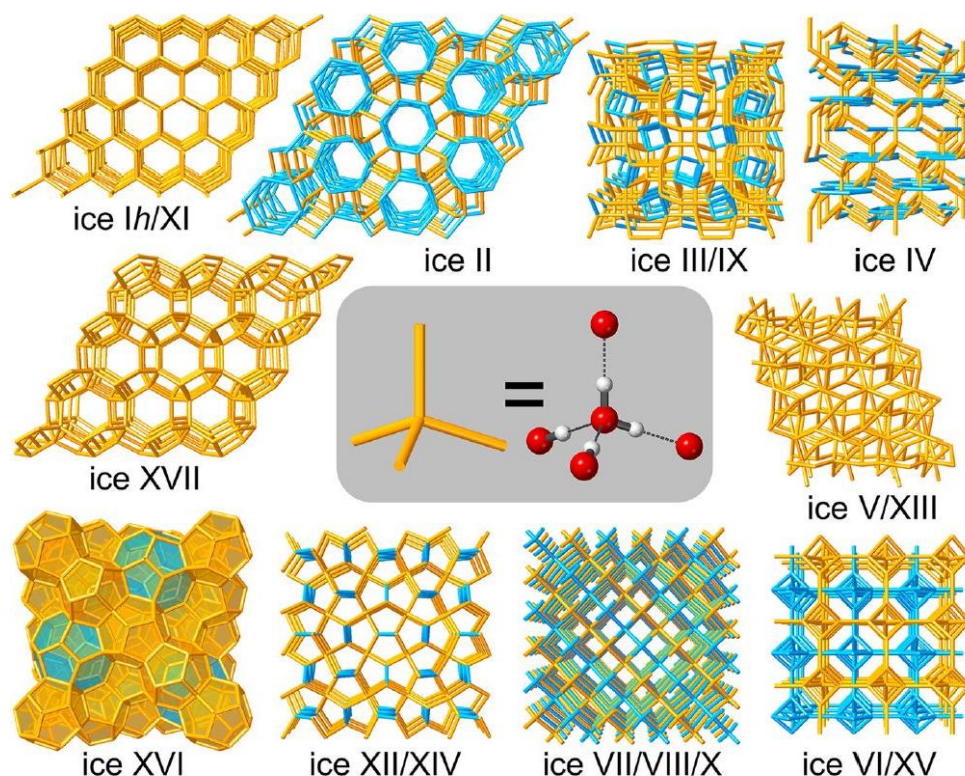


Figure 1.4: The phase diagram of ice, which displays most known crystalline phases, bar ices Ic and XVIII. Phases are grouped into hydrogen-disordered phases (orange), and hydrogen-ordered phases (blue). The red area maps the liquid region, while the green shading indicates where the polymeric ice X resides. Thermodynamic phases are shown in bold, while metastable phases are shown in lighter font weight. The dashed lines show the metastable melting lines of ices IV and XII. The dotted lines indicate extrapolated phase boundaries at low temperatures. Although ice IId has not been isolated experimentally, it has been computationally calculated as existing in the liquid region of the phase diagram. Reprinted from C. G. Salzmann, *J. Chem. Phys.*, 2019, **150**, 060901,¹⁴ with the permission of AIP Publishing.

1. Introduction

The phases of ice can be grouped into different categories, as seen by the different colour coding used in Figure 1.4. The majority of ices can be grouped into hydrogen-disordered and hydrogen-ordered phases. Hydrogen-disordered phases exist at high temperatures, and when cooled, reduce in entropy to form their hydrogen-ordered counterparts which are topologically related, as shown in Figure 1.5. These share the same oxygen network as their hydrogen-disordered counterparts but have different hydrogen positioning, which will be discussed in more detail later.



*Figure 1.5: Various phases of ice shown as rings made up of linked tetrahedra shown in their hydrogen disorder/order pairs. The blue features highlight notable structural features of the ices – for instance ices VI/XV and VII/VIII are formed by two interpenetrating networks but not hydrogen bonded network topologies. Reprinted from C. G. Salzmann, *J. Chem. Phys.*, 2019, **150**, 060901,¹⁴ with the permission of AIP Publishing.*

As would be expected, phases that exist at higher pressures tend to have greater densities. The increases in density are initially realised by the bending of hydrogen bonds, and later the interpenetration of networks.¹⁶ This leads to an array of different polymorphs such as ice II, which can be considered to be akin to ice nanotubes that are hydrogen bonded to each other. Ice IV achieves its density in an interesting manner, it contains flat six-membered rings which have a hydrogen-bonded layer ‘threaded’

through.²² Density increases achieved by the interpenetration of rings are also well illustrated in ices VI/XV and VII/VIII.¹⁶ However, not all phases have an experimentally found hydrogen -ordered or -disordered corresponding pair; examples of this are ices IV and II. Computational studies have predicted that the hydrogen-disordered counterpart of ice II, named ice II*d*, would theoretically exist in the liquid region (as indicated in Figure 1.4).²³

An important remark should be made with respect to nomenclature – a host of papers and books incorrectly name hydrogen-dis/ordered as being ‘proton’-dis/ordered. This is factually unsound as it is an actual hydrogen atom (*i.e.* a proton and electron) that exists in a bond with oxygen. In fact, the incorrect wording could potentially cause confusion with respect to discussions about ice containing defects and dopants (as is explained later on in this chapter).

1.2.1 Bernal-Fowler rules

In the early days of ice research, the analysis of ice I*h* led to a series of conjectures attempting to explain the bonding present in ice.²⁴ Bernal and Fowler, who worked just around the corner from UCL at Birkbeck College, developed ice rules to rationalise bonding in ice. The so-called Bernal-Fowler rules state that:

- (1) one hydrogen atom is found along each of the hydrogen bonds, and
- (2) two hydrogen atoms are covalently bonded to each oxygen atom to maintain the stoichiometry of H₂O.¹⁶

1.2.2 Defining ices crystallographically

Referring back to Figure 1.2, the notion of ice freezing in a tetrahedral conformation was introduced, hence ice can be thought of as H₂O tetrahedra linking in different orientations, six of which are possible, as shown in Figure 1.6.

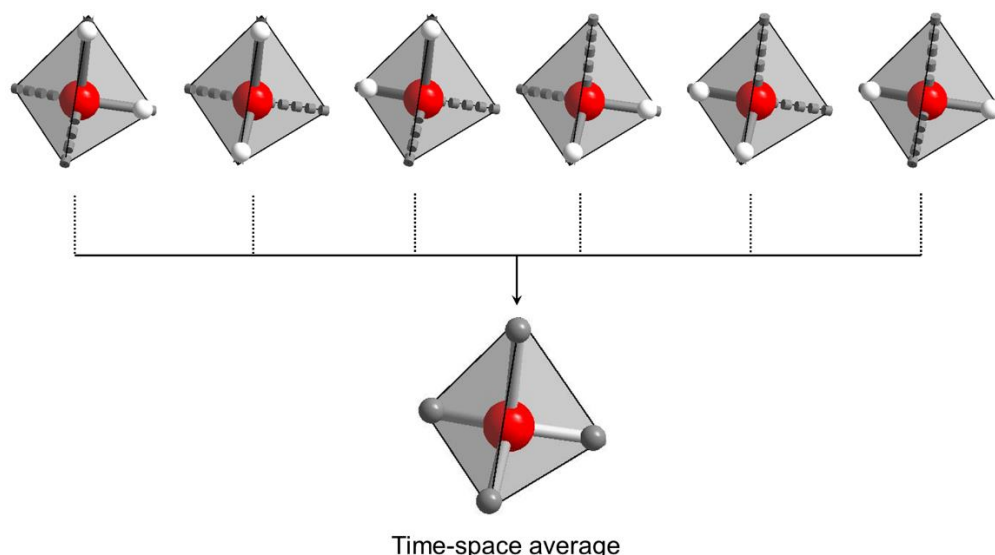


Figure 1.6: The six possible orientations of hydrogen positions in ice tetrahedra which satisfy the stoichiometry requirement given by Bernal and Fowler.²⁴ The solid bonds represent full bonds, while the dashed bonds are hydrogen bonds. This can be averaged to the H_4O tetrahedron over time, with the hydrogens (grey atoms) now assuming occupancies of a half.

If in a crystal, all the hydrogens bound to oxygens are positioned in one orientation, the resulting ice is referred to as being hydrogen-ordered. On the other hand, if the hydrogens are oriented so they adopt more than one position the resulting ice is referred to as being hydrogen disordered.

Crystallographically, hydrogen dis/order can be explained as follows as in the schematic in Figure 1.7 for square ice, a two-dimensional model to represent the H_4O tetrahedron. Hydrogen-disordered phases cannot strictly be described in terms of crystallography due to the long-range disorder of the hydrogen atoms. Instead, such structures can be described as having hydrogens with occupancies averaging 0.5; this is the manner in which a hydrogen disordered ice would appear crystallographically as diffraction maps the time-space average of a series of randomly oriented hydrogens from the six possible orientations (Figure 1.6). Conversely, in hydrogen-ordered phases the hydrogen sites have occupancies of either 0 or 1.^{16, 23} It should be noted that all except one of the hydrogen-ordered phases of ice are antiferroelectric, meaning that they have no net dipole moment.¹⁶ Ice XI has been classed as being ferroelectric,¹⁶ yet this classification has recently been questioned.²⁵

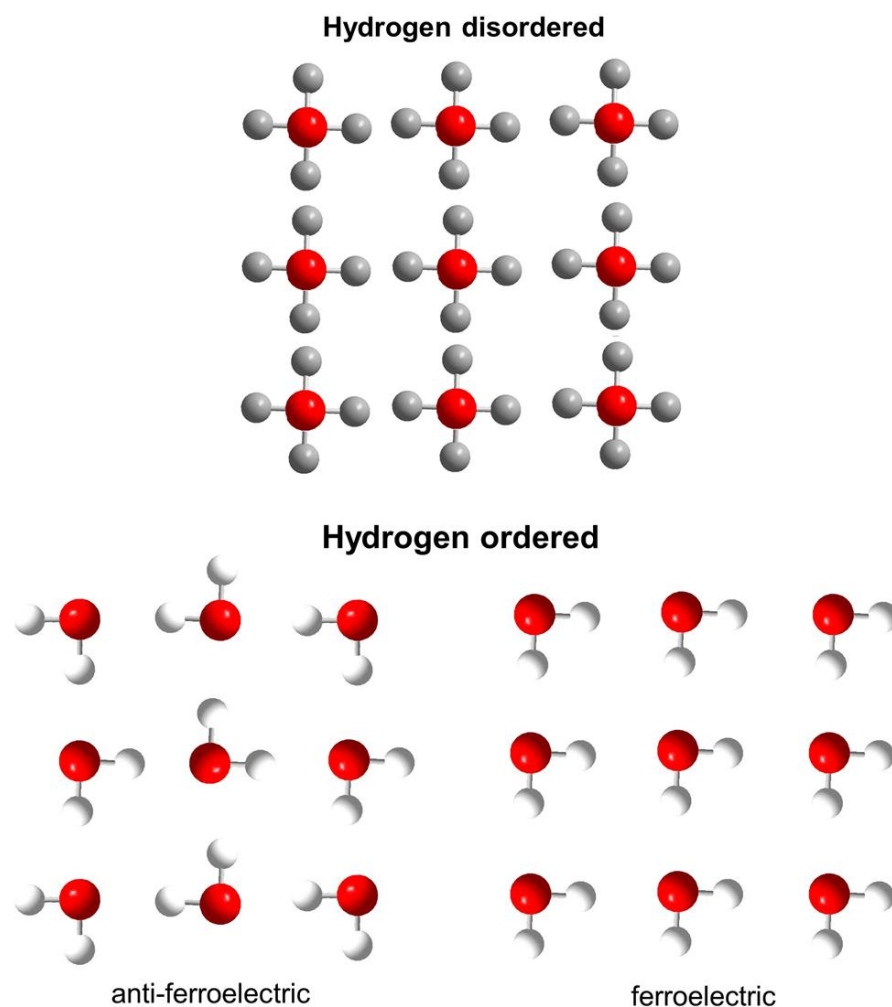


Figure 1.7: Crystallographic definition of hydrogen disordered and ordered phases of ice in terms of square ice. The red atoms show oxygens; grey atoms are half-occupied hydrogen sites, while the white atoms are of fully occupied hydrogens. Hydrogen-ordered ice can be further classified as being ferroelectric or antiferroelectric, where a net dipole moment either exists or is non-existent.

The determination of hydrogen occupancies is usually achieved with neutron diffraction, though here deuterated analogues are used due to their preferential scattering properties compared to protium.³

Ordering of hydrogens occurs at lower temperatures whereby entropy decreases in accordance with the third law of thermodynamics.²⁶ In practice, it is difficult to access highly ordered states, as disorder can easily be retained because of the slowing down of molecular reorientation of the water molecules.^{16, 27, 28}

1.2.3 Pauling entropy

To provide a benchmark in the expected molar entropy change between a completely hydrogen-ordered and a completely hydrogen-disordered state, one can consider the

1. Introduction

entropies of a fully ordered and fully disordered state (which is referred to as the Pauling entropy⁸).¹⁶

From the six different orientations of ice in Figure 1.6, a derivation of the zero-point configurational entropy of ice can be elicited. Boltzmann's relation states that the molar entropy, S , can be found from the gas constant, R , and the number of configurations, W :

$$S = R \ln W \quad \text{Equation 1.1}$$

To determine the molar configurational entropy of a hydrogen-disordered state it can be considered that there are $2N$ hydrogens per N oxygen atoms which can be positioned in two places. Also, at each oxygen site, there are 16 possible arrangements of oxygen. However, of all these arrangements only 6 are allowed. Hence, at each oxygen site, W is determined as the following:

$$\begin{aligned} W &= 2^{2N} \left(\frac{6}{16}\right)^N & \text{Equation 1.2} \\ &= 4^N \left(\frac{3}{8}\right)^N \\ &= \frac{3}{2} \text{ microstates} \end{aligned}$$

Therefore, for a hydrogen-disordered state: $S = R \ln \frac{3}{2}$.

There is only one arrangement for an hydrogen-ordered ice, *i.e.* $W=1$, so $S = 0$.

Hence, the determination of the difference in molar configurational entropy, ΔS , is as follows:

$$\begin{aligned} \Delta S &= \text{Entropy of hydrogen-disordered ice} - \text{Entropy of hydrogen-ordered ice} \\ &= R \ln \frac{3}{2} - R \ln 1 \\ &= R \ln \frac{3}{2} \\ &= 3.37 \text{ J mol}^{-1} \text{ K}^{-1} \end{aligned}$$

This difference in molar configurational entropy is called the Pauling entropy.⁸

1.2.4 Ordering parameters

In reality, only several phases of ice (such as ices *Ih*, *VI* and *VII*) are either fully ordered or fully disordered with respect to their hydrogen positions.²⁹ Ices *III* and *V* are

examples of phases, which although originally classified as being hydrogen disordered,³⁰⁻³² possess a degree of partial order.^{29, 33} This is reflected in the fact that their associated hydrogen/deuterium occupancies are not equal to 0, 1 or 0.5. In such cases, the fractional occupancies of hydrogens are usually described with occupancy probabilities denoted by Greek letters, such as α and β .^{29, 34}

For example, if the hydrogen occupancy is given by α , so it goes that the occupancy of the remaining hydrogen-bonded site to the same oxygen must be given by $(1 - \alpha)$, as in Figure 1.8, so that along one hydrogen bond only one hydrogen atom exists.²⁹ This is because geometrically, along a bond connecting two oxygens, the occupancy of hydrogen must equal one in accordance with Bernal-Fowler rules.³⁵ This greatly simplifies the way in which hydrogen occupancies within an ice phase are defined by reducing the number of parameters that describe occupancies and hence the state of hydrogen order/disorder. Ice V, which is schematically represented in Figure 1.8, represents the structurally most complex form of a hydrogen-disordered ice which requires four separate ordering parameters: α , β , γ and δ .²⁹ Its hydrogen-ordered counterpart – ice XIII – is actually the most structurally complex ice phase, and it requires 8 distinct ordering parameters.

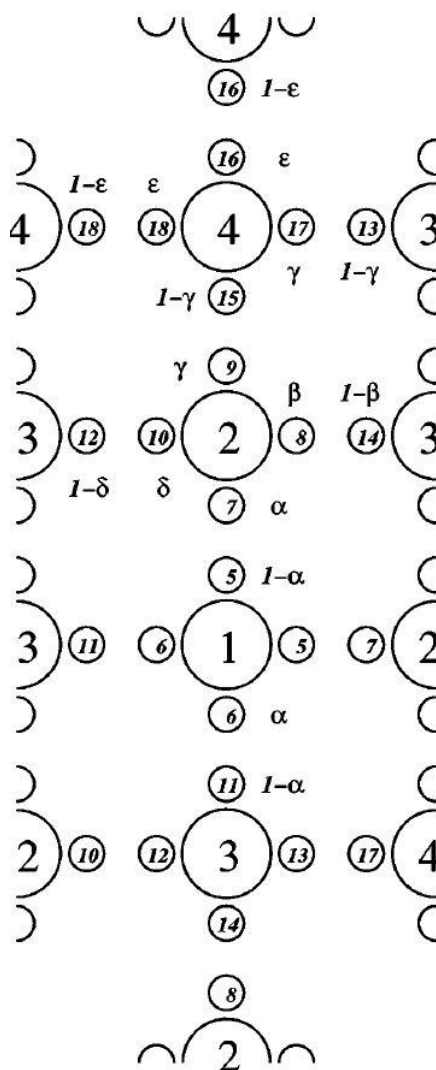


Figure 1.8: Local environment of non-equivalent atoms in ice V, the most structurally complex hydrogen-disordered ice, reflected by its four ordering parameters. The large and small circles represent numbered oxygen and hydrogen atoms respectively, while the Greek letters are their corresponding ordering parameters. Reprinted from L. G. MacDowell, E. Sanz, C. Vega and J. L. F. Abascal, *J. Chem. Phys.*, 2004, **121**, 10145-10158,²⁹ with the permission of AIP Publishing.

Howe and Whitworth developed an extensive approach to estimate the entropy of partially ordered phases which considered the occupancy parameters (linked to specific atoms) and the coupling between occupancies.³⁶ MacDowell *et al.* also demonstrated that the entropy calculation could be split into two terms, the first is the configurational free energy found in simulations, while the second term is added *a posteriori* and provides the estimate of combinatorial entropy.²⁹ Interestingly, it was found that the random hydrogen atom occupancies did not always equate to random orientational disorder because occupancies do not completely determine the percentage of water molecules in a particular orientation.²⁹

1.2.5 Defects in ice

On the cooling of hydrogen disordered ices, the case is more often than not that hydrogen disorder is retained in the form of orientational glasses as there simply is not enough energy to reorient water molecules.^{16, 37} Defects exist in most real structures and in ice they facilitate the reorientation of hydrogens, which is influenced by both the number density of defects and their mobility.^{8, 16} Two families of defects exist – intrinsic and extrinsic, these are shown in Figure 1.9 for square ice. The former result from deficiencies within the structure, while the latter generally occur as a result of the addition of species to the structure. Both types of defects result in the local breaking of the ice rules outlined by Bernal and Fowler.^{16, 38} Interstitial defects can also occur in ice – this is where water molecules are isolated from the bulk structure.⁸

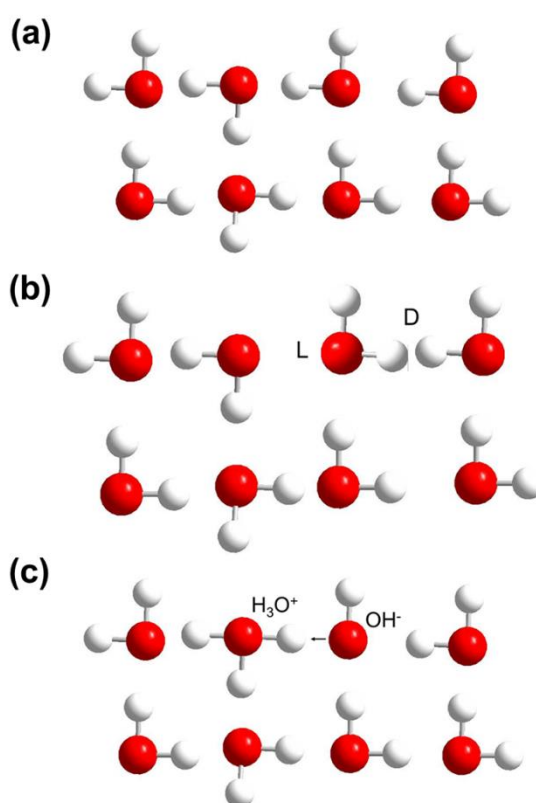


Figure 1.9: (a) A defect-free representation of square ice, which in (b) and (c) is later affected by defects. (b) shows Bjerrum defects result from the rotation of a water molecule causing the formation of an L and D defect; the nearest oxygen-oxygen 'bond' is occupied by no and two oxygens respectively. (c) illustrates ionic defects caused by a proton moving from one water molecule to another leading to the formation of H_3O^+ and OH^- defect pair. (b) and (c) illustrate embryonic defects which is where defects are formed as pairs but have the potential to separate on further molecular rotations and proton exchanges respectively. Adapted from ref.38.

Intrinsic defects are those which involve the displacement of an uncharged atom that originates from the initial structure. In the case of ice, they are known specifically as Bjerrum defects and result from the rotation of a water molecule (Figure 1.9(b)). This violates the ice rule that one hydrogen atom is found along each of the hydrogen bonds. A ‘missing’ hydrogen in a lattice is referred to as an L (or Leere) defect, while having two hydrogens the place of one is known as a D (or a Doppelbesetze) defect.³⁷ Further rotations can occur which result in the L and D defects existing far away from one another – this is often a more electrostatically favourable case.³⁸ Bjerrum defects are present in the order of 10^{-7} defects per mole of ice.⁸

Extrinsic defects are often ionic defects and involve charged species that arise from external species. H^+ ions (protons) can travel from a water molecule leading to the formation of a H_3O^+ and OH^- pair, as shown in Figure 1.9(c). This violates the Bernal-Fowler rule regarding the stoichiometry of the ice.⁸ It should also be noted that ionic defects can also result from within the structure from thermal excitations, without the addition of external species.²³ In such a case there exist approximately 10^{-13} extrinsic defects per mole of ice.⁸

1.2.6 Doped ice

Many of the first studies of ice explored the effect of defects travelling through its structure, as observed *via* conductivity measurements, because even without the addition of dopants, ice has a high conductivity.³⁹ As ice is not very susceptible to letting in impurities, initial attempts at doping involved the trace incorporation of species that were of similar molecular dimensions to it.⁸ For instance, ammonia and hydrogen fluoride were successfully incorporated as part of ice as a molecular solid.⁸ It was found that ammonia encouraged the formation of L and H_3O^+ defects, while hydrogen fluoride encouraged D and OH^- defects in ice.³⁹ The introduction of impurities affects the molecular reorientations within the ice, either aiding, or halting rotational and kinetic processes.²³ More recently, doping of high-pressure ice phases has also been explored, with the extreme case of highly doped ice VII.⁴⁰ Salty ices are discussed separately and in more detail in Chapter 1.4.3, where the focus is on ices that contain far larger concentration of impurities.

1.2.6.1 Hydrogen-ordering agents

There are only two pure ice phases which actually have a sufficient number of intrinsic defects to achieve hydrogen ordering on simply cooling – these are ices III and VII which order to form ices IX and VIII respectively.¹⁶ Because of this, many ice phases were inaccessible until base, and then, acid doping was used to introduce extrinsic defects into the ice structure and lower the energy barrier associated with molecular reorientation.

Table 1.1: Phases of ice which achieve ordering with the introduction of either an acid or base dopant as listed. Where several acid dopants are included for one phase ordering process, they are listed in order of decreasing efficacy. Adapted from Rosu-Finsen et al.²⁵

| Ordering pair | Effective dopants | Ineffective dopants |
|-----------------------|--|---|
| $I_h \rightarrow XI$ | KOH ⁴¹ , LiOH, ⁴² NaOH, ⁴³ RbOH ⁴³ | HF, ⁴⁴ Ba(OH) ₂ , ⁴⁵ KF, ⁴⁵ NH ₄ F ⁴⁵ |
| $V \rightarrow XIII$ | HCl, ⁴⁶ HF, ²⁸ LiOH ²⁵ | HClO ₄ , ³⁷ HBr, ³⁷ NaOH, ³⁷ KOH ²⁸ |
| $XII \rightarrow XIV$ | HCl ⁴⁶ | HF, ⁴⁷ NH ₃ , ⁴⁷ KOH ⁴⁷ |
| $VI \rightarrow XV$ | HCl, ⁴⁸ HF, ²⁵ HBr ²⁵ | HClO ₄ , ³⁷ LiOH, ³⁷ NaOH, ³⁷ KOH ²⁶ |

Ice XI, the hydrogen-ordered counterpart to ice I_h , was accessed on a laboratory timescale for the first time by Kawada by the use of KOH of molarities ~ 0.1 M ($\sim 1:560$ molar ratio of KOH to H₂O).^{16, 41} In order to form the ice, isothermal annealing below the hydrogen-ordering temperature needed to take place for several days, before then cooling further.¹⁶ The observation of the heat capacity on the warming of this ice gave features that could be associated with subsequent hydrogen-disordering of the ice XI to ice I_h – the onset of the disordering peak was observed at ~ 72 K.⁸ It has been proposed that KOH doping creates L and OH[−] defects.^{28, 49} It is assumed that a K⁺ ion sits in an interstitial site, however this is conjecture.⁸

The formation of ice XI in the Galaxy has been proposed, for instance on planets such as Uranus, as it facilitates the low p - T conditions required.⁵⁰ KOH doping was also attempted on further hydrogen-disordered phases, and although it did increase the size of the glass transitions of some ices on heating, was found to be ineffective as an ordering agent.⁵¹⁻⁵³ Surprisingly, it has since been found that LiOH can order ice V and form ice XIII.²⁵

Acid doping has also proven to be very successful in accessing three additional phases of ice – ices XIII, XIV and XV.^{48, 54} Unlike with the basic dopants, the molarities required here are approximately a magnitude of molarity lower at 0.01 M (~1:5600 molar ratio of HCl to H₂O).¹⁶ It is thought that D and H₃O⁺ defects aid ordering when acid dopants are used.^{28, 49} H₃O⁺ defects are thought to initiate a domino effect in the way that they move through the structure, causing a succession of concerted reorientations.²⁵ An extensive study by Rosu-Finsen *et al.* explored the factors affecting the ordering strength of different acid and base dopants on ices V and VI.²⁵ In the end, the high solubility of HCl in ice, along with its high acid strength, which meant that the anion was only bound to the H⁺ weakly, were used to justify its superiority in ordering both ices V and VI.²⁵

Currently, there still are quite large gaps in the understanding of how both basic and acidic dopants work. Much more computational work needs to be performed in order to develop an understanding of the mechanics taking place on the molecular scale.³⁷ Also more experimental data on the solubility of dopants in ice *Ih* and other ice phases under pressure needs to be obtained.³⁷

1.2.6.2 Hydrogen-disordering agents

Intriguingly there have been other consequences of doping in ice, it was discovered by Shephard *et al.*²³ that in the case of using NH₄F as a dopant, ice II could be removed from the phase diagram in a selective fashion. Within ice, the incorporation of NH₄F leads to the substitution of H₂O tetragonal units by pairs of NH₄⁺ and F⁻ ionic species and the subsequent hydrogen-disordering of the ice as shown in Figure 1.10.²³

Generally, for ice *Ih* and several other high-pressure phases of ice, the inherent lack of total hydrogen-bond order within their respective structures can allow for NH₄F inclusion.²³ However, ice II requires an extremely topologically constrained hydrogen-bond network, which was unachievable with the presence of NH₄F.²³ It should be noted that this was the first instance of a dopant being used to omit, not access, a phase from the ice phase diagram.

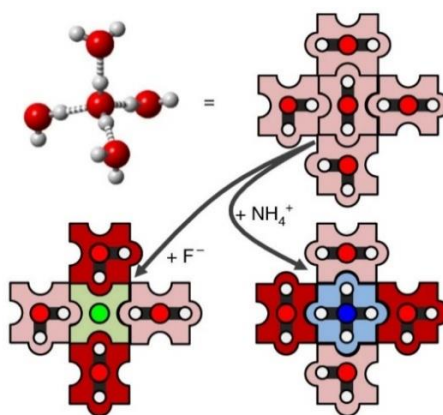


Figure 1.10: Schematic illustrating the disordering effect of NH_4F within ice. A fully hydrogen ordered molecule of ice (top left) can be represented in a two-dimensional square ice model (top right). The square ice is then shown and after disordering by fluoride (bottom left) and ammonium (bottom right) ions. Reprinted by permission from Springer Nature: Springer Nature, *Nature Physics*. J. J. Shephard, B. Slater, P. Harvey, M. Hart, C. L. Bull, S. T. Bramwell and C. G. Salzmann, *Nat. Phys.*, 2018, **14**, 569-572.²³

It is hoped that further studies into NH_4F -doped ice will help resolve anomalies in the pressure-temperature range of ice II on cooling, as shown by *in-situ* neutron diffraction.²³ NH_4F has also been shown to be a hydrogen-disordering agent in the case of ice VII/VIII where it facilitated the retention of disorder, forming a partially disordered ice VIII.⁵⁵

1.2.7 Hydrogen order from an enthalpy standpoint

A schematic plot of enthalpy against temperature can be used to describe the processes that occur to hydrogen-disordered ices upon cooling and then subsequent heating.

In Figure 1.11, the enthalpy, H , represents the degree of hydrogen disorder of the ice, which is related to its entropy *via* the second law of thermodynamics. The glass transition, $T_g(\text{pure})$, represents the temperature at which, on cooling, reorientation dynamics are frozen in, leading to the formation of a so-called glassy state. The cooling of a sample can also lead to hydrogen ordering if the sample reaches the onset temperature of hydrogen ordering (T_o) while still in a dynamic state. The black line represents the dynamic equilibrium line, which is the crossover point between dynamic and glassy states; the individual coloured lines show where molecular reorientation dynamics are frozen.

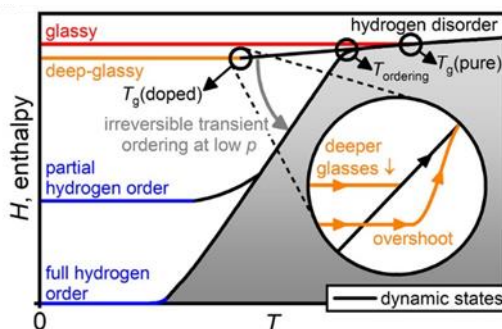


Figure 1.11: Thermodynamic routes taken upon the cooling of hydrogen-disordered ice samples shown with respect to enthalpy and temperature, leading to the formation of either glassy, deep-glassy, partial hydrogen order and full hydrogen order states. $T_g(\text{pure})$ refers to the glassy transition temperature of a pure ice, T_{ordering} refers to the temperature at which an ice begins to order and $T_g(\text{doped})$ is the glass transition temperature of a doped ice. The inset shows a magnification of the region around the glass transition temperature of a doped ice, $T_g(\text{doped})$, and it refers specifically to the heating at ambient pressure of a previously cooled deep-glassy ice sample. Different pathways can be observed upon heating such a sample, as discussed in the text. Reproduced from <https://pubs.acs.org/doi/10.1021/acs.jpcclett.0c00125>,⁵⁶ with permission from the American Chemical Society.

Each phase of ice will have its own unique values for temperatures of interest and enthalpies associated with specific states.¹⁶ Additionally, enthalpies will vary depending on whether a protiated or deuterated ice is being investigated; this is a result of the kinetic isotope effect.²⁸

Generally, low temperatures indicate low entropy states: the third law of thermodynamics states that at absolute zero a perfect crystal exhibits full order, hence $S = 0$. This point of complete hydrogen order is represented by the bottom left of the schematic. Conversely, higher temperatures lead to higher entropy states. A fully hydrogen-disordered state can therefore be marked at the top right of the schematic, where enthalpy and temperature are high. A range of processes can occur with different starting points and destinations of the enthalpic landscape. Four possible pathways are now discussed.

The pathway for a glassy state (red line, Figure 1.11) shows the cooling of a pure, undoped sample of hydrogen-disordered ice, which reaches its $T_g(\text{pure})$ before the onset temperature of hydrogen ordering (T_o), and is consequently trapped in a glassy state on further cooling.⁵⁷ This occurs when there are a lack of intrinsic defects in the ice *i.e.* in ice Ih, V, VI, XII and XI.^{16, 51}

The pathway for a deep-glassy state (orange line, Figure 1.11) presents a similar but slightly more complicated scenario to that of a pure glassy state. Here, doped ice is cooled while hydrogen ordering is suppressed (for instance by the application of excess pressure),⁵⁶ yet it is still able to experience a slight degree of hydrogen ordering as it remains in a dynamic state when it passes T_o due to the presence of the dopant. As this glassy state is lower in enthalpy than that of a pure, undoped ice, it is referred to specifically as a deep-glassy state, with its glass transition temperature occurring at $T_g(\text{doped})$. Slow relaxation dynamics are typical in deep-glassy states, which means that in this pathway, the value of $T_g(\text{doped})$ is not fixed, but dependent upon certain factors.⁵⁷ The slow relaxation dynamics are able to justify the unusual property of increased pressures during cooling, enabling the accessing of deeper glassy states.⁵⁷ Additionally, it is also known that slower cooling of a sample while under pressure leads to deeper glassy states.⁵⁷ Sub- T_g annealing at ambient pressure also produces deeper glassy states.⁵⁷ It should be noted that deeper states can also be achieved in this way for an undoped ice.

The next pathway shown is that where a partially hydrogen ordered state (top blue line, Figure 1.11) is formed. Although reorientation dynamics remain active on cooling below both T_g and T_o , the ice is unable to sustain reorientation dynamics for much longer and eventually at a point above zero entropy, drops out of equilibrium with static states.⁵⁷ This causes the sample to retain a degree of hydrogen disorder, hence it is partially (dis)ordered.

Lastly, the most extreme change in enthalpy is presented which shows a hydrogen-disordered ice cooling with sufficient dynamics below T_g , T_o and remaining to do so while approaching $T = 0$ K to form a fully hydrogen-ordered ice (lower blue line, Figure 1.11).¹⁶ In this case, the initial state is that of a fully hydrogen disordered state transforming to the fully hydrogen ordered state, which goes along with a change in configurational entropy of $R \ln \frac{3}{2}$ ($3.37 \text{ J mol}^{-1} \text{ K}^{-1}$).¹⁶

The heating of deep-glassy ices to reform hydrogen-disordered ices has incited debate among researchers in their attempt to disentangle the processes observed in calorimetry and diffraction. Possible pathways of the heating of deep-glassy states are depicted in the circular inset of Figure 1.11. The more relaxed a deep-glassy state is, the further it drops in enthalpy and the slower the relaxation dynamics it has.⁵⁷ The

degree of relaxation within the state and the specific enthalpies it has with respect to the dynamic equilibrium line affects the order of processes seen on the heating of the ice at ambient pressure. Deep glasses that are particularly relaxed and lower in enthalpy will have slow dynamics on heating.⁵⁷ As it takes longer for the molecular dynamics to unfreeze, the measured enthalpy overshoots the dynamic equilibrium line while still experiencing stunted dynamics.⁵⁷ Such overshoots do not produce latent heat. Hence, it is not possible to calculate entropy changes from them.¹⁴ This is probably one of the few occasions where it becomes necessary to differentiate between the temperature at the dynamic equilibrium line, the fictive temperature (T_f),⁵⁸ and the glass transition temperature ($T_g(\text{doped})$) which always occurs at higher temperatures.⁵⁸ The larger the difference between these temperatures, the greater the overshoot effect is. Such a case is demonstrated for deep-glassy ice VI, shown in scan (3) of Figure 1.12.

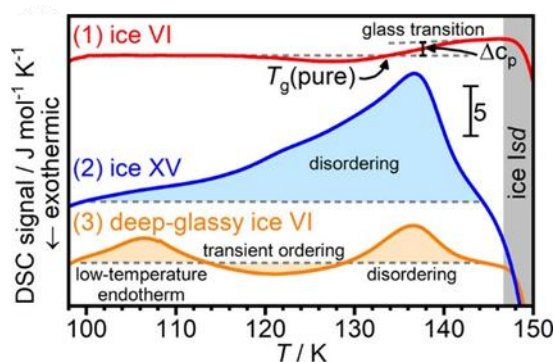


Figure 1.12: Ice VI/XV formed via different methods heated from 93 K in a DSC at 10 K min⁻¹ at ambient pressure. The colours here correspond to those in Figure 1.11, with the red line in (1) deriving from a glassy state, the blue line in (2) coming from an ordered state and (3) coming from a deep-glassy state. (1) shows an undoped ice VI sample being heated and (2) shows an ice XV sample being heated. (3) presents a more complicated scenario related to a deep-glassy state, where the dotted line is an eye-guide to appreciate exo/endo-thermic processes. Reproduced from <https://pubs.acs.org/doi/10.1021/acs.jpcclett.0c00125>,⁵⁶ with permission from the American Chemical Society.

Depending on how relaxed the sample is, the more pronounced the overshoot effect can be – this leads to the appearance of an endotherm in calorimetry.^{56, 57} In some cases, after the reorientation dynamics are unfrozen, the measured enthalpy could find itself well above the dynamic equilibrium line.⁴ In such a situation, to attain a lower enthalpy, the sample then drops in its enthalpy to follow the dynamic equilibrium line during heating. This reduction in enthalpy can cause exothermic ‘transient ordering’, and it is able to occur on heating as pressure is not applied to the sample in the way it is on

cooling during the preparation of the sample.⁴ The further heating of the sample leads to the inevitable hydrogen disordering of the ice which occurs near what was the hydrogen-ordering temperature on cooling. However, due to hysteresis effects it is likely that conversion to the more disordered state will not be at the exact same temperature.²⁸ It should be highly stressed that the processes that occur to deep-glassy states are dictated by kinetics, hence features observed in calorimetry need to be observed *via* structural determination methods if one wishes to also characterise the structures obtained properly.⁵⁷ This is because the kinetic nature of the processes means that they will not necessarily be identical depending on heating rates used in calorimetry or between different pressures and cooling rates used on the formation of the ice. For instance, endotherms may be found to disappear depending on the degree of relaxation obtained, neither do they go along with a change in latent heat.^{14, 57}

Gasser *et al.* incorrectly assigned a deep-glassy state of ice VI to be a new hydrogen-ordered phase of ice XV, which they named β -XV.^{56, 57, 59} The authors claimed that ice β -XV was more and differently ordered than ice XV.⁵⁷ A low temperature endotherm that they used to justify the existence of this phase was found to appear or disappear depending on the heating rate used in calorimetry.^{56, 57, 59} Deuterated analogues could also not be isolated of the phase.⁵⁹ Eventually, Rosu-Finsen *et al.* disproved the existence of ice β -XV and correctly identified it to be a form of deep-glassy ice VI using neutron spectroscopy and diffraction of protiated samples.^{56, 57}

1.3 Amorphous ices

As well as having crystalline forms, ice also exhibits a number of non-crystalline or amorphous forms; hence ice displays polyamorphism.^{37, 60, 61} These ices possess no long range structure and have been considered as disordered or collapsed crystals.

Amorphous ice was first prepared in 1935 by depositing warm water vapour onto a cold substrate which formed a microporous material able to adsorb gases. It was named amorphous solid water (ASW) and is likely to be the most abundant type of water in the universe.⁶⁰

The different types of amorphous ice are strictly metastable forms, so even though they are often referred to as ‘phases’ and ‘states’, it should be noted that these are not strictly thermodynamically correct terms.⁶⁰ With this in mind, it is useful to put into context the regions of pressure and temperature that amorphous ices can exist in (Figure 1.13).

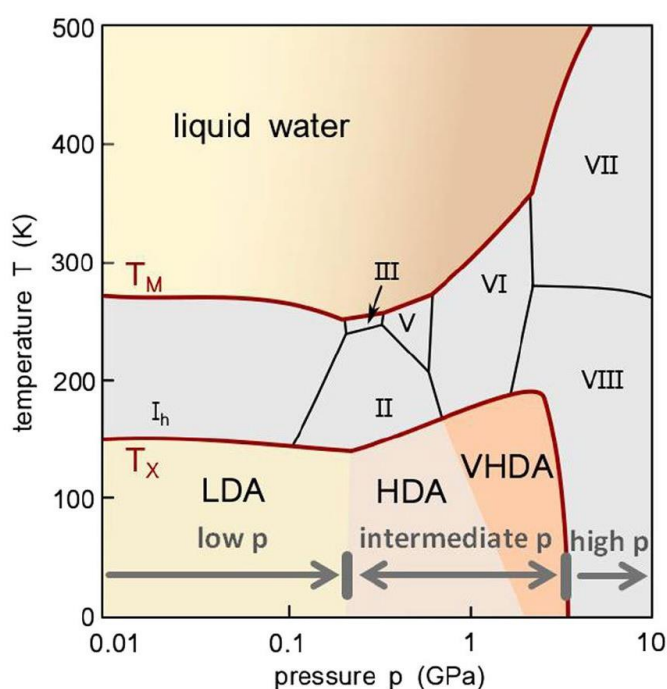


Figure 1.13: The ‘phase diagram’ of amorphous ices in context with their thermodynamically stable crystalline ice counterparts. T_M is the melting line between crystalline modifications and the liquid. T_X is the crystallisation temperature, above this temperature water crystallises rapidly. The blue shaded region bounded by T_M and T_X is referred to as “No man’s land” as here no amorphous forms can be found. Taken from Stern, J., Loerting, T. Crystallisation of the amorphous ices in the intermediate pressure regime. *Sci Rep* 7, 3995 (2017),⁶² with open access article rights (<http://creativecommons.org/licenses/by/4.0/>).

1. Introduction

Amorphous forms of ice can generally be grouped into three classes which allude to their relative densities: these are low-density amorphous ice (LDA); high-density amorphous ice (HDA); and very high-density amorphous ice (vHDA). Controversy exists however, as to whether HDA and vHDA are actually distinct. As can be seen in Figure 1.13, depending on the density of the amorphous ice, it will exist at either relatively lower- or higher-pressure ranges. Since the preparation of ASW, an entire family of amorphous forms have emerged, and they are summarised in Table 1.2 below.

Table 1.2: Bulk amorphous solid ice forms categorised with respect to density and preparation method. Data adapted from reference 60.

| | Sub-types of amorphous ice | Preparation method/sample history | Density / g cm⁻³ |
|---|---|---|------------------------------------|
| Low-density amorphous ice (LDA) | Amorphous solid water (ASW) | Water vapour deposition ^{63, 64} | 0.94 ⁶⁵ |
| | Hyperquenched glassy water (HGW) | Cooling of liquid droplets at 10 ⁷ K s ⁻¹ ⁶⁶ | 0.94 ⁶⁵ |
| | Low-density amorphous ice I (LDA I) | Heating uHDA at <0.1 GPa to 130 K ^{67, 68} | 0.94 ⁶⁵ |
| | Low-density amorphous ice II (LDA II) | Decompression of vHDA at 140 K to ≤ 0.05 GPa ⁶⁸⁻⁷⁰ | 0.94 ⁶⁸ |
| | Low-density amorphous ice from ice VII (LDA(ice VII)) | Heating of ice VII at ambient pressure to 125 K ⁷¹ | - |
| High-density amorphous ice (HDA) | Unannealed high-density amorphous ice (uHDA) | Compression of ice Ih at 77 K to > 1.2 GPa ⁷² | 1.15 ⁷³ |
| | Expanded high-density amorphous ice (eHDA) | Annealing uHDA at 0.18-0.30 GPa to 130 K ⁷⁴ | - |
| | | Decompression of vHDA at 140 K at 0.07 GPa ^{67,70} | 1.13 |
| | | Compression of LDA at 130-140 K to > 0.4 GPa ⁷⁵ | Fig. 5 in ref. 60 |
| | Relaxed high-density amorphous ice (rHDA) | Annealing uHDA at 0.3-1.9 GPa ⁷⁶ | 1.20 to 1.40 ⁷⁶ |
| Very high-density amorphous ice (vHDA) | Very high-density amorphous ice (vHDA) | Annealing uHDA at ≥ 0.8 GPa to > 160 K ⁷³ | 1.26 ⁷³ |
| | | Compression of LDA at ≥ 125 K to ≥ 1.2 GPa ⁷⁷ | - |
| | | Compression of ice Ih at ≥ 130 K to ≥ 1.2 GPa ⁷⁸ | - |

Amorphous ices can be further classed depending on their preparation method. For instance, there are at least four variants of LDA, all of which are made *via* different

routes. It should be noted that Table 1.2 is unlikely to be fully comprehensive; there will undoubtedly be more types of each ice that can be formed from different synthesis pathways.⁶⁰ Despite their inherent lack of long-range order, radial distribution functions can also be used to corroborate density data. Nearest neighbour coordination numbers can be calculated from the integration of the first peak of $g_{OO}(r)$, which shows that LDA, HDA and vHDA have 4-, 5- and 6- nearest neighbours.⁶⁰ This applies to quenched samples studied at ambient pressure. Here it should be noted that the LDA values apply to both LDA I, LDA II, HGW and ASW highlighting their structural similarity.^{60, 79} Additionally, Shephard *et al.* noted that LDA formed from ice VII was distinct from LDA I and LDA II, which themselves were deemed to be structurally identical.⁷¹

Interestingly, some uHDA can also be made from crystalline phases.^{71, 80} A synthesis route of an amorphous form (uHDA) deriving from a crystalline ice phase was first prepared by ‘melting’ ice I at 1 GPa and 77 K, as indicated in Table 1.2.⁸⁰

Depending on the degree of relaxation within the amorphous ice, the mass density of the ice will either change significantly with time or stay the same.⁶⁰ The latter case is that of a well-relaxed glass which can be considered as equilibrated with respect to the metastable state (not crystalline state).⁶⁰ The closer the sample is to its glass transition temperature T_g , the closer it is to such a state.⁶⁰ However, in reality an endless number of states of relaxation could be present in an amorphous ice form, hence Winkel *et al.* stated that it was best that each of the three forms of amorphous ice be considered as lying in a part of a larger energy mega-basin able to describe all the varying degrees of structural relaxation.⁶⁰

1.4 Ices with other species

Ice abundantly co-exists with a host of materials in nature.⁸ This is illustrated, for instance, beyond the realms of the Earth in the Solar System, where many bodies are known to host ice – planets have icy moons and comets are composed of ice, and these often form mixtures with carbon.^{81, 82}

Ammonium fluoride shares the same crystal structure as ice at ambient pressure, which has enabled it, unlike many other inorganic solutes, to combine well with ice over a large concentration range.¹⁴

Ice is also well-known to form caged structures as clathrate hydrates with gases like methane that have seeped out of old organic matter trapped in ancient ice fields such as those in Canada and Siberia.^{83, 84} Fears exist around the release of these gases which would be liberated on the warming of the planet thereby exacerbating global warming.⁸⁵ Clathrate hydrates also pose an issue to gas pipelines, which they are often found to block.^{84, 85} Clathrate hydrates are also of relevance to this thesis as during the course of neutron experiments, argon gas was used as a pressure medium and also formed clathrate hydrates.

Also, rather unusually and contrary to common opinion, ice can under some circumstances form structures with high concentrations of salt (*e.g.* in a 6:1 molar ratio of water-to-salt) such as LiCl.^{40, 86} These structures have been synthesised on Earth, but it has been proposed that they could occur naturally in the wider Solar System, which provides more favourable pressures and temperatures for their formation.⁶

1.4.1 Ice and ammonium fluoride mixtures

Generally ionic impurities cannot be incorporated into ice due to incompatible sizes of their radii which causes them to be forced out of the ice lattice as it assumes a new hexagonal conformation. This view of insolubility within ice was taken as an absolute fact⁸⁷ until Kathleen Lonsdale at UCL noted that Laue X-ray photographs of ice and NH₄F were extremely similar in their nature – both of them produced diffuse star-shaped patterns.^{87, 88} It was already known that both ice (*P*6₃/*mmc*) and NH₄F (*P*6₃*mc*) shared a hexagonal conformation as seen in Figure 1.14, and that they both had molecules and ions respectively of very similar sizes.⁸⁹⁻⁹¹

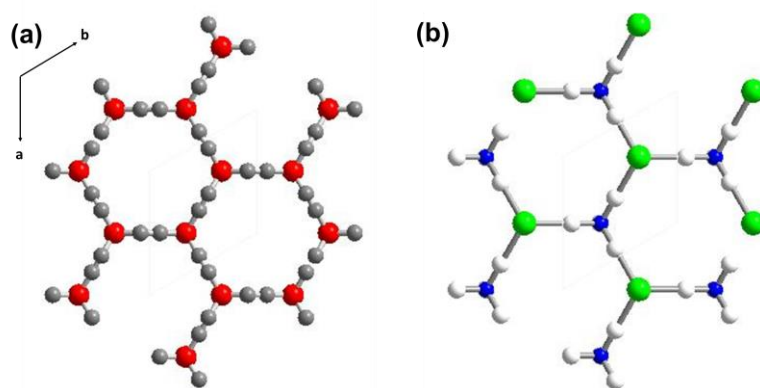


Figure 1.14: Representations of (a) ice and (b) NH_4F highlighting their shared hexagonal conformation. In the ice structure (a), the oxygens are red and the hydrogen atoms are shown in grey to show their half occupancies. In NH_4F (b), the fluorine atoms are green, nitrogen atoms are blue, and the hydrogen atoms are white because they have occupancies equalling one. Both structures share the same axis system shown on the left.

A consequence of the similarities in the two molecules is that they have similar lattice parameters. In ice, a and c are 4.440 and 7.17 Å, while they are 4.5176 and 7.353 Å in NH_4F .⁹² The two species share similar hydrogen bond lengths too, for instance $\text{OH}\dots\text{O}$ in water and $\text{NH}\dots\text{F}$ in NH_4F are 2.76 and 2.71 Å.⁹² With this knowledge, the potential for the two species to form solid solutions was explored and first reported by Yatlov and Polyakova⁹³ and very soon after by Brill and Zaromb⁹⁴. On entering ice, NH_4^+ and F^- ions replace oxygen atoms which can be visualised for two-dimensional square ice as shown previously in Figure 1.10.

Brill and Zaromb determined that ice was able to form solid solutions with NH_4F in mixed crystals of up to 10 mol% NH_4F . In their work published in *Nature*, they reported several findings which included the detection of ammonium ions in ice and a variation in melting temperature of ice with different compositions of NH_4F .⁸⁷ Many subsequent studies focussed on the effect of a variety of different parameters as NH_4F content within ice was increased.^{87, 95-97} It was demonstrated that a large decrease in dielectric relaxation time occurred on increasing amounts of the ionic compound, which was justified by the increased amount of defect mobility.^{87, 95-97} Zaromb and Brill were able to establish that between 0.002 to 0.5 mol% NH_4F activation energies for dielectric relaxation were ~4 kcal/mol, while for pure ice they were ~13 kcal/mol, demonstrating the quite potent effect of NH_4F even in relatively low concentrations.⁹⁴

Lyashchenko and Malenkov investigated the effect of varied NH_4F composition in ice from XRD patterns collected between 213.15 and 243.15 K.⁹² As the two

compounds share the same symmetry, and are composed of atoms with similar electronic properties, the resulting patterns of pure NH_4F and H_2O are identical in appearance,⁹² with a slight peak shift towards higher values of 2θ in NH_4F . The authors themselves state that only a 2% difference in unit cell parameters exist between the pure end members.⁹² Mixtures of several compositions were prepared and demonstrated decreasing a and c lattice parameters with increasing NH_4F content; their reported values⁹² are reproduced in Figure 1.15.

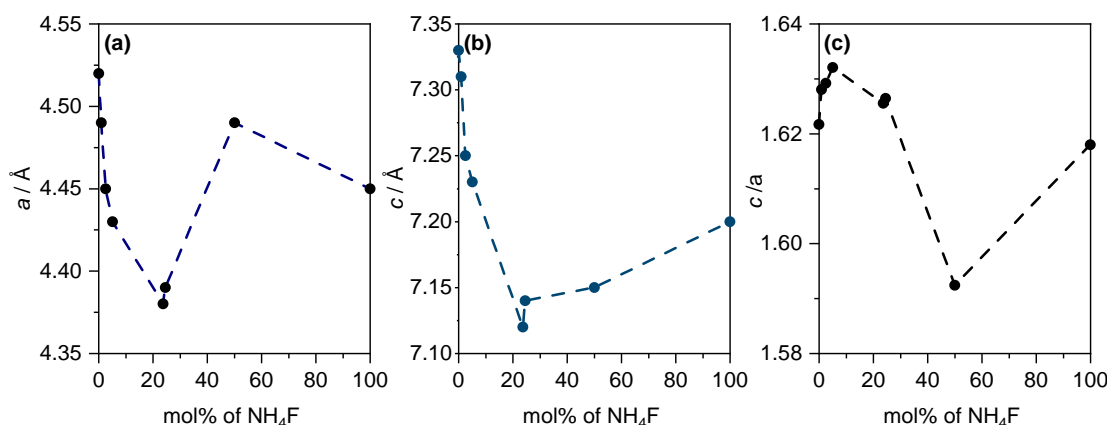


Figure 1.15: Variation in lattice constants on addition of NH_4F to ice found from XRD. (a), (b) and (c) show changes in a , c and c/a respectively. Data was collected between 233.15 to 243.15 K with the exception of the 23.7 and 50 mol% NH_4F samples which were performed at 213.15 K. The plots are reproduced from data in ref. 92.

The contraction of the structure with increasing NH_4F content was rationalised by the increased electronegativity of the fluoride ion compared to that of oxygen, leading to shorter bond lengths.⁹² Lyashchenko *et al.* also found that ice- NH_4F did not subscribe to Vegard's rule despite having identical crystal structures, hence knowledge of the lattice parameters of a certain composition would be unable to shed any light regarding the mol% of NH_4F within a solid solution.⁹²

Yatlov and Polyakova were the first researchers to produce a binary phase diagram of NH_4F -ice.⁹³ Shortly afterwards, a set of binary phase diagrams from 0 – 35 mol% NH_4F were prepared by Labowitz and co-workers, over a two-part series of papers, which are now combined and presented in Figure 1.16.^{98, 99}

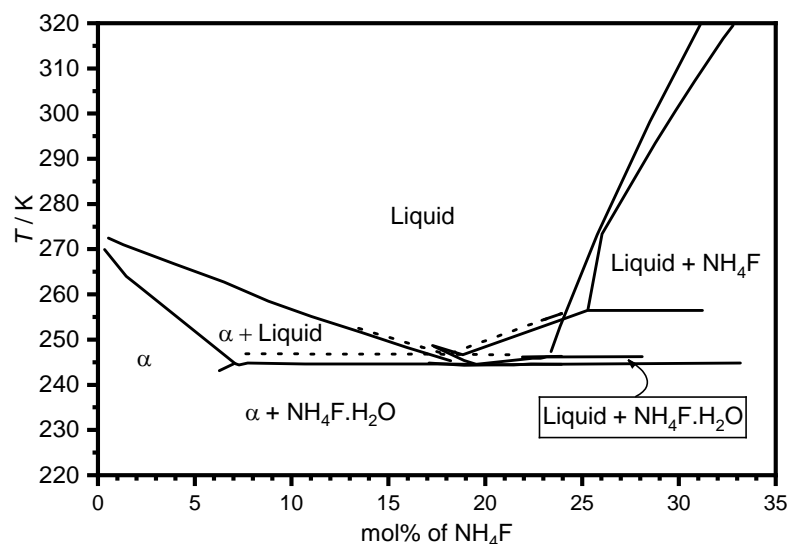


Figure 1.16: A reproduction of a combination of Labowitz *et al.*'s binary-phase diagrams of NH_4F -ice.^{98, 99} Dotted lines refer to data collected by Yatlov and Polyakova.⁹³ α refers to the solid solution.

On the mixing of the two compounds came about the discussion of the existence of ammonium fluoride monohydrate ($\text{NH}_4\text{F} \cdot \text{H}_2\text{O}$).⁹⁸ By Schreinemaker's method of wet residues, Labowitz *et al.* stated that they were able to prepare this compound by studying the ternary system NH_4F - NH_4I - H_2O .⁹⁸ They claim that from a solution containing 22.84 mol% NH_4F at 245.7 K, they were able to conclusively prove the existence of the monohydrate.⁹⁸ The earlier study by Yatlov and Polyakova also reported the existence of the monohydrate after the analysis of the dry residue of a mixture containing 28.5 mol% NH_4F stirred at 254.2 K.^{93, 98} A series of additional solid phases are reported in Yatlov and Polyakova's work: ice, ice + $\text{NH}_4\text{F} \cdot \text{H}_2\text{O}$, $\text{NH}_4\text{F} \cdot \text{H}_2\text{O} + \text{NH}_4\text{F}$, and NH_4F . However Labowitz *et al.*,⁹⁹ and later discussions by Zaromb *et al.*,⁹⁴ question the reliability of the determination of these compositions.⁹⁴

Interestingly, Levi *et al.* stated that NH_4F did not enter the ice structure in a stoichiometric fashion.⁹⁶ From Figure 1.16 it can be seen that Labowitz observed the pure solid solution up to around a maximum of 6 mol% NH_4F . The eutectic point of the system was found to occur at ~19 mol% NH_4F .⁹⁹ Labowitz and co-workers^{98, 99} found discrepancies between their liquidus line data and that of Yatlov and Polyakova⁹³, as seen by the dotted line at higher temperatures.

Zaromb and Brill conducted a series of experiments of mixed solutions of NH_4F and ice, and in similarity to Labowitz *et al.*,^{98, 99} also plotted binary phase-diagram data in comparison to Yatlov and Polyakova as shown in reproduction in Figure 1.17.⁹⁴

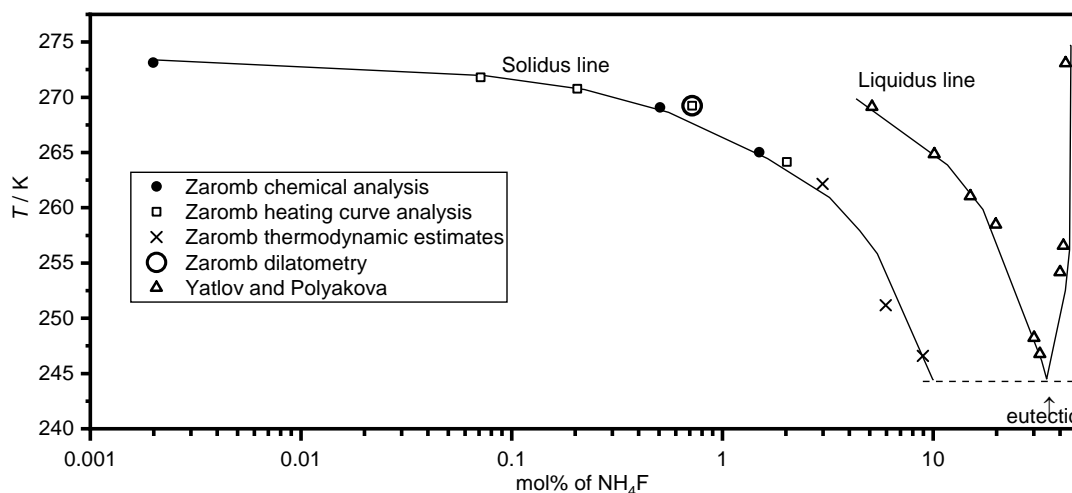


Figure 1.17: Reproduction of Zaromb and Brill's phase diagram of the $\text{NH}_4\text{F}-\text{H}_2\text{O}$ system.⁹⁴ Data points were collected from a series of experiments as indicated in the legend.

Surprisingly, the eutectic point highlighted in Figure 1.17,⁹⁴ as supposedly found by Yatlov and Polyakova is not in agreement with Labowitz *et al.*'s reported eutectic at 19 mol%, but instead occurs closer to 30 mol% NH_4F . For some reason it also appears to be in disagreement with the data of Yatlov and Polyakova that was plotted in Labowitz's phase diagram (Figure 1.16).

Other publications from around the same time also make reference to a monohydrate, but there appear to be inconsistencies in defining it. For instance, Lyashchenko and Malenkov⁹² state that their monohydrate was composed of 50 mol% NH_4F , while Labowitz *et al.*⁹⁸ and Yatlov *et al.*⁹³ state that their monohydrates occur at 22.84 and 28.5 mol% respectively. Since it was first reported in the 50s and 60s, not much mention of a monohydrate has been made, with the last mention of it in 1970.¹⁰⁰ Presumably, a definitive characterisation of a monohydrate would have to take place *via* a method able to distinguish between the different heavy atoms in the compound, probably using an indirect structure determination technique and not X-ray diffraction.

Overall, although there appear to have been many breakthroughs in understanding the $\text{NH}_4\text{F}-\text{H}_2\text{O}$ system, for instance, that NH_4F was able to solubilise well within ice compared to other species, much remains unknown. There are several discrepancies in experimental data which could have arisen from a plethora of circumstances. These include the fact that NH_4F is difficult to handle due to its high hygroscopicity, and it also readily converts to HF .¹⁰¹ Even comparatively simple studies, such as the XRD performed by Lyashchenko *et al.* were performed with

inconsistency between data points with respect to sample temperatures and collection time of data.⁹² Given the length of time that has passed since these initial investigations were made, hopefully in the near future some clarity will be achieved, for example, regarding the existence of the monohydrate and phase boundaries that exist along its binary phase diagram.

While work on NH_4F -ice mixtures at ambient pressure has remained stagnant, renewed interest has instead focussed on the behaviour of these mixtures at elevated pressures.²³ Shephard *et al.* showed for the first time the effect of NH_4F -ice mixtures while under pressure by considering it from two angles: firstly, the effect of pressure on ice prepared from a set concentration of 2.5 mol% NH_4F ; and secondly the influence of varying the concentration of NH_4F in ice at a set pressure of 0.3 GPa.²³ The interaction of NH_4^+ and F^- ions in ice under pressure was found to have far reaching consequences – it completely inhibited the formation of ice II.²³ A phase diagram for 2.5 mol% NH_4F -ice was reported (Figure 1.18), which was able to clearly show the effect the impurity had on the phase boundaries of the remaining phases of ice III and V.²³

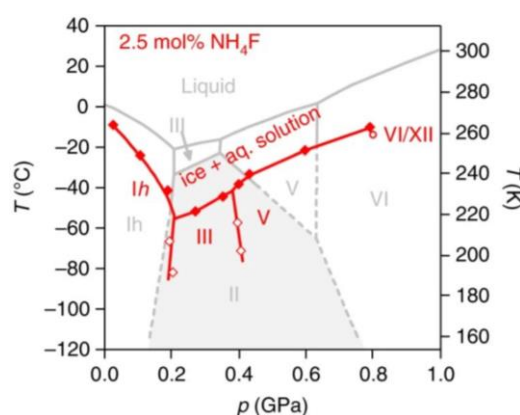


Figure 1.18: The phase diagram of ice containing 2.5 mol% NH_4F in red, overlaid on top of a faded-out phase diagram of pure ice. Ice II no longer forms in the presence of NH_4F , and the liquidus line is also shifted to lower temperatures. Reprinted by permission from Springer Nature: Springer Nature, *Nature Physics*. J. J. Shephard, B. Slater, P. Harvey, M. Hart, C. L. Bull, S. T. Bramwell and C. G. Salzmann, *Nat. Phys.*, 2018, **14**, 569-572.²³

At a set pressure of 0.3 GPa, the effect of concentration of NH_4F in ice was explored through experiments looking into changes in volume on the isobaric heating of the ice (Figure 1.19).²³ The use of volume change plots has commonly been used to demonstrate the changing of one phase of ice to another, as this often goes along with volume changes in the ice sample while it is under pressure.²⁸

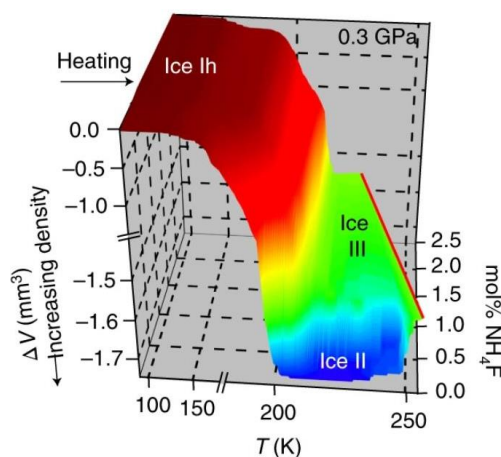


Figure 1.19: Nominal changes in volume of samples of NH_4F -ice solid solutions at 0.3 GPa from 0 to 2.5 mol% from 100 K up to the beginnings of incongruent melting. Reprinted by permission from Springer Nature: Springer Nature, *Nature Physics*. J. J. Shephard, B. Slater, P. Harvey, M. Hart, C. L. Bull, S. T. Bramwell and C. G. Salzmann, *Nat. Phys.*, 2018, **14**, 569-572.²³

The differently coloured regions in the volume change plot indicate the presence of specific phases. On the initial heating of the samples ice Ih is present, however, on further heating of samples of concentrations above 0.5 mol%, the only other phase to form before melting is ice III (shown largely by the green regions).²³ At lower concentrations, a basin can be seen to be forming (dark blue), which signals the gradual reappearance of ice II.²³

Neutron diffraction carried out on samples of 2.5 and 0.25 mol% ND_4F in D_2O ice at the same pressure-temperature conditions have also been able to highlight that the solubility of ammonium fluoride must be less than the reported mole percentage.²³ This conclusion has been drawn from the fact that lattice constants are a very sensitive indicator of NH_4F incorporation in ice,²³ as demonstrated earlier in the work by Lyashchenko *et al.*⁹² Samples of 2.5 and 0.25 mol% ice III that were collected at 0.3 GPa and 200 K had their a lattice constants determined, with the ice III containing less ND_4F , being larger by $0.100 \pm 0.001\%$.²³ However, on heating this sample into the ice II region where the sample converts to ~80 w% ice III with the remainder being ice II, and then cooling back again, the a lattice parameter is then within 10% error of the 2.5 mol% ND_4F sample,²³ suggesting that the impurities flood into the ice III.

The nature of ice II and the strict topological order it possesses can explain why it cannot form in the presence of NH_4F . Unlike the other ices in the phase diagram which surround it, ice II does not contain ionic and Bjerrum defects.²³ This finding is

supported by results of dielectric spectroscopy of ice II.³¹ As no ionic or Bjerrum defects are available to screen the ions that enter the structure, they enter as topological defects.²³ Flux diagrams can be used to explain the hydrogen displacement present before and after the addition of the ions (right-hand plots, Figure 1.20).²³

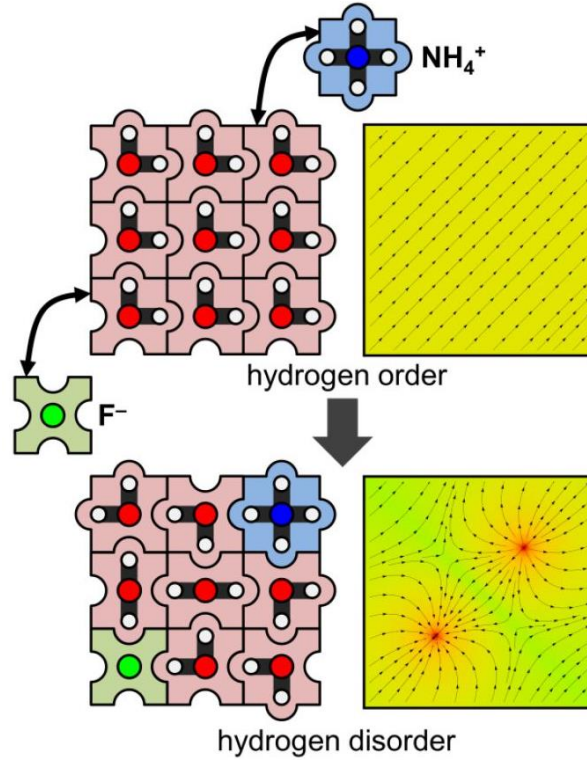


Figure 1.20: Ice II in square ice representation before the addition of NH_4F (top) and after the addition of NH_4F (bottom). The right-hand plots show the flux field of hydrogen displacement. In the case of ice II, the flux field is free of disruption of orientational order (top), however the addition of NH_4F disorders over large distances (bottom). Reprinted by permission from Springer Nature: Springer Nature, *Nature Physics*. J. J. Shephard, B. Slater, P. Harvey, M. Hart, C. L. Bull, S. T. Bramwell and C. G. Salzmann, *Nat. Phys.*, 2018, 14, 569-572.²³

The flux lines shown in Figure 1.20 connect two dopant sites and will undoubtedly be very entangled and intertwined in the three-dimensional version of a structure with NH_4F .²³ Even if an NH_4^+ and F^- ion are separated by only a significantly small distance, with correspondingly ‘small’ flux tubes, a large disturbance in the topological order is experienced, meaning the ice II structure cannot be maintained.²³ This is because the enthalpy cost per ion scales to $\sim x^{-1/3}$, where x describes the dopant fraction. Other phases such as ices *Ih*, III and V, which are instead seen in the stability region that would host ice II in a pure H_2O ice, do not suffer from the same issue as they do not require such a strictly topologically ordered structure.²³ Computational studies carried out in the

supplementary information, which involved statistical dynamics calculations on square ice analogues, also highlight how small quantities of NH_4F still have a substantial effect – a 2% defect fraction is associated with 20% orientational disorder.²³

The Gibbs free energy of ice II can be considered in comparison to ice III, liquid water and a theoretically disordered ice II called ice II d (Figure 1.21).²³

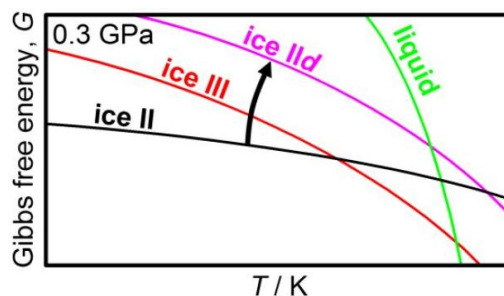


Figure 1.21: Gibbs free energy of ices at 0.3 GPa as a function of temperature. Upon doping the ice II curve follows the direction of the arrow, moving towards the pink curve for ice II d . Reprinted by permission from Springer Nature: Springer Nature, *Nature Physics*. J. J. Shephard, B. Slater, P. Harvey, M. Hart, C. L. Bull, S. T. Bramwell and C. G. Salzmann, *Nat. Phys.*, 2018, **14**, 569-572.²³

As illustrated in Figure 1.21, the possibility of obtaining the disordered counterpart of ice II – ice II d – seems possible in the region of stability of liquid water, explaining why it has not been experimentally detected so far.²³ In the cases where ice II was detected in the neutron diffraction data for ices prepared from 0.25 mol% ND_4F , tests were carried out to determine that the ice II formed was indeed ordered and not just a disordered form of ice II.²³ The data was fit to a simulated structure of ice II d , where the occupancies of the deuteriums were allowed to deviate from either 0 or 1, which would imply a disordered structure, however these occupancies never deviated from values of ordered ice II.²³

Shephard *et al.* predicted that the effect of ammonium fluoride as a disordering agent would be visible in other regions of the phase diagram, in particular on phases exhibiting high degrees of order, such as ice VIII.²³ Salzmann *et al.* were able to demonstrate that deuterated ice VIII doped with 2.5 mol% ND_4F , studied *via* neutron diffraction on the PEARL beamline at ISIS Neutron and Muon Source,¹⁰² did exhibit 31.2% residual disorder as a consequence of the ammonium fluoride.⁵⁵ On reaching the p - T region of ice VII/VIII, a cascade of phase transitions were observed which are illustrated by diffraction data in Figure 1.22 below.

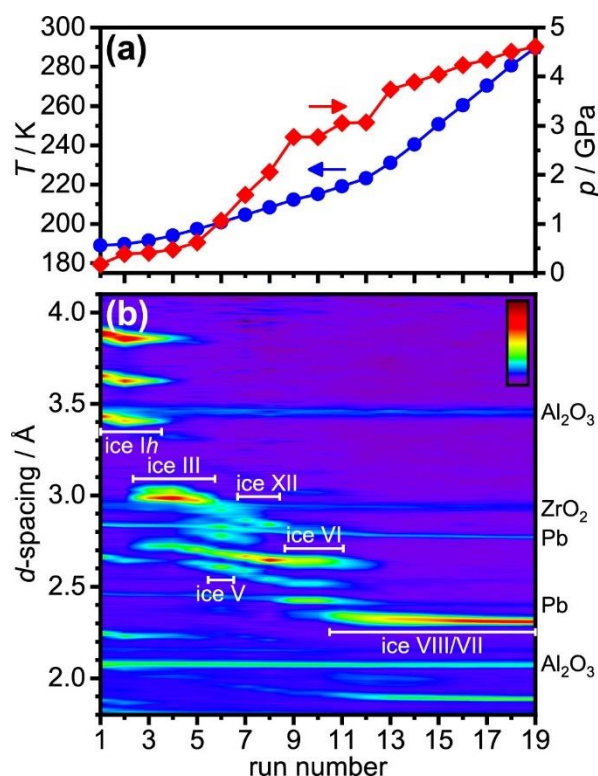


Figure 1.22: (a) p - T route taken of 2.5 mol% ND_4F -doped ice, with (b) corresponding diffraction patterns shown as contour plots, to form doped ice VII/VIII. In (b) the appearance of different ice polymorphs is highlighted on the contour, some peaks from the cell are also marked on the side of the plot. Reprinted with permission from C. G. Salzmann, Z. Sharif, C. L. Bull, S. T. Bramwell, A. Rosu-Finsen and N. P. Funnell, *J. Phys. Chem. C*, 2019, **123**, 16486-16492.⁵⁵ Copyright (2019) American Chemical Society.

The diffraction data in Figure 1.22(b) demonstrates that ice Ih, III, V, XII, VI and VII/VIII are able to form with the addition of 2.5 mol% ND_4F , confirming the ability of the dopant to solubilise well in ice, even under pressure.⁵⁵

Diffraction patterns displayed in Figure 1.23(a) of doped ice VII, doped ice VIII and pure ice VIII were collected in order to assess the effect of the dopant on hydrogen ordering *via* determination of their corresponding deuterium occupancies. The data was fit to a model of ice VIII with the $I4_1/amd$ – this structural model, which is lower symmetry than the ice VIII, could be used to fit both ices VII and VIII.⁵⁵ The ice VII model placed nitrogen atoms and fluorine atoms in oxygen sites, with the assumption that deuterium atoms would also take the same coordinates of the deuterium atoms already present in the structure of ice VII.

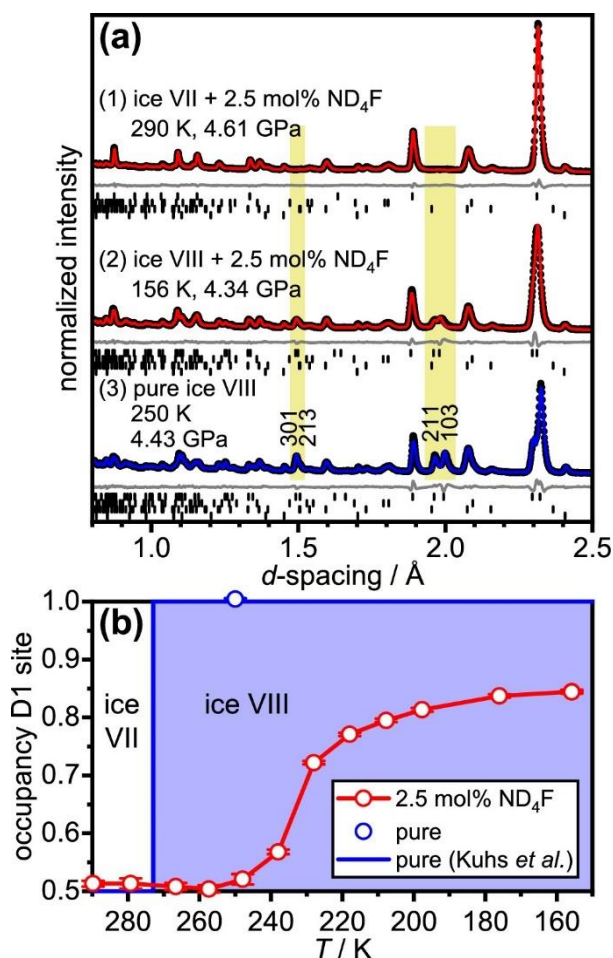


Figure 1.23:(a) Rietveld fits of (1) ND₄F-doped ice VII at 290 K and 4.61 GPa, (2) ND₄F-doped ice VIII at 156 K and 4.34 GPa, and (3) pure D₂O ice VIII at 250 K and 4.43 GPa. The diffraction data is given by the black circles, with fits of doped samples in red, and of the undoped sample in blue. The residuals of the fits are shown by the grey lines. Tickmarks are illustrated for ice VII/VIII, ZrO₂, Al₂O₃ and Pb, going from top-to-bottom. Specific ice VIII peaks are highlighted in yellow. (b) The refined occupancies of the D1 deuterium site of the doped ice VII/VIII in red and the undoped ice sample given by the blue circle. The blue lines which refer to a pure ice VII/VIII sample being cooled are from a study by Kuhs et al.¹⁰³ Reprinted with permission from C. G. Salzmann, Z. Sharif, C. L. Bull, S. T. Bramwell, A. Rosu-Finsen and N. P. Funnell, *J. Phys. Chem. C*, 2019, **123**, 16486-16492.⁵⁵ Copyright (2019) American Chemical Society.

Prior to even calculating the deuterium occupancies, a visible difference can be seen in the highlighted region at ~ 2.0 Å, which gives rise to the 211 and 103 peaks of ice VIII. In the pure ice VIII pattern (numbered (3) in Figure 1.23(a)), these two peaks are especially sharp and well defined – a result of the high level of symmetry intrinsic to the ice VIII structure. However the addition of the NH₄F, as seen in pattern (2) of Figure 1.23(a), shows the same peaks with less definition. The doped ice VII on the other hand, as seen in pattern (1) of Figure 1.23(a), is completely devoid of the 211 and 103 peaks

and exhibits full hydrogen disorder as highlighted by the calculated occupancies in Figure 1.23(b). For the doped ice VIII, the occupancy of the D1 deuterium site, used as an indicator of hydrogen order, does not reach a value of 1, but instead peaks at 0.844, meaning that it never displays full hydrogen order. As well as inhibiting hydrogen order, the NH_4F was also attributed with slowing the kinetics at low temperatures associated with the phase transition of the cooling of ice VII to form ice VIII. The far-longer, drawn-out process can also be appreciated in Figure 1.23(b), where the phase transition occurs over a 60 K window as seen by the blue line. In contrast, for the pure equivalent (blue line, Figure 1.23(b)), the phase transition occurs so rapidly that any intermediate stages between the fully disordered ice VII to the fully ordered ice VIII cannot be observed by diffraction in the same pressure range of ~ 3 GPa.^{55, 103} However recent work conducted at far higher pressures closer to 10 GPa have demonstrated the ability to slow the dynamics of the ice VII-VIII phase transition.¹⁰⁴

On the assumption that the hydrogen disordering effect was restricted to first neighbour interactions, the deuterium sites interacting with ND_4^+ would have occupancies not exceeding 0.024, and deuterium sites interacting with F^- would not have occupancies larger than 0.977. Proof of the far-reaching effect of the hydrogen disordering is clear from the calculated deuterium occupancies of 0.156 and 0.844 for the D2 and D1 sites.⁵⁵

The disordering effect of NH_4F in preventing ice II formation was rationalised by the formation of ‘flux-tubes’ disrupting long range hydrogen order over long distances (Figure 1.20). The same logic can be applied in the case of ice VIII, which is well reported to be almost free of ionic and Bjerrum defects, and hence highly responsive to the inclusion of topological defects, which cannot be shielded. The highly disordered ice VIII that forms in the presence of just 2.5 mol% ND_4F further confirms the low defect level present in pure ice VIII. Salzmann and co-workers’⁵⁵ study was very important in truly defining NH_4F as a hydrogen disordering agent, as the work by Shephard *et al.*,²³ which demonstrated the disappearance of ice II, considered a region of the phase diagram with also included the competing phases of ice III and ice V. Ices VII and VIII exist as the sole phases in a higher pressure range of the phase diagram, hence by examining the effect of NH_4F on hydrogen ordering in ice VIII, any potential effect of the dopant would clearly be realised in the doped ice VIII.⁵⁵

Looking to the future of NH_4F -ice solid solution research, efforts need to be directed towards bridging the gap between pure ice and pure ammonium fluoride, as Shephard *et al.*²³ and Salzmann *et al.*⁵⁵ have begun to lay the groundwork for. Undoubtedly, the field of study into the effect of NH_4F in ice must surely be laden with hidden gems alluding to the intrinsic properties of both ice and ammonium fluoride.

1.4.2 Clathrate hydrates and filled ices

Clathrate hydrates are structures of ice cages which trap gaseous species as inclusion compounds. The gaseous ‘guest’ species do not form chemical bonds with the ice cage ‘host’, which is itself formed of hydrogen-bonded water networks (Figure 1.24); hence clathrate hydrates are non-stoichiometric species.

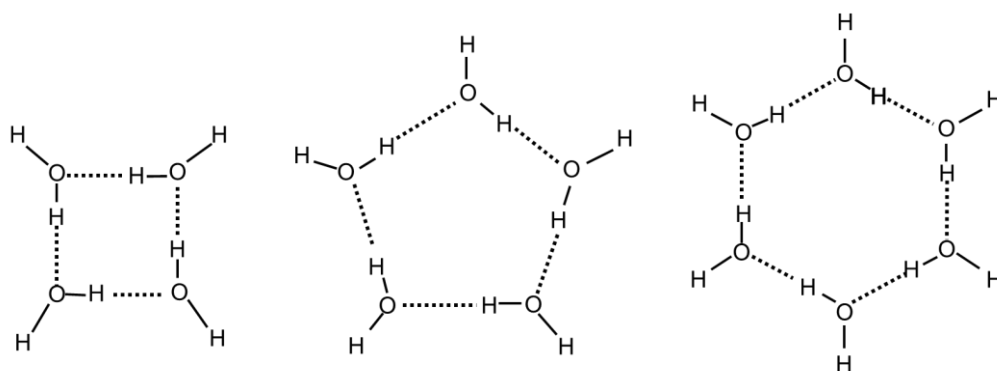


Figure 1.24: Hydrogen-bonded networks which link to form clathrate cages.¹⁰⁵

A family of different hydrate structures are known to exist, and these are often specific to the pressure range in which they occur. The hydrogen-bonded networks displayed in Figure 1.24 further link to one another to form cavities; these are described with nomenclature which label the number of vertices of the polygon and the number of polygons which link together. For example, 5^{12} describes a cavity which is formed of 12 pentagons. In fact the most common clathrates that form – cubic and hexagonal – can all be formed with the 5^{12} building block shown in Figure 1.25.

Cubic clathrate hydrates form from ambient pressure – these clathrate hydrates are typically denoted by CS-I or CS-II, the former comprises 5^{12} cavities joined at the vertices, while the latter is formed from the 5^{12} cavities being linked at the face.⁸⁴ As different sized voids are then present within each structure this means that CS-I and CS-II can then also accommodate $5^{12}6^2$ and $5^{12}6^4$ respectively.⁸⁴ The hexagonal

structure is also constructed from 5^{12} cavities, but its structure is more complex, as can be seen in Figure 1.25.⁸⁴

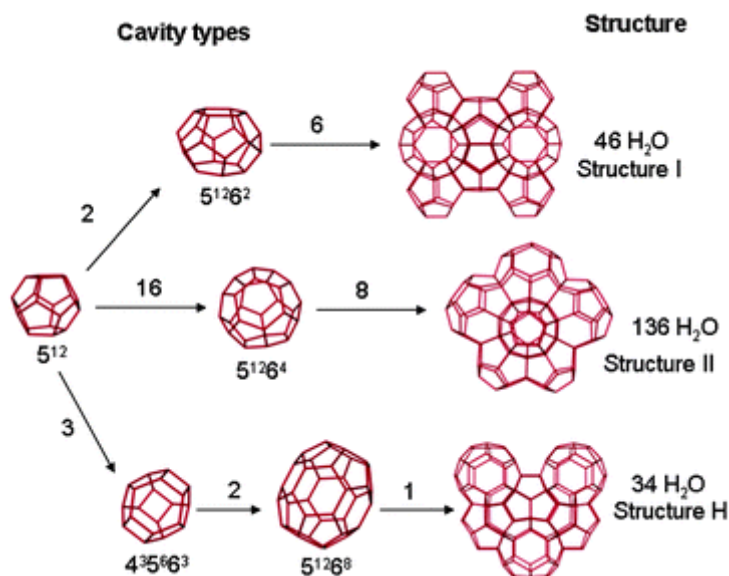


Figure 1.25: Common types of clathrate hydrate shown in relation to the building block cavities from which they are formed. Structures I, II and H refer to CS-I, CS-II and HS clathrate hydrates respectively. Republished with permission of Royal Society of Chemistry, from A. Perrin, O. M. Musa and J. W. Steed, *Chem. Soc. Rev.*, 2013, **42**, 1996-2015;⁸⁴ permission conveyed through Copyright Clearance Center, Inc.

Given their similarities to the structure of ice, it perhaps is of no surprise that clathrate hydrates are commonly observed when ices are being studied with a gaseous pressure medium. For instance, in this thesis argon clathrate hydrate structures are encountered in neutron diffraction experiments.

The most simple argon clathrate hydrate to form is the CS-II and it is observed at ambient pressure.^{106, 107} Neutron diffraction carried out by Manakov *et al.* demonstrated that the argon CS-II clathrate hydrate is stable up to pressures of 4.6 kbar.¹⁰⁷ The increase in pressure marginally decreased the cell parameters and volume; refinement of CS-II from 3.4 and 4.3 kbar gave lattice constants of 17.075 and 16.974 Å respectively. From 4.6 to 7.7 kbar the same authors recorded the presence of a hexagonal structure clathrate hydrate – HS-III – which, they determined from refinement of their neutron data, must host 5 argon atoms per cage. On further increasing the pressure to 7.7 kbar, they recorded a tetragonal clathrate hydrate that had not been seen before. This hydrate, TS-IV, was stable up until 9.5 kbar and was noted as hosting two argon atoms per cage.¹⁰⁷

1. Introduction

Methane is another gas which commonly forms hydrates with ice.^{83, 108} Its lowest pressure clathrate hydrate, MH-I, is known to be present on the seafloor.¹⁰⁸ During the formation of each of the hydrates, high-pressure ice phases are formed as side products as the water ratio decreases.¹⁰⁸ On the application of further pressure, the clathrate hydrates of methane transform into ‘filled ices’, as shown in Figure 1.26.¹⁰⁸

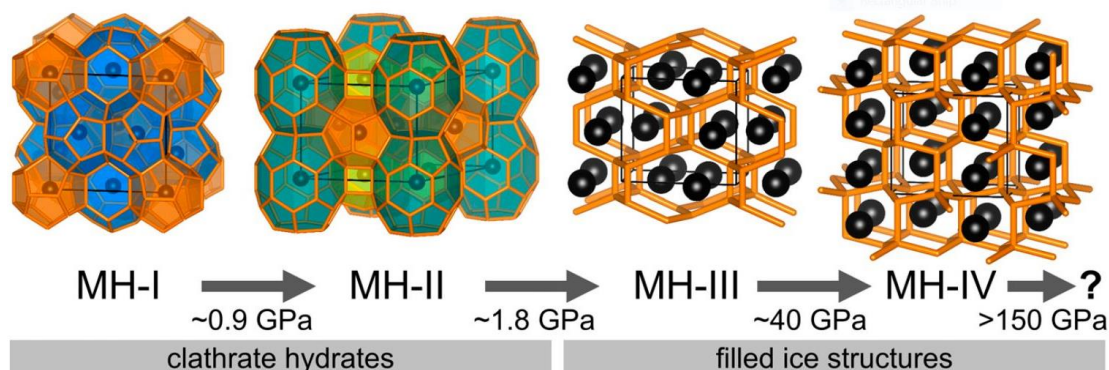


*Figure 1.26: Methane and ice structures which at low pressures start off as caged but eventually adopt a filled ice structure at pressures exceeding ~ 1.8 GPa. The MH-IV filled ice has a water network like that seen in hexagonal ice. Reproduced with under the nonexclusive License to Publish from PNAS post-2018, taken from C. G. Salzmann, PNAS, 2019, **116**, 16164-16166.¹⁰⁸*

Filled ices come about when the caged structure breaks down to form ice networks into which guest species can still be present.¹⁰⁸ This can be seen in the way that methane still fills the open channels in MH-III and MH-IV. Intriguingly, the MH-IV water network is very similar to that of hexagonal ice, despite existing at pressures above 40 GPa, which for pure ice cannot procure a hexagonal ice network.¹⁰⁸

1.4.3 Salty ices

Here, the focus lies on the ability of LiBr, LiCl and NaCl to form structures with ice whereby ions are fully included within the structural framework. More conclusive and promising results of the formation of these so-called ‘salty’ ices exist over an extended p - T range for the lithium salts compared to NaCl with respect to similarities with pure ice.⁸⁶

Although ice is known to accept trace quantities of impurities, it was a commonly held opinion up until recently that ice was unable to host impurities in larger concentrations.⁸⁶ In nature, mono- and di-hydrates are found for several simple salts, however they do not resemble ice structurally, due to their low water content.⁸⁶ Having

said this, it has now been known for some decades that glasses can be prepared from LiCl and LiBr.¹⁸

A method developed by researchers addressed the issue of ion expulsion on the freezing of salty solutions by employing a method similar to that utilised in the formation of amorphous ices³⁷ – hyper-cooling.^{18, 109} Additionally, Ruiz *et al.* found that dilute LiCl (mole fraction < 0.25) could be retrieved as an amorphous solid provided it was cooled at $\sim 10^7$ K s⁻¹ similar to LDA.¹¹⁰ The presence of salt in ice intriguingly assisted with undercooling and amorphisation.⁸⁶ Water-to-salt ratios can also be defined as $R = \text{water molecules} / \text{ion}$.⁸⁶ LiCl, LiBr and NaCl formed salty ices best at ratios equalling 6, 5.6 and 10.2 respectively, corresponding to their eutectic compositions.⁸⁶

The limited concentration range in which lithium salts are able to form glasses at ambient pressure is demonstrated in Figure 1.27. Crystals form at either end of the composition range shown from 0 to 30 mol%, with only a small gap lending itself to the formation of glasses.

The data shown in Figure 1.27 was largely collected in the 1980s and 1990s.¹⁸ More recently it has emerged that the compression of glassy states found at ambient pressure could lead to several other states that were not just alike but exactly the same to that of pure ice.⁸⁶ Further states can be prepared bearing resemblance to HDA, vHDA, ice VII and ice X by initially increasing the amount of salt and then varying the p - T conditions.⁸⁶

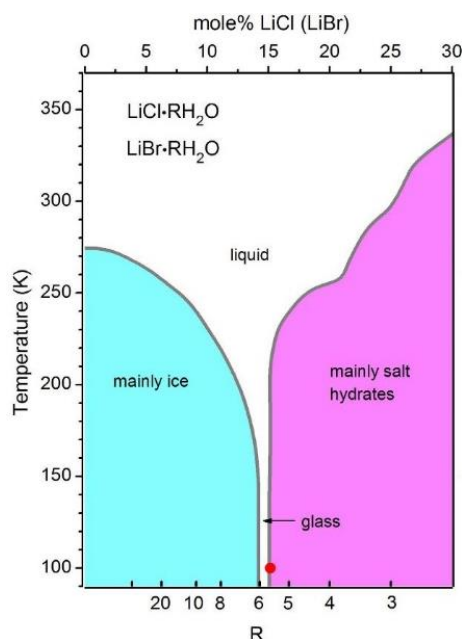


Figure 1.27: Schematic metastable phase diagrams of $\text{LiCl} \cdot \text{RH}_2\text{O}$ and $\text{LiBr} \cdot \text{RH}_2\text{O}$. Only between ~ 5.5 to $6 R$ can a glass be formed on supercooling. In all other cases, low salt concentrations lead to the formation of structures that are mainly ice-like, while on the opposite end, high salt concentrations give rise to salt hydrates. The red dot indicates the experimental conditions used by Klotz et al. to study the species at different pressures and temperatures.¹⁸ Taken from S. Klotz, K. Komatsu, F. Pietrucci, H. Kagi, A. A. Ludl, S. Machida, T. Hattori, A. Sano-Furukawa and L. E. Bove, *Sci. Rep.*, 2016, **6**, 32040,¹⁸ with open access publishing rights (<http://creativecommons.org/licenses/by/4.0/>).

For $R < 12$, simply cooling salty solutions was enough to prepare salty HDA (sHDA).⁸⁶ The electrorestrictive effect of the ions was attributed to the formation of sHDA rather than salty LDA as the shifting of water due to the polarising effect of the ions¹¹¹ calls for a tighter, and more ordered, configuration of molecules.⁸⁶ HDA-type salty compounds have been shown to be similar to eHDA of pure ice.⁸⁶

The temperature annealing of LiBr and LiCl between 80 to 150 K above pressures of 2 GPa, has been shown to lead to the formation of salty-vHDA (svHDA), which goes along with a change from a mainly four-fold coordination in the sHDA to a six-fold coordination.⁸⁶ NaCl sHDA starts off with an already higher coordination number of six while at ambient pressure, which on the further application of pressure gradually increases to eight at pressures exceeding 8 GPa.⁸⁶ This could imply that polymorphism is a trait of tetrahedrally coordinated systems and can be extended to electrolytic systems.⁸⁶

The preference for salty ice forming glassy states is illustrated by the halting of crystallisation until pressures of 10 GPa, which for pure water begins happening at

significantly lower pressure of 2 GPa.⁸⁶ Orientational disorder is brought about by the presence of the ions inhibiting the formation of hydrogen-ordered crystalline phases.⁸⁶

The further compression of salty glass leads to an ice VII-type structure being formed. Ion inclusion into lattices can be well shown in neutron diffraction.⁴⁰ Figure 1.28 shows neutron diffraction performed on the LiCl.6D₂O at 4 GPa and 280 K.

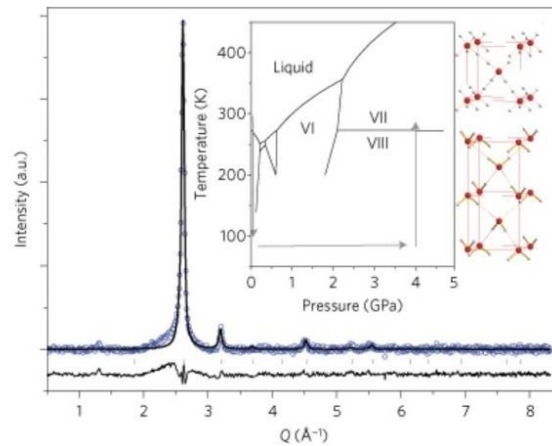


Figure 1.28: Neutron diffraction pattern of LiCl.6D₂O at 4 GPa and 280 K. The raw data is given by blue circles. The black line running through the data is the Rietveld fit, and the lower black line shows the residuals. The inset shows the *p*-*T* route that would be followed to prepare ice VII for pure ice. Reprinted by permission from Springer Nature: *Nature Materials* S. Klotz, L. E. Bove, T. Strassle, T. C. Hansen and A. M. Saitta, *Nat. Mater.*, 2009, 8, 405-409.⁴⁰

The presence of tails at the major peak from the 110 reflection is a consequence of Huang scattering, which is indicative of the inclusion of the LiCl into the ice VII. It was found that salty ice VII had several different properties in relation to pure ice VII, notably a larger cell volume as a result of the incorporation of Li and Cl ions into its structure.⁴⁰ These increases in volume were found to be proportional to the size of ion, not the quantity of salt which is thought to be a consequence of the layout of the ice VII structure, whereby its high density derives from interpenetrating networks.¹⁸

Ions can adopt interstitial positions or substitutional positions, with the smaller ions (Li⁺) taking the former positions and larger ions (Cl⁻, Br⁻) residing in the latter positions in place of oxygen atoms.⁸⁶ Lithium ions are strongly expected to be able to induce strong ionic conduction by moving around between sites.⁸⁶

Additionally, a degree of orientational disorder incomparable to that seen in ice VII is made very clear by the absence of the 111 reflection, which derives from oxygen

atoms that are so extremely displaced as a result of salt inclusion. The high density of ions is thought to have disrupted the hydrogen bond networks to such an extent that, within a given spherical volume, almost a quarter of the hydrogen bonds were broken (which is visualised in Figure 1.29(a) and (b)). This had a strong effect on the positioning of dipole moments, as shown in the probability distribution functions in Figure 1.29(c) and (d). The originally anisotropic dipoles present in pure ice VII (Figure 1.29(c)) become isotropic on the introduction of ions (Figure 1.29(d)).¹⁸

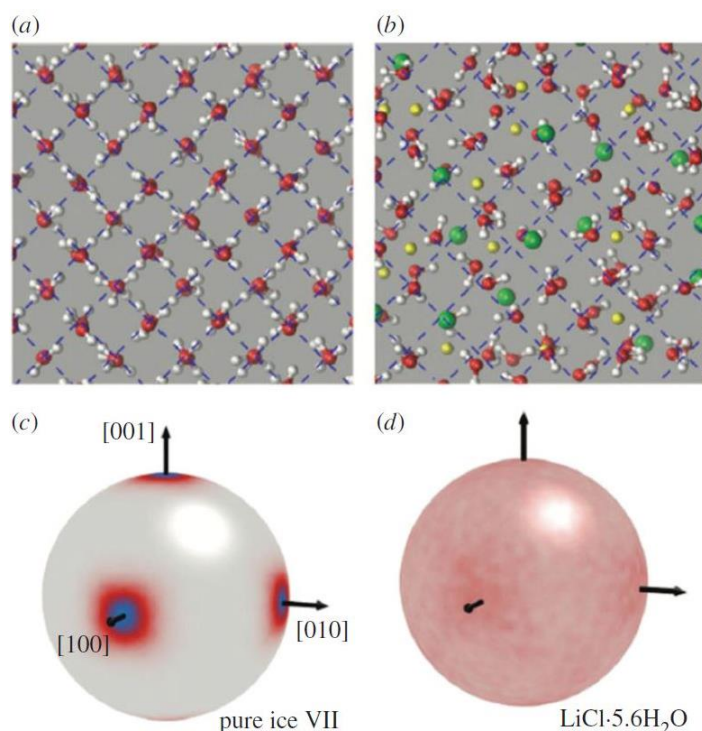


*Figure 1.29: A comparison in the molecular configurations between (a) pure ice VII and (b) salty ice VII with corresponding probability distribution functions of the dipole moments of the two (c) and (d) respectively. A loss in anisotropy between the pure ice VII and the salty ice VII is apparent from the uniform distribution of charge seen in (d). Reprinted from S. Klotz, K. Komatsu, F. Pietrucci, H. Kagi, A. A. Ludl, S. Machida, T. Hattori, A. Sano-Furukawa and L. E. Bove, *Sci. Rep.*, 2016, **6**, 32040¹⁸ under the Creative Commons CC BY license.*

Hosting the ions within the structure, as visualised in Figure 1.29(b), leaves the rotational degrees of freedom of the water molecules frozen in motion while translation degrees of freedom are fixed. Thus, Klotz *et al.* state that only partial crystallisation takes place in the salty ice VII structure.¹⁸ Salty ice VII-type structures are unable to obey ice rules and neither can be termed as hydrogen disordered.⁸⁶

The ability to prepare salty NaCl-type ice VII remains a challenge as retrieved samples have indicated mixtures of pure ice VII alongside expanded salty ice VII.⁸⁶

Pushing the pressure boundaries further, salty ice VII has been observed to transform to ice X by tracking in Raman spectroscopy.⁸⁶ Even with small concentrations such as $R = 50$, the phase transition is able to shift by at least 10 GPa. On increasing the amount of salt, transitions can also be observed to shift to higher pressures.⁸⁶ It was found that the size of the ion and type of ion alone cannot be used to justify this shift in pressures.⁸⁶

An unusual feature of these high-pressure salty ices is that they cannot be retrieved by quenching and releasing to ambient pressure¹⁶ in the manner that their pure ice counterparts are able to.¹⁸ They instead revert to a glassy state as seen in Figure 1.30.¹⁸

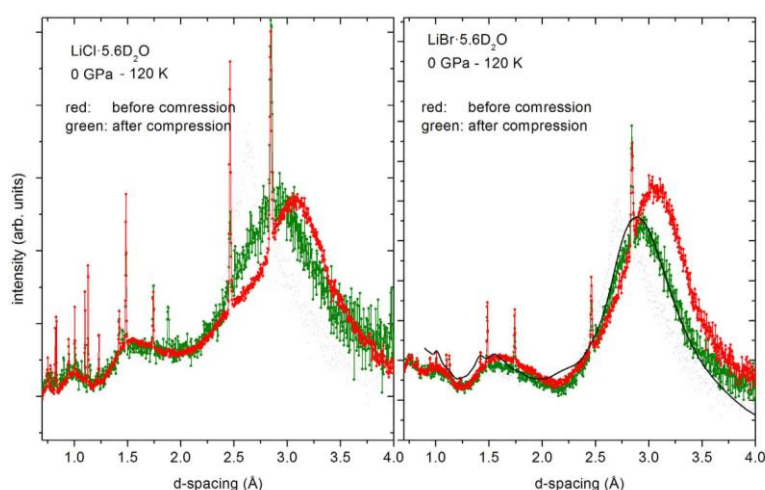


Figure 1.30: Demonstration of memory effects retained by salty ices in the glassy state before compression (red lines) and after decompression (green lines) for (a) $\text{LiCl} \cdot \text{RH}_2\text{O}$ and (b) $\text{LiBr} \cdot \text{RH}_2\text{O}$. The black line is of HDA, which is structurally similar to the 'after compression'-state.¹⁸ Taken from S. Klotz, K. Komatsu, F. Pietrucci, H. Kagi, A. A. Ludl, S. Machida, T. Hattori, A. Sano-Furukawa and L. E. Bove, *Sci. Rep.*, 2016, **6**, 32040,¹⁸ with open access publishing rights (<http://creativecommons.org/licenses/by/4.0/>).

Perhaps even more intriguing is that that the end glassy materials do not retain the same structural character as the starting glasses.¹⁸ The structure retrieved is also noted to be very similar to HDA, which is overlaid over the bromine recovered sample in Figure 1.30(b). This indicates the presence of memory effects from the ice VII phase which required high density packing.¹⁸

1.5 Ammonium fluoride

Ammonium fluoride is a fascinating material to study as a result of its many parallels with the water-ice system.^{14, 112, 113} For instance, the two materials experience strong hydrogen bonding and share three isostructural phases.^{22, 112} This is despite the fact that NH_4F is an ionic species which would have been expected to bear a stronger resemblance to the other ammonium halides, all of which share similar traits amongst their different polymorphs.¹¹³ The likeness between water and NH_4F is partly evident from the shape of the boundaries in the NH_4F phase diagram, which is shown in Figure 1.31. When considering the network topologies of the NH_4F phases, it should be noted that only rings of even-numbered atoms can form due to the stoichiometry of the species. Additionally, NH_4F phases do not experience hydrogen order/disorder in the manner that ice does. Consequently, the phase diagram of NH_4F is far less diverse than that of ice.

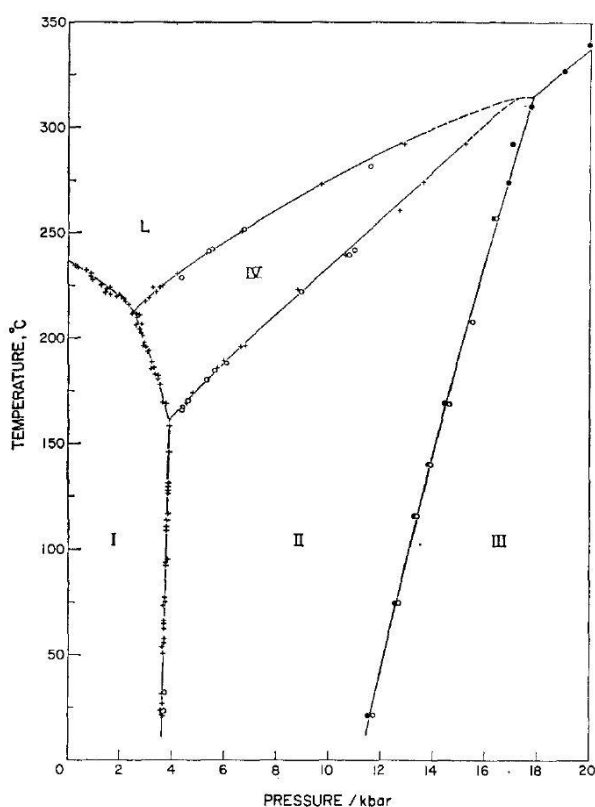


Figure 1.31: The phase diagram of ammonium fluoride up to 2 kbar. Reprinted from A. K. Kuriakose and E. Whalley, *J. Chem. Phys.*, 1968, **48**, 2025-2031,¹¹³ with the permission of AIP Publishing.

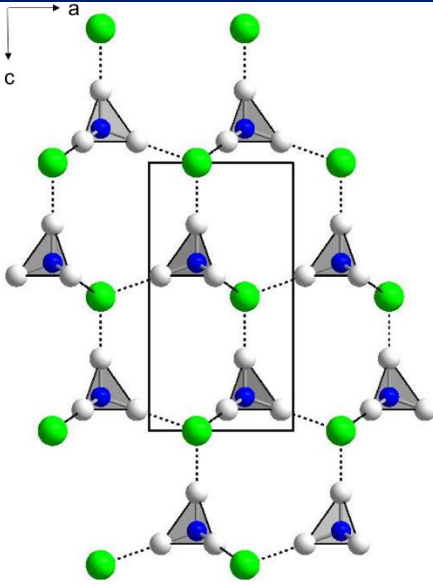
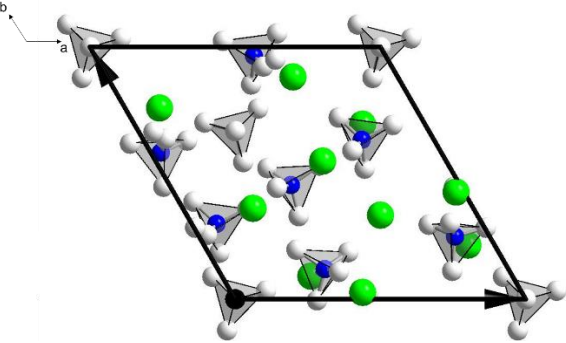
Fortunately the high-pressure phases of NH_4F I, II and III can be examined while under pressure, as well as being studied on cooling and releasing to low pressures where they

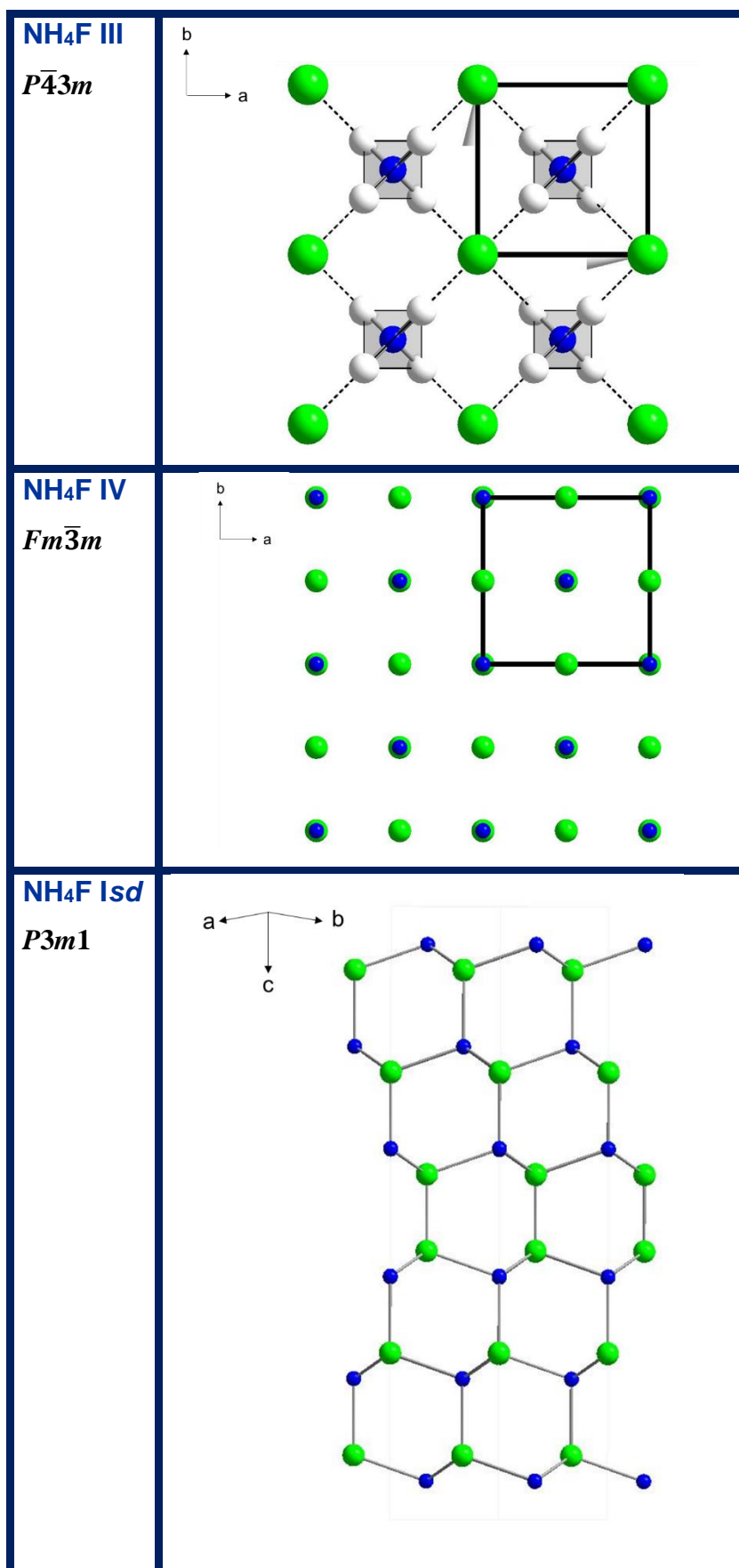
1. Introduction

can exist in a metastable state at low temperatures^{114, 115} at which slow molecular reorientation dynamics exist¹⁶ allowing for their study.

A summary of the known polymorphs of NH_4F is provided in Table 1.3. As Nabar *et al.* stated that they observed stacking faulted variants of NH_4F on heating NH_4F II and III at ambient pressure,¹¹⁵ the last structure displayed is for a stacking disordered variant of NH_4F I (NH_4F Isd).

Table 1.3: Crystal structures of the polymorphs of NH_4F reported with their space groups. Nitrogen, fluorine and hydrogen atoms are shown by blue, green and white spheres respectively. Hydrogen bonds between fluorine atoms and hydrogen atoms are shown by black dotted lines. The hydrogen positions are not shown in NH_4F IV and NH_4F Isd, as they are unknown for the former, and do not affect the structure for the latter.

| Phase | Crystal structure |
|--|--|
| NH_4F I <i>P6₃mc</i> |  |
| NH_4F II <i>R3c</i> |  |



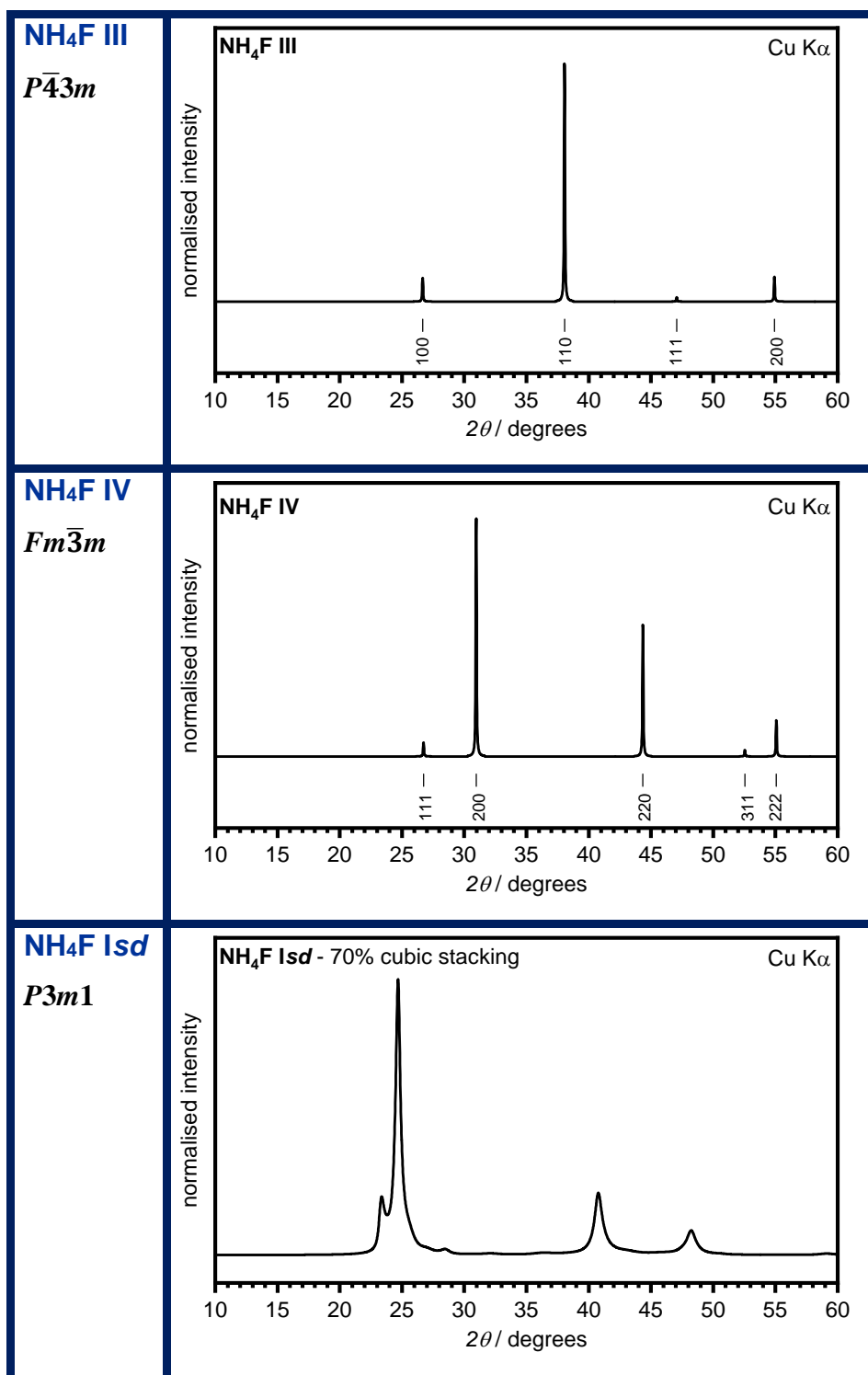
1. Introduction

The space group for stacking disordered NH_4F has been listed as $P3m1$ by analogy with the space group for AgI , which has the same starting space group of $P6_3mc$.¹¹⁶

Simulated XRD patterns of each phase have also been generated for $\text{Cu K}\alpha$ radiation and are displayed in Table 1.4.

Table 1.4: Simulated XRD patterns using $\text{Cu K}\alpha$ radiation of the known polymorphs of NH_4F shown with their Miller indices. Prepared by the author.

| Phase | Simulated XRD pattern |
|---|--|
| $\text{NH}_4\text{F I}$ $P6_3mc$ | <p>Simulated XRD pattern for $\text{NH}_4\text{F I}$ ($P6_3mc$) using $\text{Cu K}\alpha$ radiation. The plot shows normalized intensity versus 2θ / degrees from 10 to 60. The pattern features several sharp peaks corresponding to the following Miller indices: 100, 002, 101, 102, 110, 103, 200, 112, 201, 004, 202, and 104.</p> |
| $\text{NH}_4\text{F II}$ $R3c$ | <p>Simulated XRD pattern for $\text{NH}_4\text{F II}$ ($R3c$) using $\text{Cu K}\alpha$ radiation. The plot shows normalized intensity versus 2θ / degrees from 10 to 60. The pattern features many sharp peaks corresponding to the following Miller indices: 012, 110, 104, 202, 122, 300, 211, 024, 006, 214, 116, 220, 125, 131, 018, 312, 223, 134, 036, 306, 217, 208, 042, 315, 321, 404, 226, 119, 128, 410, 1010, 324, 143, and 413.</p> |



As NH₄F I and ice *Ih* have already been discussed at length in Chapter 1.3.1, the other phases of NH₄F are discussed in greater depth. With respect to transition entropies determined from the slopes of the phase boundaries^{113, 117} and bands observed in Raman spectroscopy¹¹² it has been suggested that phases of NH₄F also exhibit hydrogen order and disorder; for the phases this concerns, more detail will be provided in the

upcoming text. A final remark to be made here concerns the observation of stacking faulted metastable phases that arise from the heating from 77 K of NH₄F II and NH₄F III at ambient pressure that was reported by Nabar *et al.*¹¹⁵ The authors tentatively named the stacking faulted phases NH₄F V, VI and VII.¹¹⁵ These are discussed under the sections of text relating to NH₄F II and NH₄F III.

1.5.1 NH₄F I

NH₄F I is the thermodynamically stable phase at ambient pressure and adopts a wurtzite structure with space group symmetry $P6_3mc$.^{89, 113} It is isostructural with hexagonal ice *Ih* (space group $P6_3/mmc$).^{89, 113} It is reported that NH₄F I and ice *Ih* have structural parameters that do not differ by more than 4%,¹¹³ which results in their similar characteristics and their ability to mix well as solid solutions.^{92, 113}

1.5.2 NH₄F II

Kuriakose *et al.* stated that the compression of NH₄F I led to its transformation to NH₄F II at ~0.38 GPa.¹¹³ On the initial assumption that NH₄F shared a large number of similarities with the other ammonium halides, it was originally incorrectly proposed that NH₄F II was tetragonal.¹¹⁸ It was later determined that NH₄F II was in fact rhombohedral with the space group $R3c$,¹¹⁹ and also isostructural with ice IV¹²⁰ (space group $R\bar{3}c$).

When NH₄F II is prepared from the compression of the NH₄F I, it does so *via* the reorientation mechanism proposed by Engelhardt and Kamb,¹²⁰ referred to as the Engelhardt-Kamb-collapse (EKC).²² This involves the shifting or rotating of layers of the oxygen framework which then can allow for the threading through of hydrogen bonds.^{22, 120} The identical mechanism is also seen in the transformation of ice I to ice IV,^{22, 120} however as a result of hydrogen disorder in ice I, the EKC mechanism is only favourable at higher temperatures.²² This is discussed in far greater detail in Chapter 5 which focusses on the pressure-induced amorphisation of NH₄F-ice solid solutions.

1.5.2.1 Stacking faulted NH₄F V

Nabar *et al.* noted that heating NH₄F II at ambient pressure from 77 K led to its conversion to a stacking faulted variant, labelled tentatively as NH₄F VI, at a temperature of 120 K. On further heating NH₄F VI was then observed to transform to NH₄F I at 230 K. Nabar *et al.* reported the peak positions the new phase NH₄F V, which are now displayed in Figure 1.32 with respect to their reported relative intensities.

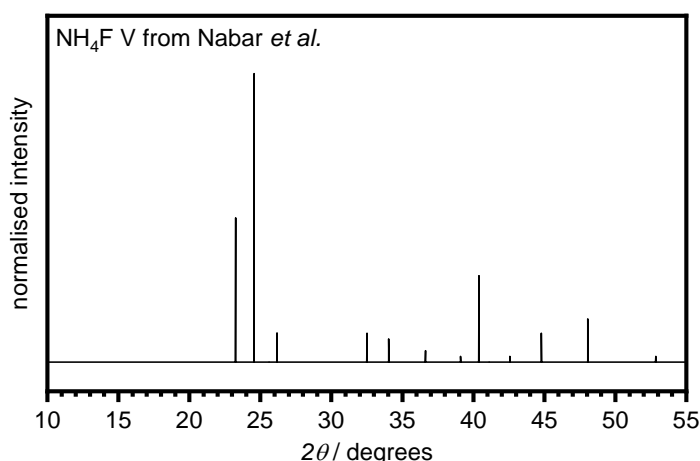


Figure 1.32: Simulated XRD pattern of $\text{NH}_4\text{F V}$ using $\text{Cu K}\alpha$ radiation, prepared from intensity data published by Nabar *et al.*¹¹⁵

Nabar *et al.* found that $\text{NH}_4\text{F V}$ shared similarities with $\text{NH}_4\text{F I}$ and a hypothetical sphalerite (or cubic zinc blende-type) structure.¹¹⁵ Shephard *et al.* showed that a stacking disordered material could be formed on the heating of $\text{NH}_4\text{F II}$ while under pressure.²² The stacking disordered product, which the authors propose is most likely what was reported to be $\text{NH}_4\text{F V}$ by Nabar and co-workers, was found to contain 76.6% cubic stacking.²²

The XRD pattern also contained the characteristic features of the stacking disordered material, namely the asymmetry associated with peak broadening.¹³ The peak profiles unfortunately have not been reported by Nabar *et al.*¹¹⁵ hence it is difficult to ascertain the degree of stacking faults that would have existed in their material.

1.5.3 $\text{NH}_4\text{F III}$

Kuriakose *et al.* stated that the compression of $\text{NH}_4\text{F II}$ to ~ 1.16 GPa caused it to transform to $\text{NH}_4\text{F III}$. The structure of $\text{NH}_4\text{F III}$ is cubic with a space group symmetry of $\text{P}\bar{4}3\text{m}$. It is isostructural with ice VII and is similarly formed of two interpenetrating cubic networks which do not make contact with one another.^{55, 112, 115} The crystal structure of $\text{NH}_4\text{F III}$ can be derived from reducing the space group symmetry of ice VII (space group symmetry $\text{Pn}\bar{3}\text{m}$). The unit cell parameters used to fit the collected XRD pattern of $\text{NH}_4\text{F III}$ (shown in a later chapter in Figure 6.4) are reported for the first time in Table 1.5.

Table 1.5: Calculated unit cell data for NH_4F III with space group symmetry $P\bar{4}3m$ and lattice parameter $a = (3.284192 \pm 0.000112) \text{ \AA}$. The values were calculated from reducing the symmetry of an ice VII cell and then performing a Rietveld refinement of a sample of NH_4F III at ambient pressure and 95 K.

| | Multiplicity | x | y | z | Occupancies |
|----|--------------|---------|---------|---------|-------------|
| N1 | 1 | 0.00000 | 0.00000 | 0.00000 | 1 |
| F1 | 1 | 0.50000 | 0.50000 | 0.50000 | 1 |
| H1 | 4 | 0.67000 | 0.67000 | 0.67000 | 1 |

Nabar *et al.* also listed XRD peak positions and intensities of NH_4F III,¹¹⁵ however it appears that many of the peaks that they reported, which could not be assigned, can be attributed to traces of ice Ih and NH_4F I.

In addition to what Kuriakose and co-workers reported,¹¹³ Bellin *et al.* have proposed that on increasing the pressure of NH_4F III past 10 GPa, the structure of NH_4F III transforms yet again, but to a tetragonal form.¹¹² They describe this as an order-to-disorder transition with a likeness to that seen in tetragonal hydrogen-ordered ice VIII, which on heating converts to its cubic hydrogen-disordered counterpart ice VII.¹¹² Raman spectroscopy was performed which illustrated the lattice and bending modes experience a splitting at lower temperatures that indicate the transformation from the disordered cubic phase to ordered tetragonal phase. To explain the splitting observed in the Raman spectroscopy, Bellin *et al.*¹¹² suggested that the two structures contain differently bonded ammonium ions, as demonstrated in Figure 1.33.

Figure 1.33(a) and (b) show the distorted cubic cell and the ordered tetragonal cell respectively. The two can be differentiated by the lowest NH_4^+ tetrahedron in (b), which is described as an ‘anti-tetrahedron’ (and highlighted by the red bonds) as it has experienced a rotation. It has been proposed that rotation occurs from the breaking and reforming of hydrogen bonds with the central nitrogen species. If the disordered anti-

tetrahedrons exists, it would mean that the fluorine ions are hydrogen bonded to hydrogen atoms either three or five times, which appears unlikely to happen in reality.

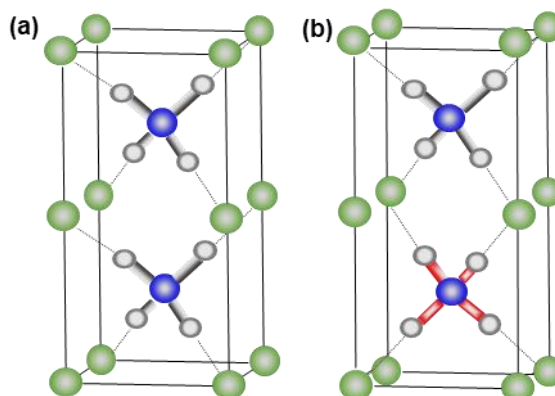


Figure 1.33: The disordered and ordered $\text{NH}_4\text{F III}$ structures represented as distorted tetragonal cells to draw comparisons between the two. (a) The disordered structure which on cooling orders to (b) the tetragonal ordered $\text{NH}_4\text{F III}$ structure.¹¹² Nitrogen, hydrogen and fluorine atoms are represented by blue, white and green spheres respectively. In (b) the lower tetrahedron's red bonds highlights the changed hydrogen positions on its rotation, as suggested by Raman and computational studies.¹¹² Adapted from Figure 8 in ref.112.

A caveat needs to be placed here regarding the terms of ‘order’ and ‘disorder’. In ice physics, labelling a phase as either hydrogen ordered or disordered is dependent upon the crystallographic determination of the occupancies of the hydrogen atoms (or deuterium atoms) bonded to the oxygen atoms of its framework.²⁹ In the study by Bellin *et al.*,¹¹² although there is a clear difference in the Raman spectra of the structures, there has been no crystallographic backup to definitively call these structures ‘disordered’ and ‘ordered’. Nevertheless, the terms ‘order’ and ‘disorder’ appear to relate moreso to a 90° rotation of the ammonium ion.

1.5.3.1 Stacking faulted $\text{NH}_4\text{F VI}$ and $\text{NH}_4\text{F VII}$

Nabar and co-workers investigated the effect of heating $\text{NH}_4\text{F III}$ from 77 K at ambient pressure.¹¹⁵ They noted that $\text{NH}_4\text{F III}$ transformed into $\text{NH}_4\text{F VI}$ at 120 K, which then converted to $\text{NH}_4\text{F VII}$ at 200 K – the latter two phases being stacking faulted variants. Eventually, the $\text{NH}_4\text{F VII}$ then turned into $\text{NH}_4\text{F I}$ at 230 K. The stacking faulted variant phases are shown in Figure 1.34.

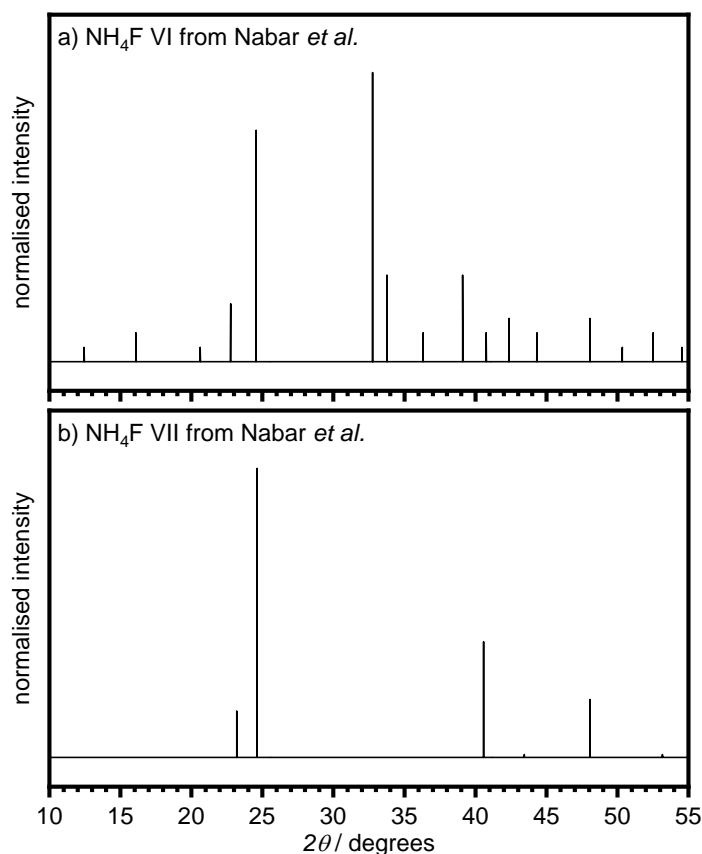


Figure 1.34: Simulated XRD patterns of (a) NH_4F VI and (b) NH_4F VII under $\text{Cu K}\alpha$ radiation, prepared from intensity data published by Nabar *et al.*¹¹⁵

Nabar and co-workers stated that NH_4F VI (Figure 1.34(a)) appeared to be very structurally similar to NH_4F II.¹¹⁵ This can certainly be observed from the number of peak positions they share.

1.5.4 NH_4F IV

The final solid phase of NH_4F and only phase which does not share an isostructural counterpart with ice is NH_4F IV. NH_4F IV was prepared by Calvert and Whalley by crossing the NH_4F I to NH_4F IV boundary and the NH_4F II to NH_4F IV boundary at a range of temperatures between ~ 450 to ~ 475 K.¹¹⁷ Calvert *et al.* proposed that the structure of NH_4F IV is similar to that of NaCl , whose space group is $Fm\bar{3}m$.¹¹⁷ It was stated that the nitrogen atoms take the 4a position, while the fluorine atoms sit in the 4b position and that the lattice parameter $a = (5.77 \pm 0.04)$ Å.¹¹⁷ In this thesis, an attempt was made to come up with fractional coordinates of the unit cell of the high-pressure polymorph, which matched up with the intensities that were provided by Calvert *et al.*¹¹⁷ Table 1.6 displays, for the first time, the structural data that accurately matches up with the diffraction intensities reported by Calvert and co-workers for a sample of

NH₄F IV at 4 kbar and ~450 K. The authors did not state if that sample could be retrieved on cooling and releasing to ambient pressure.¹¹⁷

*Table 1.6: Structural data for NH₄F IV with the cubic space group $Fm\bar{3}m$ which has the lattice parameter $a = (5.77 \pm 0.04) \text{ \AA}$, as determined from Calvert *et al.*'s suggestion that the material is isostructural with NaCl. The positions of the hydrogen atoms are unknown.*

| | Multiplicity | x | y | z | Occupancies |
|----|--------------|---------|---------|---------|-------------|
| N1 | 4 | 0.00000 | 0.00000 | 0.00000 | 1 |
| F1 | 4 | 0.50000 | 0.50000 | 0.50000 | 1 |

On the description of NH₄F IV, it was suggested that the orientations of the ammonium ions are likely disordered.¹¹⁷ This could be in the same manner as discussed by Bellin *et al.* with respect to their tetragonal NH₄F III.¹¹² Additionally, Calvert and Whalley noted that the physical appearance of NH₄F IV, compared to the turbid NH₄F I, II and III, was very clear.¹¹⁷ This suggested that NH₄F IV had plastic characteristics and a closeness to the liquid state, however the authors stated that thermodynamic results implied that free rotation was unlikely to be present.¹¹⁷ Interestingly, other ammonium halide phases that were described as being isostructural with NH₄F IV did not have the same clear appearance.¹¹⁷ These isostructural phases apparently possessed ammonium ion disorder but were free of plastic characteristics.¹¹⁷ This led Calvert *et al.* to stress that the terminology surrounding disorder and plasticity needed to be used with caution as ammonium ion disorder did not necessarily result in plasticity.¹¹⁷

1.5.5 Liquid NH₄F

The heating of NH₄F IV results in the phase transformation to the liquid.¹¹³ The liquid is not obtained on the heating of NH₄F I at ambient pressure, as this is known instead to sublime and decompose to HF and NH₃.¹²¹ Kuriakose *et al.* stated that the liquid is more likely to be to an ionic liquid than a molecular liquid as a result of tracking density changes on its formation from the melting of NH₄F I under pressure.¹¹³ The density of the molecular liquid would be expected to be smaller than the solid, however the melting of NH₄F I to form liquid NH₄F causes a decrease in volume.¹¹³ Hence Kuriakose *et al.* came to the conclusion that liquid NH₄F must be ionic.¹¹³

1.6 Aims of this thesis

This thesis aims to uncover properties of ice using NH_4F by charting the influence of NH_4F in ice over different concentrations and p - T ranges, as well as assessing characteristics of pure NH_4F which may be similar to pure ice. Due to the strong similarities between NH_4F and ice, as well as ammonium fluoride's high solubility and ability to interfere with hydrogen ordering, NH_4F seems like an ideal material to probe and achieve a better understanding of the properties of ice. This research also aligns with the emerging trend to explore the 'chemical' dimension of ice research by looking into properties of ices with dopants of a shared structure with ice.¹⁴

The specific aims are to explore:

- (a) the effect of NH_4F doping on the phase diagram of ice with respect to the potential addition or removal of phases that would be seen in the pure phase diagram; this extends to consider if any phases that are metastable in pure ice become stable.
- (b) the effect on hydrogen ordering or disordering NH_4F has in ice from a kinetic and thermodynamic standpoint.
- (c) the influence of varying the concentration of NH_4F in ice on the process of pressure-induced amorphisation.
- (d) whether stacking disorder or amorphisation occurs upon heating of high-pressure polymorphs of NH_4F , as suggested in early literature, and then to quantify the degree of cubicity the samples have.

1.7 References

1. E. A. Zheligovskaya and G. G. Malenkov, *Russ. Chem. Rev.*, 2006, **75**, 57.
2. J. L. Finney, *Philos. Trans. R. Soc. B*, 2004, **359**, 1145-1165.
3. C. Lobban, PhD thesis, University College London, 1998.
4. S. Damodaran and K. L. Parkin, in *Fennema's Food Chemistry (5th Edition)*, CRC Press.
5. P. Atkins and J. de Paula, *Atkins' Physical Chemistry*, OUP Oxford, 2010.
6. J. Carroll, *Natural Gas Hydrates - A Guide for Engineers (3rd Edition)*, Elsevier, 2014.
7. G. Wypych, in *Handbook of Solvents, Volume 1 - Properties (3rd Edition)*, ChemTec Publishing.
8. V. F. Petrenko and R. W. Whitworth, *Physics of Ice*, OUP Oxford, 1999.
9. L. del Rosso, M. Celli, F. Grazzi, M. Catti, T. C. Hansen, A. D. Fortes and L. Ulivi, *Nat. Mater.*, 2020, DOI: 10.1038/s41563-020-0606-y.
10. K. Komatsu, S. Machida, F. Noritake, T. Hattori, A. Sano-Furukawa, R. Yamane, K. Yamashita and H. Kagi, *Nat. Commun.*, 2020, **11**, 464.
11. W. F. Kuhs, C. Sippel, A. Falenty and T. C. Hansen, *PNAS*, 2012, **109**, 21259-21264.
12. W. Kuhs, F., D. Bliss, V. and J. Finney, L., *J. Phys. Colloques*, 1987, **48**, C1-631-C631-636.
13. T. L. Malkin, B. J. Murray, C. G. Salzmann, V. Molinero, S. J. Pickering and T. F. Whale, *Phys. Chem. Chem. Phys.*, 2015, **17**, 60-76.
14. C. G. Salzmann, *J. Chem. Phys.*, 2019, **150**, 060901.
15. C. G. Salzmann, B. J. Murray and J. J. Shephard, *Diamond Relat. Mater.*, 2015, **59**, 69-72.
16. C. G. Salzmann, P. G. Radaelli, B. Slater and J. L. Finney, *Phys. Chem. Chem. Phys.*, 2011, **13**, 18468-18480.
17. M. Millot, F. Coppari, J. R. Rygg, A. Correa Barrios, S. Hamel, D. C. Swift and J. H. Eggert, *Nature*, 2019, **569**, 251-255.
18. S. Klotz, K. Komatsu, F. Pietrucci, H. Kagi, A. A. Ludl, S. Machida, T. Hattori, A. Sano-Furukawa and L. E. Bove, *Sci. Rep.*, 2016, **6**, 32040.

19. S. A, Classic Kit: Bridgman's seal, [https://www.chemistryworld.com/opinion/classic-kit-bridgmans-seal/3004901.article#/,](https://www.chemistryworld.com/opinion/classic-kit-bridgmans-seal/3004901.article#/) (accessed 30/04/20, 2020).
20. P. W. Bridgman, *Proc. Am. Acad.*, 1912, **47**, 441-558.
21. G. Tammann, *Ann. Phys.*, 1900, **307**, 1-31.
22. J. J. Shephard, S. Ling, G. C. Sosso, A. Michaelides, B. Slater and C. G. Salzmann, *J. Phys. Chem. Lett.*, 2017, **8**, 1645-1650.
23. J. J. Shephard, B. Slater, P. Harvey, M. Hart, C. L. Bull, S. T. Bramwell and C. G. Salzmann, *Nat. Phys.*, 2018, **14**, 569-572.
24. J. D. Bernal and R. H. Fowler, *J. Chem. Phys.*, 1933, **1**, 515-548.
25. A. Rosu-Finsen and C. G. Salzmann, *J. Chem. Phys.*, 2017, **148** 244507.
26. J. J. Shephard and C. G. Salzmann, *Chem. Phys. Lett.*, 2015, **637**, 63-66.
27. F. Yen and Z. H. Chi, *Phys. Chem. Chem. Phys.*, 2015, **17**, 12458-12461.
28. C. G. Salzmann, P. G. Radaelli, J. L. Finney and E. Mayer, *Phys. Chem. Chem. Phys.*, 2008, **10**, 6313-6324.
29. L. G. MacDowell, E. Sanz, C. Vega and J. L. F. Abascal, *J. Chem. Phys.*, 2004, **121**, 10145-10158.
30. E. Whalley, J. B. R. Heath and D. W. Davidson, *J. Chem. Phys.*, 1968, **48**, 2362-2370.
31. G. J. Wilson, R. K. Chan, D. W. Davidson and E. Whalley, *J. Chem. Phys.*, 1965, **43**, 2384-2391.
32. E. Whalley and D. W. Davidson, *J. Chem. Phys.*, 1965, **43**, 2148-2149.
33. C. Lobban, J. L. Finney and W. F. Kuhs, *J. Chem. Phys.*, 2000, **112**, 7169-7180.
34. C. Knight and S. J. Singer, *J. Chem. Phys.*, 2006, **125**, 064506.
35. S. J. Singer and C. Knight, in *Adv. Chem. Phys.*, John Wiley & Sons, Inc., 2011, DOI: 10.1002/9781118135242.ch1, pp. 1-74.
36. R. Howe and R. W. Whitworth, *J. Chem. Phys.*, 1987, **86**, 6443-6445.
37. J. Finney, *Water: A Very Short Introduction*, OUP Oxford, 2015.
38. M. de Koning and A. Antonelli, *J. Phys. Chem. B*, 2007, **111**, 12537-12542.
39. E. Pettinelli, B. Cosciotti, F. Di Paolo, S. E. Lauro, E. Mattei, R. Orosei and G. Vannaroni, *Reviews of Geophysics*, 2015, **53**, 593-641.
40. S. Klotz, L. E. Bove, T. Strassle, T. C. Hansen and A. M. Saitta, *Nat. Mater.*, 2009, **8**, 405-409.
41. S. Kawada, *J. Phys. Soc. Jpn.*, 1972, **32**, 1442-1442.

42. H. Abe and S. Kawada, *J. Phys. Chem. Solids*, 1991, **52**, 617-621.
43. Y. Tajima, T. Matsuo and H. Suga, *J. Phys. Chem. Solids*, 1984, **45**, 1135-1144.
44. M. Ueda, T. Matsuo and H. Suga, *J. Phys. Chem. Solids*, 1982, **43**, 1165-1172.
45. T. Matsuo and H. Suga, *J. Phys. Colloques*, 1987, **48**, C1-477-C471-483.
46. C. G. Salzmann, P. G. Radaelli, A. Hallbrucker, E. Mayer and J. L. Finney, *Science*, 2006, **311**, 1758.
47. K. W. Köster, V. Fuentes-Landete, A. Raidt, M. Seidl, C. Gainaru, T. Loerting and R. Böhmer, *Nature Comm.*, 2015, **6**.
48. C. G. Salzmann, P. G. Radaelli, E. Mayer and J. L. Finney, *Phys. Rev. Lett.*, 2009, **103**, 105701.
49. C. G. Salzmann, A. Hallbrucker, J. L. Finney and E. Mayer, *Phys. Chem. Chem. Phys.*, 2006, **8**, 3088-3093.
50. H. Fukazawa, A. Hoshikawa, Y. Ishii, B. C. Chakoumakos and J. A. Fernandez-Baca, *Astrophys. J.*, 2006, **652**, L57-L60.
51. Y. P. Handa, D. D. Klug and E. Whalley, *J. Phys.*, 1987, **48**, 435-440.
52. Y. P. Handa, D. D. Klug and E. Whalley, *Can. J. Chem.*, 1988, **66**, 919-924.
53. B. Minčeva-Šukarova, G. Slark and W. F. Sherman, *J. Mol. Struct.*, 1988, **175**, 289-293.
54. C. G. Salzmann, P. G. Radaelli, A. Hallbrucker, E. Mayer and J. Finney, in *Physics and Chemistry of Ice*, ed. W. F. Kuhs, The Royal Society of Chemistry, 2007, DOI: 10.1039/9781847557773-00099, pp. 521-528.
55. C. G. Salzmann, Z. Sharif, C. L. Bull, S. T. Bramwell, A. Rosu-Finsen and N. P. Funnell, *J. Phys. Chem. C*, 2019, **123**, 16486-16492.
56. A. Rosu-Finsen, A. Amon, J. Armstrong, F. Fernandez-Alonso and C. G. Salzmann, *J. Phys. Chem. Lett.*, 2020, **11**, 1106-1111.
57. A. Rosu-Finsen and C. G. Salzmann, *Chem. Sci.*, 2019, **10**, 515-523.
58. P. Badrinarayanan, W. Zheng, Q. Li and S. L. Simon, *J. Non-Cryst. Solids*, 2007, **353**, 2603-2612.
59. Tobias M. Gasser, A. V. Thoeny, L. J. Plaga, K. W. Köster, M. Etter, R. Böhmer and T. Loerting, *Chem. Sci.*, 2018, **9**, 4224-4234.
60. T. Loerting, K. Winkel, M. Seidl, M. Bauer, C. Mitterdorfer, P. H. Handle, C. G. Salzmann, E. Mayer, J. L. Finney and D. T. Bowron, *Phys. Chem. Chem. Phys.*, 2011, **13**, 8783-8794.
61. O. Mishima, *Proc Jpn Acad Ser B Phys Biol Sci*, 2010, **86**, 165-175.

62. J. Stern and T. Loerting, *Sci. Rep.*, 2017, **7**, 3995.
63. E. F. Burton, W. F. Oliver and J. C. McLennan, *Proceedings of the Royal Society of London. Series A - Mathematical and Physical Sciences*, 1935, **153**, 166-172.
64. E. F. Burton and W. F. Oliver, *Nature*, 1935, **135**, 505-506.
65. D. T. Bowron, J. L. Finney, A. Hallbrucker, I. Kohl, T. Loerting, E. Mayer and A. K. Soper, *J. Chem. Phys.*, 2006, **125**, 194502.
66. E. Mayer, *J. Appl. Phys.*, 1985, **58**, 663-667.
67. O. Mishima, L. D. Calvert and E. Whalley, *Nature*, 1985, **314**, 76-78.
68. K. Winkel, D. T. Bowron, T. Loerting, E. Mayer and J. L. Finney, *J. Chem. Phys.*, 2009, **130**, 204502.
69. K. Winkel, M. S. Elsaesser, E. Mayer and T. Loerting, *J. Chem. Phys.*, 2008, **128**, 044510.
70. K. Winkel, M. Bauer, E. Mayer, M. Seidl, M. S. Elsaesser and T. Loerting, *J. Phys.: Condens. Matter*, 2008, **20**, 494212.
71. J. J. Shephard, S. Klotz, M. Vickers and C. G. Salzmann, *J. Chem. Phys.*, 2016, **144**, 204502.
72. O. Mishima, L. D. Calvert and E. Whalley, *Journal De Physique*, 1984, **45**, 239-242.
73. T. Loerting, C. Salzmann, I. Kohl, E. Mayer and A. Hallbrucker, *Phys. Chem. Chem. Phys.*, 2001, **3**, 5355-5357.
74. R. J. Nelmes, J. S. Loveday, T. Strässle, C. L. Bull, M. Guthrie, G. Hamel and S. Klotz, *Nature Physics*, 2006, **2**, 414-418.
75. O. Mishima, *J. Chem. Phys.*, 1994, **100**, 5910-5912.
76. C. G. Salzmann, T. Loerting, S. Klotz, P. W. Mirwald, A. Hallbrucker and E. Mayer, *Phys. Chem. Chem. Phys.*, 2006, **8**, 386-397.
77. T. Loerting, W. Schustereder, K. Winkel, C. G. Salzmann, I. Kohl and E. Mayer, *Phys. Rev. Lett.*, 2006, **96**, 025702.
78. O. Mishima, *Nature*, 1996, **384**, 546-549.
79. K. Amann-Winkel, R. Böhmer, F. Fujara, C. Gainaru, B. Geil and T. Loerting, *Rev. Mod. Phys.*, 2016, **88**, 011002.
80. O. Mishima, L. D. Calvert and E. Whalley, *Nature*, 1984, **310**, 393-395.
81. G. Filacchione, M. C. De Sanctis, F. Capaccioni, A. Raponi, F. Tosi, M. Ciarniello, P. Cerroni, G. Piccioni, M. T. Capria, E. Palomba, G. Bellucci, S.

- Erard, D. Bockelee-Morvan, C. Leyrat, G. Arnold, M. A. Barucci, M. Fulchignoni, B. Schmitt, E. Quirico, R. Jaumann, K. Stephan, A. Longobardo, V. Mennella, A. Migliorini, E. Ammannito, J. Benkhoff, J. P. Bibring, A. Blanco, M. I. Blecka, R. Carlson, U. Carsenty, L. Colangeli, M. Combes, M. Combi, J. Crovisier, P. Drossart, T. Encrenaz, C. Federico, U. Fink, S. Fonti, W. H. Ip, P. Irwin, E. Kuehrt, Y. Langevin, G. Magni, T. McCord, L. Moroz, S. Mottola, V. Orofino, U. Schade, F. Taylor, D. Tiphene, G. P. Tozzi, P. Beck, N. Biver, L. Bonal, J. P. Combe, D. Despan, E. Flamini, M. Formisano, S. Fornasier, A. Frigeri, D. Grassi, M. S. Gudipati, D. Kappel, F. Mancarella, K. Markus, F. Merlin, R. Orosei, G. Rinaldi, M. Cartacci, A. Cicchetti, S. Giuppi, Y. Hello, F. Henry, S. Jacquino, J. M. Reess, R. Noschese, R. Politi and G. Peter, *Nature*, 2016, **529**, 368-372.
82. S. O. Halukeerthi, J. J. Shephard, S. K. Talewar, J. S. O. Evans, A. Rosu-Finsen and C. G. Salzmann, *J. Phys. Chem. A*, 2020, **124**, 5015-5022.
 83. E. Chuvilin, B. Bukhanov, D. Davletshina, S. Grebenkin and V. Istomin, *Geosci. J.*, 2018, **8**, 12.
 84. A. Perrin, O. M. Musa and J. W. Steed, *Chem. Soc. Rev.*, 2013, **42**, 1996-2015.
 85. I. Chatti, A. Delahaye, L. Fournaison and J.-P. Petit, *Energy Convers. Manage.*, 2005, **46**, 1333-1343.
 86. L. E. Bove and U. Ranieri, *Philos. Trans. R. Soc. A*, 2019, **377**, 20180262.
 87. R. Brill and S. Zaromb, *Nature*, 1954, **173**, 316-317.
 88. K. Lonsdale, *Nature*, 1946, **158**, 582-582.
 89. C. G. V. Beek, J. Overeem, J. R. Ruble and B. M. Craven, *Can. J. Chem.*, 1996, **74**, 943-950.
 90. G. W. Gross and R. K. Svec, *J. Phys. Chem. B*, 1997, **101**, 6282-6284.
 91. H. W. W. Adrian and D. Feil, *Acta Crystallogr. A*, 1969, **25**, 438-444.
 92. A. K. Lyashchenko and G. G. Malenkov, *J. Struct. Chem.*, 1969, **10**, 616-617.
 93. V. S. Yatlov and E. M. Polyakova, *J. Gen. Chem. (U.S.S.R.)*, 1945, **15**.
 94. S. Zaromb and R. Brill, *J. Chem. Phys.*, 1956, **24**, 895-902.
 95. S. Zaromb, *J. Chem. Phys.*, 1956, **25**, 350-356.
 96. L. Levi, L. Lubart and H. Gränicher, *Physik der kondensierten Materie*, 1968, **7**, 368-371.
 97. R. Brill, H. Ender and A. Feuersanger, *Zeitschrift für Elektrochemie, Berichte der Bunsengesellschaft für physikalische Chemie*, 1957, **61**, 1071-1075.

98. L. C. Labowitz and E. F. Westrum, *J. Phys. Chem.*, 1961, **65**, 403-408.
99. L. C. Labowitz and E. F. Westrum, *J. Phys. Chem.*, 1961, **65**, 408-414.
100. A. Tranquard and G. Coffy, *Comptes Rendus Hebdomadaires Des Seances De L Academie Des Sciences Serie C*, 1970, **270**, 416-+.
101. G. Brauer, *Handbook of Preparative Inorganic Chemistry*, Academic Press, 1963.
102. C. L. Bull, N. P. Funnell, M. G. Tucker, S. Hull, D. J. Francis and W. G. Marshall, *High Pressure Res*, 2016, **36**, 493-511.
103. W. F. Kuhs, J. L. Finney, C. Vettier and D. V. Bliss, *J. Chem. Phys.*, 1984, **81**, 3612-3623.
104. K. Komatsu, S. Klotz, S. Machida, A. Sano-Furukawa, T. Hattori and H. Kagi, *Proceedings of the National Academy of Sciences*, 2020, **117**, 6356.
105. J. W. Steed and J. L. Atwood, in *Supramol. Chem.*, John Wiley & Sons, Ltd, 2009, DOI: 10.1002/9780470740880.ch7, pp. 385-440.
106. J. S. Loveday and R. J. Nelmes, *Phys. Chem. Chem. Phys.*, 2008, **10**, 937-950.
107. A. Y. Manakov, V. I. Voronin, A. V. Kurnosov, A. E. Teplykh, V. Y. Komarov and Y. A. Dyadin, *J. Incl. Phenom. Macrocycl. Chem.*, 2004, **48**, 11-18.
108. C. G. Salzmann, *PNAS*, 2019, **116**, 16164-16166.
109. A. A. Ludl, L. E. Bove, D. Corradini, A. M. Saitta, M. Salanne, C. L. Bull and S. Klotz, *Phys. Chem. Chem. Phys.*, 2017, **19**, 1875-1883.
110. G. N. Ruiz, L. E. Bove, H. R. Corti and T. Loerting, *Phys. Chem. Chem. Phys.*, 2014, **16**, 18553-18562.
111. F. Li, L. Jin, Z. Xu and S. Zhang, *Applied Physics Reviews*, 2014, **1**, 011103.
112. C. Bellin, A. Mafety, C. Narayana, P. Giura, G. Rousse, J.-P. Itié, A. Polian, A. M. Saitta and A. Shukla, *Phys. Rev. B*, 2017, **96**, 094110.
113. A. K. Kuriakose and E. Whalley, *J. Chem. Phys.*, 1968, **48**, 2025-2031.
114. P. T. T. Wong and E. Whalley, *Rev. Sci. Instrum.*, 1972, **43**, 935-937.
115. M. A. Nabar, L. D. Calvert and E. Whalley, *J. Chem. Phys.*, 1969, **51**, 1353-1356.
116. R. L. Smith, M. Vickers, M. Rosillo-Lopez and C. G. Salzmann, *Crystal Growth & Design*, 2019, **19**, 2131-2138.
117. L. D. Calvert and E. Whalley, *J. Chem. Phys.*, 1970, **53**, 2151-2155.
118. B. Morosin and J. E. Schirber, *J. Chem. Phys.*, 1965, **42**, 1389-1390.

- 119. A. Lawson, R. Roof, J. Jorgensen, B. Morosin and J. Schirber, *Acta Crystallogr. Sect. B: Struct. Sci.*, 1989, **45**, 212-218.
- 120. H. Engelhardt and B. Kamb, *J. Chem. Phys.*, 1981, **75**, 5887-5899.
- 121. R. Kaneda, S. Yamamoto and K. Nishibata, *Fixed points on the high-pressure scale identified by phase transitions in ammonium fluoride*, U.S. National Bureau of Standards, 1971.

2 Experimental methods and characterisation techniques

This chapter focuses on the materials used and the preparation of samples *via* a variety of methods. It also touches on the techniques utilised to find structural and thermodynamic properties of the ices over the course of this research. To appreciate each technique, a brief theory section precedes each characterisation technique.

2.1 Purity of materials used

Milli-Q® Ultrapure water was used in all experiments, either on its own or to prepare other solutions. Ammonium fluoride (NH_4F) and heavy water (D_2O) were purchased from Sigma Aldrich with reported purities (and catalogue numbers) of 98% trace metals basis (216011-100G) and 99 atom% (435767-25G) respectively. Standard solutions of 0.01 M HCl (catalogue number: 13-1760) were also bought from Sigma Aldrich. After opening, the solutions were kept in containers covered in Bemis™ Parafilm™ from Thermo Fisher Scientific to both maintain the isotopic integrity of samples and prevent samples from hydrating.

2.2 Handling of NH_4F

Given the hygroscopicity of NH_4F ,^{1, 2} it was ground up using a porcelain pestle and mortar (to increase its surface area on drying) and stored in a desiccator attached to a house vacuum, only being taken out very quickly when needed. Ammonium fluoride exists in an equilibrium with HF and NH_3 .² The liberation of HF means that solids or solutions containing NH_4F could not be stored in glass, which HF etches;² instead solids and liquids were stored in polyethylene bottles.

2.3 Preparation of solutions and mixtures

2.3.1 NH_4F -based solutions and mixtures

NH_4F has a solubility of 83.5 g in 100 g of water at 25°C,¹ hence preparing solutions up to ~30 mol% NH_4F simply involved the dissolution of the solid in water. For concentrations above this value, the required mol% of H_2O and NH_4F were mixed together in polyethylene containers before being shaken rapidly and pipetted into a precooled pestle and mortar at 77 K. This is demonstrated in Figure 2.1.

2. Experimental methods and characterisation techniques

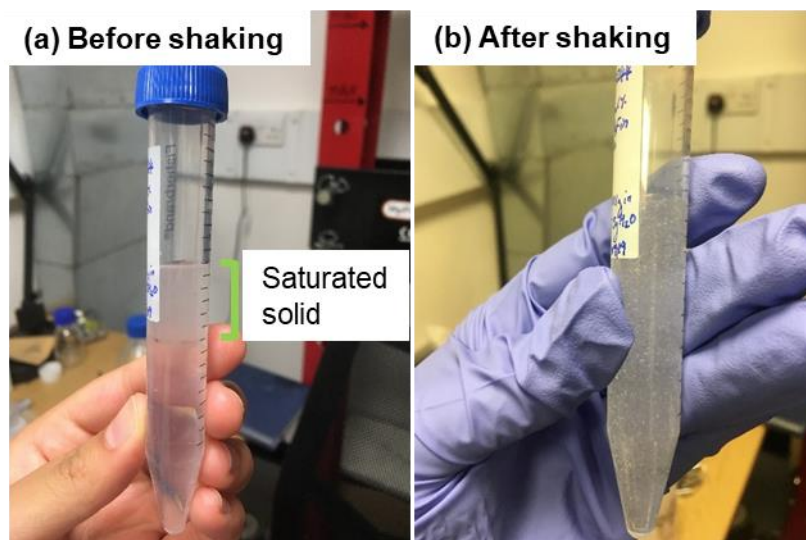


Figure 2.1: 35 mol% NH_4F - H_2O mixture at room temperature. (a) shows the mixture before shaking – the green bracket highlights the separation of the saturated solid. (b) shows the same mixture after shaking rapidly; in this case the solid is dispersed throughout the water and is ready to be ground up in a precooled pestle and mortar.

The shaking allowed a temporary full dispersion of the NH_4F in the water. The mixture was then ground-up until it was assumed that complete homogenous mixing had occurred, which was usually after ~ 5 mins. These frozen NH_4F - H_2O mixtures were used for subsequent investigations.

2.3.2 ND_4F -based solutions

Deuterated ammonium fluoride was made *via* wet-chemistry methods within a fume hood. The experiments were performed within a polyethylene reaction vessel which had been placed within a silicone oil bath set at 120°C . A gas inlet of nitrogen was fed into the reaction vessel to keep the system as inert as possible.

ND_4F was prepared by deuterating a starting material of NH_4F . This was achieved by heating NH_4F (98 % trace metals basis) in excess D_2O and allowing the exchange of hydrogen with deuterium until all liquid had boiled off. Generally, for masses ~ 1 g of NH_4F , $\sim 10\text{ cm}^3$ of D_2O was added until it had boiled off; the addition of D_2O was repeated twice to ensure a high probability degree of full deuteration.

Solutions of 2.5 mol% ND_4F were then prepared by adding set masses of the deuterated solid to D_2O and mixing thoroughly.

2. Experimental methods and characterisation techniques

2.4 Sample preparation techniques

In all cases the ice samples that were made were polycrystalline. These samples were handled under liquid nitrogen to prevent any potential transformation that could occur on heating; such transformations were unlikely to occur at 77 K due to the low temperature environment.³ The samples were kept at 77 K in a storage dewar which was topped up with liquid nitrogen on a weekly basis.

2.4.1 Splat-quenching

A copper plate was positioned inside a large polystyrene box which was filled with liquid nitrogen. Initially the plate was fully submerged in the liquid to ensure it had sufficiently cooled down without any ice *I_h* forming on top of it. The liquid level was then reduced to the level of the plate and the solution was rapidly pipetted over the cold surface. The frozen droplets were quickly retrieved using precooled tweezers to prevent any potential contamination of ice *I_h* which was prone to form on the plate.

2.4.2 High-pressure samples

2.4.2.1 Frimo HyPress 30 tonne hydraulic press

A few samples were prepared using a hydraulic press which was operated by pulling a lever to achieve set pressures in tonnes. The only samples in this thesis that were prepared using this apparatus were several ice V/XIII samples (Chapter 7.2) whose DSC data are shown.

2.4.2.2 Zwick Roell Universal Testing Machine

All other high-pressure samples were prepared using a Zwick Roell Proline Z100TN Universal Testing Machine. This was a far superior setup compared to the formerly mentioned Frimo HyPress.

The Zwick press had a series of advanced features, such as control over the rate of the application of force (this was almost always set to 5 kN min⁻¹), and the ability to track the displacement of the driving piston head during compression, which allowed it to provide more information regarding volume changes within samples.

Samples were prepared in one of three ways depending on the precursors in question:

- (1) Ice could be prepared by pipetting set volumes of solutions into indium foils lining a pre-cooled hardened steel pressure die.

2. Experimental methods and characterisation techniques

- (2) For powdered ice mixtures of NH_4F and ice, the ground-up powder was spooned into indium foils lining the precooled pressure die. In these instances, as it was not possible to know the amount of sample put in, it was also not possible to determine the volumes of samples.
- (3) For samples of pure NH_4F , a set mass of solid was very rapidly transferred into the steel pressure die lined with indium foils. Steel pressure die pistons were placed on top of the solid NH_4F and then the entire set up was compressed at room temperature to reach the known pressures of each phase. The precooling step followed for the ice samples could be skipped as NH_4F is already a solid at ambient conditions and hence can be compressed immediately. After reaching the pressures of interest and observing the phase transitions on the Zwick software the samples were then cooled with liquid nitrogen prior to sample retrieval in order to slow reorientation dynamics down and preserve the high-pressure phases in the same manner as performed for ice. For safety purposes, as experiments involving pure NH_4F are not performed in our group, in the case of a potential sudden pressure collapse, the compression rate used here was 1 kN min^{-1} (however, after performing the experiments it became apparent that this was not necessary).

To track the temperature of the sample, a K-type thermocouple was attached to the pressure die with thermal paste and Teflon tape. Temperature data were recorded using a Lake Shore temperature controller which was linked to a LabView program. With the sample held at 77 K, it was compressed to set pressures before being left to heat up isobarically to set temperatures. For sample retrieval, the ice samples were cooled to liquid nitrogen temperature by either slow-cooling (at 2.5 K min^{-1}) or quenching (at $\sim 40 \text{ K min}^{-1}$) by pouring liquid nitrogen into the sample container. Eventually the pressure was released from the samples and all further sample handling was performed under liquid nitrogen.

Samples were prepared by force control of the piston head; this meant that a set force was applied to the pressure dies and the samples were allowed to heat isobarically. This setup is demonstrated in closer detail by the schematic in Figure 2.2(a) which shows the drive piston of the Zwick (G) compressing the sample (C). During the experiments, the temperature of the sample is measured while the displacement of the drive piston (G) is tracked on the Zwick software. By use of interpolation, one can then

2. Experimental methods and characterisation techniques

plot the change of displacement of the drive piston head (G) with temperature (Figure 2.2(b)). By taking into account the volume of the sample and the radius of the plunging die (D), the change of volume of the sample can be determined as seen in Figure 2.2(c).

The ability to track the piston head meant that phase transitions could be observed as these went along with changes in volume of the ice phases. Examples of phases seen and known to occur for the isobaric heating of 0.01 M HCl ice at 0.5 GPa, which are documented in literature, are shown in Figure 2.2(b) and (c).⁴ The charting of drive-piston displacement was an invaluable tool in correctly isolating phases of ice which are known to exist in specific p - T windows.

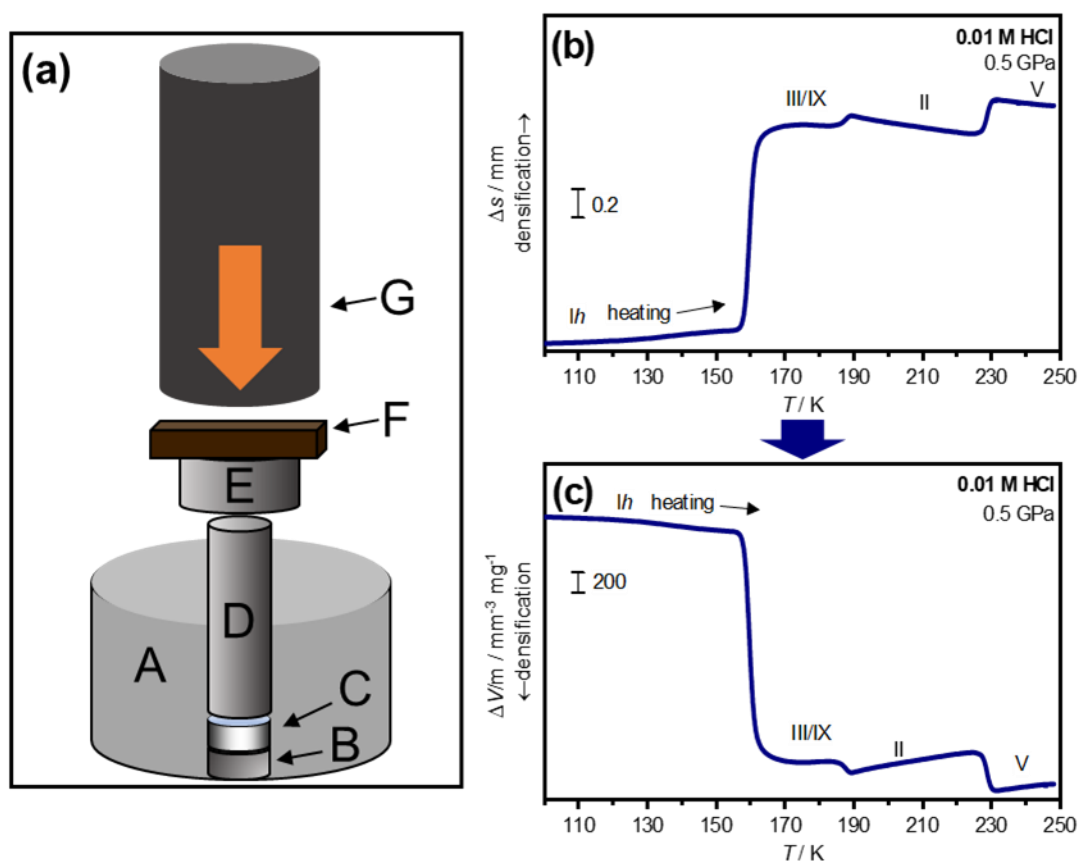


Figure 2.2: (a) a basic schematic of pressure die apparatus. A shows the die body, B: the core die, C: the sample encased in indium, D: the die plunger, E: a piece of hardened steel, F: a Bakelite piece and G: the drive piston of the Zwick Roell machine. (b) is the displacement of driving piston recorded on the Zwick as a function of temperature at 0.5 GPa. If (b) is manipulated, a plot can be created which takes the point of reference of the sample as shown in (c), which displays the change in volume of the sample as a function of temperature at 0.5 GPa.

To reach different pressures, specific pressure dies were used; this was also dictated by the software limit of 90,000 N given by the Zwick Roell machine. The smaller the

2. Experimental methods and characterisation techniques

radius of the die, the higher the pressure that could be achieved. Specific pressures could be reached by taking into account that pressure is the force of the driving divided by the area of the piston face in contact with the sample. Four Specac pressure dies (which are actually specialised for the preparation of FTIR KBr pellets) were used with diameters of 1.3, 1.0, 0.8 and 0.5 cm and could withstand maximal pressures of 0.6, 1.0, 1.7, and 2.5 GPa respectively.

2.4.3 PEARL, ISIS experiments

PEARL is situated in Target Station 1 at the ISIS Neutron and Muon Source. Experiments conducted on the PEARL beamline were from proposal number RB1710176. Figure 2.3 illustrates the instrument with respect to the incident beam which has been optimised for the use of the Paris-Edinburgh (PE) cell. However, the experiments conducted on PEARL in this thesis utilised gas cells to take advantage of the high counting statistics it provides.

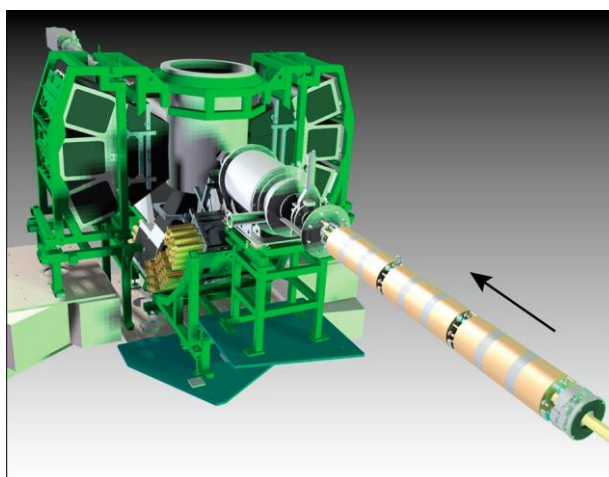


*Figure 2.3: The PEARL beamline visualised with a PE cell in the direct path of an incident beam (indicated by the arrow) which has come from a moderator. Around the sample are a series of 12 detector banks. Reproduced with permission from Taylor and Francis Group taken from C. L. Bull, N. P. Funnell, M. G. Tucker, S. Hull, D. J. Francis and W. G. Marshall, *High Pressure Res*, 2016, **36**, 493-511.⁵*

Depending on the pressure ranges required specific sample containers were chosen. The lowest pressures were achieved with a TiZr gas cell which could achieve maximal pressures of 0.5 GPa. The mixed CuBe/TiZr gas cell could reach slightly higher maximal pressures of 0.8 GPa, however elemental traces of the gas cell existed in the diffraction data collected.

The data is recorded as a function of time-of-flight. The Sample Environment Control Interface (SECI) software allows for control of temperature controllers, data

2. Experimental methods and characterisation techniques

acquisition and a series of other functions. The diffraction data from PEARL is collected over 12 detector modules which can be visualised using the Mantid Software package.⁶ This also allows for the data reduction, corrections and conversion to more usable .gss and .dat formats for data analysis using GSAS software.^{5, 6}

All the sample containers used contained Bridgman-type seals (Figure 2.4) which allowed for pressures above 0.4 GPa to be reached.^{5, 7} Bridgman seals were originally developed for the compression of liquids but can be used for the compression of solid samples too.⁸

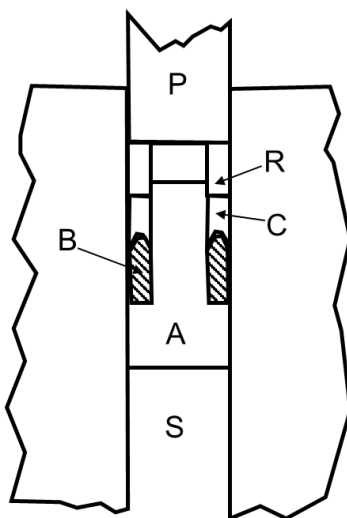


Figure 2.4: Schematic of a Bridgman seal. P defines the drive piston, A represents the steel plug touching the sample, R and C are two other rings of hard and soft steel respectively while B is rubber. S describes the position of the sample. Adapted from ref 8.

High pressures can be reached because unlike earlier seals, the sample (S) and its steel plug (A) is kept some distance from the driving piston (P) with rings of hard steel (R), soft steel (C) and rubber plugs (B) and a small gap of empty space.⁸ This circumvented the issue of the sample leaking around the sides of the piston, which previously prevented pressures from being maintained, let alone being increased.⁸

The general method to prepare ice at the Rutherford Appleton Laboratory involved the freezing of solutions of 2.5 mol% ND₄F in D₂O (which had been previously prepared at UCL, as discussed in section ‘ND₄F-based solutions’). A polystyrene box containing a porcelain pestle and mortar was precooled with liquid nitrogen. Ice powder was then formed from pipetting the 2.5 mol% ND₄F in D₂O and grinding it with the pestle and mortar. This powdered ice was then transferred with precooled tools to the precooled sample containers.

2. Experimental methods and characterisation techniques

2.4.3.1 TiZr and CuBe gas cells on PEARL

Ice powder was transferred into sample cans (Figure 2.5) that were closed with Bridgman seals (Figure 2.4) while under liquid nitrogen.

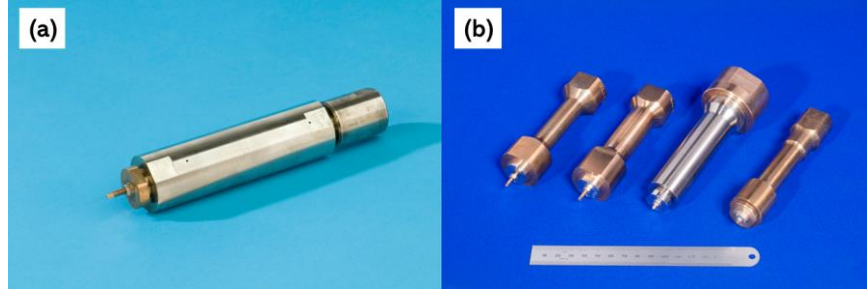


Figure 2.5: Gas cells used on the PEARL beamline. (a) shows a TiZr cell, while (b) shows two-layer CuBe and TiZr cells. Images taken from ref. 9.

The TiZr cans used, such as the one shown in Figure 2.5(a), could withstand pressures of 0.5 GPa^{7, 9, 10} Meanwhile the CuBe cans were specifically CuBe and TiZr two-layer cells (CuBe/TiZr) which could withstand pressures of 0.8 GPa (Figure 2.5(b)).^{7, 9, 10} Argon gas was used as the pressuring medium.

The experimental p - T conditions are provided for the CuBe/TiZr gas cell and TiZr gas cell in Table 2.1 and Table 2.2 respectively.

Table 2.1: Range of p - T s recorded of powdered 2.5 mol% ND₄F in D₂O in a CuBe/TiZr can

| CuBe/TiZr can, containing powdered 2.5 mol% ND ₄ F in D ₂ O | | |
|---|------------------------|------------------------|
| T / K | p / GPa | $\sim \mu\text{Amp h}$ |
| 200 | 0.05 \rightarrow 0.3 | 50 |
| 200 \rightarrow 216 | 0.3 \rightarrow 0.5 | 50 |
| 221 \rightarrow 250 | 0.5 \rightarrow 0.8 | 50 |
| 250 \rightarrow 300 | 0.8 | 50 |

Table 2.2: Range of p - T s recorded of powdered 2.5 mol% ND₄F in D₂O in a TiZr can

| TiZr can, containing powdered 2.5 mol% ND ₄ F in D ₂ O | | |
|--|-----------------------|------------------------|
| T / K | p / GPa | $\sim \mu\text{Amp h}$ |
| 210 | 0 | 50 |
| 200 | 0 | 150 |
| 210 | 0.3 | 1500 |
| 210 \rightarrow 150 | 0.3 | 150 |
| 150 | 0.3 | 1500 |
| 150 \rightarrow 220 | 0.3 | 150 |
| 200 \rightarrow 246 | 0.3 \rightarrow 0.5 | 50 |
| 223 | 0.5 | 50 |
| 198 | 0.5 | 1720 |

2. Experimental methods and characterisation techniques

2.5 Diffraction

Diffraction is the most important structural characterisation tool used to identify phases. In this work, X-ray diffraction (XRD) and neutron diffraction (ND) were utilised.

2.5.1 Crystallinity

Rather fittingly, it was the structure of the six-cornered snowflake that prompted Johannes Keppler to link the effect of the internal order of a structure on its resulting external order.¹¹ Presently, structures are generally grouped in terms of their long-range order – those without such order are classed as amorphous while those with long range order are crystalline.

A unit cell is defined as a building block which when repeated in all directions gives rise to a lattice. Unit cells can be described in three dimensions when considered as a parallelepiped with 6 parameters: a , b , c and α , β and γ , as shown in Figure 2.6.¹² The lattice constants a , b and c are the lengths of the unit cell along different axes. Planes within structures are described by Miller indices – h , k , l – which define the number on divisions of the a , b and c axes respectively (Figure 2.6). The plane spacing is denoted d_{hkl} . This is crucial as the distance between planes can help identify specific crystal structures in diffraction.

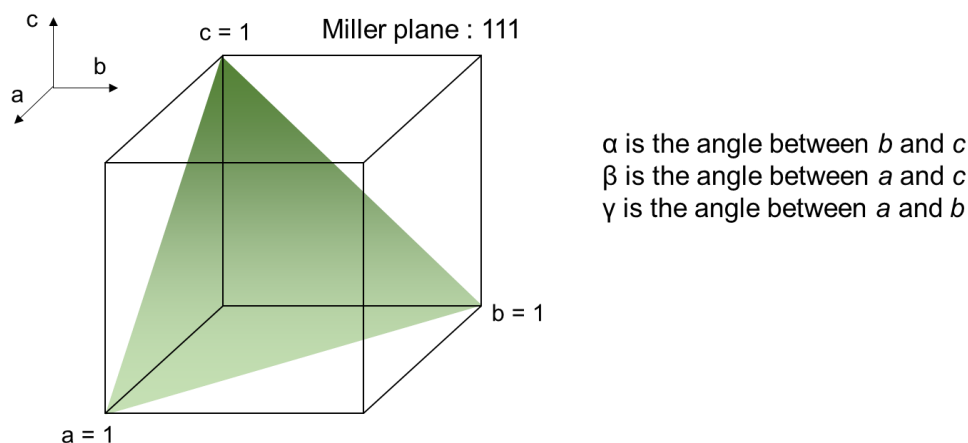


Figure 2.6: A unit cell showing reference axes, the definition of the three unit cell angles and alongside a visualisation of Miller planes going through a unit cell which are defined based on the reference axes.

Four unique unit cells exist, which when combined with 7 different crystal families give rise to 14 different Bravais lattices. The implementation of translational symmetry can be used to give more detailed descriptions of structures which now can be described as belonging to one of 230 space groups. This simplifies the description of the entire

2. Experimental methods and characterisation techniques

crystal structure, which can be generated by applying a range of symmetry operations to the asymmetric unit.¹¹

2.5.2 Diffraction

Diffraction describes the spreading of waves when a wavefront passes through a slit.¹³ In order to describe diffraction in which the point source of radiation is well away from the resulting diffraction, the Huygens-Fresnel principle can be employed.¹⁴ It describes how the wavefront of radiation can itself be considered to be a new source of secondary wavelets. The direction of propagation of the secondary wavelets is at a tangent to the original wavefront.¹⁴

When waves interfere with each other and are in-phase, constructive interference occurs, while if the waves are out-of-phase, destructive interference occurs. In crystal structure determination, diffraction is a crucial tool. In this case, points in the lattice themselves can be treated as point sources of radiation. Depending on the type of radiation (e.g. X-ray, neutron or electron) different interactions occur leading to the retrieval of different information. In the case of X-ray diffraction, the electrons in the lattice interact with incoming X-rays to vibrate, and in turn, become a source of electromagnetic radiation which leaves the structure. With neutron diffraction, the nucleus interacts with incoming neutrons before the neutrons eventually exit the sample.¹⁵

2.5.2.1 Bragg's Law

Conceptually diffraction is easily understood with Bragg's Law which considers reflections from atoms in crystal planes. Here the path difference of waves between planes scattered from adjacent planes provides the relationship below:

$$(AB + BC) = (d_{hkl}\sin\theta + d_{hkl}\sin\theta) = 2d_{hkl}\sin\theta \quad \text{Equation 2.1}$$

This can be demonstrated for both constructive and destructive interference (Figure 2.7)

2. Experimental methods and characterisation techniques

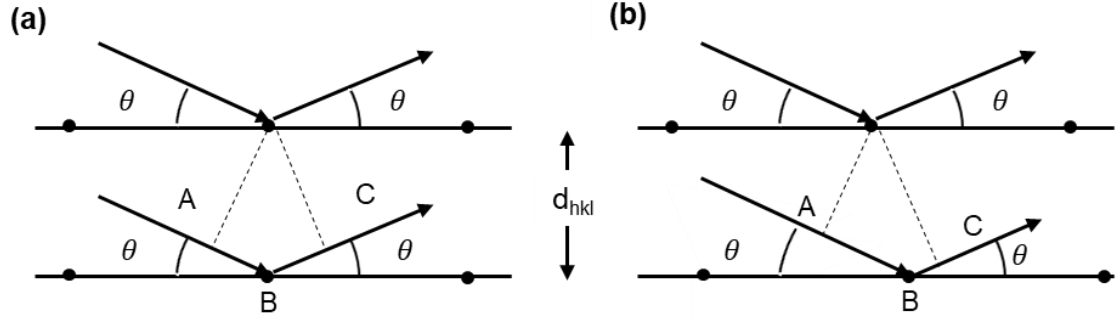


Figure 2.7: (a) constructive and (b) destructive path differences in travelling light. In (a) the path length adds up to an integer number of wavelengths leading to constructive interference. The pathlength in (b) is non-integer leading to destructive interference.

and Equation 2.1 can also be adapted to:

$$n\lambda = 2d_{hkl}\sin\theta \quad \text{Equation 2.2}$$

where for constructive interference n is an integer, and for destructive interference n is a non-integer.

2.5.3 Intensity

The intensity of waves collected in diffraction is proportional to the sum of total scattering from the unit cell of a material.¹⁶ If atoms are considered as discrete scattering centres, the atomic structure factor, F_{hkl} , can be derived, which considers how atoms scatter radiation.¹¹

This is described by the structure factor:

$$\begin{aligned} \text{Structure factor, } F_{hkl} &= \frac{\text{amplitude scattered by the atoms in the unit cell}}{\text{amplitude scattered by a single electron}} \\ &= \sum_{n=0}^{n=N} f_n \exp 2\pi i (hx_n + ky_n + lz_n) \end{aligned} \quad \text{Equation 2.3}$$

The structure factor itself is defined by several other quantities, including the atomic scattering factor, f , and the Miller indices of the planes of the crystal.

The atomic scattering factor is also known as the atomic form factor and can be represented by the equation:

$$\text{Atomic scattering factor, } f = \frac{\text{amplitude scattered by atom}}{\text{amplitude scattered by a single electron}} \quad \text{Equation 2.4}$$

It describes the scattering power of a single atom and is dependent upon the element of the atom in question, the type of radiation interacting with the atom and the angle the radiation is scattering at.¹¹

2. Experimental methods and characterisation techniques

2.5.4 Atomic structure factors and scattering length

In X-ray diffraction, the wavelength of the X-rays is on a similar length scale to that of the space between atoms, hence the electrons act as point sources which scatter the incoming radiation. However, as electrons have a probability of being distributed over the entire volume of an atom, the scattering from individual electrons can cause the final scattered radiation to be out-of-phase. In the case of X-ray diffraction, a drop-off in intensity is found over a longer distance (*i.e.* for species with larger radii) as there are more instances for destructive interference to occur (Figure 2.8).

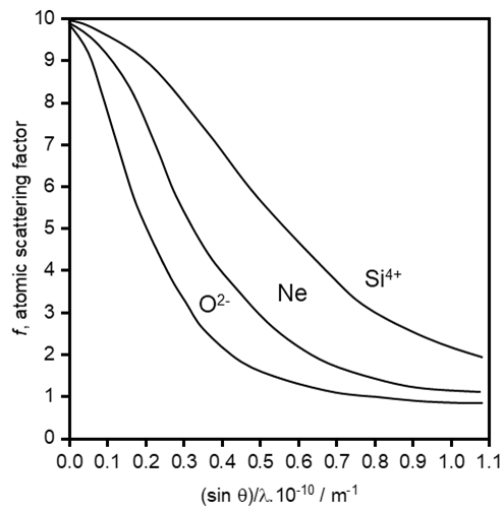


Figure 2.8: Variation of the scattering factor with angle. Atoms with higher Z have a higher scattering factor at a given angle. All atoms have their scattering factor taper off with increasing angle. Adapted from Fig. 9.1 in ref. 11.

Neutron diffraction, on the other hand, does not possess the same issue of drop off in scattering factors as the wavelength of neutrons far larger than that of electrons, rendering it insensitive to electronic distribution. Hence, the nucleus can be considered to be point-like, leading to no drop-off in intensity of the atomic scattering factor with increasing angle.¹⁵

From the definition of scattering factor, one can see that there exists an electronic contribution. Given the differing sensitivity to electronic contribution from both X-ray and neutron diffraction, it can be stated that atomic scattering factors follow a more consistent trend with increasing angle for X-ray diffraction than for neutron diffraction. The analogous quantity in neutron diffraction is termed the neutron scattering length, b .

2. Experimental methods and characterisation techniques

In fact, in the case of neutron diffraction there is no linear trend with atomic number, instead atomic scattering factor is dependent on qualities of the atomic nucleus. This is taken advantage of when studying materials that are especially affected by the drop-off in intensity with angle. This is demonstrated in Figure 2.9 where a clear linear dependence is demonstrated for scattering factors with increasing atomic number, while for neutron scattering there does not appear to be a systematic trend with increasing atomic number.

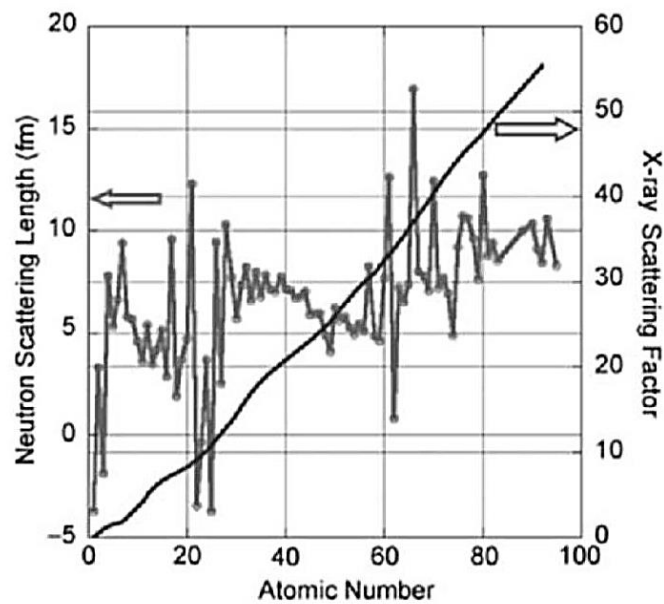


Figure 2.9: Comparison of the dependence of atomic number on scattering factor from X-ray diffraction, in comparison to the lack on linear dependence on atomic number for scattering length in neutron diffraction. Reproduced with permission by Elsevier from ref. 17.

Another advantage of considering neutron cross sections is that they can assume positive or negative values. Hence, a material that is composed of a mixture of species of negative and positive neutron scattering lengths can be combined in such a manner that the net scattering factor is null – making them prime materials for use as sample containers for neutron diffraction, as in the case of TiZr. This is demonstrated in Table 2.3.

2. Experimental methods and characterisation techniques

Table 2.3: X-ray structure factors and neutron scattering lengths for a variety of species. Data taken from ref.16.

| Species | X-ray structure factor, $f(\theta=0)$ | Neutron scattering length, b / fm |
|------------|---------------------------------------|-------------------------------------|
| H | 1 | -3.74 |
| D | 1 | 6.67 |
| O | 8 | 5.80 |
| Al | 13 | 3.45 |
| Ar | 18 | 1.91 |
| Ti | 22 | -3.44 |
| Zr | 40 | 7.16 |
| 68%Ti32%Zr | 27.8 | 0.00 |

The elements of importance in ice studies are hydrogen and oxygen. For general structural information, in particular the positioning of the oxygens in the lattice which are generally unique for each hydrogen-order/disorder pair, X-ray diffraction is sufficient as a characterisation tool. This is because the scattering ability of oxygen is great enough to not taper off drastically with scattering angle. Unfortunately, not a great deal can be inferred with regards to the positioning of the hydrogens. It is for this reason that generally neutron diffraction is employed when more information is required regarding hydrogen atoms. However, in order to gain good quality information, the higher neutron scattering length of deuterium compared to hydrogen makes deuterated ices the preferred ice studied.¹⁶

2.5.5 X-ray diffraction (XRD)

X-ray diffraction is a relatively widespread characterisation technique. It can be performed on both single crystal samples and powdered samples. In this project all samples were analysed as powders and kept at low temperatures in order to characterise the ices without them transforming on heating.³

X-rays are generated *via* a cathode ray tube which is a filament to which a voltage is applied. The element within the tube determines the wavelength of the resulting energy that hits the sample. The most common types of radiation are Cu ($\lambda = 1.5 \text{ \AA}$) and Mo ($\lambda = 0.7 \text{ \AA}$). The X-rays are directed towards a sample within a specific holder which is placed on a sample stage and then set to either spin or rock in order to obtain a powder average. At each rotation angle of the sample stage, the X-rays that have diffracted off the crystal are collected by a detector which picks up readings of intensity for each corresponding angle.

2. Experimental methods and characterisation techniques

2.5.5.1 Low temperature XRD

Low temperature powder X-ray diffraction (PXRD) was performed at UCL for the phase identification (phase ID) of samples. This diffraction was carried out using a standard Stoe Stadi P diffractometer with Cu K α 1 radiation at 40 kV, 30 mA and monochromated by a Ge 111 crystal. The data from this was collected with Mythen 1K linear detector. The low temperature of PXRD was achieved by ensuring the sample remained in a stream of nitrogen gas provided by an Oxford Instruments CryojetHT.

After ices were made, they were powdered and transferred in a purpose-built sample holder while being kept under liquid nitrogen. The sample holder used for the majority of analysis was a brass sample holder which had Kapton® windows to allow for X-rays to not be affected. Kapton® capillaries were also used for several samples; however, owing to the increased difficulty of transferring the capillaries onto the low temperature setup compared to the brass cells this holder was not prevalently used. Both holders took advantage of the fact that Kapton® can withstand extreme temperatures (−269 to 400°C).¹⁸

When the samples were placed into the sample holder position of the instrument, they were quickly placed in the stream of nitrogen provided by an Oxford Instruments CryojetHT. This ensured that the temperature of the samples was at least 95 K, well below the temperature of any phase transition to stacking disordered (ice *Isd*) that would be expected for the ice phases investigated.¹⁹ Using an accompanying computer program (OxCom), the temperature of the samples could be controlled; this was used when heating to get to phase transitions.

A typical XRD pattern is displayed in Figure 2.10 which shows a sample of ice *Ih*. While characterising high-pressure ice samples at low temperatures, the formation of external ice *Ih* on the sample holder was common and could be seen by the appearance of the particularly strong ‘trident’ peaks, which are highlighted in green in Figure 2.10. This would occur as a result of condensation of water in the air surrounding the sample and in the flow of nitrogen gas of the sample which could not always remain moisture-free.

2. Experimental methods and characterisation techniques

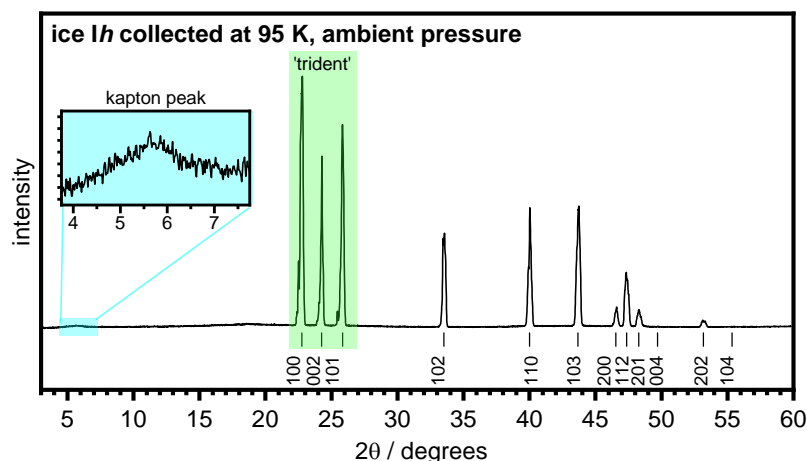


Figure 2.10: XRD pattern of ice Ih collected at 95 K and ambient pressure. The blue-shaded region centred at ~5.5 degrees shows a peak from the Kapton foils used in the sample holder. This did not interfere with phase ID, as for the ice phases investigated no characteristic peaks occurred in this region. The green-shaded region highlights the identifying feature of regular ice I, commonly referred to simply as the ‘trident’, owing to its appearance. While characterising high-pressure samples, the formation of external ice Ih on the sample holder was common and could be seen by the appearance of these particularly strong peaks.

Additionally, Kapton® could be identified from the presence of a broad feature centred at 5.5°, as highlighted in the blue-shaded region of Figure 2.10.

2.5.6 Neutron diffraction (ND)

Unlike X-ray diffraction, neutron diffraction is not so readily available as generating neutrons is not a straightforward process. Neutrons are generated at one of two types of sources, spallation and reactor.²⁰

Reactors produce neutrons *via* the fission of Uranium-235 which produces neutrons after being fired with an initial neutron. This generally produces neutrons which are 2 MeV. In order to bring the energy of the resulting neutrons to a more useable value, moderators are used to ‘cool’ them to energies of a lower order (*i.e.* to the tens of meV range). A well-known reactor source of neutrons is the Institute Laue-Langevin (ILL) in Grenoble, France.¹⁶

Spallation sources use high energy protons fired at heavy metal nuclei which lead to the release of neutrons among other particles. These are generally not produced in a constant fashion, leading to this form of neutron production to be referred to as ‘pulsed’. Here, in a similar way to neutrons formed at reactors, the neutrons produced are also too high in energy to be used directly and need to be moderated. All neutron

2. Experimental methods and characterisation techniques

data included in this report was carried out at the ISIS Muon and Neutron Source in Harwell, Oxford, which is a spallation source.¹⁶

2.5.6.1 Low temperature ND

Ices were prepared for use in gas cells as mentioned in section 2.4.3. The temperatures of the gas cells were regulated by helium cryostats. Diffraction data was converted using the Mantid software⁶ on the PEARL beamline to enable the refining of data using GSAS software.²¹

2.6 Differential scanning calorimetry (DSC)

Differential scanning calorimetry (DSC) is a thermal analysis method which can provide thermodynamic parameters of a sample such as how the heat capacity of a material changes as a function of temperature.²² Specifically, it measures the change in the difference in the heat flow rate to the sample and to a reference while both sample and reference are changed in temperature.²² It is useful to determine phases transitions, heat capacities and glass transitions of materials. There are two types of differential scanning calorimeters: heat flow (or power compensation) and heat flux, they provide the same insights as one another, however they operate slightly differently.²²

Heat flow calorimeters maintain the temperature of a reference and sample pan which are held in individual microfurnaces. If an exo/endothermic process occurs in the sample pan, its individual furnace either increases or decreases the power provided to it to maintain linear changes to the temperature in accordance with the temperature program defined by the user.²³ This is achieved using a second differential control loop.²³ Heat flow calorimeters directly measure the power provided in the compensation process. Meanwhile heat flux calorimeters do not directly measure power, but instead measure temperature differences between the sample and reference pans which are kept in the same furnace.²³ The corresponding heat flow is then measured from the temperature difference between the two pans.

In a heat flow calorimeter, the quantity that is usually measured is the flow of energy given in either mW or J s⁻¹ as a function of either time or temperature.²⁴ Calorimeter software requires users to input the mass of sample into the program to determine the heat capacity, and hence the signal provided is usually given by:

2. Experimental methods and characterisation techniques

$$\begin{aligned} \text{DSC signal (W/g)} &= \text{heat capacity (J K}^{-1} \text{ g}^{-1}) \times \text{scanning rate (K s}^{-1}) \\ \frac{dH}{dt} &= \frac{dH}{dT} \times \frac{dT}{dt} \end{aligned} \quad \text{Equation 2.5}$$

This allows information relating to changes in enthalpies of transitions, glass transitions and heat capacities of samples to be determined.

2.6.1 Low temperature DSC

Perkin Elmer DSC 8000 Advanced Double Furnace differential scanning calorimeter was used as it had a base temperature of 93 K, ideal for analysing ice samples. A helium exchange gas was used with a flow rate of 40 mL / min. DSC pans made of stainless steel were precooled in liquid nitrogen before pieces of ice were placed into them and screwed shut. The pans were then quickly transferred to the DSC before specific temperature programs were performed. These were often at a heating rate of 10 K min⁻¹ as this provided a good signal-to-noise ratio; heating rates of less than 2.5 K min⁻¹ were not used for this reason. To scale the DSC signal so that thermograms were comparable to one another, two approaches were used depending on what the sample in question was. The main issue lies with the fact that when filling the sample pans at low temperatures it is not possible at the moment of filling to know the mass of sample and hence the associated number of moles it has. To address this, pure H₂O (D₂O) ice samples were heated beyond the endothermic transition of melting, which has known enthalpy of melting of 6012 J mol⁻¹ (6280 J mol⁻¹).²⁵ This allowed for the number of moles to be determined. Following this, the heating and cooling programs were repeated to collect baseline data which was then subtracted from the original scans to obtain background corrected scans. The background subtracted scans were then divided by the number of moles and the heating rate to obtain a signal with the units J mol⁻¹ K⁻¹ allowing for the comparison between different samples. For samples of 0.01 M HCl ice, the same melting values were taken, given the relatively small proportion of acid. Meanwhile, samples of ice that were a mixture of NH₄F and H₂O had their pans weighed with and without sample to determine the sample mass. Then, depending on the ratio of NH₄F to H₂O, the moles of NH₄⁺: F⁻: H₂O were determined to scale the signal. The weighing of pans with and without sample was also performed on pure solid NH₄F samples. Data was converted to a usable format using the Pyris software which accompanied the DSC.

2. Experimental methods and characterisation techniques

2.7 Raman spectroscopy

Raman spectroscopy is an absorption spectroscopy technique which probes vibrational and rotational transitions in molecules. A selection rule for Raman activity is that a sample must experience a change in polarisability, α , when it is exposed to an electric field.

Monochromatic light is focused onto a sample, which causes radiation to be scattered as the incident radiation collides with the molecules within the sample. This gives rise to three scattering scenarios that are depicted in Figure 2.11.

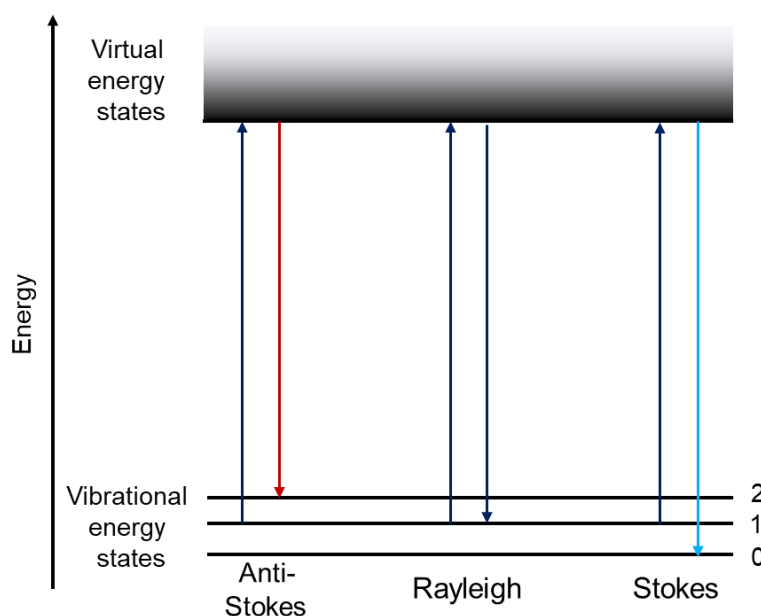


Figure 2.11: The three potential scattering events in Raman spectroscopy. If the scattering is elastic, Rayleigh scattering occurs (middle). Inelastic scattering can also occur in the form of anti-Stokes scattering, which is where the scattered photon has a higher frequency than the incident radiation (left). Stokes scattering occurs when the scattered radiation has a lower frequency than the scattered radiation (right).

If the incident photon's energy is equal to the energy scattered back, the transition is referred to as a Rayleigh scattering event. However, if the energy scattered back is less than that of the incident photon, the resulting frequency of the scattered photon is smaller – this is referred to as a Stokes scattering event. Similarly, if the scattered photon has a larger energy than the incident radiation, anti-Stokes scattering occurs. As the net absorption is what is measured, Raman spectroscopy records the intensity of the scattered radiation as a function of wavenumber shift (which is usually reported in reciprocal centimetres).

2. Experimental methods and characterisation techniques

2.7.1 Low temperature Raman

Raman spectroscopy was carried out on a Renishaw Ramascope spectrometer with a He-Ne laser wavelength of 632.8 nm. The Raman shifts of the spectra were calculated by using the sharp emission lines of a neon-discharge lamp.²⁶ Continuous scanning was used; four accumulations of regions of interest were collected in order to reduce the noise-to-signal ratio by half. The collection time of each scan varied between (150 to 250) s depending on the sensitivity of the region. To collect data of the ice samples, a low temperature, low pressure (10^{-2} mbar) environment was created by using an Oxford Instruments Microstat^N. The temperature was regulated with an Oxford Instruments Temperature Controller and an Oxford instruments Nitrogen Gas Flow Controller. Small pieces of ice were ground up while placed on the cryostat stage, which was covered in liquid nitrogen. Liquid nitrogen was also used as the cooling medium, which allowed for the analysis of samples at ~ 78 K. The apparatus was also linked to a temperature control unit which meant the sample could be heated to set temperatures, at a rate of ~ 5 K min^{-1} for annealing, before being brought back to liquid nitrogen temperatures for data collection.

The samples of ice that were investigated contained 5 w% D₂O in order to measure decoupled vibrations.²⁷ This introduced a small number of O–D oscillators which blocked any coupling stretching transitions,²⁷ leading to a partially polarised region being analysed.²⁸ The significance of the decoupled vibrations is that they allow one to see effects from very localised regions of ice.²⁷ The O–D decoupled region is centred at ~ 2500 cm^{-1} . Work by Carr *et al.* has also demonstrated that coupled vibrations increase in their broadening with increasing stacking disorder in ice samples.²⁷

In the case of ice, there are several general spectral regions of interest, which are shown in Figure 2.12 for ice *Ih*.

2. Experimental methods and characterisation techniques

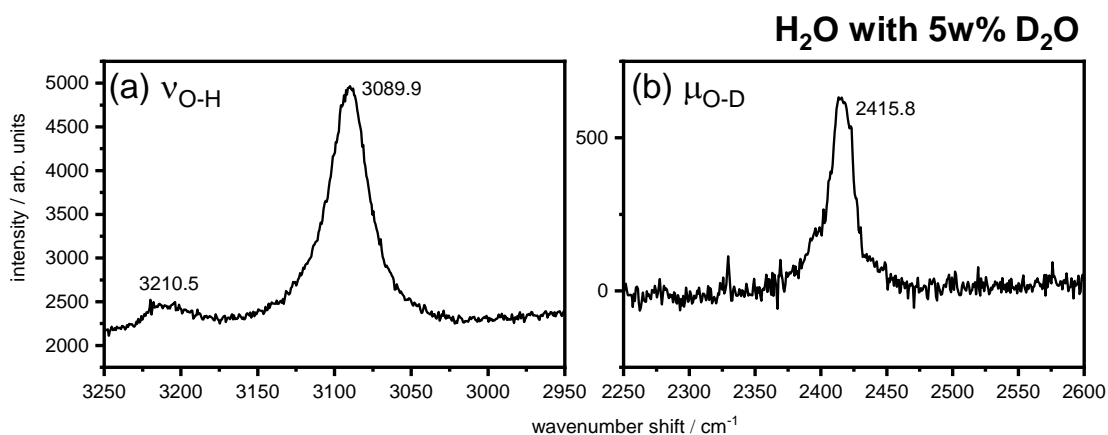


Figure 2.12: Raman spectra of ice Ih at 78 K at $\sim 10^{-2}$ mbar showing: (a) O–H coupled regions centred at ~ 3100 cm⁻¹ and; (b) O–D decoupled regions ~ 2400 cm⁻¹. Depending on the phase being studied, the regions that these are centred at will vary slightly.

Stretching (ν) of coupled O–H generally occur in the $3600 - 3100$ cm⁻¹ range, as demonstrated in Figure 2.12(a).²⁹ Decoupled O–D stretching (μ) is shown in Figure 2.12(b) and occurs over the range of $2600 - 2300$ cm⁻¹.²⁹ Another spectral range is also sometimes studied at much lower energies between $750 - 200$ cm⁻¹ where the spectrum results from librational and translational modes.²⁹

2. Experimental methods and characterisation techniques

2.8 Software

Some of the software used is listed in the following subsections. All graphs were prepared in OriginPro software. Diamond 3.2 was used to draw crystal structures. PowderCell 2.4 was used to simulate XRD patterns from structure files.

2.8.1 MCDIFFaX

MCDIFFaX is used to determine stacking probabilities of a layered material.³⁰ It embeds DIFFaX, a software developed by Mike Treacy,³¹ which can simulate diffraction patterns of materials with defined stacking faults, but it takes the software further by implementing Monte Carlo type refinement approach. DIFFaX generates patterns based on the input of several parameters such as lattice constants, fractional coordinates of each atom, and Cagliotti terms u , v and w parameters (associated with full width half maximum broadening, $\Gamma(\theta)$). The Gaussian/Lorentzian ratio of each peak is a function of the broadening.

The associated equation for full width half maximum broadening, $\Gamma(\theta)$ is:

$$\Gamma(\theta) = \sqrt{u \tan^2(\theta/2) + v \tan(\theta/2) + w} \quad \text{Equation 2.6}$$

MCDIFFaX embeds DIFFaX into a least-square environment and applies Monte Carlo algorithms to find the best values of stacking probabilities, lattice constants, peak profiles and thermal parameters. The parameters are varied until a low χ^2 is achieved between the experimental XRD data and the simulated XRD pattern as generated by MCDIFFaX. A defining feature of MCDIFFaX is that the use of a *Monte Carlo* parameter reduces the likelihood of the Monte Carlo refinements becoming trapped in a local χ^2 minimum.

Stacking disorder can be considered in terms of memory effects present. Stacking probabilities are denoted by Φ and either subscripts 'c' or 'h' to describe cubic or hexagonal stacking present respectively. The amount of cubic stacking is referred to as the cubicity of the material and it is denoted by Φ_c . In the initial parts of the refinement, it is assumed that zero memory effects are present, meaning that the stacking of a particular layer is not influenced by the stacking of the previous layer. It is often found that fits provided by MCDIFFaX are optimised with the introduction of first order memory effects being refined. First order memory effects describe when the stacking of a particular layer is dependent on the stacking of the previous layer. Φ_{cc}

2. Experimental methods and characterisation techniques

describes a cubic stacking event after another cubic stacking event, while Φ_{hc} describes a cubic stacking event after a hexagonal stacking event. Given that only cubic or hexagonal stacking can occur, the stacking probabilities Φ_{ch} and Φ_{hh} are expressed as $(1 - \Phi_{cc})$ and $(1 - \Phi_{hc})$ respectively. Such first order memory effects can be visualised using a plot called a ‘stackogram’ which is shown in Figure 2.13.

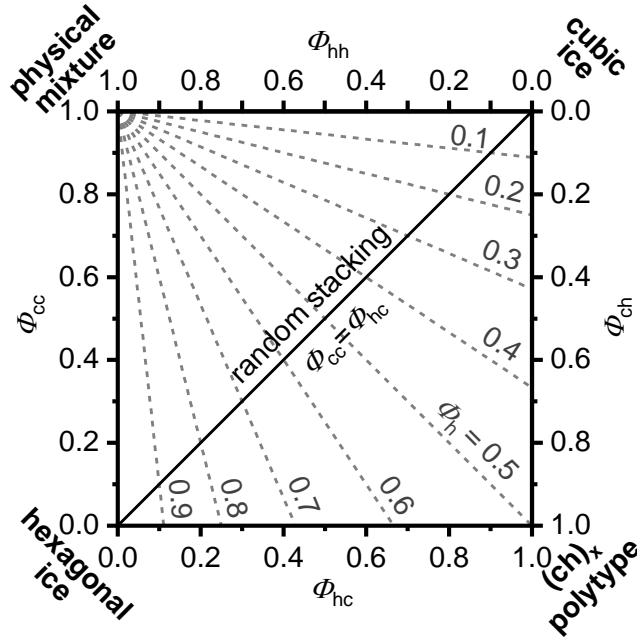


Figure 2.13: Stackogram of ice. Black solid line shows where materials with random stacking of layers would lie, while the dotted lines radiating from the top left-hand corner describe materials with constant hexagonality.³²

Stackograms plot Φ_{cc} against Φ_{hc} and provide information regarding the type of stacking sequences in a material, as indicated by the four corners of the diagram defining possible end-member states. These end-member states describe a physical mixture, cubic ice, $(ch)_x$ polytype ice and hexagonal ice. Polytype $(ch)_x$ ice describes alternating stacking of hexagonal and cubic sequences of ice.

Cubicity is given by:

$$\Phi_c = \frac{\Phi_{hc}}{\Phi_{hc} - \Phi_{ch}} \quad \text{Equation 2.7}$$

The associated hexagonality, Φ_h , is given by $1 - \Phi_c$.

MCDIFFaX was used to analyse X-ray diffratograms of high-pressure ammonium fluoride phases which covered a 2θ range of 10° to 60° . These were of NH_4F II and

2. Experimental methods and characterisation techniques

NH₄F III, recorded initially at 95 K, and then from 100 to 270 K in steps of 10 K. An example of NH₄F II at 140 K is provided in Figure 2.14.

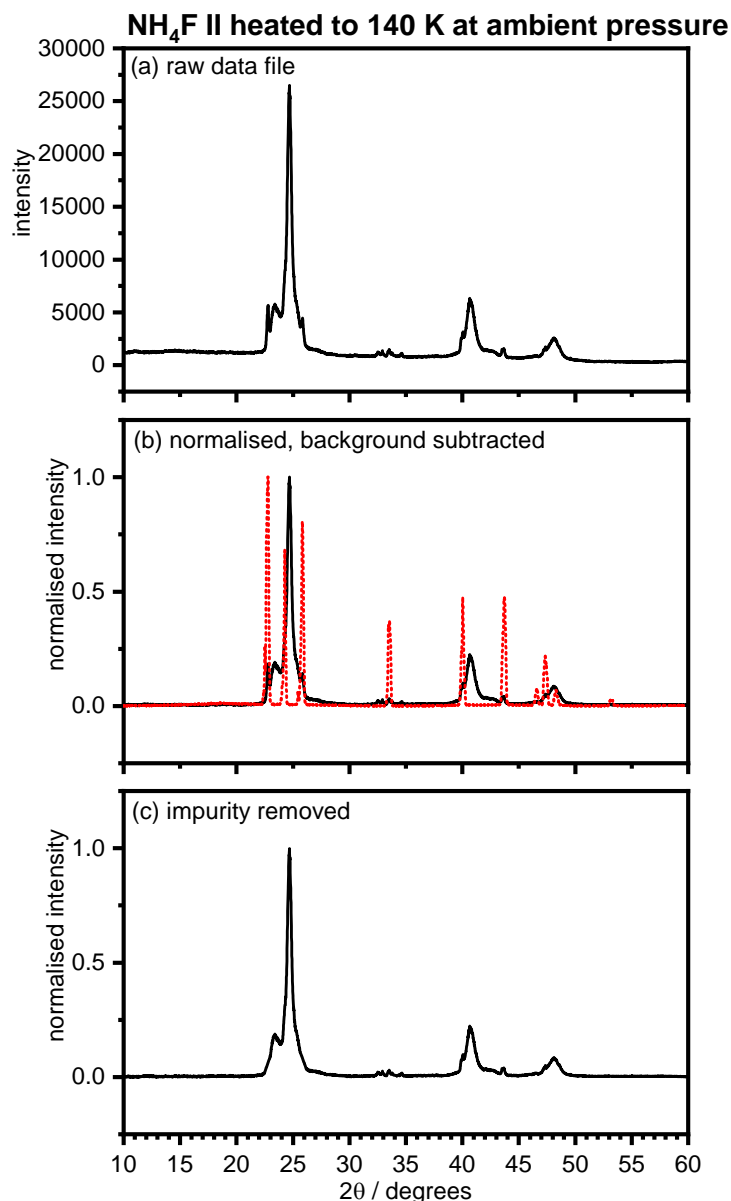


Figure 2.14: XRD data from a sample of NH₄F II heated to 140 K at ambient pressure. (a) the raw data, (b) the data after normalising and background subtraction being performed. Here the red dotted line shows where ice Ih peaks lie, which helps determine where intensity needs to be reduced to remove the impurity. (c) the purity-free data ready to use as an input file in MCDIFFaX.

The raw data is shown in Figure 2.14(a), however several processes needed to be applied to use it. The data needed to be background subtracted (this was performed within OriginPro software) and normalised, as seen in Figure 2.14(b). However, there were quite large impurity peaks resulting from external ice Ih on the sample holder. In

2. Experimental methods and characterisation techniques

Figure 2.14(c), these impurity peaks were removed by a linear interpolation of points between the impurity peaks.

2.8.2 General Structure Analysis System - GSAS

General Structure Analysis System²¹ (GSAS) was used with its graphical user interface EXPGUI.³³ GSAS was used to model X-ray and neutron diffraction data for phase identification, determine lattice parameter values and to calculate weight fractions of samples that were mixed-phase. GSAS allowed for the inclusion of restraints which put into place the Bernal-Fowler ice rules that have been discussed previously in the introduction. Hence, hydrogens bonded to an oxygen that were meant to have a combined occupancy of 1 were controlled by the implementation of atom constraints; this meant the rules concerning the occupancies of hydrogens/deuteriums were observed. The GSAS software was used to implement Rietveld refinement. In Rietveld refinement a model is created based on the input of parameters, such as space group symmetry, lattice parameters and instrumental parameters, to create a model of experimental data collected.³⁴ The residual, S , between the model and experimental data is minimised in a least-squares environment by changes to the model³⁴:

$$S = \sum_i w_i (y_i - y_{ic})^2 \quad \text{Equation 2.8}$$

Here $w_i = \frac{1}{y_i}$ and represents a weighting factor, y_i is the observed intensity at the i th step, y_{ic} is the calculated intensity at the i th step.³⁴ On the convergence of the residual, S , and a good visual fit of the data being observed, the refinement was taken to be completed.

2. Experimental methods and characterisation techniques

2.9 References

1. W. M. Haynes, *CRC Handbook of Chemistry and Physics*, CRC Press Inc., 91st edn., 2010-2011.
2. G. Brauer, *Handbook of Preparative Inorganic Chemistry*, Academic Press, 1963.
3. C. G. Salzmann, P. G. Radaelli, B. Slater and J. L. Finney, *Phys. Chem. Chem. Phys.*, 2011, **13**, 18468-18480.
4. C. G. Salzmann, P. G. Radaelli, J. L. Finney and E. Mayer, *Phys. Chem. Chem. Phys.*, 2008, **10**, 6313-6324.
5. C. L. Bull, N. P. Funnell, M. G. Tucker, S. Hull, D. J. Francis and W. G. Marshall, *High Pressure Res*, 2016, **36**, 493-511.
6. O. Arnold, J. C. Bilheux, J. M. Borreguero, A. Buts, S. I. Campbell, L. Chapon, M. Doucet, N. Draper, R. Ferraz Leal, M. A. Gigg, V. E. Lynch, A. Markvardsen, D. J. Mikkelsen, R. L. Mikkelsen, R. Miller, K. Palmen, P. Parker, G. Passos, T. G. Perring, P. F. Peterson, S. Ren, M. A. Reuter, A. T. Savici, J. W. Taylor, R. J. Taylor, R. Tolchenov, W. Zhou and J. Zikovsky, *Nucl. Instrum. Methods Phys. Res. A*, 2014, **764**, 156-166.
7. S. Klotz, *Techniques in High Pressure Neutron Scattering*, CRC Press, 2012.
8. S. A, Classic Kit: Bridgman's seal, <https://www.chemistryworld.com/opinion/classic-kit-bridgmans-seal/3004901.article#/>, (accessed 30/04/20, 2020).
9. High pressure gas cells, <http://www.isis.stfc.ac.uk/sample-environment/sample-containers/high-pressure-gas-cells/high-pressure-gas-cells8936.html>).
10. C. J. Ridley and K. V. Kamenev, *Zeitschrift für Kristallographie - Crystalline Materials*, 2014, **229**, 171-199.
11. C. Hammond, *The basics of crystallography and diffraction*, Oxford : Oxford University Press, Fourth edition. edn., 2015.
12. H. Fritzsche, J. Huot and D. Fruchart, *Neutron Scattering and Other Nuclear Techniques for Hydrogen in Materials*, Springer International Publishing, 2016.
13. O. K. Ersoy, in *Diffraction, Fourier Optics and Imaging*, DOI: doi:10.1002/9780470085004.ch1.

2. Experimental methods and characterisation techniques

14. M. Samiullah, in *A First Course in Vibrations and Waves*, Oxford University Press, Oxford, 2015, DOI: 10.1093/acprof:oso/9780198729785.003.0010.
15. D. S. Sivia, *Elementary Scattering Theory: For X-ray and Neutron Users*, OUP Oxford, 2011.
16. C. Lobban, PhD thesis, University College London, 1998.
17. M. Hosokawa, K. Nogi, M. Naito and T. Yokoyama, in *Nanoparticle Technology Handbook (2nd Edition)*, Elsevier, 2012.
18. A. Leone, A. Forleo, L. Francioso, S. Capone, P. Siciliano and C. Di Natale, *Sensors and Microsystems: Proceedings of the 19th AISEM 2017 National Conference*, Springer International Publishing, 2017.
19. Y. P. Handa, D. D. Klug and E. Whalley, *Can. J. Chem.*, 1988, **66**, 919-924.
20. M.-E. Donnelly, PhD thesis, University of Edinburgh, 2016.
21. A. C. Larson and R. B. Von Dreele, "*General Structure Analysis System (GSAS)*", *Los Alamos National Laboratory Report LAUR 86-748* 2000.
22. G. Höhne, W. F. Hemminger and H. J. Flammersheim, *Differential Scanning Calorimetry*, Springer Berlin Heidelberg, 2013.
23. W. M. Groenewoud, in *Characterisation of Polymers by Thermal Analysis*, ed. W. M. Groenewoud, Elsevier Science B.V., Amsterdam, 2001, DOI: <https://doi.org/10.1016/B978-044450604-7/50002-9>, pp. 10-60.
24. P. Gabbott, in *Principles and Applications of Thermal Analysis*, 2008, DOI: 10.1002/9780470697702.ch1, pp. 1-50.
25. J. J. Shephard and C. G. Salzmman, *Chem. Phys. Lett.*, 2015, **637**, 63-66.
26. K. Burns, K. B. Adams and J. Longwell, *J. Opt. Soc. Am.*, 1950, **40**, 339-344.
27. T. H. G. Carr, J. J. Shephard and C. G. Salzmman, *J. Phys. Chem. Lett*, 2014, **5**, 2469-2473.
28. B. Minceva-Sukarova, W. F. Sherman and G. R. Wilkinson, *Spectrochim. Acta A*, 1985, **41**, 315-318.
29. C. G. Salzmman, A. Hallbrucker, J. L. Finney and E. Mayer, *Phys. Chem. Chem. Phys.*, 2006, **8**, 3088-3093.
30. T. L. Malkin, B. J. Murray, C. G. Salzmman, V. Molinero, S. J. Pickering and T. F. Whale, *Phys. Chem. Chem. Phys.*, 2015, **17**, 60-76.
31. M. M. J. Treacy, J. M. Newsam and M. W. Deem, *P. Roy. Soc.-Math. Phys. Sci.*, 1991, **433**, 499-520.

2. Experimental methods and characterisation techniques

32. C. G. Salzmänn, B. J. Murray and J. J. Shephard, *Diamond Relat. Mater.*, 2015, **59**, 69-72.
33. B. H. Toby, *J. Appl. Crystallogr.*, 2001, **34**, 210-213.
34. R. A. Young, *The Rietveld Method*, Oxford University Press, 1995.

3 Mapping the phase diagram of H₂O-NH₄F mixtures

3.1 H₂O-NH₄F mixtures at ambient pressure

This section explores H₂O, NH₄F and their mixtures at ambient pressure. The effects of the addition of NH₄F to ice are explored, with lattice constants and onset temperatures of melting and freezing reported and compared to data collected in the 1960s.¹⁻³

3.1.1 X-ray investigations into ice-ammonium fluoride mixtures

In similarity to the work conducted by Lyashchenko *et al.*,¹ XRD measurements of ice, ammonium fluoride and mixtures of the two were carried out and are shown in Figure 3.1. As ice and NH₄F are isostructural (Figure 3.1(d)) with the space groups $P6_3/mmc$ and $P6_3mc$ respectively,⁴ their XRDs have the same appearance. Lyashchenko *et al.*'s work was not carried out at a constant temperature and had varying data collection times.¹ This poses an issue as lattice constants, which are sensitive to temperature, cannot have trends measured accurately and data quality may not be consistent. Unlike with Lyashchenko *et al.*'s work, the data shown for the experiments in Figure 3.1 was all collected at 95 K and all over the same period of time of ~25 mins.

Pure H₂O ice *Ih* is displayed in Figure 3.1(a) alongside tickmarks and Miller indices of the reflections of its Bragg peaks. XRD patterns of ice and NH₄F are shown in Figure 3.1(b) for the composition range of 10 to 50 mol% NH₄F in ice, for which there is proper mixing of the two species (*i.e.* separate peaks are not seen for the two species). This indicates the formation of solid solutions of the mixed species as the resulting phase is homogeneous.⁵ Increasing NH₄F content can be seen by the overall peak shift as highlighted in the inset of Figure 3.1(b) for the 102 peak, which has larger 2θ values. Figure 3.1(c) displays the pattern collected of pure NH₄F I, which has the same symmetry as the above patterns; this sample did contain some impurity which seems to be attributable to ammonium bifluoride which NH₄F is known to convert to.⁶ From analysis in GSAS^{7, 8} however, it was calculated as being present in less than 7 w% of the sample.

From the XRD patterns collected, lattice constants were determined of the samples in similarity to work performed by Lyashchenko *et al.* in 1968.¹ However, given the length of time separating these studies, and the level of accuracy to which

3. Mapping the phase diagram of H₂O-NH₄F mixtures

lattice constants are reported to in Lyashchenko *et al.*'s work, it is likely that values reported here may be more accurate.

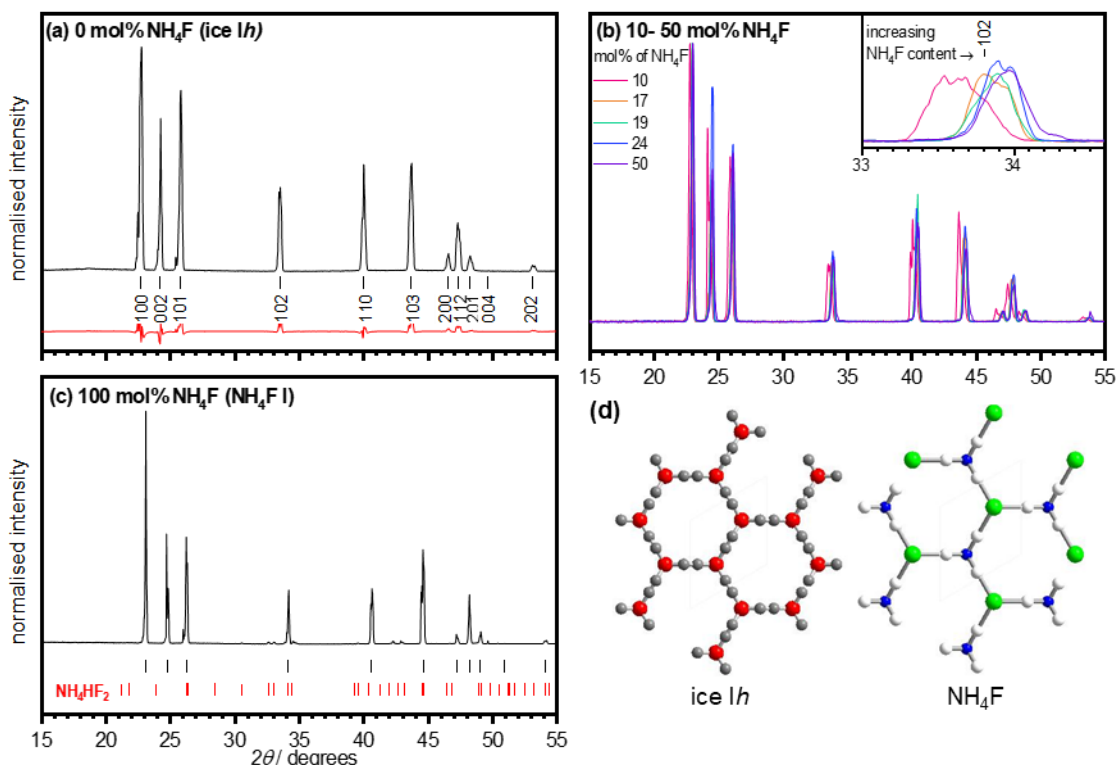


Figure 3.1: XRD patterns at 95 K at ambient pressure of (a) H₂O ice Ih, (b) H₂O-NH₄F mixtures ranging from 10 to 50 mol%, as indicated in the legend and (c) NH₄F I. In (a), the red line indicates the residuals from the Rietveld fit to Fortes' lattice constants.⁹ The red tick marks in (c) show the presence of the impurity ammonium bifluoride. (d) highlights the structural similarities of H₂O and NH₄F.

This is largely due to the fact that the ice Ih pattern was calibrated against Fortes' new values of ice Ih.⁹ Lyashchenko and coworkers quote their lattice parameters to two significant figures, with pure water having lattice parameters a and c as 4.52 and 7.35 Å respectively between 233.15 to 243.15 K.¹ Fortes, on the other hand, is able to quote a and c as 4.51783(6) and 7.35630(19) Å at 244.96(1) K.⁹ Although these values are in agreement with each other, the ability to quote lattice parameters and temperatures to a greater degree of accuracy is now taken advantage of. Fortes' lattice parameters for ice Ih were collected with a silicon standard data on the High-Resolution Powder Diffractometer beamline at ISIS, which has one of the longest primary neutron flight-path instruments in the world.⁹ These values are now taken as the new gold standard of lattice constants of H₂O and D₂O ice Ih at ambient pressure.⁹

3. Mapping the phase diagram of H₂O-NH₄F mixtures

Peak positions in an XRD pattern are dependent upon the lattice constants of the unit cell of a material and the zero shift associated with the instrument collecting the XRD data.¹⁰ The XRD instrument did not have a known zero shift that could be reliably used, hence it needed to be determined. Literature values reported by Fortes for ice *Ih* are known to be: $a = 4.49703(3) \text{ \AA}$, $c = 7.32220(9) \text{ \AA}$ at 95.00(1) K.⁹ For the data reported in Figure 3.1(a), Fortes' lattice constants were added to the GSAS model as fixed values and the zero shift was refined. The zero shift was found to be -4.13409 centidegrees, which could then be used in the subsequent determination of lattice parameters of the mixtures of ice and NH₄F and of the pure NH₄F. The refined lattice constants, as well as the c/a ratios are provided Table 3.1 and Figure 3.2.

Table 3.1: Lattice constants of solid solutions of NH₄F-ice calculated from the XRD patterns shown in Figure 3.1. The values at 0 mol% NH₄F are the literature values given by Fortes⁹ which were used to 'calibrate' the rest of the measurements.

| NH₄F mol% | $a / \text{\AA}$ | $c / \text{\AA}$ | c/a |
|-----------------------------|------------------------------------|------------------------------------|-------------------------|
| 0 | 4.4970* | 7.3222* | 1.628 |
| 10 | 4.4811 | 7.3037 | 1.630 |
| 17 | 4.4583 | 7.2588 | 1.628 |
| 19 | 4.4540 | 7.2501 | 1.628 |
| 24 | 4.4522 | 7.2410 | 1.626 |
| 50 | 4.4460 | 7.2295 | 1.626 |
| 100 | 4.4374 | 7.1763 | 1.617 |

For comparison, the determined lattice parameters and their associated c/a ratios are given in Figure 3.2 alongside the values that were obtained by Lyashchenko *et al.*¹ These data were all fit to a cell of ice *Ih* using GSAS⁷ and its EXPGUI⁸.

3. Mapping the phase diagram of H₂O-NH₄F mixtures

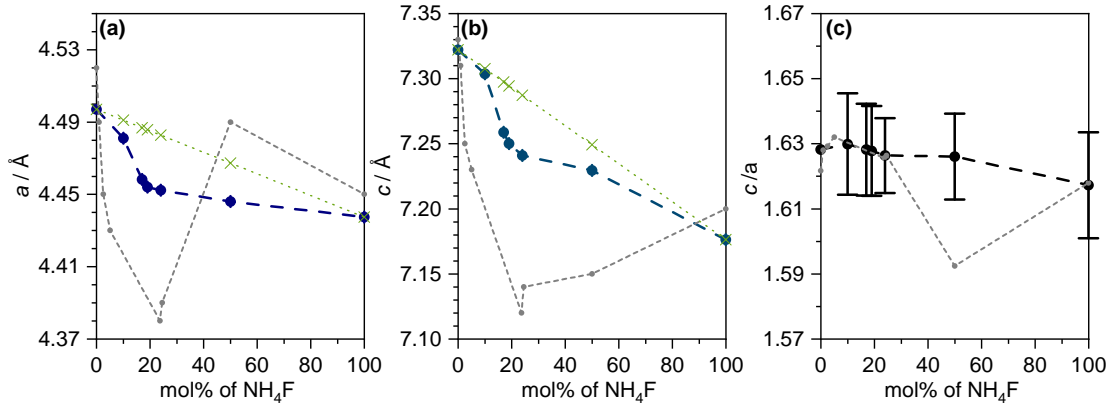


Figure 3.2: Lattice parameters of NH₄F-ice samples of between 0 to 100 mol% NH₄F shown by the large navy, teal and black circles. (a): the *a* lattice parameter, (b): the *c* lattice parameter and (c): the associated *c/a* ratios. Lyashchenko *et al.*'s values are shown by the grey points. The green crosses mark calculated values of lattice constants that would obey Vegard's Law. Errors are plotted, but only largely visible for *c/a*.

On increasing the concentration of NH₄F in ice, both *a* and *c* lattice parameters decrease, and the volume of the unit cell decreases, with the pure NH₄F experiencing a volume contraction of 4% compared to the pure ice *Ih*. Although the pure ice sample provided by Lyashchenko *et al.*¹ has a larger lattice parameter than the pure ammonium fluoride sample, and lattice parameters of their mixtures have values lying in between, a strictly direct relationship between NH₄F mol% and lattice constant is not followed, as can be seen, for example, by the analogous point at 50 mol% NH₄F in Figure 3.2(a).

The green crosses in Figure 3.2 give the expected values of the solid solutions if they were to follow Vegard's Law,¹¹ which were calculated using the following equation:

$$a_{\text{NH}_4\text{F}_{(1-x)}\text{H}_2\text{O}_{(x)}} = (1 - x)a_{\text{NH}_4\text{F}} + xa_{\text{H}_2\text{O}} \quad \text{Equation 3.1}$$

In Equation 3.1, *a* describes the lattice constant and *x* the molar fraction.

For the lattice constants of pure ice and NH₄F, Fortes' value was used and the calculated lattice constants of pure NH₄F shown in Table 3.1 were used. From Figure 3.2, it is quite clear that a negative deviation¹² from Vegard's Law exists for the *a* lattice constant, however it seems that for the *c* lattice constant, up to 10 mol%, Vegard's Law does hold.

3. Mapping the phase diagram of H₂O-NH₄F mixtures

3.1.2 Calorimetric investigations into ice-ammonium fluoride mixtures

Differential scanning calorimetry was also performed on the mixtures of NH₄F and ice, a selection of which are illustrated in Figure 3.3. These do not include pure NH₄F as it decomposes on heating and does not experience melting. The first heats of the DSC data were all very inconsistent due to the different sizes of the crystallites and irregular contact with the pans, hence the solid solutions were frozen and then the second heats of each scan were taken, all of which proved to provide more consistent data as these would have now had good thermal contact with the pans.¹³

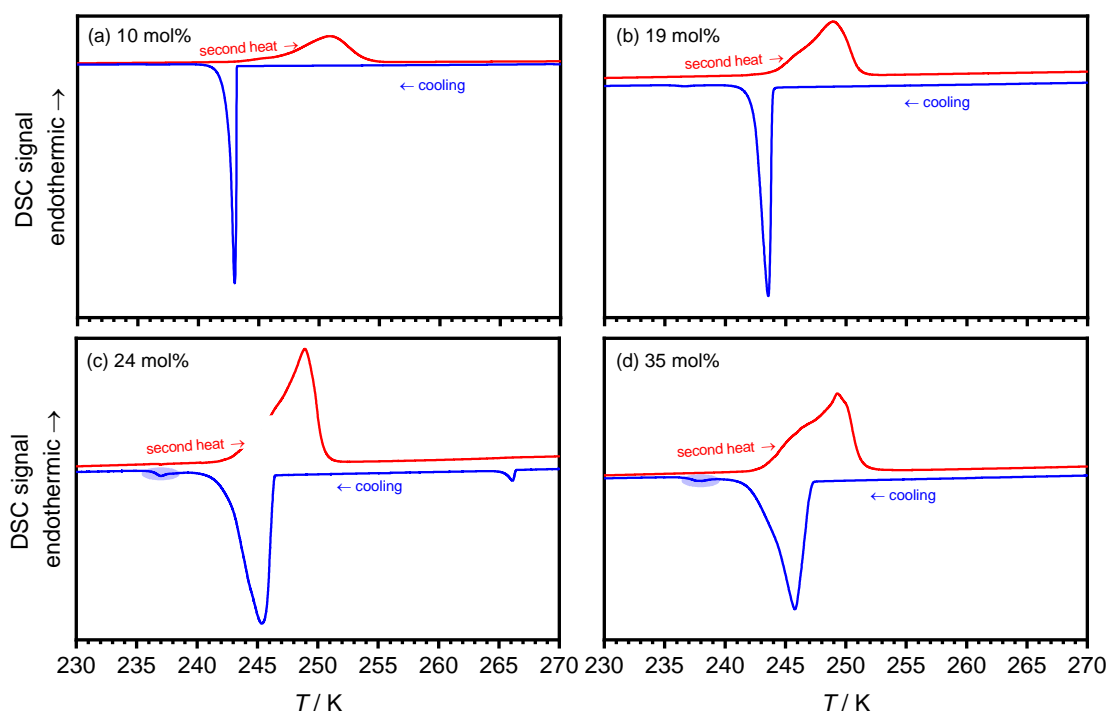


Figure 3.3: A range of DSC scans of NH₄F-ice solid solutions. With increasing NH₄F content, the freezing process takes place over a larger temperature range. (a), (b), (c) and (d) show 10, 19, 24 and 35 mol% NH₄F-ice respectively in similarity with the compositions explored by Labowitz et al.³ The 19 mol% NH₄F-ice sample is the reported eutectic composition by Labowitz et al.³ (c) and (d) contain small kinks, highlighted with blue shading, which likely result from eutectic impurities. All thermograms were collected with a heating rate of 10 K min⁻¹.

The DSCs of the solid solutions vary in their appearance, depending on the concentration of NH₄F present. For the lower concentrations, such as the 10 mol% NH₄F sample, the heating scans look the most symmetric, suggesting that most of the processes occurring on melting are of a similar nature. With increasing NH₄F concentration, the melting curves appear to become more asymmetric, as the effect of incongruent melting becomes more pronounced. From the melting and freezing curves

3. Mapping the phase diagram of H₂O-NH₄F mixtures

collected, the corresponding melting and freezing points on the different solid solutions were determined and are displayed in Figure 3.4.

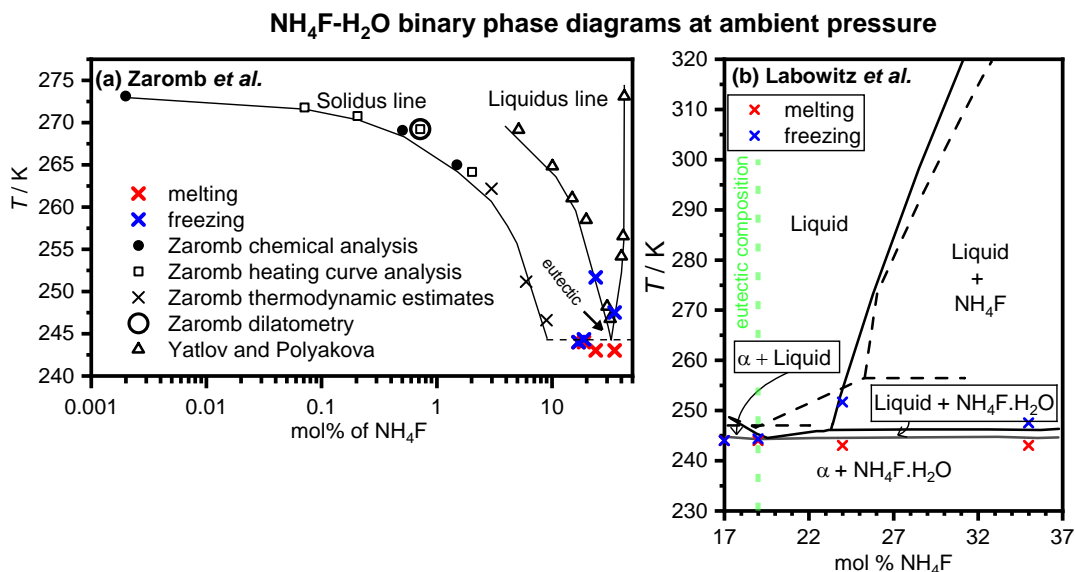


Figure 3.4: Freezing and melting point data from DSC data in this study overlaid on (a) Zaromb's¹⁴ data and (b) Labowitz *et al.*'s data^{2,3} where α denotes the solid solution. Both phase diagrams also include data from Yatlov and Polyakova¹⁵: in (a) this is indicated by the open triangles while in (b) their data is given by the dashed lines.

Binary phase diagrams of the NH₄F-H₂O system have been reported by Zaromb *et al.*¹⁴ (Figure 3.4(a)) and Labowitz *et al.*^{2,3} (Figure 3.4(b)), which highlight a eutectic line^{2,3,14} and also rather intriguingly the presence of a peritectic line.^{2,3} DSC from this study is overlaid on both Figure 3.4(a) and Figure 3.4(b). A peritectic line was inferred by both Yatlov and Polyakova and Labowitz *et al.* from the discontinuity of the slope boundary between the 'Liquid' phase and 'Liquid + NH₄F' phase at 256.4 K and 246.0 K respectively. Although a discrepancy in the temperatures of the peritectic line exists between the two studies,^{2,15} they both still observed a peritectic line. As the peritectic line would indicate the presence of another solid compound, both sets of co-workers attempted to elucidate the potential presence of another chemical species and, through work involving wet residues, it was suggested that a compound which was the monohydrate of NH₄F – *i.e.* NH₄F.H₂O – must exist with the Liquid phase between the peritectic and eutectic lines.² However, the presence of the peritectic line indicates that the monohydrate is likely to be highly thermally unstable, and it has barely been mentioned in literature since the 1960s. At the eutectic line, the phases expected to be in equilibrium are α and NH₄F.H₂O, while at the peritectic line the Liquid, NH₄F.H₂O, α and NH₄F are expected to co-exist.

3. Mapping the phase diagram of H₂O-NH₄F mixtures

Labowitz *et al.*^{2,3} reported a eutectic point of the system for 19 mol% NH₄F as indicated by the green line in Figure 3.4(b); this appears to be in line with the results obtained from the DSC melting and freezing curves. Zaromb *et al.*'s¹⁴ phase diagram in Figure 3.4(a) also includes data from Yatlov and Polyakova's study (shown by the open triangles), which reported a eutectic point at closer to 30 mol% NH₄F.¹⁴ The melting and freezing points from the DSCs at around this molar composition at 35 mol% NH₄F, as shown in Figure 3.3(d), have differences of at least 5 K between each other. This suggests that this molar composition does not produce a eutectic point, as these are characterised by especially sharp melting and freezing points.¹⁶ Additionally, the potential for the eutectic point being at 30 mol% NH₄F is further discredited by the way in which the DSC scans of the 24 and 35 mol% NH₄F solid solutions have small kinks (Figure 3.3(c) and (d)), which are likely to indicate the presence of eutectic impurities, meaning that the eutectic composition is not at or between these molar compositions.^{13, 17}

3.1.3 Conclusions

Overall, it has been demonstrated that ice and NH₄F mix well to form solid solutions between 0 to 50 mol% NH₄F, as highlighted by the XRD patterns in Figure 3.1(b). The lattice constants for ice and ammonium fluoride mixtures have been shown for the first time in more than 60 years and are calibrated with the most up-to-date reference lattice constants, as determined by Fortes.⁹ From calculation of lattice constants, ice and NH₄F mixtures increase in their density with increasing NH₄F content, with there being a 4% density increase between pure ice *Ih* and pure NH₄F. This agrees with data collected by Lyashchenko *et al.* who stated that the density increase must occur due to the introduction of fluoride ions, which due to their greater electronegativity compared to oxygen, create stronger hydrogen bonds and therefore cause the structure to contract.¹ It appears that up to a concentration limit of 10 mol% NH₄F, the mixtures of ice and NH₄F do follow Vegard's Law,¹¹ which can give an indication of molar percentage compositions of such mixtures.

Calorimetric data supports Labowitz *et al.*'s eutectic composition reported at 19 mol% NH₄F.³ More work needs to be performed to determine the potential existence of a monohydrate, which Labowitz *et al.*^{2,3} and several other authors from the time (in the 1960s) appear to have isolated.^{1, 18, 19} However, due to the indistinguishability of the

3. Mapping the phase diagram of H₂O-NH₄F mixtures

monohydrate using XRD, another reliable technique will need to be adopted to confirm or disprove its existence.

3.2 Mixtures of ice and ammonium fluoride at 0.5 GPa

Previous work by Shephard *et al.* considered the effect of NH₄F-ice mixtures in the 0 to 2.5 mol% NH₄F concentration range, determining that ice II no longer formed at concentrations below 0.5 mol% NH₄F.²⁰ This chapter investigates the effect of adding increased amounts of NH₄F to ice at 0.5 GPa to see how this affects the phases of ice that appear over the entire concentration range from 0 to 100 mol% NH₄F. It is expected that at lower concentrations of NH₄F, ice V-type structures will dominate, while at higher concentrations ice IV/ NH₄F II-type structures will form, as pure NH₄F exists as NH₄F II in this *p-T* range and it is isostructural with ice IV.²¹

3.2.1 From 0 to 2.5 mol% NH₄F

The effect of NH₄F concentration on solid solutions of ice between 0 to 2.5 mol% NH₄F was investigated through volume change (ΔV) plots. These were obtained from the isobaric heating of the mixed composition ices (0, 0.05, 0.1, 0.25, 0.5, 1.0 and 2.5 mol% NH₄F) from liquid nitrogen temperature up until they were found to start melting. Figure 3.5 shows the resultant 3D- ΔV plot for the composition range.

In Figure 3.5, the phases that occur for the isobaric heating of the doped ices over the concentration gradient are indicated. It is already well known that the isobaric heating of pure ice at 0.5 GPa observes the following phase sequence: ice *I_h*, ice III/IX, ice II and then ice V.²² On increasing the concentration of NH₄F in ice, the ice II step very quickly disappears and gives way to the presence of ice V in the original ice II stability region at concentrations above 0.1 mol% NH₄F. At the highest concentration of 2.5 mol% NH₄F, only three phases can be seen to emerge on heating – ices *I_h*, III and V. Onset melting temperatures (T_{om}) were also determined from the ΔV plots and are indicated with the red line in Figure 3.5; the addition of NH₄F to ice causes the T_{om} values to steadily decline as would be expected from the presence of the impurity

3. Mapping the phase diagram of H₂O-NH₄F mixtures

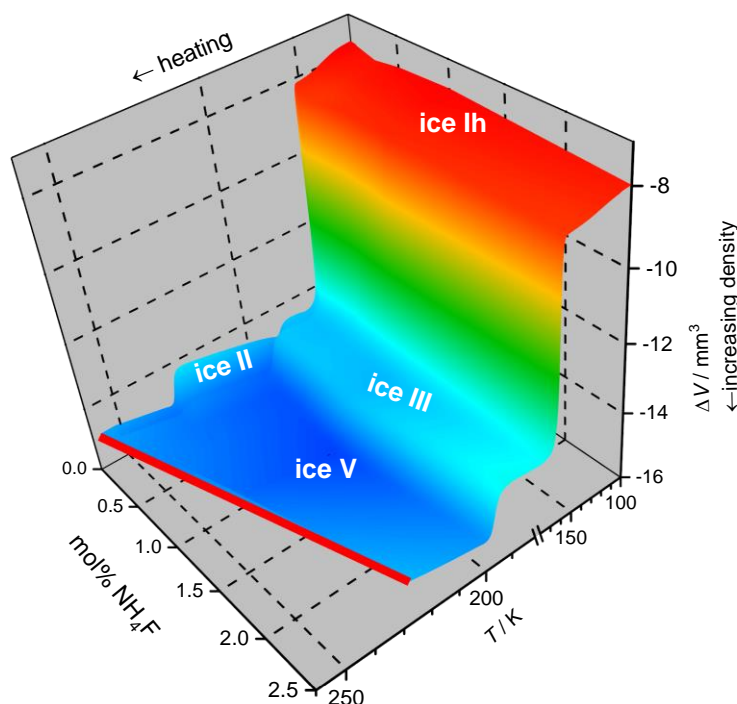


Figure 3.5: Change in volume (ΔV) plots in 3D from 0 to 2.5 mol% NH₄F-ice on isobaric heating at 0.5 GPa. The red line shows the temperatures of the onset of incongruent melting.

At the lower NH₄F-concentration end, several samples were quenched in order to reconfirm the presence of ices II and V, as depicted in Figure 3.6. In particular, a comparison can be made between that of pure ice and ice containing 0.1 mol% NH₄F.

Figure 3.6(a) and (b) show that the major phases that occur on quenching pure ice at 215 K and 250 K are ices II and V respectively. On slightly increasing the concentration to 0.1 mol% NH₄F (as in Figure 3.6(c) and (d)), the samples quenched at 210 and 240 K show that ices II and V are also present. However as can be seen in Figure 3.6(c), although the sample quenched at 210 K contains ice II, it does not make up the main composition of the sample, instead ice V is present at 62 w%.

3. Mapping the phase diagram of H₂O-NH₄F mixtures

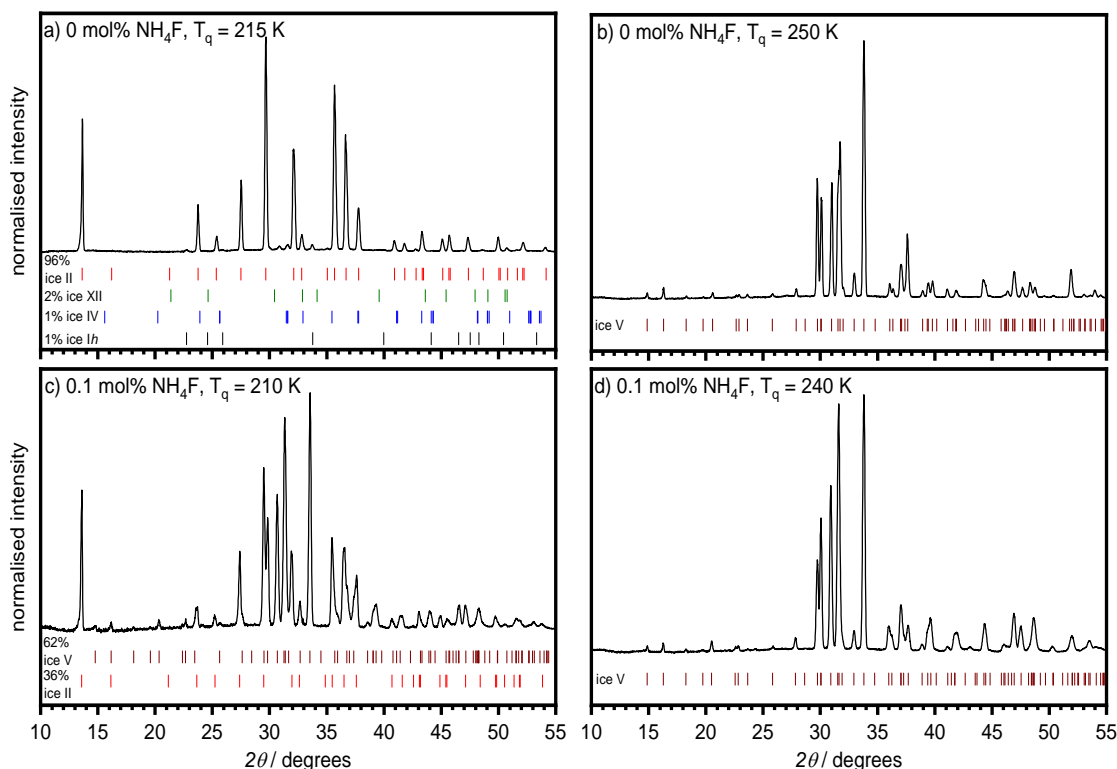


Figure 3.6: XRD patterns of 0 mol% NH₄F samples quenched at (a) 215 K and (b) 250 K. XRDs of 0.1 mol% NH₄F quenched at (c) 210 K and (d) 240 K.

This must be a consequence of the presence of NH₄F still being able to block the formation of ice II to an increasing extent.

3.2.2 Beyond 2.5 mol% NH₄F

As in Shephard *et al.*'s work performed at 0.3 GPa, NH₄F was shown to be able to selectively switch off the formation of ice II at 2.5 mol% NH₄F and definitely above 0.5 mol% NH₄F, as determined for 0.3 GPa.²⁰ It still remains unknown territory however, as to what occurs on increasing the concentration of NH₄F beyond its solubility limit and on increasing the concentration to 100 mol% NH₄F. The compression of pure NH₄F at 0.5 GPa is reported to give rise to NH₄F II, which beyond ~440 K converts to NH₄F IV.^{23, 24} The highest temperature phase that can be accessed in this study is NH₄F II, which is isostructural with ice IV (Figure 3.7).²¹

3. Mapping the phase diagram of H₂O-NH₄F mixtures

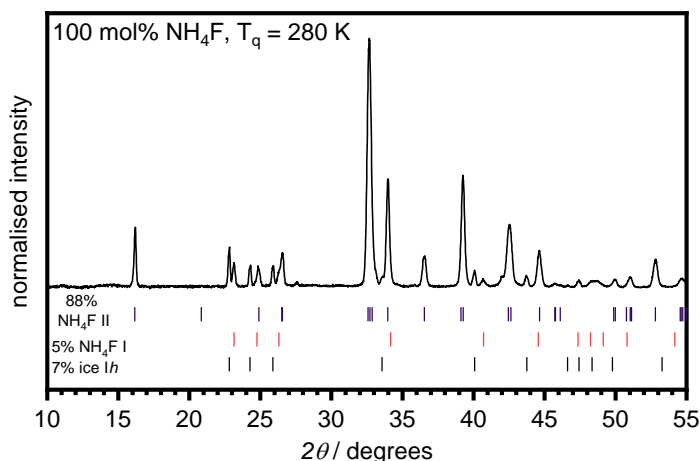


Figure 3.7: NH₄F II is obtained on heating 100 mol% NH₄F at 0.5 GPa. The sample was quenched at 280 K. The XRD was collected at 95 K at ambient pressure.

Based on the pure end members – ice and NH₄F – the logic assumed was that at lower concentrations of NH₄F, ice V-type structures would occur, whereas at higher NH₄F concentrations ice IV/NH₄F II-type structures would emerge.

Volume change plots are shown here in 2D to illustrate the progression of phases that occur on the isobaric heating of NH₄F-ice samples of different compositions (Figure 3.8). NH₄F-ice mixtures were compressed to 0.5 GPa using the Zwick Universal Testing Machine after having been cooled with liquid nitrogen to 77 K. After the samples were compressed to 0.5 GPa, the liquid nitrogen surrounding the samples being compressed by the piston cylinder was removed and the samples were allowed to heat under ambient conditions (*i.e.* they were not heated using an external heat source). The heating rate therefore was not constant but reached its maximum of $\sim 5 \text{ K min}^{-1}$ at around 110 K.

3. Mapping the phase diagram of H₂O-NH₄F mixtures

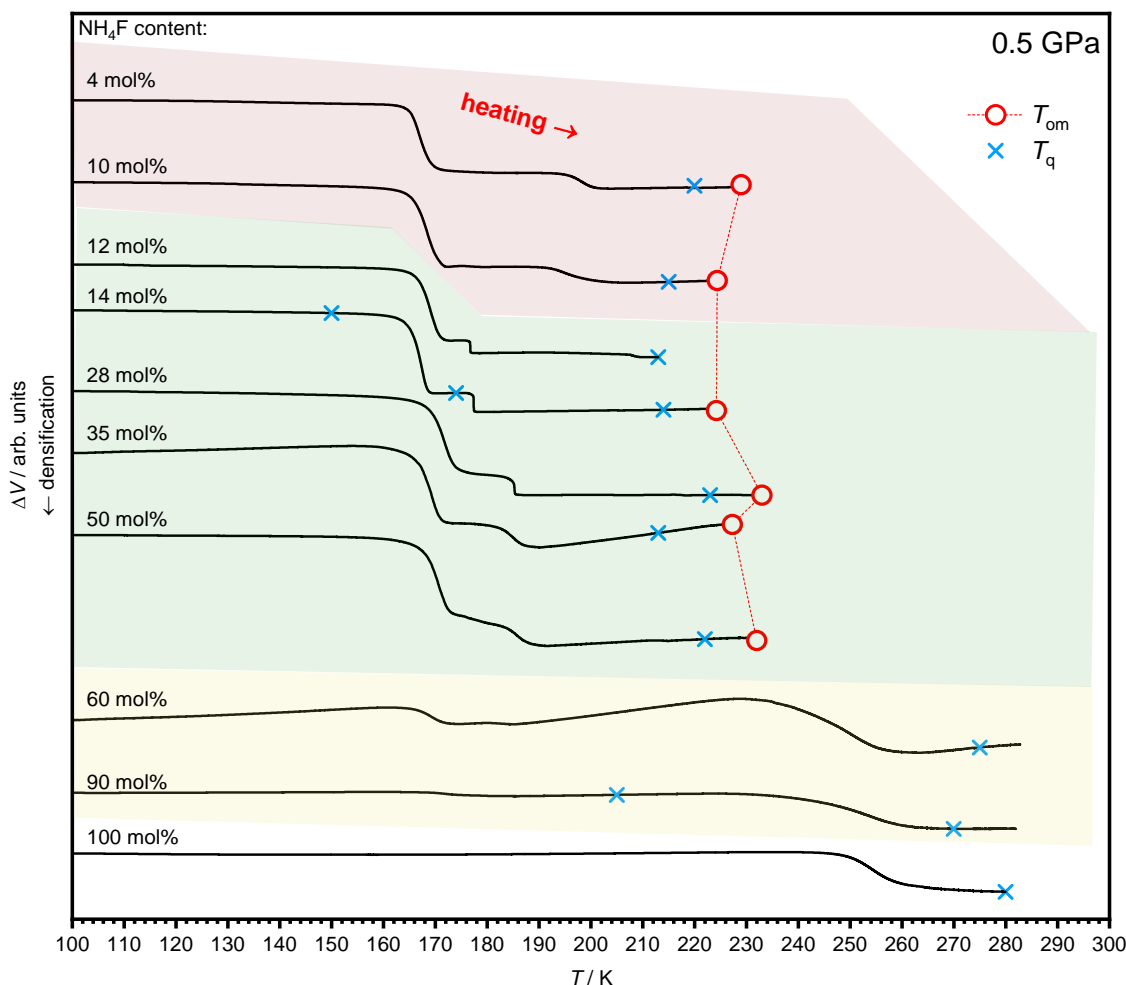


Figure 3.8: Volume change traces of a range from 4 to 100 mol% NH₄F-ice samples heated isobarically at 0.5 GPa until they began melting, as given by the red open circles (T_{om}). Samples were quenched at temperatures, T_q , (blue crosses); most samples were obtained at the highest temperature plateau. An arbitrary scale is provided as unknown volumes of NH₄F-ice mixtures were used beyond the solubility limit of NH₄F in water.

The ΔV plots in Figure 3.8 vary in their appearance depending on the composition of NH₄F – this has been highlighted by the differently shaded regions. For instance, a marked difference can be seen between the 10 mol% and 12 mol% NH₄F traces, where for the 12 mol% trace the second step exists for a smaller temperature window.

It should also be noted that on heating the samples of NH₄F content greater than 50 mol%, the samples were no longer found to melt below room temperature, due to the samples now being more NH₄F-like. On the assumption that far higher temperatures could have been reached, these samples would have been expected to transform to NH₄F IV before eventually melting at temperatures exceeding ~500 K.^{23, 24}

3. Mapping the phase diagram of H₂O-NH₄F mixtures

3.2.2.1 Up to 10 mol% NH₄F, holding on to ice V character

Samples quenched up to 10 mol% NH₄F were still found to produce ice V-like samples as demonstrated by the XRDs in Figure 3.9.

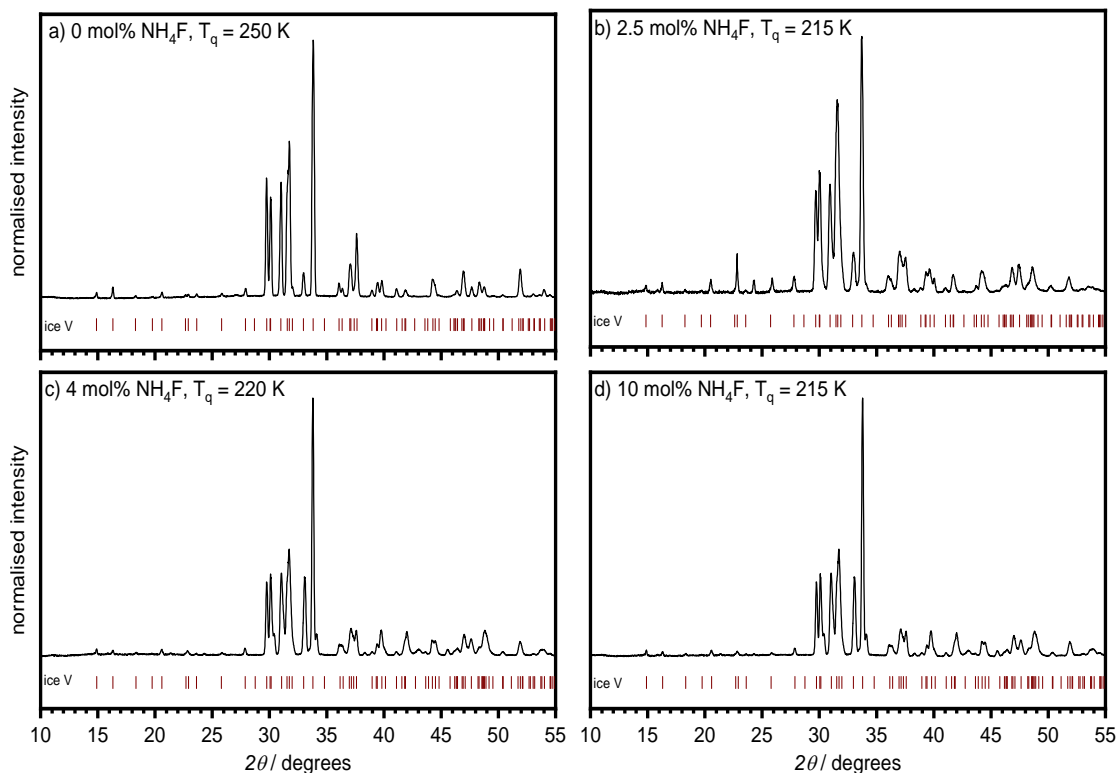


Figure 3.9: Highest temperature phases up to and including 10 mol% NH₄F, all of which were found to have an ice V-type structure.

Although the samples in Figure 3.9 all show the ice V structure, they differ slightly in appearance. The 0 mol% NH₄F sample (Figure 3.9(a)) has peaks that are particularly well-defined and sharp. The addition of NH₄F sees the peaks in the XRD patterns growing broader. However from 2.5 mol% NH₄F to 10 mol% NH₄F (in Figure 3.9(b) to (d)), all the peaks, by eye, appear to share similar widths.

Rietveld refinements were also performed on the ice V-like samples to assess the effect of NH₄F inclusion on the unit cell of the compressed solid solutions (Figure 3.10).

3. Mapping the phase diagram of H₂O-NH₄F mixtures

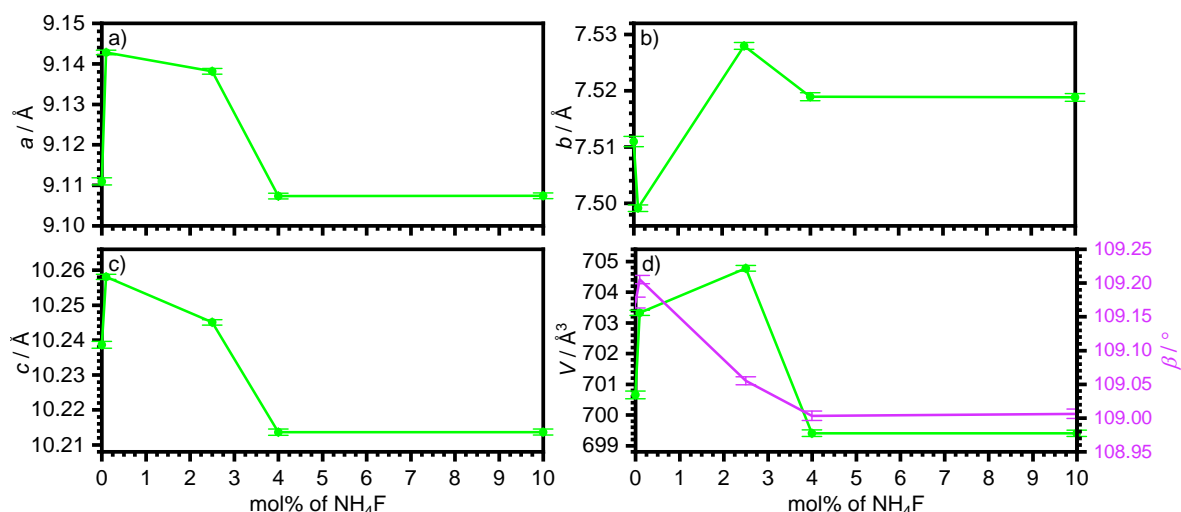


Figure 3.10: Lattice parameters (a): a , (b): b , (c): c . (d) displays the unit cell volume (in green) and monoclinic angle data (in pink) of ice V-like samples as a function of mol% of NH₄F.

Ice V exists in the monoclinic space group $A2/a$.²² The overall cell volume of the ice V-type structure increases by less than half a percent between 0 mol% and 4 mol% NH₄F, before then falling to below 700 Å³ (Figure 3.10(d)). The monoclinic angle, β , is also seen to decline with increasing NH₄F content. This could be a result of the increasing quantities of fluorine ions causing a greater electrostatic pull between the hydrogen bonds. This phenomenon has been observed for mixtures of pure NH₄F and ice at ambient pressure, as discussed by Lyashchenko *et al.*¹ and seen in the previous subchapter (Chapter 3.1). Beyond 4 mol% NH₄F, it seems that the cell volume has contracted as much as possible as the volume, and all the other lattice constants at 10 mol% NH₄F are within error of the values associated with sample at 4 mol% NH₄F.

3.2.2.2 12 mol% to 50 mol% NH₄F, the unexpected dominance of ice XII-type structures

Contrary to expectations, it was found that above 10 mol% NH₄F at 0.5 GPa, ice IV-type structures were not the dominant phase just below the melting line. Instead an ice XII-type structure was found to form, and it could easily be quenched and retrieved at ambient pressure as illustrated in the XRDs in Figure 3.11. This is unlike any known preparation method for ice XII which is notoriously metastable.^{25, 26} When ice XII was first discovered by Lobban *et al.* in the 1990s, it was found that the ice could be produced *via* very specific conditions, involving slow cooling rates of 2.5 K h⁻¹ (~0.042 K min⁻¹) between 270 to 260 K at 0.55 GPa.²⁵ The resulting sample of ice XII could not be recovered at ambient pressure.²⁵ Ice XII has since been found to be retrievable

3. Mapping the phase diagram of H₂O-NH₄F mixtures

at ambient pressure, if formed from HDA. Isobaric heating of HDA between pressures of 0.7 to 1.5 GPa with fast heating rates $\geq 15 \text{ K min}^{-1}$ from 77 K can yield ice XII reproducibly.²⁷

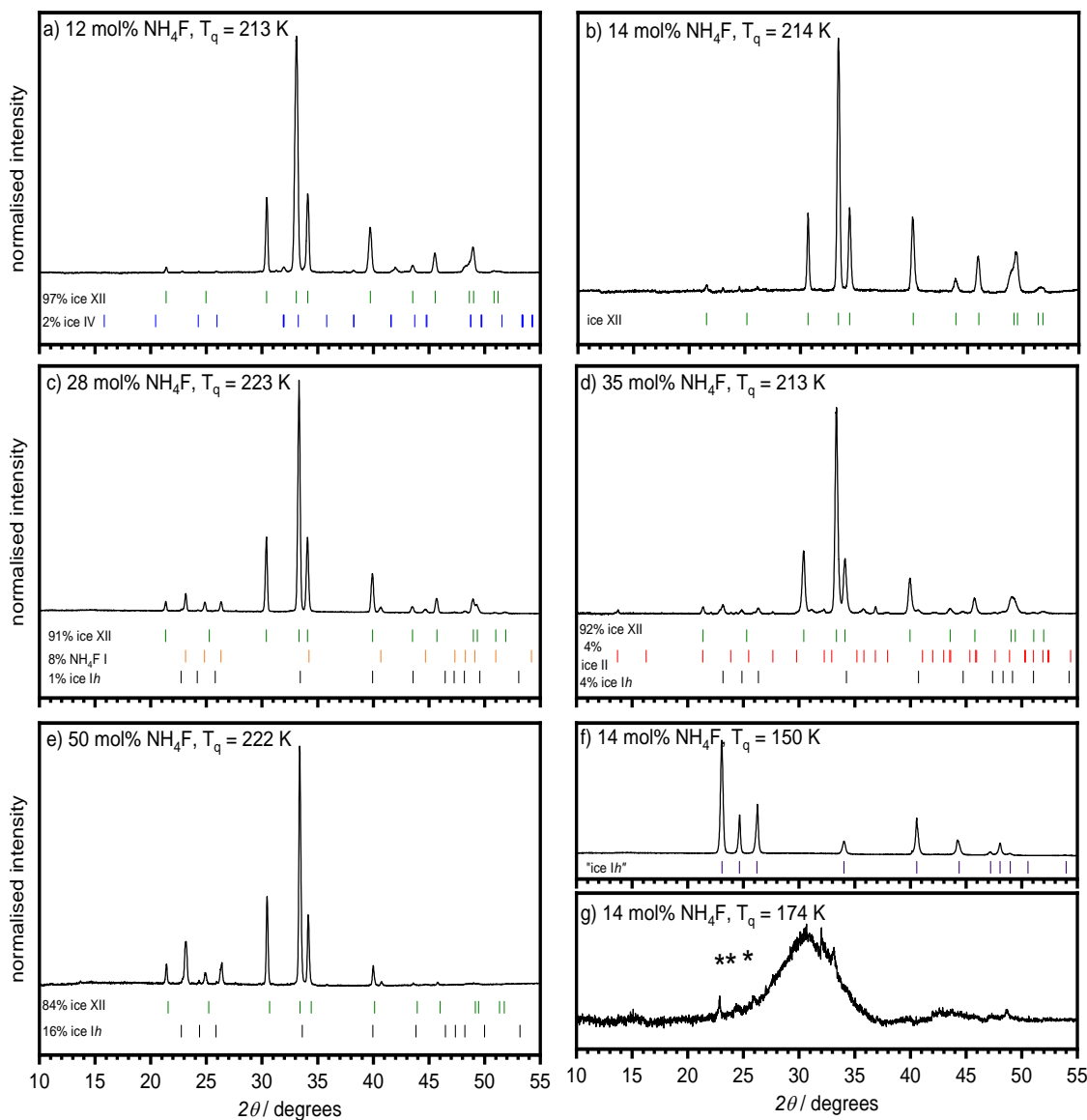


Figure 3.11: (a) to (e) 12 to 50 mol% NH₄F highest temperature XRD patterns, all of which establish ice XII as the dominant phase. (f) shows an ice Ih-type phase isolated at the first volume change step and (g) shows an uHDA-like structure that forms in the step before ice XII for 14 mol% NH₄F-ice. The asterisks in (g) indicate ice Ih impurities and two peaks can be seen at 32° and 33° which appear to relate to the ice IV/NH₄F II-type structure.

The XRD patterns in Figure 3.11(a)-(e) prove that ice XII forms right up to 50 mol% NH₄F. Although there are a few high-pressure ice trace impurities, it can be proven that these are simply caused by minor errors, as the 50 mol% NH₄F sample (Figure 3.11(e))

3. Mapping the phase diagram of H₂O-NH₄F mixtures

is completely phase pure. The ice *I_h* in the 50 mol% NH₄F sample simply results from external ice on the XRD sample holder.

In Figure 3.11(a), 4 w% of the sample appears to contain ice IV. This could have resulted from ice forming inside the piston apparatus during sample preparation or maybe improper mixing of the solution, yet the first option appears to be more likely given that the solution is at a composition below the solubility limit of NH₄F²⁸ in water. In Figure 3.11(c), some ice *I_h*/NH₄F I is present which will have undoubtedly arisen from the incomplete conversion of a prior phase (Figure 3.11(f)). Surprisingly, a uHDA-type structure begins to emerge (Figure 3.11(g)) in the volume step before ice XII for the 14 mol% NH₄F sample. As far as reported in the literature, uHDA can only be prepared at extremely low temperatures, usually below 80 K, on the compression of ice *I_h*, so this presents a rather unusual situation as the sample prepared here was quenched at 174 K and was not prepared with a fast compression rate.^{29,30} The presence of the uHDA-type structure also lends to the fact that this sample at 14 mol% NH₄F is more ice-like, as pure NH₄F does not exist in amorphous forms.²¹ Having said this, two peaks which could initially be mistaken for noise at ~32° and 33° are concurrent with peaks that are observed for pure NH₄F II (Figure 3.7). This implies that a thermodynamic and kinetic ‘tug-of-war’ must ensue on the heating of the 14 mol% NH₄F sample, which is eventually absent of any NH₄F II features (Figure 3.11(b)).

In Figure 3.11(d), the 35 mol% NH₄F sample contains some ice II. The solubility limit of NH₄F in H₂O at room temperature equates to ~30 mol% NH₄F in water.²⁸ Consequently, this was the first sample to be prepared from the grinding of a solution of ice and NH₄F in a pestle and mortar which had been precooled in liquid nitrogen. Presumably, given that this was the first time this was carried out, the mixture was not ground as well as possible, leading to the retention of pure ice domains which were able to form ice II in the absence of NH₄F. This is further supported by the fact that the sample with the highest NH₄F concentration shown – 50 mol% NH₄F, Figure 3.11(e) – was devoid of ice II.

The XRD patterns of samples belonging to the ice XII-type structures (tetragonal space group *I* $\bar{4}$ 2*d*)²⁵ were also analysed in GSAS^{7,8} to determine their lattice constants (Figure 3.12).

3. Mapping the phase diagram of H₂O-NH₄F mixtures

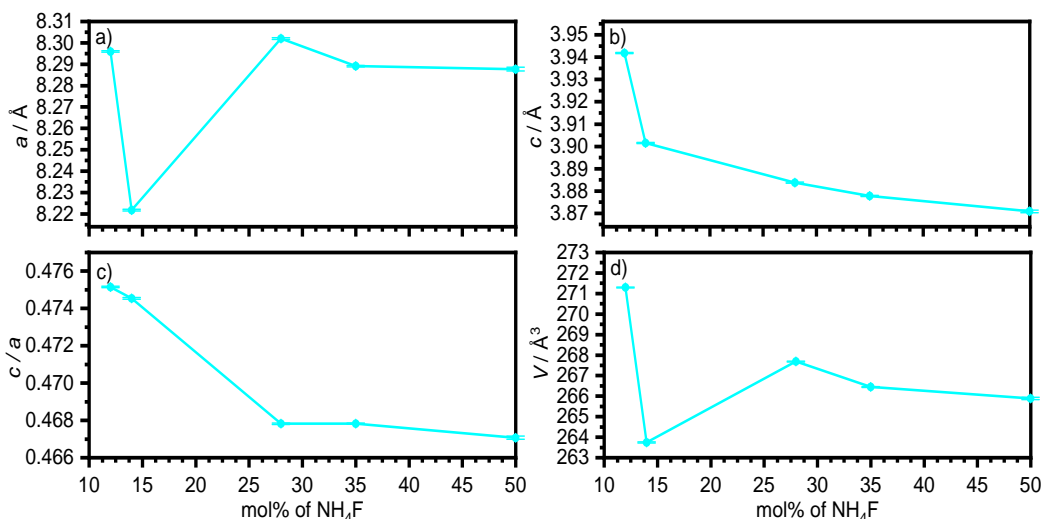


Figure 3.12: Lattice constants of (a) a , (b) c , (c) the tetragonal distortion and (d) the volume of the unit cell of ice XII-type structures in the 12 to 50 mol% NH₄F range.

As can be seen in Figure 3.12(a), there does not appear to be a systematic change in the a lattice constant. Meanwhile in Figure 3.12(b) it can be seen that the c lattice constant smoothly declines in its value with increasing NH₄F content, which is also reflected in the tetragonal distortion in Figure 3.12(c). Overall from Figure 3.12(d), it appears that the volume of the unit cell also decreases with increasing quantities of NH₄F, which was also found to be the case for ice V in Figure 3.10(d). Again, it remains a valid argument that as more NH₄F is introduced into the structure, the collective electrostatic pull of the fluorine ions becomes greater, leading to an even greater contraction.¹

Ice XII was first officially isolated in the 0.5 GPa region using *in-situ* neutron diffraction by Lobban *et al.*²⁵ O’Keeffe also noted that the structure of ice XII was remarkable as it was the first experimentally observed structure to be composed of tetrahedral nets that had 7- and 8-membered rings.³¹ Other tetrahedral nets observed for silicates and zeolites have never been observed to have rings formed of more than 6-membered rings, and it was theoretically proposed as an impossible event.³¹ Despite this, it was found that ice XII is formed of 7- and 8-membered rings and it is the densest form of ice without interpenetrating elements.³² Lobban *et al.* noted that the p - T region where ice XII was found was also able to host ices IV and V. The conversion of ice XII to ice V by the cooling of the ice at 0.55 GPa coincided with a noticeable pressure increase of the sample cell. This led Lobban *et al.* to draw the conclusion that ice XII must have a higher density than ice V.²⁵ The authors were in fact correct about their observations and it was determined that ice XII, IV and V had densities of 1.4365,

3. Mapping the phase diagram of H₂O-NH₄F mixtures

1.4361 and 1.4021 g cm⁻³ respectively at 0.5 GPa and 260 K.²⁵ It was reasoned that ice XII can exist with a high density as a result of its rings being able to distort greatly. Given that ice XII is formed of the largest number of rings without interpenetration compared to all other ices, it means that the strain within the rings is distributed over a larger number of vertices. Hence, ice XII is more able to withstand ring-strain compared to other ices in the same *p-T* range.

In these experiments involving NH₄F, it appears that ice XII-type structures preferentially form in place of ice V, as the presence of the fluorine ions lead to shorter resultant bonds. These shorter bonds in a denser structure are less able to withstand the strain needed for the bending of bonds in ice V, and hence transform to the entirely different and denser crystal structure of ice XII. Ice V has been demonstrated to have interpenetrating features, even being termed an ‘autoclathrate’³³ as it contains O–H–O bonds which interpenetrate 8-membered rings of the same network.^{33, 34} Although ice IV can also form metastably in the same *p-T* region, the overall tighter structure enforced by the fluorine ions most likely inhibit its formation which would be likely to have rings that are too constricted to allow for the ‘threading through’²⁵ of ice IV networks. Of ice IV, V and XII, the latter is the only ice not to contain interpenetrating features.^{32, 33}

3.2.2.3 60 mol% to 90 mol% NH₄F, the eventual separation of mixtures

Beyond 50 mol% NH₄F, ice XII is no longer the dominant phase – instead a family of ices/NH₄F structures begin to appear as shown in Figure 3.13 for 60 mol% and 90 mol% NH₄F. As can be seen in Figure 3.13(a), NH₄F II-type structures begin forming at 60 mol% NH₄F-ice – this is at a far greater concentration than was initially thought to be able to give rise to NH₄F II. NH₄F-ice XII is still present at 40 w%.

3. Mapping the phase diagram of H₂O-NH₄F mixtures

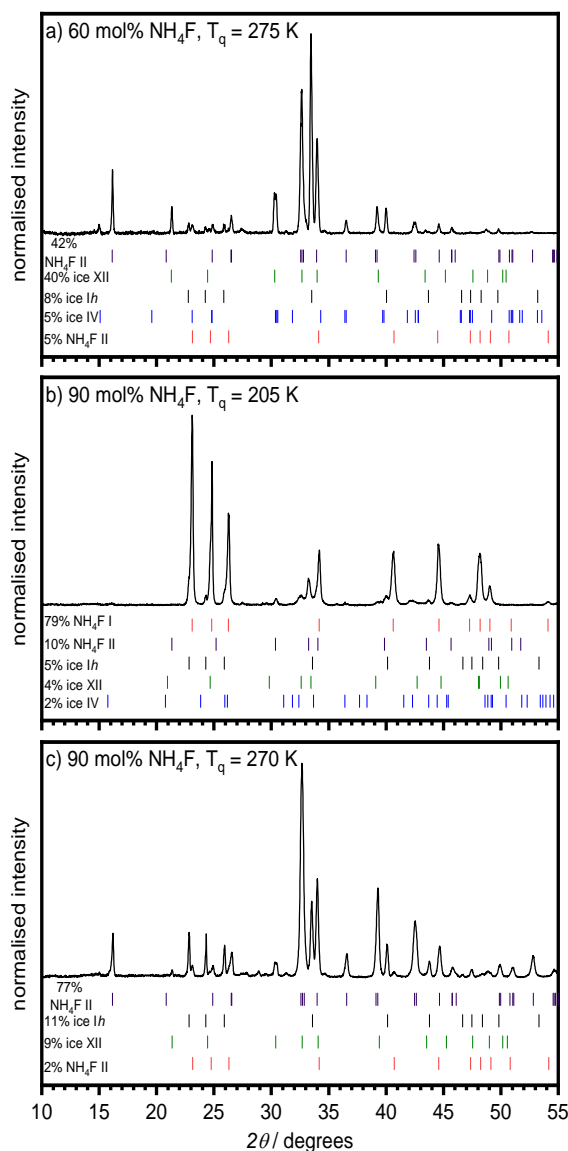


Figure 3.13: XRD patterns of (a) 60 mol% NH₄F quenched at 275 K, (b) 90 mol% NH₄F quenched at 205 K and (c) 90 mol% NH₄F quenched at 270 K.

Interestingly ice IV is also present in the sample, which can be seen particularly well in the peak at $\sim 9^\circ$ (this Bragg reflection also exists for the NH₄F II-type structure with a corresponding peak at $\sim 11^\circ$). This appears to suggest that the NH₄F-ice mixture is saturated with NH₄F, and that phase separation must occur, creating pockets of NH₄F-ice (at saturation point) and NH₄F with H₂O in small quantities, leading to the formation of ice XII-type structures and NH₄F II-type structures respectively. The impurity peaks of ice Ih and NH₄F may result from the phase that exists prior to this – NH₄F I – which is shown in Figure 3.13(b). On increasing the concentration to 90 mol% NH₄F, the ice XII-like content drops fourfold in its w%, with the leading phase now being NH₄F II-like, as would be expected given its mol% proximity to pure NH₄F. The reduction of

3. Mapping the phase diagram of H₂O-NH₄F mixtures

ice XII-type content on getting closer to a 100% concentration of NH₄F can be justified by the fact that ice XII is composed of 7- and 8-membered ring structures.

Although NH₄F should be able to form 8-membered rings, and in fact any even number of rings, the presence of 7-membered rings would be disallowed as they would constitute an odd number of heavy atoms, which does not exist for the stoichiometry of NH₄F. Going back to Figure 3.8, an interesting comparison can be made between the ΔV traces of 50 mol% NH₄F, 60 mol% NH₄F and 90 mol% NH₄F. The trace of the 60 mol% NH₄F is somewhat in between in character of the compositions either side of it. It possesses the long plateau of the 90 mol% sample, while also having a step similar to that of the 50 mol% sample ($T \sim 170$ to 180 K), which is related to the presence of ice XII-type structures. This further explains the mixed composition of the 60 mol% NH₄F sample of ice XII and NH₄F II.

Unlike at compositions below 60 NH₄F mol%, no amorphous forms exist in this NH₄F concentration window.

3.2.3 Conclusions

By considering this small fixed-pressure cross-section of the phase diagram at 0.5 GPa, some quite seismic insights have been gathered regarding the thermodynamic landscape with respect to increasing NH₄F content in ice beyond the solubility limit right up to 100 mol% NH₄F. These are summarised in Figure 3.14:

Consistent with studies by Shephard *et al.* at 0.3 GPa, ice II was found to be blocked at 0.5 mol% NH₄F.²⁰ In this subchapter, the blocking of ice II formation was also found to hold true for samples at 0.5 GPa up to 10 mol% NH₄F. For samples exceeding this NH₄F concentration, the structure which emerged in place of ice V-type structures – ice XII – was unexpected. Up to 50 mol% NH₄F, it appears that ice XII-type structures form instead of NH₄F-ice V due to the exceptionally contracted unit cell which is unable to withstand the strain that would form NH₄F-ice V rings.

3. Mapping the phase diagram of H₂O-NH₄F mixtures

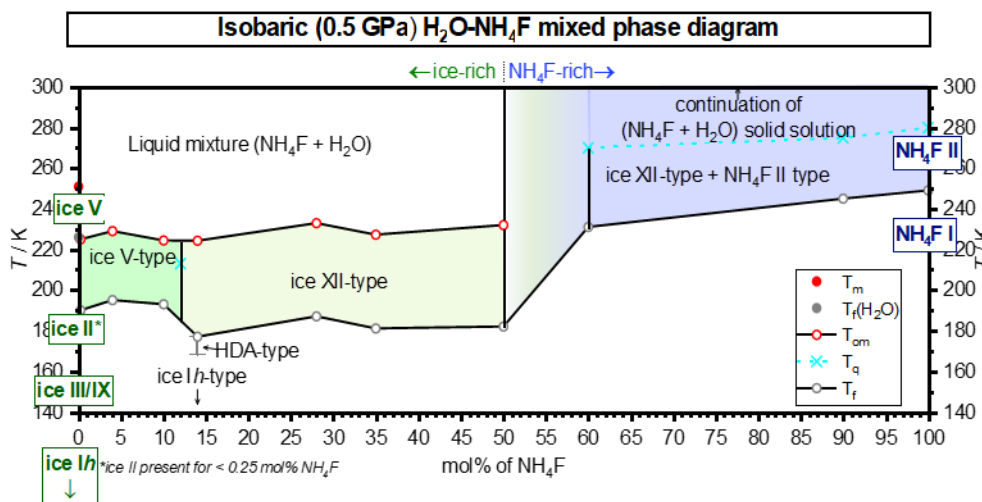


Figure 3.14: Binary phase diagram at 0.5 GPa for the H₂O-NH₄F system, as a function of NH₄F mol% across the entire composition range. At the far left, for the pure ice V, the melting temperature is denoted by T_m , and the temperature at which the final phase emerged at is given by $T_f(\text{H}_2\text{O})$. The phases observed for the end members are shown by the olive- and navy-bordered text at either end of the phase diagram. T_q and T_{om} indicate temperatures that samples were quenched at and where onset melts occurred respectively. To provide a feel for where the ‘phase boundaries’ of observed structure-types occur, the temperatures at which the last observable phases emerged at are given by T_f . Below 0.25 mol% NH₄F, ice II is still able to form, but afterwards is replaced by ice V. Ice V-type structures are then found up to 12 mol% NH₄F, at which point ice XII-type structures then dominate up until the ‘monohydrate’ composition. The region between 50 to 60 mol% NH₄F, as demarcated by the green-lilac colour gradient, was not investigated. In the realm of NH₄F-rich mixtures, mixtures of NH₄F-ice XII and ice-NH₄F II exist. At 100 mol% NH₄F, NH₄F II is present as documented in the literature.^{23, 24}

It seems that NH₄F is fully saturated in ice at ~50 mol% NH₄F, as at concentrations beyond this level, phase mixtures begin to emerge between ice XII and NH₄F II. However, increasing concentrations of NH₄F in these mixtures leads to a greater w% of NH₄F II, as would be expected.

Although for the ice-rich mixtures containing ice XII-like structures the impurities present were only in the tens of w%, it would be ideal that if these experiments were repeated that the solid solutions were more homogenous. This likely means grinding for longer durations and pipetting the solid solutions into the liquid nitrogen in a manner that would make it easier to grind more thoroughly using the pestle and mortar. It would be beneficial to compare samples of ice XII prepared at concentrations between 12 to 50 mol% NH₄F using *in-situ* neutron diffraction to make any comparisons or realise differences between these ices and the ice XII prepared by Lobban *et al.*²⁵

3. Mapping the phase diagram of H₂O-NH₄F mixtures

3.3 References

1. A. K. Lyashchenko and G. G. Malenkov, *J. Struct. Chem.*, 1969, **10**, 616-617.
2. L. C. Labowitz and E. F. Westrum, *J. Phys. Chem.*, 1961, **65**, 403-408.
3. L. C. Labowitz and E. F. Westrum, *J. Phys. Chem.*, 1961, **65**, 408-414.
4. C. G. V. Beek, J. Overeem, J. R. Ruble and B. M. Craven, *Can. J. Chem.*, 1996, **74**, 943-950.
5. F. H. William, *Elementary Materials Science*, ASM International, 2013.
6. G. Brauer, *Handbook of Preparative Inorganic Chemistry*, Academic Press, 1963.
7. A. C. Larson and R. B. Von Dreele, "*General Structure Analysis System (GSAS)*", *Los Alamos National Laboratory Report LAUR 86-748* 2000.
8. B. H. Toby, *J. Appl. Crystallogr.*, 2001, **34**, 210-213.
9. A. D. Fortes, *Acta Crystallographica Section B*, 2018, **74**, 196-216.
10. C. Lobban, PhD thesis, University College London, 1998.
11. L. Vegard, *Zeitschrift für Physik*, 1921, **5**, 17-26.
12. P. Alope and S. Divinski, *Handbook of Solid State Diffusion, Volume 1 - Diffusion Fundamentals and Techniques*, Elsevier.
13. M. Wagner, in *Thermal Analysis in Practice - Fundamental Aspects*, Hanser Publishers.
14. S. Zaromb and R. Brill, *J. Chem. Phys.*, 1956, **24**, 895-902.
15. V. S. Yatlov and E. M. Polyakova, *J. Gen. Chem. (U.S.S.R.)*, 1945, **15**.
16. D. W. A. Sharp, *The Penguin Dictionary of Chemistry*, Penguin Books, 3rd Edition edn., 2003.
17. TMS, in *TMS 2010, 139th Annual Meeting and Exhibition - Supplemental Proceedings, Volume 2 - Materials Characterization, Computation, Modeling and Energy*, TMS (The Minerals, Metals & Materials Society).
18. A. Tranquard and G. Coffy, *Comptes Rendus Hebdomadaires Des Seances De L'Academie Des Sciences Serie C*, 1970, **270**, 416-+.
19. J. P. Buettner and A. W. Jache, *Inorg. Chem.*, 1963, **2**, 19-22.
20. J. J. Shephard, B. Slater, P. Harvey, M. Hart, C. L. Bull, S. T. Bramwell and C. G. Salzmann, *Nat. Phys.*, 2018, **14**, 569-572.
21. J. J. Shephard, S. Ling, G. C. Sosso, A. Michaelides, B. Slater and C. G. Salzmann, *J. Phys. Chem. Lett.*, 2017, **8**, 1645-1650.

3. Mapping the phase diagram of H₂O-NH₄F mixtures

22. C. G. Salzmann, P. G. Radaelli, J. L. Finney and E. Mayer, *Phys. Chem. Chem. Phys.*, 2008, **10**, 6313-6324.
23. A. K. Kuriakose and E. Whalley, *J. Chem. Phys.*, 1968, **48**, 2025-2031.
24. C. Bellin, A. Mafety, C. Narayana, P. Giura, G. Rousse, J.-P. Itié, A. Polian, A. M. Saitta and A. Shukla, *Phys. Rev. B*, 2017, **96**, 094110.
25. C. Lobban, J. L. Finney and W. F. Kuhs, *Nature*, 1998, **391**, 268-270.
26. J. Stern and T. Loerting, *Sci. Rep.*, 2017, **7**, 3995.
27. C. G. Salzmann, I. Kohl, T. Loerting, E. Mayer and A. Hallbrucker, *Can. J. Phys.*, 2003, **81**, 25-32.
28. W. M. Haynes, *CRC Handbook of Chemistry and Physics, 94th Edition*, CRC Press, 2013.
29. T. Loerting, K. Winkel, M. Seidl, M. Bauer, C. Mitterdorfer, P. H. Handle, C. G. Salzmann, E. Mayer, J. L. Finney and D. T. Bowron, *Phys. Chem. Chem. Phys.*, 2011, **13**, 8783-8794.
30. O. Mishima, L. D. Calvert and E. Whalley, *Nature*, 1984, **310**, 393-395.
31. M. O'Keeffe, *Nature*, 1998, **392**, 879-879.
32. C. G. Salzmann, *J. Chem. Phys.*, 2019, **150**, 060901.
33. R. A. B. Devine, *The Physics and Technology of Amorphous SiO₂*, Springer US, 2012.
34. B. Kamb, A. Prakash and C. Knobler, *Acta Crystallogr.*, 1967, **22**, 706-715.

4 Mapping the 2.5 mol% NH₄F-ice phase diagram up to 1.7 GPa

GPa

4.1 Isobaric ice IX↔III heat cycling at 0.3 GPa on PEARL

4.1.1 Introduction

This chapter focuses on the hydrogen disorder/order pair of ices III/IX, which are also discussed in detail more extensively in the introduction to Chapter 7.1. Hence this introduction covers the aspects of the nature of phase transitions between the two phases, which is relevant to this chapter.

Ices III and IX are a hydrogen disorder/order pair that exist predominantly in the 0.3 GPa pressure region.^{1, 2} Although ice IX is obtained by the cooling of ice III, the cooling rate is a very important factor in determining whether or not ice IX forms.²⁻⁵ A host of studies by many different researchers have concluded that unless ice III is cooled at a rate greater than 1 K min⁻¹, the ice III will always convert to ice II, and not ice IX.²⁻⁵ This behaviour can be explained using a schematic diagram of relative Gibbs free energies of the ices that exist at 0.3 GPa (as well as the liquid), as shown in Figure 4.1.

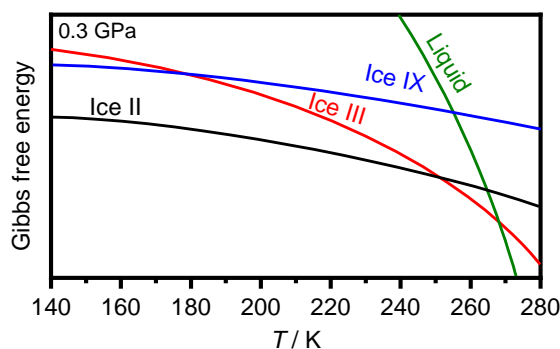


Figure 4.1: Schematic of the relative Gibbs free energy curves of the phases of ice and the liquid at 0.3 GPa. The lower the line relating to Gibbs free energy for a given temperature, the more thermodynamically stable a phase is. Adapted from Fig 11.11 in Petrenko and Whitworth.¹

Every phase has a Gibbs free energy function which can be drawn as a curved surface for given pressure and temperature coordinates.¹ Gibbs free energy curves of different phases can be compared to elucidate whether a phase will be stable (it will be the lowest curve), or if phases can co-exist at a given p - T coordinate (the curves overlap at a given point).¹

4. Mapping the 2.5 mol% NH₄F-ice phase diagram up to 1.7 GPa

As illustrated in Figure 4.1, for a large temperature region, ice II has the lowest Gibbs free energy, and hence is the most stable phase because of its low entropy.¹ However, for a small temperature window of ~10 K just before the ice melts, ice III has the lowest Gibbs free energy. If the ice III is cooled it re-enters the temperature region at which ice II is most stable, hence the only way to bypass the formation of ice II is to cool at a fast rate (greater than 1 K min⁻¹) to form the kinetic product of ice IX.²⁻⁵ Even though the resultant ice IX will have a Gibbs free energy higher than ice II for the same temperature, at low temperatures the kinetics associated with the phase transition slow down,⁶ preventing the conversion to ice II.¹

Although this does mean that ice IX can be isolated, it has completely hindered the ability of researchers to observe the transition between ices III and IX over a long enough timescale to collect changes in hydrogen occupancies and the unit cell which occur over the course of the transition.⁴ This is unlike the situation for other hydrogen disorder/order ices pairs. For instance, ices V/XIII, ices VI/XV and ices XII/XIV have been studied while heat cycling using a variety of techniques, such as ND, Raman spectroscopy and DSC to assess changes in properties (such as lattice constants) over the course of the ordering transition.⁷⁻¹² Londono *et al.* stated that on the lowering of temperature of ice III “it was...not possible to collect data at stages of the transformation of cooling”.⁴ The heating of ice IX poses a similar issue, where the heating can also inadvertently lead to the entering of the ice II stability field, and the inability to reform ice III.^{3, 4, 13}

4.1.2 Aims

To observe the reversible transition between the hydrogen disorder/order pair of ices III and IX for the first time, as facilitated by the inclusion of 2.5 mol% ND₄F in D₂O ice as an anti-ice II agent.

4.1.3 Outline of the experiment at ISIS

Armed with the knowledge that 2.5 mol% NH₄F in ice effectively inhibited the formation of ice II,¹⁴ a sample of 2.5 mol% ND₄F-D₂O ice, contained in a TiZr can (described in Chapter 2.4.4.1) was investigated. An experimental pathway was carried out on the PEARL beamline at ISIS (Figure 4.2(a)), the resulting diffraction data of which is shown in Figure 4.2(b).

4. Mapping the 2.5 mol% NH_4F -ice phase diagram up to 1.7 GPa

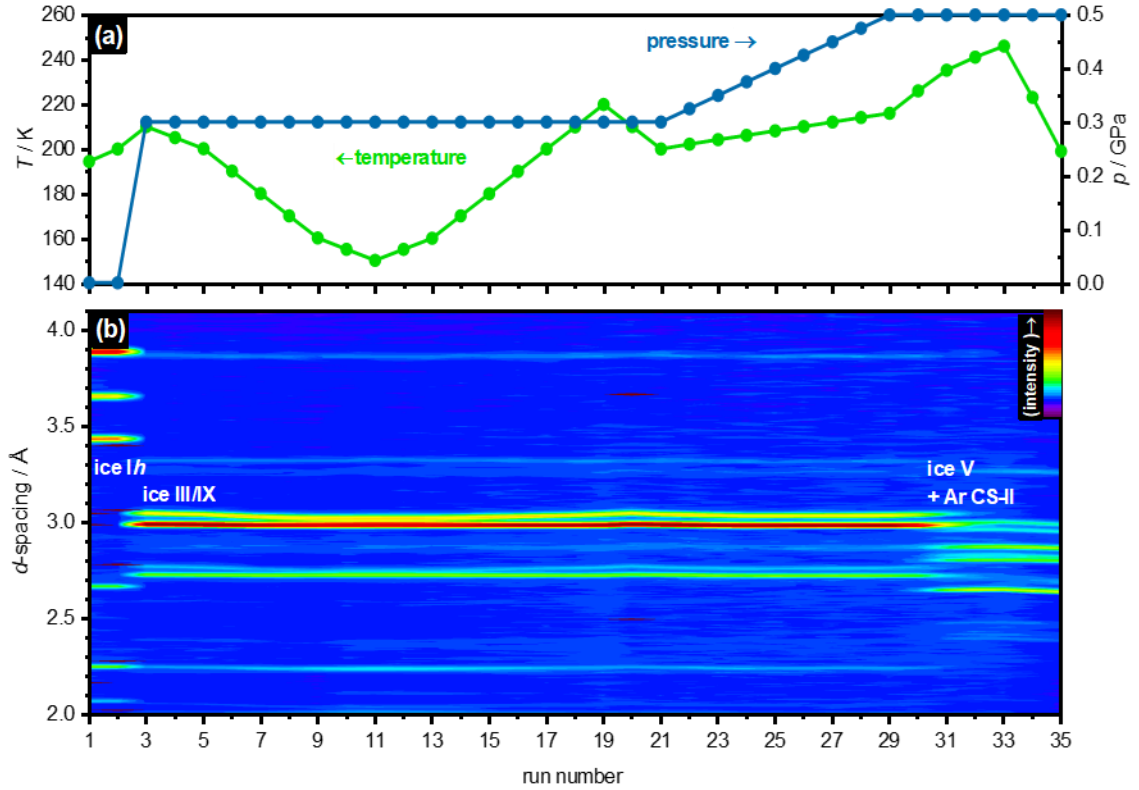


Figure 4.2: (a) p - T pathway of the experiment at the PEARL beamline with (b) the resulting diffraction data of the 2.5 mol% ND_4F - D_2O ice. The data shown here can be split into three different regimes. Runs 1-2 show where ice Ih was present before pressurising the sample. Runs 3-22 demonstrate the p - T range for which ices III/IX exist. Runs 23- 35 show the ice III being compressed and heated before eventually converting to ice V.

The beginning of the experiment (runs 1 and 2) involved the compression of the doped ice Ih. The presence of this phase is indicated by the three peaks at ~ 3.4 , ~ 3.6 and ~ 3.9 Å that belong to the ice Ih trident. From runs 3 to 22 all data were collected under isobaric conditions at 0.3 GPa, a pressure region that hosts ices III/IX and also ice II under ‘normal’ pure ice circumstances. Taking advantage of the ND_4F dopant to remove any possibility of ice II formation, in this pressure region the ice III that initially formed was cooled over an extended time period to form ice IX at lower temperatures. At first glance the diffraction data for runs 3 to 22, where the sample was held at 0.3 GPa at 210 K was brought down to 150 K and then brought back up to 220 K, looks almost identical. However, on closer inspection, one can appreciate that a pair of peaks centred at ~ 3.05 Å are initially a distance apart but then grow closer together. This represents the phase transition from tetragonal ice III to pseudocubic¹⁵ ice IX on slow cooling, which is discussed in further detail later in the text. Going up to run number 29, ice III persists at the higher temperature and pressure, but it gradually gives way to

4. Mapping the 2.5 mol% NH₄F-ice phase diagram up to 1.7 GPa

ice V at ~240 K at 0.5 GPa, as seen by the ice III peak at 2.73 Å disappearing on further heating, and the emergence of peaks with ~2.6, ~2.8, ~2.95 and ~3.0 Å *d*-spacing values. As well as this, increasing quantities of Ar CS-II begin to form as a result of using argon as the pressurising medium. Shephard *et al.* reported a phase diagram for 2.5 mol% NH₄F, which saw ice III converting to ice V at lower pressures, closer to 0.4 GPa.¹⁴ However, the phase line boundaries reported by Shephard *et al.* were determined *via* volume changes in a piston cylinder experiment, which would have likely involved the application of pressure of different crystal domains. In the case of the experiments carried out at ISIS, the pressure was achieved using argon as a gas medium, and would have meant that a more isotropic pressure was applied to the sample, resulting in the later than expected observation of the phase transition of ice III to ice V.

4.1.4 First observation of the reversible conversion between ices III ↔ IX at 0.3 GPa

Cross-sections from Figure 4.2(b) of runs 3 and 11 can be taken to see the ice III and ice IX patterns (recorded over a period of greater than 9 hours each) which are shown in Figure 4.3.

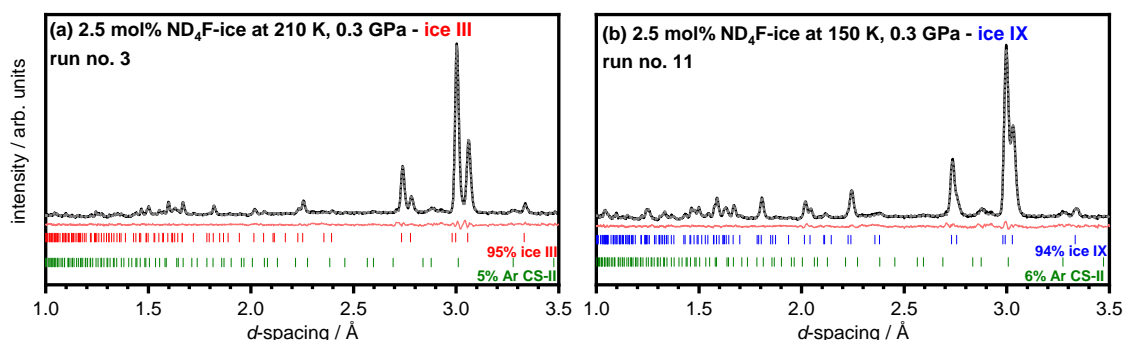


Figure 4.3: ND data of 2.5 mol% ND₄F-D₂O ice (black lines) recorded at 0.3 GPa with Rietveld fits (grey dotted lines) and residuals (light red lines). (a) ice III collected at 210 K and (b) ice IX collected at 150 K. Tickmarks and w% are given for the ices and the argon clathrate hydrate.

The similarity between the diffraction data in Figure 4.3(a) and Figure 4.3(b) highlight the shared tetragonal space group symmetry (*P*4₁2₁2) of the hydrogen disorder/order ice pair.² Comparing the two patterns however, differences can be ascertained, the most noticeable is that of the two peaks belonging to the 102 and 201 reflections at ~3.05 Å which for ice III are distinctly apart, while for the ice IX the peaks begin to merge together as the ice achieves its pseudocubic¹⁵ structure. Additionally, two discrete peaks

4. Mapping the 2.5 mol% NH₄F-ice phase diagram up to 1.7 GPa

at ~ 2.7 Å and 2.8 Å which belong to 211 and 112 reflections respectively in ice III (Figure 4.3(a)) merge together in the ordered ice IX counterpart (Figure 4.3(b)).

Data from the refinements of the patterns in Figure 4.3 are shown in Table 4.1 for 2.5 mol% ND₄F ice III and in Table 4.2 for 2.5 mol% ND₄F ice IX.

Table 4.1: Fractional coordinates, atomic displacement parameters and occupancies for 2.5 mol% ND₄F ice III at 210 K and 0.3 GPa. The associated lattice constants are $a = 6.66444$ Å, $c = 6.878615$ Å

| | Multiplicity | x | y | z | B_{iso} | Occupancies |
|----|--------------|----------|---------|----------|------------------|-------------|
| O1 | 8 | 0.11662 | 0.30712 | 0.28796 | 2.169 | 0.951 |
| O2 | 4 | 0.39001 | 0.39001 | 0.00000 | 2.169 | 0.951 |
| N1 | 8 | 0.11662 | 0.30712 | 0.28796 | 2.169 | 0.024 |
| N2 | 4 | 0.39001 | 0.39001 | 0.00000 | 2.169 | 0.024 |
| F1 | 8 | 0.11662 | 0.30712 | 0.28796 | 2.169 | 0.024 |
| F2 | 4 | 0.39001 | 0.39001 | 0.00000 | 2.169 | 0.024 |
| D3 | 8 | 0.24392 | 0.33418 | 0.16301 | 2.165 | 0.386 |
| D4 | 8 | 0.13611 | 0.40094 | 0.40497 | 2.165 | 0.418 |
| D5 | 8 | -0.00674 | 0.33519 | 0.2185 | 2.165 | 0.582 |
| D6 | 8 | 0.11669 | 0.17689 | 0.30217 | 2.165 | 0.614 |
| D7 | 8 | 0.31346 | 0.37308 | 0.10277 | 2.165 | 0.614 |
| D8 | 8 | 0.37504 | 0.55389 | -0.03285 | 2.165 | 0.386 |

Table 4.2: Fractional coordinates, atomic displacement parameters and occupancies for 2.5 mol% ND₄F ice IX at 150 K and 0.3 GPa. The associated lattice constants are $a = 6.669404$ Å, $c = 6.797101$ Å

| | Multiplicity | x | y | z | B_{iso} | Occupancies |
|----|--------------|----------|---------|----------|------------------|-------------|
| O1 | 8 | 0.11662 | 0.30712 | 0.28796 | 2.038 | 0.951 |
| O2 | 4 | 0.39001 | 0.39001 | 0.00000 | 2.038 | 0.951 |
| N1 | 8 | 0.11662 | 0.30712 | 0.28796 | 2.037 | 0.024 |
| N2 | 4 | 0.39001 | 0.39001 | 0.00000 | 2.037 | 0.024 |
| F1 | 8 | 0.11662 | 0.30712 | 0.28796 | 2.037 | 0.024 |
| F2 | 4 | 0.39001 | 0.39001 | 0.00000 | 2.037 | 0.024 |
| D3 | 8 | 0.26206 | 0.29855 | 0.15721 | 2.692 | 0.116 |
| D4 | 8 | 0.12078 | 0.40118 | 0.40279 | 2.692 | 0.078 |
| D5 | 8 | -0.01735 | 0.33244 | 0.21678 | 2.692 | 0.922 |
| D6 | 8 | 0.11627 | 0.15723 | 0.2978 | 2.692 | 0.883 |
| D7 | 8 | 0.29844 | 0.36322 | 0.10687 | 2.692 | 0.884 |
| D8 | 8 | 0.39689 | 0.47758 | -0.08331 | 2.692 | 0.117 |

The starting coordinates for the refinement of the ices in Table 4.1 and Table 4.2 were taken from La Placa *et al.*⁵ It can be seen that N and F atoms have also been included to account for their 2.5 mol% presence in the D₂O ice. For every ND₄F atom added, two oxygens are replaced with one nitrogen atom and one fluorine atom, which leads to the dopant atoms' occupancies not equalling 0.025 but 0.024.

4. Mapping the 2.5 mol% NH₄F-ice phase diagram up to 1.7 GPa

From the occupancies calculated in Table 4.1 and Table 4.2, these ices can be defined by their deuterium ordering parameters α and β , which in this instance are equal to the occupancies of deuterium atoms labelled D3 and D4 respectively. For the doped ice III, α and β are 0.386 and 0.418, and for the doped ice IX they are 0.116 and 0.078 respectively. La Placa reported values of α and β as 0.034 and 0.051 in his paper “On a nearly proton-ordered structure for ice IX” for a sample of ice IX that had been quenched at ~0.3 GPa.⁵ The values of α and β obtained for the 2.5 mol% ND₄F-doped ice IX are closer to 0.5 than La Placa’s, indicating that they experience a greater degree of hydrogen disorder than a sample of regular ice IX, which must result from the presence of the dopant. The ordering parameter values of the doped ice IX are as would be expected as they indicated a larger degree of hydrogen disorder in comparison to values obtained by La Placa *et al.*⁵ for pure ice IX. Lobban *et al.* also calculated ordering parameters of samples of ice III – at 250 K and 0.3 GPa; α and β were determined as being equal to 0.36 and 0.53 respectively,¹⁶ not differing a great deal from the doped ice III reported in this chapter.

The ordering transition can also be observed over the temperature range of 220 to 150 K as displayed in Figure 4.4 which displays data from runs 3 to 22. The data for each run was collected over a period of ~20 mins. However, runs 3 and 11 were collected over times greater than 9 hours and 15 mins.

Figure 4.4(a) again highlights how the 102 and 201 peaks can be seen to grow closer together on the conversion from ice III to IX on isobaric cooling at 0.3 GPa. Changes in lattice constants can be seen in Figure 4.4(b) and (c). For ice III a is smaller while c and the volume are larger compared with ice IX, which is in accordance with literature on pure ices III and IX.⁴ From assessing the way in which the lattice constants change (or remain constant) with changing temperature, one can ascertain the point at which the phase change between ices III and IX occurs. On cooling from 210 K to 190 K, the a lattice constant remains constant, suggesting that it remains in the ice III state for this temperature range, yet on further cooling a can be seen to increase, until it finally levels off 160 K suggesting the conversion to ice IX (Figure 4.4(b)).

4. Mapping the 2.5 mol% NH₄F-ice phase diagram up to 1.7 GPa

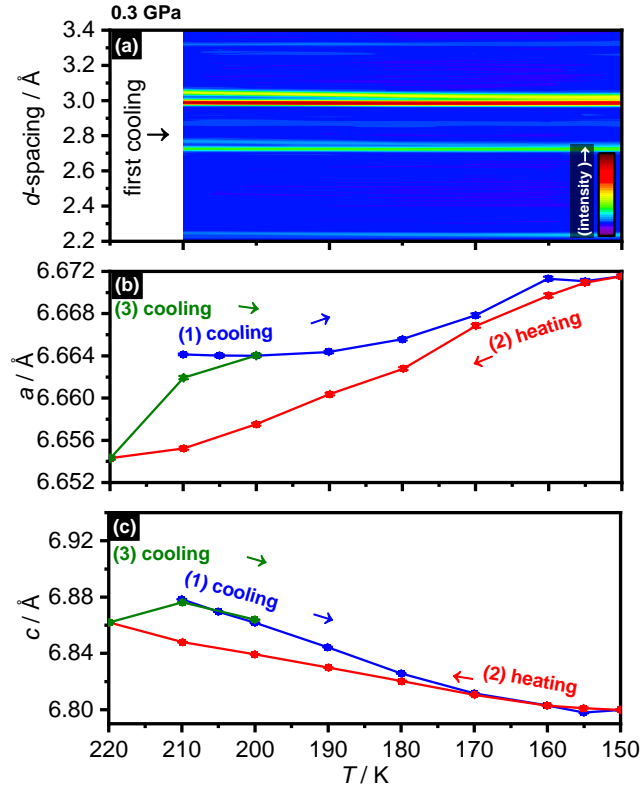


Figure 4.4: The isobaric conversion of ice III to IX in detail, where the higher-temperature end hosts ice III, and conversely the lower temperatures relate to ice IX. (a) ND data showing a narrower d -spacing range, where the converging of peaks at 2.75 Å and 3.05 Å can be seen on the conversion from ice III to IX on cooling. The reverse process is observed for the heating from ice IX to III and is therefore not shown here; (b) and (c) show the changes in lattice constants a and c on the heat cycling between ices III and IX, in the order indicated by the arrows in the figures.

On the heating of ice IX, it is clear that the ordering in the sample is retained past the temperature of 220 K as both a and c lattice parameters do not stabilize. On the heating of the ice, the a lattice constant drops smoothly up to 220 K at which point the sample is re-cooled. On finally re-cooling the sample, it appears that the sample reaches the original ice III state as its lattice parameters eventually re-join the same values reported at the start of the initial cooling. A similar trend is seen for the changes in the c lattice constant, with the exception that the lattice constant drops on transforming to the more ordered ice IX state (Figure 4.4(c)). Both a and c display hysteresis on a cycle of cooling and heating – a feature which certainly would not have been observable if ice II formation had crept in.

Based on the changes in the lattice constants, it appears that the transformation between 2.5 mol% ND₄F-D₂O ice III to IX occurs over the temperature range 190 K to 160 K. Whalley *et al.* stated that for the pure ice III/IX analogues, this transition occurs

4. Mapping the 2.5 mol% NH₄F-ice phase diagram up to 1.7 GPa

over the temperature range 208 K to 165 K.³ The disparity of ~20 K with the starting of the conversion of ice III to ice IX is likely to be lower in the doped ice due to the absence of ice II. In the doped ice phase diagram determined by Shephard *et al.*, the liquidus line at 0.3 GPa is lowered in temperature by ~60 K.¹⁴

4.1.5 Conclusions

For the first time, the tracking of the conversion between ice III and IX on slow-cooling has been observed using ND at 0.3 GPa, which, due to the presence of 2.5 mol% ND₄F in the sample, meant that it was not hindered by the appearance of, and conversion, to ice II. The collection time for each dataset during the conversion was ~20 minutes, yet remarkably the sample still did not convert to ice II. This is a landmark achievement in the history of ices III/IX as up until this point researchers have been incapable of charting the structural properties of this phase transition due to the relatively lower Gibbs free energy of ice II.^{2-5, 13, 14} Remarkably, it has been observed that the heat-cycling between ices III to IX experienced hysteresis. This work further demonstrates the importance of studying ices with dopants and highlights the potency of ice doped with NH₄F in facilitating researchers to study the phase diagram in the absence of ice II.

4. Mapping the 2.5 mol% NH_4F -ice phase diagram up to 1.7 GPa

4.2 Mapping of phases in the 0.3 to 0.8 GPa region on PEARL

While on the PEARL beamline it was decided to investigate the pressure region from 0 GPa up to 0.8 GPa to further see the influence of 2.5 mol% ND_4F -doping in ice. This had to be performed separately to the other ND data collected on PEARL as the pressure limit of the TiZr cell previously used was 0.5 GPa. In this case a two-layer cell containing both TiZr and CuBe was used (as discussed in Chapter 2.4.4.1), with the latter material enabling the higher-pressure regime to be reached. The resulting ND data is shown in Figure 4.5.

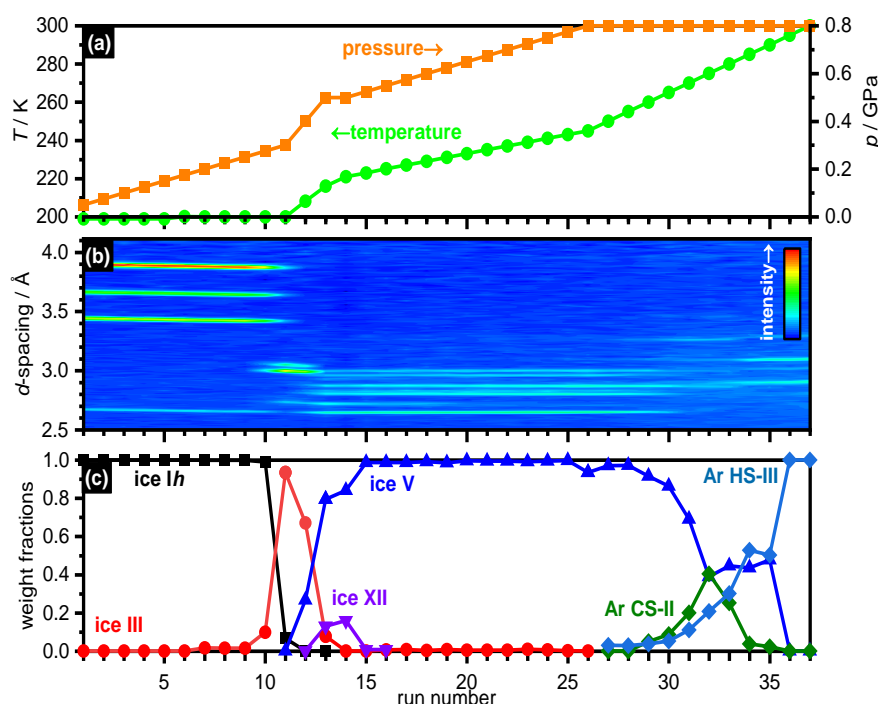


Figure 4.5: 2.5 mol% ND_4F -ice pressurised in a two-layer CuBe/TiZr cell up to 0.8 GPa. (a) The p - T pathway given by run number, which produced (b) the ND data shown as a contour plot with the changing p - T conditions. The data in (b) was probed by Rietveld analysis to determine the resulting weight fractions of the phases that emerged. Consistent with Shephard et al., no ice II formation is observed,¹⁴ with ices III and V materialising instead.

Runs 1 to 11 involved the isothermal compression of 2.5 mol% ND_4F -ice from 0.05 to 0.3 GPa at 200 K. As would be the case for pure ice, the initial product on cooling was ice Ih, as identifiable by the strong ‘trident’ peaks at ~ 3.4 , ~ 3.6 and ~ 3.9 Å in Figure 4.5(b). The further pressurising of the ice Ih sample is reflected by the trident peaks very slightly shifting towards lower d -spacings, as the unit cell begins to contract. By run 10 from pressures of 0.275 GPa, ice Ih drops to ~ 10 w%, but instead of being replaced by ice II, as would happen for pure ice, the ND_4F dopant makes the formation

4. Mapping the 2.5 mol% NH₄F-ice phase diagram up to 1.7 GPa

of ice III more energetically favourable as discussed by Shephard *et al.*¹⁴ The presence of the ice III is visible in runs 10 to 13 from two new peaks that become prominent at ~ 3.0 and ~ 3.05 Å, which can be attributed to the characteristic 102 and 201 peaks of the tetragonal structure. From the phase diagram of 2.5 mol% NH₄F-doped ice as reported by Shephard *et al.*,¹⁴ it was expected that ice III would have emerged at an earlier pressure of ~ 0.2 GPa, however it should be noted that, compared to Shephard *et al.*'s study,¹⁴ in these experiments the pressure was very gradually increased in small steps, and with a gas medium, which gently exerts pressure. Shephard and co-workers produced their samples by compressing ice using a piston cylinder, in which the ice crystals would have been grinding against each other inducing a faster phase change.¹⁴ In this study the use of the gas medium may have also slowed the rate at which ice III formed.

The next p - T regime from runs 11 to 26, which involves the simultaneous compression from 0.3 to 0.5 GPa while heating from 200 to 216 K, hosts ices III, V and XII, despite being in the 'regular' ice II stability field as is apparent from the ice phase diagram.¹⁷ Past 0.3 GPa, ice III, is replaced by ice V, as seen by the emergence of peaks at d -spacings below at ~ 2.6 , ~ 2.8 , ~ 2.95 and ~ 3.0 Å. Surprisingly, a peak at ~ 2.7 Å was also observed and ascribed to metastable ice XII formation; it only ever existed however up to ~ 20 w% in runs 13 to 14, before eventually transforming fully to ice V up to the pressure of 0.8 GPa. Ice XII is known to exist in the ice V stability region, as reported initially by Lobban *et al.*¹⁸ The final runs of 26 to 37 involve the isobaric heating of the ice V which was found to persist until 260 K, followed by traces of a cubic argon clathrate hydrate (CS-II), which eventually fully converted to the hexagonal argon clathrate hydrate (HS-III), as demonstrated by the weight fractions below the contour plot. The structural parameters of the observed clathrate hydrates were taken from results presented by Manakov *et al.*¹⁹ The phase diagram prepared by Shephard *et al.*,¹⁴ based on volume changes to ice in a piston cylinder, also suggested that isobarically heating the sample from 250 to 300 K may allow for the formation of ice VI, however this was not observed in the experiment potentially as a result of the clathrate hydrates preferentially developing in the argon-rich environment. Shephard *et al.*¹⁴ also observed the formation of the argon clathrate hydrate CS-II in their ND work, but did not see the hexagonal polymorph as they did not venture above pressures higher than 0.3 GPa.

4. Mapping the 2.5 mol% NH₄F-ice phase diagram up to 1.7 GPa

4.2.1 Conclusions

Consistent with Shephard *et al.*, ice II did not emerge at any point of the mapping, a large part of which covered the known stability field of ice II.¹⁴ Instead, as also seen in the previous subchapter 4.1 (which considered the phase transition between ices III and IX), in the absence of ice II, ices III and V were observed. However, no ice VI was seen in the high p - T , despite having been reported by piston cylinder experiments conducted by Shephard and co-workers.¹⁴ In the place of where ice VI was expected to exist argon clathrate hydrates were observed. Lobban *et al.* also encountered similar issues while using a helium gas medium as a pressurising agent while surveying the ice II region.²⁰ Hence, for a true understanding of the phases that occur in the high p - T region, which in this case relates to near the liquidus line at ~0.8 GPa, it would be ideal to not use gas pressure, but instead survey the region under some form of mechanical pressure.

4. Mapping the 2.5 mol% NH₄F-ice phase diagram up to 1.7 GPa

4.3 Volume-change mapping of the 2.5 mol% NH₄F-ice phase diagram up to 1.7 GPa

4.3.1 Aims

Following the mapping of the 2.5 mol% NH₄F-ice phase diagram performed by Shephard *et al.*¹⁴ which established the phases that occur along the liquidus line from 0 to 0.8 GPa, the aim was to further identify the phases that occur at higher pressures of up to 1.7 GPa. The effect of 2.5 mol% NH₄F in ice at higher pressures has not been explored in a systematic fashion involving volume changes and the phases that occur at each volume ‘step’. It is unknown whether NH₄F will inhibit or encourage the formation of different phases, in addition to the already recognised outcome of ice II.¹⁴

4.3.2 Volume change plots from 0.5 to 1.7 GPa

In order to expand on the known 2.5 mol% NH₄F-ice phase diagram, it was decided that, in a manner similar to that in Chapter 3.2, volume changes of 2.5 mol% NH₄F-ice should be tracked during the isobaric heating of samples from liquid nitrogen temperature at 77 K until the samples melted (Figure 4.6). In addition to following the outcome of the heating of 2.5 mol% NH₄F-ice, samples of pure H₂O ice were also heated to draw comparisons and see any potential effect of the presence of NH₄F. From the ΔV plots, phase changes could be ascertained from sharp volume changes that appeared as steps. Below 1.3 GPa, samples were quenched at temperatures T_q at all the steps observed, while at pressures above 1.3 GPa only the highest temperature phase was retrieved for phase ID. The phase identification was performed by carrying out a Rietveld analysis to determine the weight fractions of phases present. The XRD patterns at each step are reported in the Appendix.

4. Mapping the 2.5 mol% NH₄F-ice phase diagram up to 1.7 GPa

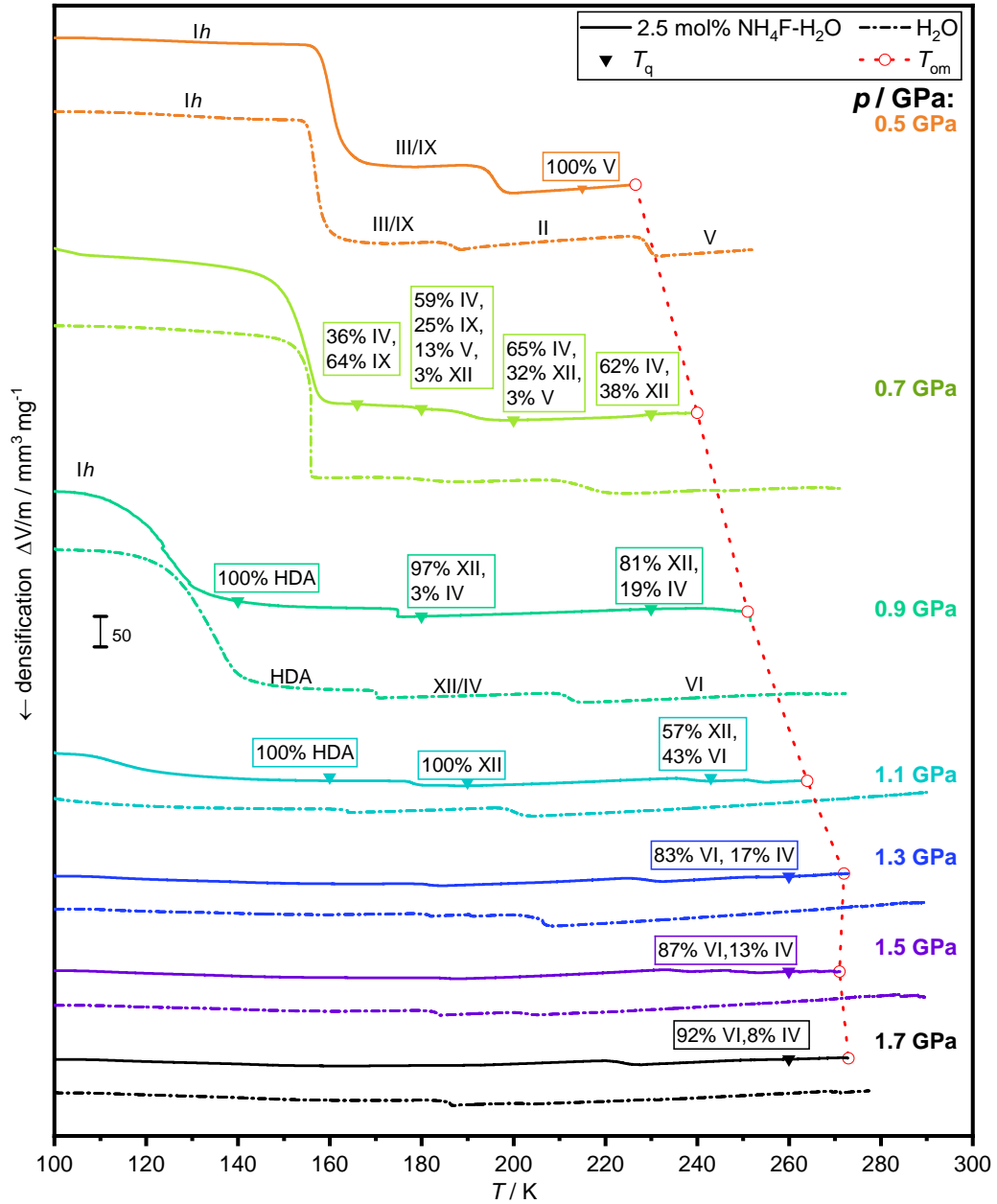


Figure 4.6: ΔV traces of 2.5 mol% NH₄F-ice (solid lines) and pure H₂O ice (dashed lines) between 0.5 to 1.7 GPa, with each pressure colour-coded. Samples that were quenched are given by the triangles with their calculated weight percentages placed above. The onset melts (T_{om}) are given by the open circles. Of particular note is the sample prepared at 1.1 GPa with $T_q = 190$ K, which resulted in pure 2.5 mol% NH₄F-ice XII. The phases noted to appear for pure water at 0.5 GPa are from ref.21 and those for the pure H₂O phases at 0.9 GPa are from ref.22.

As expected from the work performed by Shephard *et al.*¹⁴ no ice II was seen to form over the entire pressure range. It appears that no other phases are restricted from forming in their entirety in the manner that ice II is, further demonstrating the strict topological order that the ice II structure adheres to in comparison to the other ice phases.^{14, 17} Interestingly, it can also be seen that HDA forms. It is known that NH₄F

4. Mapping the 2.5 mol% NH₄F-ice phase diagram up to 1.7 GPa

does not experience pressure-induced amorphisation, but that ice does;²³ in Figure 4.6 it can be seen that ice doped with 2.5 mol% NH₄F can experience amorphisation, as seen in the lowest-temperature phases at 0.9 and 1.1 GPa.

4.3.3 The unusual competition between ices IV, XII and VI

Following the highest-temperature phases that form with increasing pressure, it can be seen that at 0.7 GPa 81 w% ice IV and 19 w% ice XII form, then at 0.9 GPa 62 w% ice XII and 38 w% ice IV form. At 1.1 GPa, ice IV completely disappears before reemerging at 1.3 GPa and above metastably with respect to ice VI. The appearance, disappearance and eventual emergence of ice IV is certainly baffling. Figure 4.7 summarises the evolution of the highest temperature phases that form in the 0.7 to 1.3 GPa pressure range by the Gibbs free energy schematic.

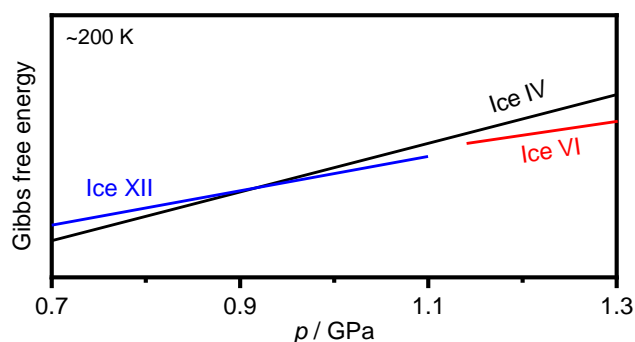


Figure 4.7: Proposed schematic of Gibbs free energies at a fixed temperature over the 0.7 to 1.3 GPa pressure range. The lower the line of Gibbs free energy, the more stable and likely a phase is to form. For the 2.5 mol% NH₄F-ice system, at the lowest pressure ices IV and XII form, with ice XII eventually growing in its dominance at 0.9 to 1.1 GPa. The highest pressures give rise to ice VI and IV. Adapted from the style of Figure 11.11 in Petrenko and Whitworth¹ and from Shephard *et al.*¹⁴

To make sense of the phases that emerge as illustrated in Figure 4.7, it is useful to recall the conclusions drawn in Chapter 3 and by Lyashchenko and Malenkov.²⁴ In both cases, the density of NH₄F-ice solid solutions increased with larger concentrations of NH₄F. The presence of NH₄F in the solid solutions, and the inclusion of the more electronegative fluorine atoms in the structural networks, led to a denser material than pure ice.²⁴ Hence, the initial solid solutions that are being pressurised in this mapping study are inherently more dense than pure ice. Consequently, this means that steric factors will inevitably play a role in the phases that result.

In the low-pressure regime of 0.7 GPa, which normally sees ice VI formation, the increased density of the compressed solid solution makes the formation of ice VI

4. Mapping the 2.5 mol% NH₄F-ice phase diagram up to 1.7 GPa

networks unfavourable. Ice VI is formed of very dense interpenetrating networks.^{1, 17, 25} The two networks that comprise the ice VI structure do not touch or have any hydrogen bonding¹⁷ and strong repulsive van der Waals forces exist between the two.²⁵ Hence, the less dense ice IV preferentially appears, even though this too contains interpenetrating elements – specifically the threading through of a hydrogen-bonded network through a six-membered ring.^{17, 23} Ice XII is also seen as this is the densest phase of ice which forms without interpenetrating elements.¹⁷ At 0.9 GPa, ice XII and ice IV formation are still favoured for similar reasons. Surprisingly, at 1.1 GPa, ice XII now appears metastably with respect to ice VI, which is seen for the first time (the appearance of ice VI by Shephard *et al.*¹⁴ was actually at lower pressures – the reason for the discrepancy is unknown). Beyond 1.1 GPa, ice XII can no longer form due to the increased pressure on the already tightly bound ice network. Instead, ices IV and VI now appear as facilitated at higher pressures despite the proximity of the closely positioned interpenetrating networks in their structures. Ice IV appears in a metastable capacity with the ice VI, presumably due to its relatively lower density, even though it is generally not observed at these pressures for pure ice. Going from 1.3 to 1.7 GPa, the quantity of ice IV does decrease from 17 w% to 8 w%, as the pressure forces out the formation of the less dense structure and favours the denser ice VI.¹ The XRD patterns collected of the samples did not indicate any unassignable peaks, indicating that the presence of the dopant did not induce the formation of any potential new phases.

4.3.4 The formation of pure 2.5 mol% NH₄F-ice XII

Remarkably, the presence of NH₄F clearly encouraged the formation of ice XII, which is metastable in the pure ice phase diagram. As can be seen from Figure 4.6, at 1.1 GPa, the 2.5 mol% NH₄F-ice sample with $T_q = 190$ K was able to produce a pure 2.5 mol% NH₄F-ice XII sample on quenching. The XRD of the sample is given by Figure 4.8.

4. Mapping the 2.5 mol% NH₄F-ice phase diagram up to 1.7 GPa

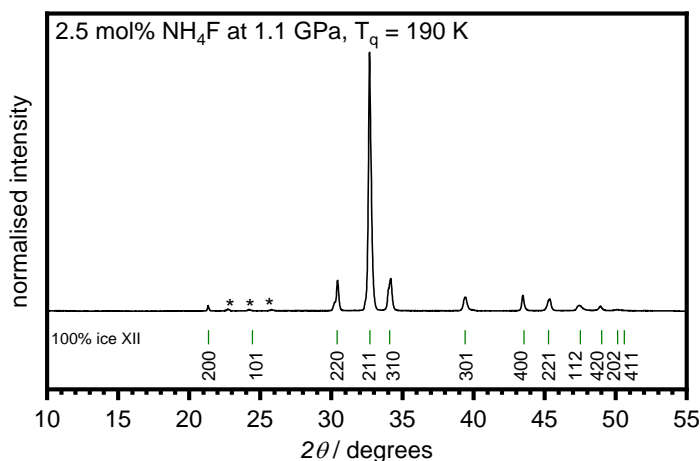


Figure 4.8: 2.5 mol% NH₄F-ice quenched at 190 K at 1.1 GPa leads to the first reported formation of an ice XII-type structure not prepared via an amorphous precursor. The lattice constants of the tetragonal unit cell with $I\bar{4}2d$ space symmetry were determined to be $a = (8.292703 \pm 0.000453) \text{ \AA}$ and $c = (4.039016 \pm 0.000381) \text{ \AA}$. The tickmarks indicate reflections of ice XII with associated Miller indices, the asterisks are from external ice Ih on the sample holder. No ice IV is present in the sample as clear from the absence of a peak at $\sim 15^\circ$.

This is unlike any other known method of ice XII formation and probably the first time that it has been prepared being absolutely phase-pure.^{18, 26, 27} On its discovery by Lobban *et al.*, ice XII was found to be extremely metastable, being formed at 0.55 GPa on slow crystallisation at 260 K.¹⁸ The sample itself could not be released to ambient pressure without transforming to another more stable phase.¹⁸ Subsequently a method was developed to prepare ice XII *via* the fast-heating of HDA (greater than 15 K min^{-1}); using this preparation method, the samples of ice XII could be released to ambient pressure under low temperature conditions (*e.g.* in liquid nitrogen) in a reproducible manner.^{26, 28} However, this method requires the experimenter to keep a very close eye on the heating rate of the initial HDA that it is prepared from, as a competition exists between the formation of ice XII with ice IV, another phase which is also metastable.^{26, 28} In Chapter 3.2, which investigated the effect of the addition of NH₄F to ice over the entire mol% range, astonishingly it was also found that some kind of ice XII-like structure formed at 0.5 GPa between 12 to 50 mol% NH₄F on the quenching of samples. However, here a low concentration of NH₄F was used to form this ice XII-like sample, which resides in a different *p-T* range.

Work by Salzmann *et al.* which considered the effect of 2.5 mol% NH₄F on the hydrogen ordering between ices VII/VIII demonstrated that NH₄F slowed reorientation dynamics in ice, which at first leads one to believe that ice IV should be formed in

4. Mapping the 2.5 mol% NH₄F-ice phase diagram up to 1.7 GPa

favour of ice XII.²⁹ However, as discussed in Chapter 3, the presence of NH₄F in ice leads to the formation of denser solid solutions, hence it was found that at 0.5 GPa, ice XII type structures form instead of ice V from 12 mol% NH₄F and above. At the pressure here of 1.1 GPa, there is an inclination to favour the formation of the denser ice XII-type structure, which unlike an ice IV structure, contains no interpenetrating features.^{17, 18} Hence, the Gibbs free energy of ice XII, when doped with 2.5 mol% NH₄F at 1.1 GPa, is lower than an ice IV-type structure. This is also likely to explain why ice VI is not the thermodynamically stable phase at 1.1 GPa at the next quenched temperature of ~240 K; like ice IV, ice VI is formed of a very dense network of interpenetrating networks.¹⁷ The two networks that comprise the ice VI structure do not touch or have any hydrogen bonding.¹⁷ NH₄F-doped ice VI is likely to experience far stronger repulsive van der Waals forces due to the greater electronegativity of nitrogen to oxygen (a consequence of which means it forms far stronger hydrogen bonds).²⁴ Thus steric factors dictate the formation of ice XII over ice IV at 1.1 GPa.

Figure 4.9 draws lattice parameter comparisons with the samples of ice XII-type structures that were prepared at 0.5 GPa which were reported in Chapter 3.2.

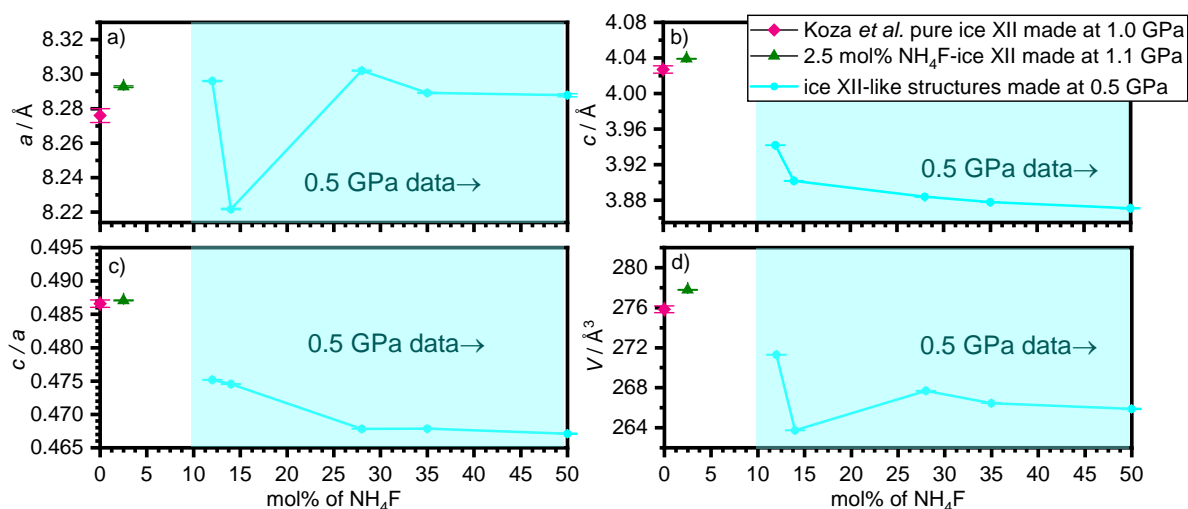


Figure 4.9: Lattice parameters of ice XII-like samples determined from samples at ambient pressure from 0 to 50 mol% NH₄F. The legend indicates the origin of the samples. The lattice parameters of the 2.5 mol% NH₄F ice XII-type structure from this study are shown as olive triangles. The lattice parameters of pure ice XII reported by Koza et al.²⁸ are shown as pink circles. The ice XII-type samples prepared at 0.5 GPa which are greater than 10 mol% NH₄F (from Chapter 3.2.2.2) are in the cyan shaded area.

As is apparent from Figure 4.9, a very large disparity exists between the 2.5 mol% NH₄F-ice sample prepared at 1.1 GPa and the samples of greater concentrations of

4. Mapping the 2.5 mol% NH₄F-ice phase diagram up to 1.7 GPa

NH₄F prepared at the lower pressure of 0.5 GPa. The values of pure ice XII are those reported by Koza *et al.* who prepared ice XII *via* HDA made at 1.0 GPa and released their sample to ambient pressure where they then obtained lattice parameters.²⁸ It can be seen in Figure 4.9(a)-(c), the lattice constants of Koza *et al.*'s ice XII and the 2.5 mol% NH₄F-ice XII are clearly not the same. Figure 4.9(c) demonstrates that the 2.5 mol% NH₄F-ice XII doped sample and the pure ice XII experience a similar degree of tetragonal distortion.

4.3.5 The final 2.5 mol% NH₄F-ice phase diagram

The data of the ΔV plots and the quenched ices' phase ID is consolidated in Figure 4.10 which places the 2.5 mol% NH₄F phase diagram over the pure ice phase diagram for the pressure regions between 0.3 to 1.7 GPa.

Although only 2.5 mol% NH₄F is present in the doped ice, the resulting phase diagram does have some stark differences to the pure ice phase diagram, for instance with the onset melting temperatures being considerably lower than the pure ice liquidus line averagely by ~40 K. The incongruent melting of the compressed solid solution cannot be tracked with the Zwick piston, but can be tracked with the gas pressure cells at ISIS. Starting at the low-pressure end of the 2.5 mol% NH₄F-ice phase diagram, it can be seen that ice III and ice V, take the place of ice II as would be observed for pure ice. As already established by Shephard *et al.*, ice II is completely removed.¹⁴ For pure ice, the pressure regime between ~0.6 GPa to past 2.0 GPa would usually give rise to ice VI, which is stable in a large expanse of the phase diagram due to its efficient interpenetrating networks.²⁵ Yet for 2.5 mol% NH₄F-ice, at 0.7 GPa, the most stable high temperature phase that arises is dissimilar to pure ice. Instead of ice VI appearing, the notoriously difficult-to-form⁶ ice IV is present, however as illustrated in Figure 4.6, ices IX, V and XII co-exist with it at that pressure. Between pressures 0.9 and 1.1 GPa, ice XII becomes the dominant phase, and remarkably can even be isolated without any impurities when quenched at 190 K at 1.1 GPa. From beyond 1.3 GPa, ice XII no longer appears, instead ice VI forms with ice IV.

4. Mapping the 2.5 mol% NH_4F -ice phase diagram up to 1.7 GPa

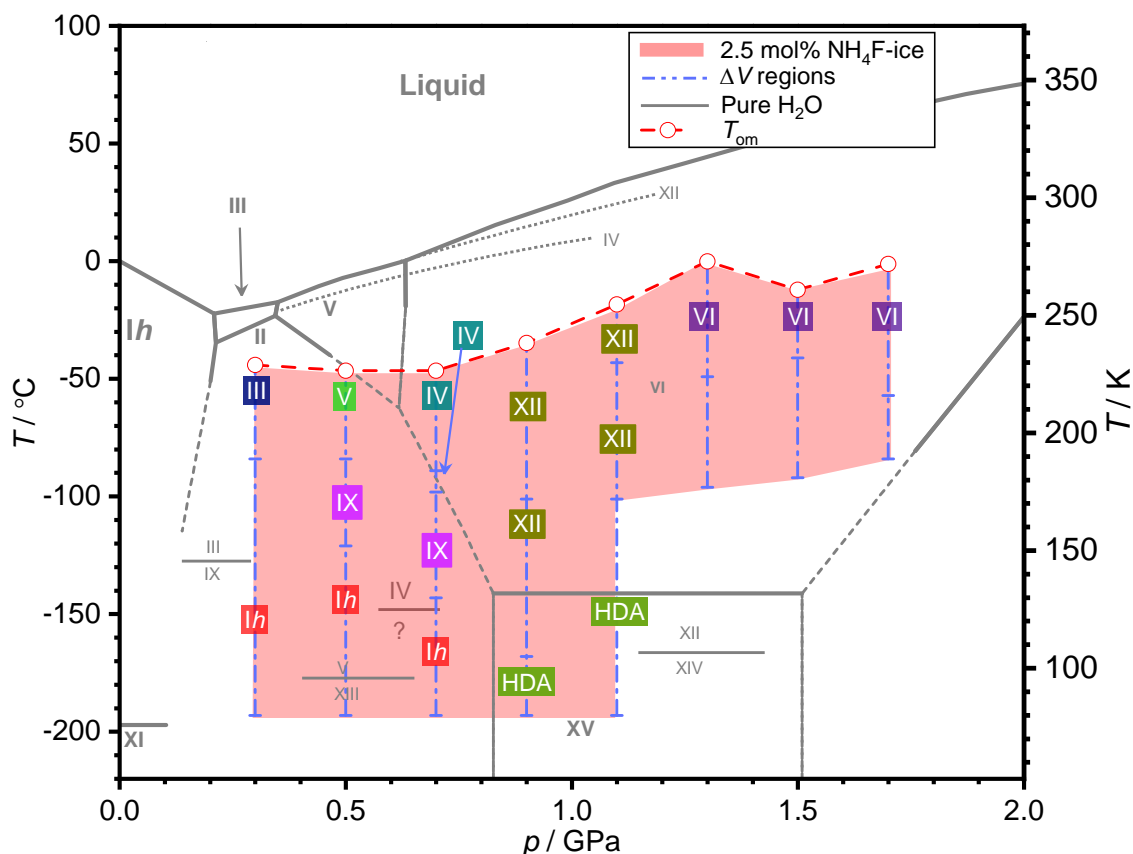


Figure 4.10: 2.5 mol% NH_4F -ice phase diagram from 0.3 GPa to 1.7 GPa shaded by the red region. The pure water phase diagram is shown by the grey lines and text. The regions surveyed in the ΔV plots are given by the lilac lines, with the horizontal lines indicating the sharp changes in volume. Noticeably, the beginning of onset melting (T_{om}), shown by the open red circles, is between 20 to 60 K lower than the pure H_2O melting transitions. The phase pure 2.5 mol% NH_4F -ice XII is obtainable at 190 K at 1.1 GPa. The data of the 0.3 GPa NH_4F -ices is from ref.14.

Surprisingly, the picture that comes to mind when rationalising the phases that exist at each pressure is actually one that relates to the phases that crystallise on heating HDA as reported by Salzmann *et al.*²² In their study, Salzmann and co-workers investigated the effect of heating rates of HDA on the crystallisation kinetics of the phases that formed in the 0.2 to 1.9 GPa pressure window.²² This was presumably in response to the discovery that different heating rates of HDA past 1.0 GPa either resulted in ice IV or ice XII formation.²⁶ They note that pairs of phases form at each pressure regime, with one forming more readily over the other depending on the heating rate. At 0.21 GPa ice Ih and ice IX are found; at 0.51 GPa ice IX and ice V form; at 0.81 and 1.21 GPa ice IV and ice XII form; while at 1.41 GPa ices XII and VI appear.²² This is all very similar to the evolution of phases seen in 2.5 mol% NH₄F-ice, with the exception that ice XII is not seen beyond 1.1 GPa as a result of the increased strain on its shorter

4. Mapping the 2.5 mol% NH₄F-ice phase diagram up to 1.7 GPa

fluorine-based bonds. Salzmann *et al.* also noted that at 0.7 GPa a more complicated situation arose, with the formation of four phases: ices IV, V, IX and XII.²² Referring back to Figure 4.6, it can also be seen that the same four phases emerge at 0.7 GPa yet in the 2.5 mol% NH₄F-ice phase diagram they appear to be more stable than for the pure ices made *via* HDA.²²

The succession of highest-temperature phases that form from 2.5 mol% NH₄F-doped ice follows the trend that would be expected with increasingly dense phases forming with the application of greater pressures.²² The emergence of ice XII, and its stability, is likely to be due to its lack of interpenetrating features¹⁷ which make its formation easier given that the starting solid solution of 2.5 mol% NH₄F-ice is undoubtedly denser as a result of the stronger electronegativity of nitrogen to oxygen.²⁴

4.3.6 Conclusions

The 2.5 mol% NH₄F-ice phase diagram has been reported for the first time over the 0.3 to 1.7 GPa pressure range. Consistent with Shephard *et al.* no ice II was observed.¹⁴ The addition of NH₄F disrupts the kinetics of the phases that form. It seems fair to assume that the increased electronegativity of the fluorine atoms in the starting solid solution lead to a denser starting material being pressurised. This then leads to steric factors playing an important role in the subsequent phases that form. For instance, the usually very stable ice VI only begins forming at pressures almost 0.5 GPa higher than would be observed for regular H₂O ice and even when the ice VI does appear it does so only by co-existing with ice IV. Normally ice IV is not even observed at these pressures from between 1.3 to 1.7 GPa, so even though both ices IV and VI both contain interpenetrating elements,¹⁷ the fact that ice IV is intrinsically less dense than ice VI¹ promotes its formation alongside ice VI. The increased density of the initial solid solution also ultimately leads to the unforeseen occurrence of ice XII being more obtainable in the 2.5 mol% NH₄F-ice phase diagram than in that of pure H₂O – being fully accessible and in a phase pure form at 1.1 GPa and stable on pressure-quenching.

This mapping study has therefore illustrated that the presence of 2.5 mol% NH₄F in ice is able to have a significant effect on the appearance of 2.5 mol% NH₄F-ices that form and hopefully can provide an insight into how the dopant influences the dynamics of phase formation. Here, it has been shown that as well as prohibiting the

4. Mapping the 2.5 mol% NH₄F-ice phase diagram up to 1.7 GPa

formation of ice II, 2.5 mol% NH₄F in ice also makes ice XII readily accessible for the first time by quenching at 190 K and 1.1 GPa.

To build on this work, it would be interesting to observe whether or not the 2.5 mol% NH₄F-ice XII formed at 190 K and 1.1 GPa could be additionally doped with HF. The aim of this would be to see if the acid dopant could induce hydrogen ordering of the ice XII to form ice XIV, in the manner that it is able to do so for the hydrogen disordered ice V to transform to its hydrogen-ordered counterpart ice XIII.³⁰

4. Mapping the 2.5 mol% NH₄F-ice phase diagram up to 1.7 GPa

4.4 References

1. V. F. Petrenko and R. W. Whitworth, *Physics of Ice*, OUP Oxford, 1999.
2. C. Knight and S. J. Singer, *J. Chem. Phys.*, 2006, **125**, 064506.
3. E. Whalley, J. B. R. Heath and D. W. Davidson, *J. Chem. Phys.*, 1968, **48**, 2362-2370.
4. J. D. Londono, W. F. Kuhs and J. L. Finney, *J. Chem. Phys.*, 1993, **98**, 4878-4888.
5. S. J. La Placa, W. C. Hamilton, B. Kamb and A. Prakash, *J. Chem. Phys.*, 1973, **58**, 567-580.
6. C. G. Salzmann, P. G. Radaelli, B. Slater and J. L. Finney, *Phys. Chem. Chem. Phys.*, 2011, **13**, 18468-18480.
7. C. G. Salzmann, P. G. Radaelli, A. Hallbrucker, E. Mayer and J. L. Finney, *Science*, 2006, **311**, 1758.
8. C. G. Salzmann, P. G. Radaelli, E. Mayer and J. L. Finney, *Phys. Rev. Lett.*, 2009, **103**, 105701.
9. J. J. Shephard and C. G. Salzmann, *Chem. Phys. Lett.*, 2015, **637**, 63-66.
10. C. G. Salzmann, A. Hallbrucker, J. L. Finney and E. Mayer, *Phys. Chem. Chem. Phys.*, 2006, **8**, 3088-3093.
11. C. G. Salzmann, B. Slater, P. G. Radaelli, J. L. Finney, J. J. Shephard, M. Rosillo-Lopez and J. Hindley, *J. Chem. Phys.*, 2016, **145**, 204501.
12. C. G. Salzmann, P. G. Radaelli, A. Hallbrucker, E. Mayer and J. Finney, in *Physics and Chemistry of Ice*, ed. W. F. Kuhs, The Royal Society of Chemistry, 2007, DOI: 10.1039/9781847557773-00099, pp. 521-528.
13. K. Nishibata and E. Whalley, *J. Chem. Phys.*, 1974, **60**, 3189-3194.
14. J. J. Shephard, B. Slater, P. Harvey, M. Hart, C. L. Bull, S. T. Bramwell and C. G. Salzmann, *Nat. Phys.*, 2018, **14**, 569-572.
15. S. W. Rabideau, E. D. Finch, G. P. Arnold and A. L. Bowman, *J. Chem. Phys.*, 1968, **49**, 2514-2519.
16. C. Lobban, J. L. Finney and W. F. Kuhs, *J. Chem. Phys.*, 2000, **112**, 7169-7180.
17. C. G. Salzmann, *J. Chem. Phys.*, 2019, **150**, 060901.
18. C. Lobban, J. L. Finney and W. F. Kuhs, *Nature*, 1998, **391**, 268-270.

4. Mapping the 2.5 mol% NH₄F-ice phase diagram up to 1.7 GPa

19. A. Y. Manakov, V. I. Voronin, A. V. Kurnosov, A. E. Teplykh, V. Y. Komarov and Y. A. Dyadin, *J. Incl. Phenom. Macrocycl. Chem.*, 2004, **48**, 11-18.
20. C. Lobban, J. L. Finney and W. F. Kuhs, *J. Chem. Phys.*, 2002, **117**, 3928-3934.
21. C. G. Salzmann, P. G. Radaelli, J. L. Finney and E. Mayer, *Phys. Chem. Chem. Phys.*, 2008, **10**, 6313-6324.
22. C. G. Salzmann, E. Mayer and A. Hallbrucker, *Phys. Chem. Chem. Phys.*, 2004, **6**, 5156-5165.
23. J. J. Shephard, S. Ling, G. C. Sosso, A. Michaelides, B. Slater and C. G. Salzmann, *J. Phys. Chem. Lett.*, 2017, **8**, 1645-1650.
24. A. K. Lyashchenko and G. G. Malenkov, *J. Struct. Chem.*, 1969, **10**, 616-617.
25. N. H. Fletcher, *The Chemical Physics of Ice*, Cambridge University Press, Cambridge, 1970.
26. C. G. Salzmann, I. Kohl, T. Loerting, E. Mayer and A. Hallbrucker, *Can. J. Phys.*, 2003, **81**, 25-32.
27. C. G. Salzmann, E. Mayer and A. Hallbrucker, *Phys. Chem. Chem. Phys.*, 2004, **6**, 1269-1276.
28. M. Koza, H. Schober, A. Tölle, F. Fujara and T. Hansen, *Nature*, 1999, **397**, 660-661.
29. C. G. Salzmann, Z. Sharif, C. L. Bull, S. T. Bramwell, A. Rosu-Finsen and N. P. Funnell, *J. Phys. Chem. C*, 2019, **123**, 16486-16492.
30. A. Rosu-Finsen and C. G. Salzmann, *J. Chem. Phys.*, 2017, **148** 244507.

5 Pressure-induced amorphisation of $\text{NH}_4\text{F-H}_2\text{O}$ mixtures

5.1 Introduction

Mishima *et al.* found that the compression of ice *Ih* to 1.0 GPa at 77 K led to the formation, and first isolation, of HDA in a process that was later termed as pressure-induced amorphisation and is often abbreviated to PIA.¹ Up until Mishima *et al.*'s discovery of HDA, the prevalent method to produce amorphous ice was from the vapour deposition onto a cold substrate, which formed the less dense and structurally different LDA.^{1, 2} As with many phenomena initially observed in ice,³ it was since found that the isothermal compression of other crystalline inorganic materials, organic materials and biomaterials³⁻⁵ also leads in a reaction pathway not resulting in a stable high-pressure polymorph, but a metastable amorphous material.⁶ Although there are many unknown processes surrounding PIA, there are two conditions that have been seen to occur as schematically represented in Figure 5.1.⁴

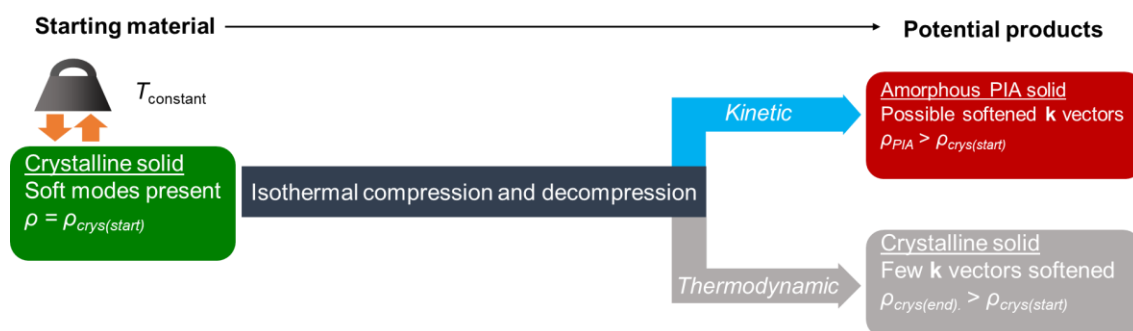


Figure 5.1: General schematic demonstrating the outcomes of isothermally compressing and decompressing a crystalline solid. PIA (light blue route) occurs when thermodynamic crystallisation (grey route) cannot be achieved. Densities of the starting crystalline solid, pressure-induced amorphised solid and final crystalline products in the schematic are given by $\rho_{\text{crys}(\text{start})}$, ρ_{PIA} and $\rho_{\text{crys}(\text{end})}$.

Firstly, the initial crystalline material must have a lower density than the final amorphous product.⁴ Hence starting materials with more open structures are more likely to experience PIA.⁴ Observations have also been made with respect to the reciprocal lattice. Generally, a phase transition might go along with a softening of **k** vectors, however a differentiation has been made with respect to the number of **k** vectors this involves, depending on whether the product is either crystalline or amorphous. In the case of PIA, simultaneous softening of a range of **k** vectors of a phonon branch occurs,

5. Pressure-induced amorphisation of $\text{NH}_4\text{F-H}_2\text{O}$ mixtures

in contrast to the softening of a single \mathbf{k} vector yielding a crystalline phase.⁴ In the case of PIA of ice I_h , the softening of phonon branches has been detected.⁷

Mechanisms rationalising the processes involved in PIA have long been surrounded with controversy.^{5, 8-10} The preparation of HDA by Mishima *et al.* led to a theory that, as the ice was prepared through the extension of the melting line of ice I_h , the amorphous ice represented a ‘melted’ solid that had a structural link to liquid water.¹ Given that the heating of HDA at ambient pressure led to the transformation to the structurally distinct and lower density LDA, it was also proposed that LDA must have a structural connection to water.¹¹ Many of the studies that have proposed the so-called two-liquid theory of water, which places a speculated second critical point of water in “No man’s land”, do not have explicit experimental evidence showing the existence of the high-density liquid (HDL) and low-density liquid (LDL) – these are the hypothetical analogues of HDA and LDA respectively.¹² This has often been put down to difficulties in being able to isolate these liquid phases which are apparently prone to crystallisation.^{2, 11, 12}

Much experimental and theoretical evidence points away from the two-liquid theory of water.^{5, 8, 13, 14} Theories have also suggested that PIA occurs as a result of a mechanical instability. Researchers have also proposed that there could be a combination of thermodynamic ‘melting’ and mechanical instabilities occurring at different parts of the PIA process.^{5, 8} Figure 5.2 shows quasi-harmonic lattice dynamics calculations performed by Tse *et al.*, which on comparison with experimental data, highlight a combination of processes.⁸

Tse *et al.* proposed that although thermodynamic ‘melting’ may occur on the compression of ice, it is only present for temperatures exceeding 160 K.⁸ However, in the low-temperature high-pressure regime (*i.e.* below 162 K) the processes that ensue are a result of mechanical instabilities where the Born conditions are broken (*i.e.* a diagonal component of the elastic constants matrix is negative⁴).⁸ It should be stressed that the onset of mechanical instability during PIA is always above the temperature of the thermodynamic melting point.⁸ Other materials which have been shown to also undergo PIA invalidate the possibility of the supposed extrapolated melting of water and the two-liquid theory that it has given rise to.^{5, 8, 9}

5. Pressure-induced amorphisation of $\text{NH}_4\text{F-H}_2\text{O}$ mixtures

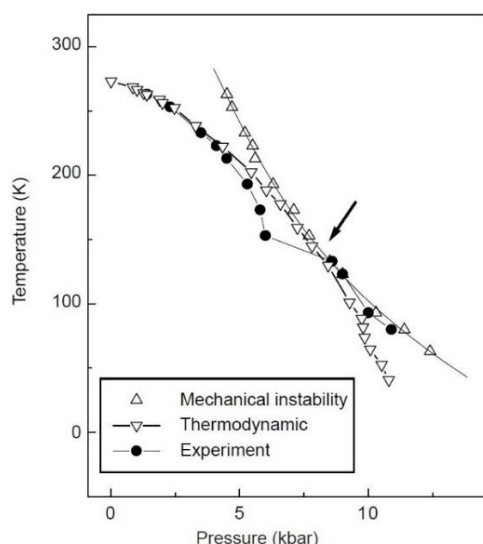


Figure 5.2: Experimental data shown alongside calculated the thermodynamic melting line and the mechanical instability line reported by Tse *et al.*⁸ The arrow indicates the crossover point of the mechanism from thermodynamic ‘melting’ to mechanical instability. Reprinted by permission from Springer Nature: Springer Nature, Nature, J. S. Tse, D. D. Klug, C. A. Tulk, I. Swainson, E. C. Svensson, C. K. Loong, V. Shpakov, V. R. Belosludov, R. V. Belosludov and Y. Kawazoe, *Nature*, 1999, **400**, 647-649.⁸

Tetrahydrofuran (THF) experiences PIA, but the decompression of the amorphous PIA form at low temperatures goes along with the sample rapidly reverting to its initial crystalline structure.⁸ The recrystallisation of the THF would not be possible had the THF experienced thermodynamic melting on amorphisation.⁸ LDA has also been described as a collapsed ill-crystalline material, which actually bears more resemblance to the ice *Ih* than to supercooled water.^{5, 8} Vibrational spectroscopy techniques, which give an idea of short-length scale interactions and are hence important in defining liquid phases, have been able to demonstrate the closeness of LDA to ice *Ih*, and highlight their disparity to the supercooled liquid.⁸

Tulk *et al.* also demonstrated that PIA appears to be a kinetically-driven process, as the much slower compression of ice *Ih* at low temperatures leads to the formation of ice IX' which on further compression transforms to ice XV' before finally settling as ice VIII' (here the prime notation, ' , denotes ices with varying degrees of hydrogen ordering).¹³ Although this does bring to light the absence of a liquid-like solid form of ice developing, it should be noted that the pressures at which ice *Ih* transforms to ice IX', ice XV' and finally ice VIII' (rather than the usual PIA pathway of ice *Ih* → HDA) occur from minimum pressure of 3 GPa which is ~2 GPa higher than when PIA for ice *Ih* occurs.¹³ Hence Tulk *et al.*'s study does not necessarily provide a direct comparison

5. Pressure-induced amorphisation of NH₄F-H₂O mixtures

between kinetic and thermodynamic routes that would be expected for ice *Ih* in the pressure regime that PIA takes place.

More definitive proof to support the formation of HDA resulting from a mechanical instability was provided by the analysis of an isostructural species – NH₄F I – (seen clearly in Figure 5.3(a)), which Mishima *et al.*¹ actually suggested as a candidate for PIA due to its negative melting line.⁵ Shephard *et al.* conducted isothermal compression experiments at 77 K of ice *Ih*, NH₄F I and their stacking disordered equivalents (Figure 5.3(b)) on the assumption that they would be likely to experience PIA.⁵

Despite the compression curves of all the samples demonstrating similar volume changes (Figure 5.3(b)), XRD performed on the samples showed that different products had formed. The ice samples both transformed to HDA, as has been previously reported in the literature, while the compressed NH₄F samples transformed to crystalline products composed of ~90 w% NH₄F II and ~10 w% NH₄F I (Figure 5.3(d)).⁵ The lack of positional hydrogen order in ice *Ih* and ice *Isd* (*i.e.* that they are hydrogen disordered), which does not exist for NH₄F, was able to explain the formation of the different products which had comparable starting structures and underwent similar pressure collapses.⁵ In both cases, the products on low-temperature compression represent the kinetic product; it was noted that the thermodynamic product of the compression of NH₄F I was expected to be actually NH₄F III not NH₄F II.^{5, 15}

5. Pressure-induced amorphisation of NH_4F - H_2O mixtures

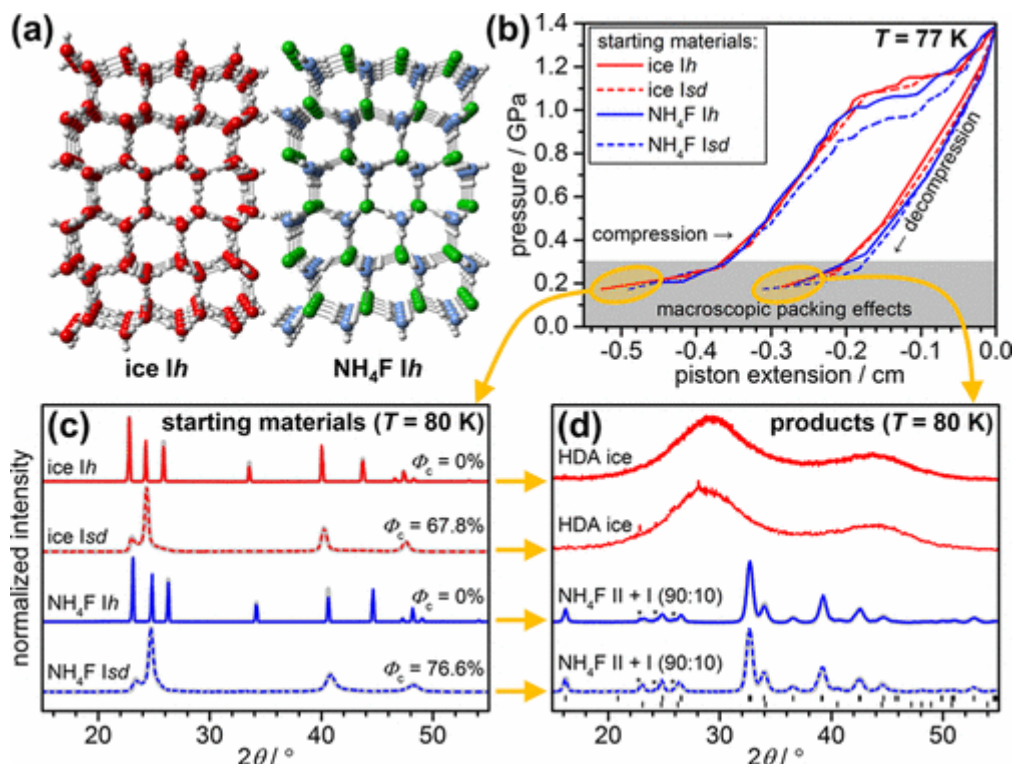


Figure 5.3: (a) The crystal structures of ice Ih and NH_4F Ih, which along with their stacking disordered analogues (b), show similar compression and decompression curves on reaching 1.4 GPa at 77 K. (c) and (d) show the XRD patterns of the starting materials before compression and the products retrieved after compression respectively. The stacking-disordered starting materials had associated cubicity values of 67.8% and 76.6%. Asterisks in (d) show positions of external ice Ih impurity peaks. Reprinted with permission from J. J. Shephard, S. Ling, G. C. Sosso, A. Michaelides, B. Slater and C. G. Salzmann, *J. Phys. Chem. Lett.*, 2017, 8, 1645-1650.⁵ Copyright 2017 American Chemical Society.

The transformation mechanism of ice Ih to ice IV was put forward by Engelhardt and Kamb¹⁶ and is referred to as the Engelhardt-Kamb collapse (or EKC) and is pictured in Figure 5.4. The same mechanism was later also used to describe the analogous transformation of NH_4F I to NH_4F II.¹⁷

5. Pressure-induced amorphisation of $\text{NH}_4\text{F}\cdot\text{H}_2\text{O}$ mixtures

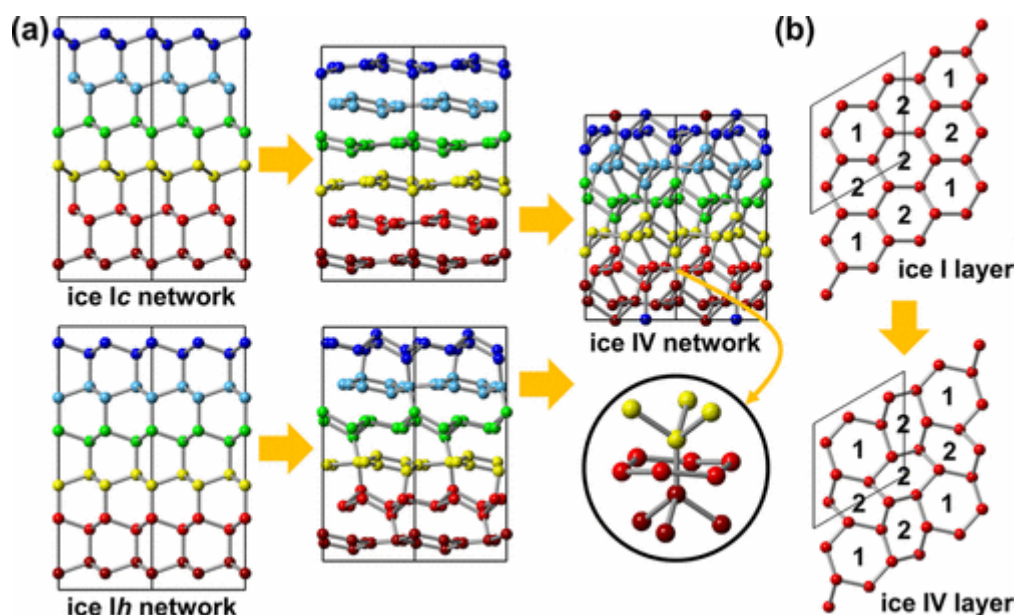


Figure 5.4: (a) Ice Ic and ice Ih networks are shown on the left to illustrate the stacking of layers, with the spheres representing nodes of the hydrogen-bonded networks, which are coloured differently between layers. The second panel shows the ice I structures viewed down the 001 direction. For ice Ic, the interlayer hydrogen bonds need to be broken and flattened before the layers are ‘re-buckled’. The ice Ih networks require a shift or rotation to achieve the characteristic ‘threading through’ of ice IV which is pictured in the inset. (b) A single layer of the ice I network being transformed to ice IV viewed along 001. The rings labelled ‘1’ experience threading through which causes the rings to flatten (increasing in their diameter) and rotate slightly. In turn the rings labelled ‘2’ are distorted, either raising or lowering the nodes which are not part of the ‘1’ rings. This forms hydrogen bonds with two layers above or below. Reprinted with permission from J. J. Shephard, S. Ling, G. C. Sosso, A. Michaelides, B. Slater and C. G. Salzmann, *J. Phys. Chem. Lett.*, 2017, 8, 1645-1650.⁵ Copyright 2017 American Chemical Society.

The EKC can apply to both hexagonally or cubically stacked ice I and NH_4F I to form ice IV and NH_4F II respectively. At 77 K however, as shown in Figure 5.3(d), it can be seen that the products are not pure ice IV and NH_4F II; this highlights that other factors are at play. Here, it is important to note that ice I experiences hydrogen disorder. This presents an issue after the breaking of hydrogen bonds and on their reforming, at which point there exists a 50% probability of a broken hydrogen bond reconnecting to another water molecule. This is due to the equal ability of the hydrogens to be either hydrogen bond acceptors or donors. If the mismatch of hydrogen bonds ‘threading-through’ the six-membered rings were not present, ice IV character would be brought about, instead of leading to HDA formation. This issue does not occur for NH_4F I, as it does not demonstrate hydrogen disorder. Hence the efficiency of the EKC mechanism is visibly more apparent in the NH_4F I which transforms to 90 w% NH_4F II. Alongside the

5. Pressure-induced amorphisation of NH₄F-H₂O mixtures

experimental evidence, DFT also confirmed the low activation barrier high probability of a theoretically hydrogen-ordered ice XIc transforming to ice IV. Therefore, Shephard *et al.* elegantly demonstrated that as PIA in ice I occurs as a result of the hydrogen disorder present in ice I, and so it cannot be possible for HDA to have a structural link to the liquid; instead PIA in ice I is in fact a consequence of a ‘derailment’ in the pathway from ice Ih to ice IV.

Despite the weighty evidence in demonstrating the unlikelihood of the connection between the amorphous ices and two liquids, PIA remains heavily utilised in the scientific battleground to either prove or disprove the nature of the structural connection between amorphous ice and water.

5.2 Aims

To supplement the knowledge laid out by Shephard *et al.*⁵ which demonstrated that PIA occurs in ice I and not NH₄F I, despite the materials being isostructural. Ice I does not transform to ice IV as a result of the derailment caused by the hydrogen disorder in the ice. In this chapter, the isothermal compression of NH₄F-ice mixtures (known to be crystalline,¹⁸ additionally demonstrated in Chapter 3.1) across the entire composition range is assessed. Particular focus is placed on determining the mol% composition of NH₄F-ice at which the crossover from PIA to recrystallisation (*i.e.* the end of derailment) occurs.

5.3 Pressure collapses of 0 to 100 mol% NH₄F-ice mixtures

Samples of NH₄F-ice mixtures across the entire composition range were prepared and compressed to 1.4 GPa at 77 K, before then being decompressed back to ambient pressure (in keeping with work carried out by Shephard *et al.*⁵). All experiments were performed isothermally at 77 K, using the same compression/decompression rate of 5 kN min⁻¹. It is worth pointing out here that Shephard *et al.*⁵ compressed their samples in the manually operated Frimo HyPress 30 tonne hydraulic press formerly discussed in Chapter 2.4.2.1. The Zwick Universal Testing machine, which was used to perform the compression in this work, yielded compression curves of the samples, as illustrated in Figure 5.5.

5. Pressure-induced amorphisation of NH_4F - H_2O mixtures

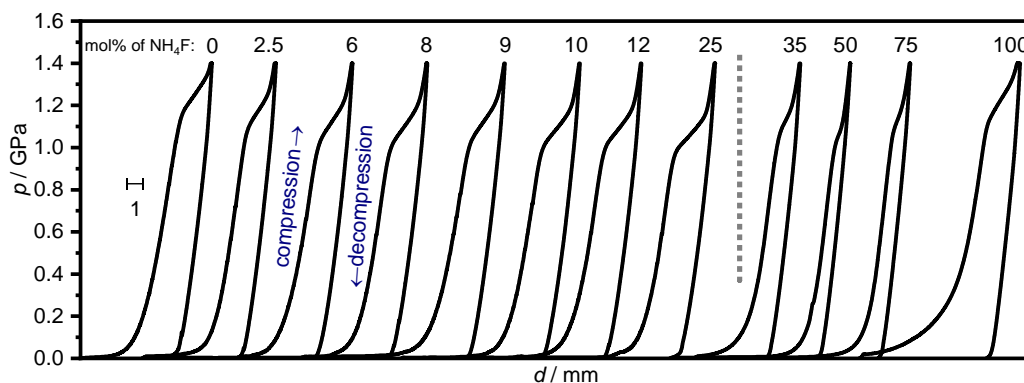


Figure 5.5: Changes in sample volume as a function of the displacement of the Zwick piston head, across the composition range of NH_4F -ice mixtures. The grey dotted line marks the point at which solubility limit was surpassed and ground-up unknown volumes of the frozen mixtures of the species were compressed at 35, 50 and 75 mol% NH_4F .

To keep conditions as consistent as possible in this work and with the experiments conducted by Shephard *et al.*⁵, 393 μL of solution ($\sim 393 \text{ cm}^3$) was frozen for compression for the samples between 0 to 25 mol% NH_4F . The known solubility limit for NH_4F in water at room temperature equates to roughly 30 mol% NH_4F ,¹⁹ hence for the samples composed of 35, 50 and 75 mol% NH_4F , frozen solid solutions of set volumes were not used. Instead solid solutions were pipetted into a pre-cooled pestle and mortar, ground up and spooned into indium cups ready for compression. As a result, the appearance of the pressure collapses of these three samples differs from the rest of the samples in Figure 5.5. At 100 mol% NH_4F , a solid of mass 407 mg ($\sim 403 \text{ cm}^3$) was compressed with a similar volume to frozen solutions.

From taking tangents of the pressure collapses in Figure 5.5, the onset pressures of assumed amorphisation and changes in volume of assumed amorphisation were elucidated and are shown in Figure 5.6(a) and Figure 5.6(b) respectively. Here the word ‘assumed’ is used as the crossover between amorphisation and crystallisation is unknown.

5. Pressure-induced amorphisation of NH_4F - H_2O mixtures

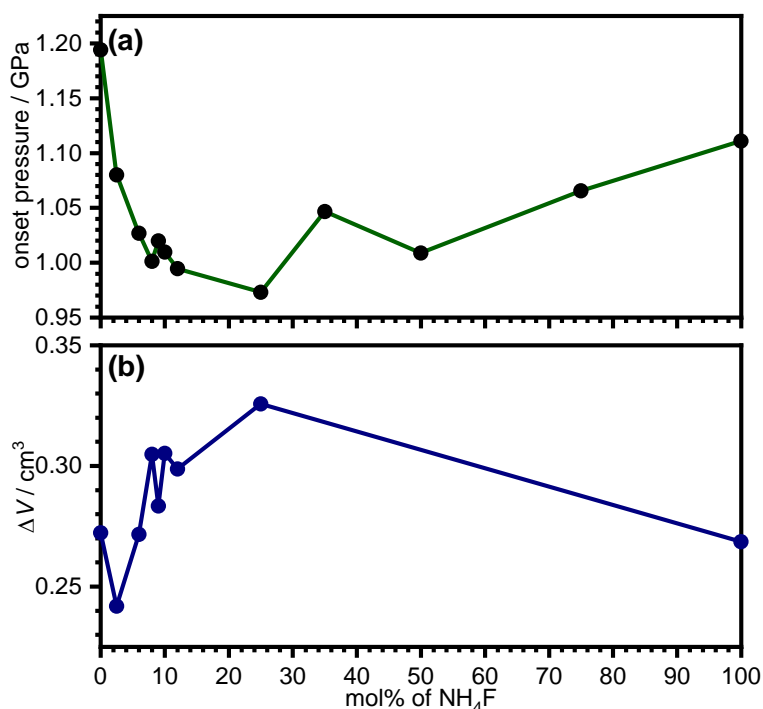


Figure 5.6: (a) Onset pressures of assumed amorphisation and (b) change in volume of the samples on assumed amorphisation. In (b), consistent with the work performed by Shephard *et al.*⁵, all samples experience similar changes in their volume on compression.

Figure 5.6(a) illustrates that the onset pressures of assumed amorphisation do not vary greatly, however it does appear that the onset pressures drop on the addition of NH_4F to ice in the low concentration range, which then picks up again past 25 mol% NH_4F . The reverse trend is seen in Figure 5.6(b) for the changes in sample volume, which appears almost as a mirror image to Figure 5.6(a), first increasing before dropping for the pure NH_4F .

5.4 Assessing the crossover of PIA to recrystallisation

The retrieved samples were analysed using a combination of XRD and DSC to observe the cut-off point of amorphisation and the advent of crystallisation.

5.4.1 XRD determination of amorphous character

To evaluate the end of PIA, XRD was performed on a range of samples that had been isothermally compressed to see the point at which HDA, the known PIA product of ice I_h , was no longer formed.

5. Pressure-induced amorphisation of NH_4F - H_2O mixtures

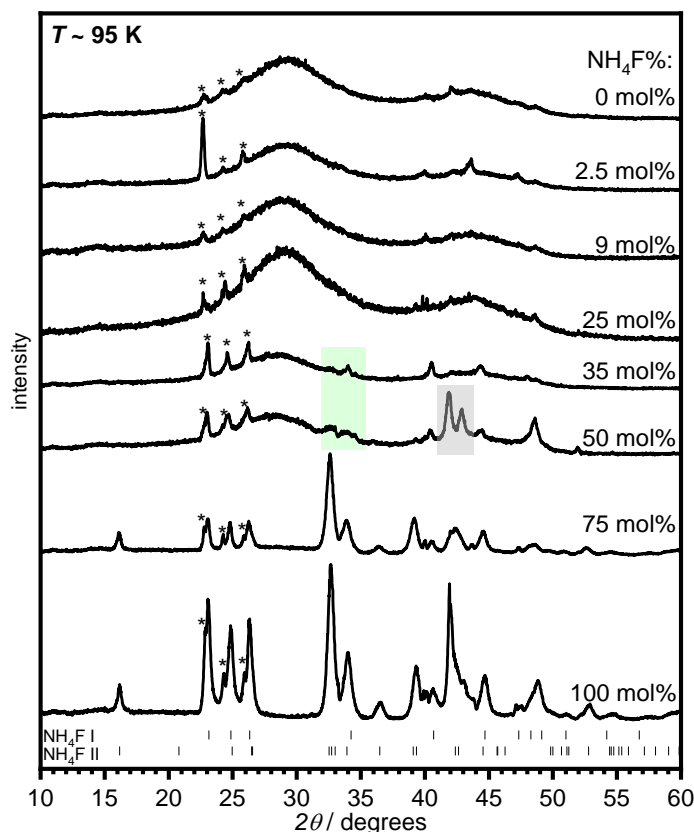


Figure 5.7: XRD patterns collected at ambient pressure at ~ 95 K of a range of isothermally compressed NH_4F -ice samples. Samples can be separated into three regimes: (1) between 0 to 25 mol% NH_4F where they are fully amorphous; (2) 35 and 50 mol% NH_4F where the samples have amorphous and microcrystalline compositions, as highlighted in green by the emergence of ice IV-type microcrystalline domains at ~ 32 to 33° . In regime (3) are 75 and 100 mol% NH_4F samples which are fully crystalline, and composed largely of NH_4F II, with some unconverted NH_4F I; the peak positions of both are indicated by tickmarks. The XRD patterns were scaled against the Kapton peak of the XRD cell at $\sim 5.5^\circ$. Asterisks indicate external ice Ih formation on the sample holder and the grey box for the 50 mol% NH_4F sample shows peaks from the sample holder.

As expected, the end members yielded HDA and NH_4F II with some NH_4F I. Between 0 to 25 mol% NH_4F , the XRD patterns contain broad features that resemble HDA, confirming the PIA of the samples. The samples of 35 and 50 mol% NH_4F were initially also assumed to be fully amorphous, however on closer inspection of the region between 32° to 33° , features that were originally attributed to be the result of a noisy signal actually indicate the emergence of peaks that are associated with the most intense peaks of the ice IV structure.²⁰ Hence from 35 mol% NH_4F , still on the water-rich side of the solid solutions, the dampening of PIA begins with the emergence of embryonic ice IV-type microcrystalline domains. The composition of 35 mol% NH_4F is lower than was assumed to give rise to some type of crystalline character. The mixed-character

5. Pressure-induced amorphisation of NH₄F-H₂O mixtures

samples were also unexpected in the sense that they did not mark a clear cut mol% composition between amorphous and crystalline products, but instead resulted in a crystalline-to-‘amorphous + microcrystalline’ transition.

From 75 mol% NH₄F, as anticipated for the NH₄F-rich solid solutions, the compressed samples yielded ‘NH₄F II-type’-rich products with some unconverted NH₄F I-type species. Rough w% of NH₄F II:NH₄F I were determined – these were 80:20 and 70:30 for the 75 mol% NH₄F and 100 mol% NH₄F samples respectively. Shephard *et al.* determined that for pure compressed NH₄F I, the product was composed of 90 w% NH₄F II. This differs slightly with the results presented here, the difference could have emerged from the dissimilar compression rates used in this study and that of Shephard *et al.*’s⁵. Despite this, both studies show that the majority of the NH₄F I starting material has converted successfully to NH₄F II.

PIA samples of 2.5, 9, 25 and 50 mol% NH₄F were analysed further by XRD on heating from 100 to 260 K at a heating rate of 10 K min⁻¹ and are shown in Figure 5.8.

The PIA of ice *Ih* leads to the formation of uHDA, the XRD pattern of which is characterised by the presence of two peaks (which are actually more like Gaussian bell curves, due to the ill-crystalline nature of the solid) centred at ~29° and ~42°, with the former peak being more pronounced. The characteristic XRD pattern of uHDA was previously shown at the top of Figure 5.7. On the heating of uHDA, a transformation occurs at ~110 K where the sample transforms to the less dense LDA (whose main feature is centred over the region known to give rise to ‘trident’ peaks in ice *Ih*). Eventually at ~130 K, LDA transforms to ice *Isd* before then turning into ice *Ih* at higher temperatures. A similar situation seems to occur for the 2.5 mol% NH₄F PIA sample on heating, as shown in Figure 5.8(a).

5. Pressure-induced amorphisation of NH_4F - H_2O mixtures

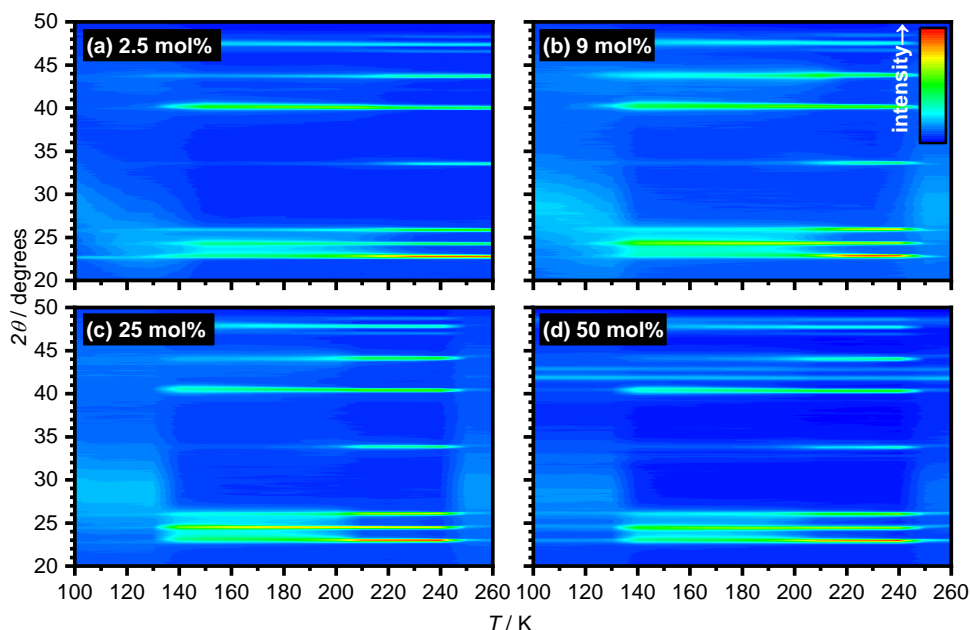


Figure 5.8: Heating XRD contours of 2.5, 9, 25 and 50 mol% NH_4F PIA samples. The intensities have been square-rooted in order to emphasise amorphous features which are present up to ~ 130 K, at which point crystallisation to a stacking disordered structure begins, before the samples finally transform to a wurtzite structure on the sharpening of the three ‘trident’ peaks centred at $\sim 23^\circ$.

From all the plots in Figure 5.8, it is evident that amorphous features persist until ~ 130 K, at which point a transformation to a stacking-disordered structure occurs which eventually changes to a wurtzite-type structure from ~ 200 K onwards. This is similar to uHDA on heating. However, it should be noted that the nature of the amorphous phases in the temperature region from ~ 95 to 130 K appears to be distinct for the uHDA, and potentially the 2.5 mol% NH_4F PIA sample, which seem to experience the same development of phase transitions at similar temperatures.

In order to fully appreciate the effect of NH_4F content on the PIA samples obtained from the solid solutions, a closer examination of the peak position data (Figure 5.9(a)) and full-width half-maxima (Figure 5.9(b)) of the primary amorphous peak obtained from XRD contour plots in the ~ 95 to 130 K temperature range is crucial.

5. Pressure-induced amorphisation of NH_4F - H_2O mixtures

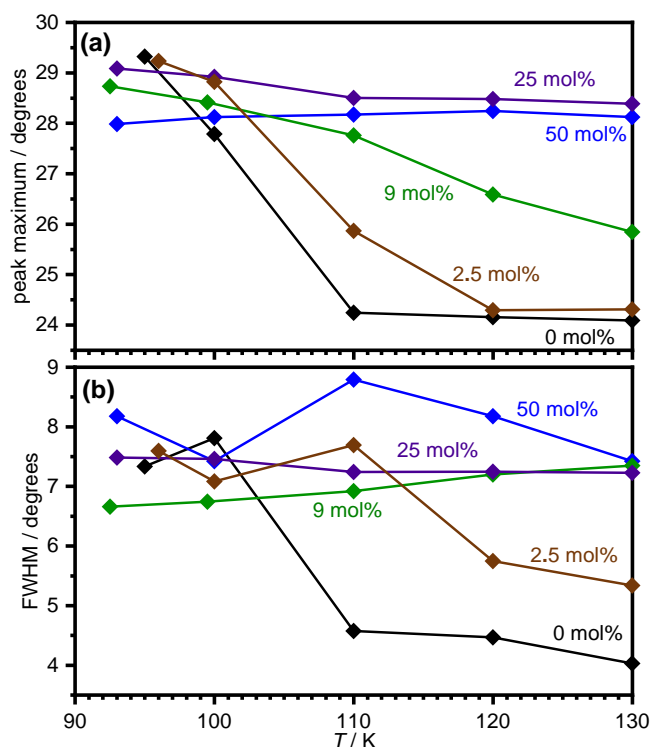


Figure 5.9: Trends observed in XRD with respect to the main 'uHDA'-type peak in the amorphous region $\sim 95 < T(\text{K}) \leq 130$ of the 0-50 mol% NH_4F -ice PIA samples. (a) Peak position at maximum of main feature and (b) full-width half-maximum of the main feature of PIA samples with 0, 2.5, 9, 25 and 50 mol% NH_4F . Data from the 0 mol% NH_4F sample has been provided with permission from Dr. Alexander Rosu-Finsen of the Salzmann group.

The differences between the uHDA sample and the NH_4F PIA samples can be fully appreciated in Figure 5.9. On increasing the NH_4F content, the position of the peak maximum (*i.e.* where the main peak is centred), appears to become more static on heating, as seen in Figure 5.9(a). Going back to the contour plots in Figure 5.8, the way the peak position 'curves in' with heating is quite obvious for the 2.5 mol% NH_4F PIA sample, however, for the 25 and 50 mol% NH_4F PIA samples the peak remains in the same place, before it abruptly transforms to some stacking disordered-type structure, entirely bypassing an LDA-like structure. This order of phase transitions, with the absence of an LDA-type intermediate, is suggestive of the emergence of ice IV-like character. Ice IV, along with several other hydrogen-disordered ices, does not transform to LDA on heating at ambient pressure, but instead converts straight to ice I_{sd} .²⁰ However, it is astonishing that despite appearing amorphous, and perhaps more uHDA-like at ~ 95 K, the 25 and 50 mol% NH_4F PIA samples also exhibit characteristics akin to heating ice IV at ambient pressure on reaching higher temperatures. Nevertheless, it is particularly surprising that the complete lack of the LDA-type 'intermediate' displays

5. Pressure-induced amorphisation of $\text{NH}_4\text{F-H}_2\text{O}$ mixtures

itself for the 25 mol% NH_4F PIA sample. This is despite the fact that, in the base temperature XRD recorded at ~ 95 K in Figure 5.7, there are no ice IV-like microcrystalline domains.

With respect to the FWHM of the ‘Gaussian’-like XRD peaks of the amorphous ice mixtures, whose trends are laid out in Figure 5.9(b), it also seems that the addition of NH_4F inhibits the narrowing of the peak on heating which occurs for pure uHDA. It is also visibly apparent in the contour plots of the 25 and 50 mol% NH_4F PIA samples in Figure 5.8(c) and (d), that the uHDA-like structure remains unchanged right up until crystallising. Hence, it appears as though simply one amorphous form exists (which is presumably closer to uHDA than LDA) which then turns straight to a stacking disordered structure.

This puts into question the connection between HDA and liquid water, as for the 25 and 50 mol% NH_4F PIA samples, and arguably for the 9 mol% NH_4F PIA sample, no LDA-type material is present. If HDA and LDA do hold structural links with liquid water, surely an LDA-type structure would still form on heating the PIA products. It is also staggering that an LDA-like structure – the theoretical analogue of the so-called LDL – definitely disappears at concentrations as low as 25 mol% NH_4F , which is still on the water-rich side of the samples investigated.

5. Pressure-induced amorphisation of $\text{NH}_4\text{F}\text{-H}_2\text{O}$ mixtures

5.4.2 Calorimetric insights into the character of the compressed solid solutions

Having gathered from the XRDs that amorphous character begins disappearing from at least 35 mol% NH_4F , samples over the entire composition range were heated in the DSC (Figure 5.10).

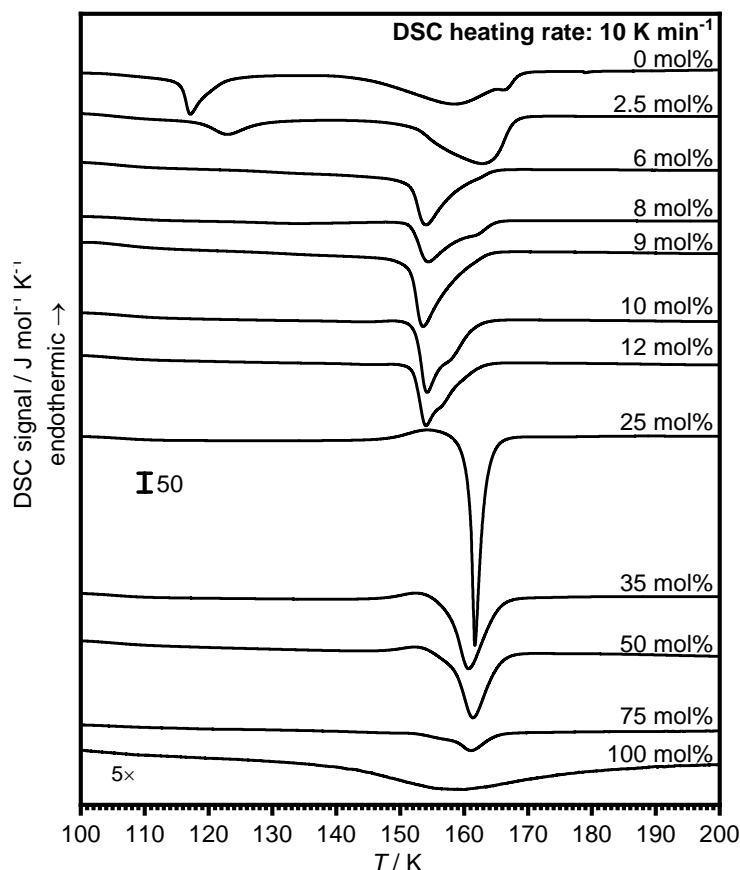


Figure 5.10: DSCs on heating of the isothermally compressed samples. The samples were all scaled by dividing by the number of moles from H_2O , NH_4^+ and F^- . The 100 mol% NH_4F sample was extremely weak and is hence magnified five-fold. All scans were performed at 10 K min^{-1} .

In the case of pure ice, in the uppermost thermogram of Figure 5.10, uHDA transforms to LDA ($\sim 115 \text{ K}$) before then crystallising to ice *Isd* ($\sim 145 \text{ K}$).²¹ A similar trend is seen for the 2.5 mol% NH_4F sample, albeit at temperatures shifted higher and with the phase transitions occurring over a larger temperature range. From concentrations as low as 6 mol% NH_4F , the HDA-type to LDA-type feature disappears, with single transition instead occurring at $\sim 150 \text{ K}$.

At 25 mol% NH_4F a uniquely distinct exotherm appears, which is preceded by a very pronounced glass transition with a $\Delta C_p = 28.5 \text{ J mol}^{-1} \text{ K}^{-1}$, with an onset temperature of 141 K and an end temperature of 150.6 K. Here it is also of interest to

5. Pressure-induced amorphisation of NH₄F-H₂O mixtures

note that LiCl-H₂O solutions are also able to form glasses. In fact, Ruiz *et al.* attempted a study of the PIA of LiCl-H₂O solutions up to the mole fraction of $x = 0.25$ LiCl, yet above $x = 0.12$, the quenched solutions prior to compression were glassy.²² Additionally, ΔC_p values associated with glass transitions of LiCl confined in silica at ~ 145 K were found to range between 1.14 to 2.40 J g⁻¹ K⁻¹ depending on the size of the silica pores used.²³ The glass transition associated with the 25 mol% NH₄F sample is reminiscent of the glass transition that occurs for H₂O ice IV which occurs at 139.8 K and ends at 147.1 K and with a $\Delta C_p = 1.2$ J mol⁻¹ K⁻¹.²⁰ Although the ΔC_p for the 25 mol% NH₄F PIA sample is an order of magnitude larger than that for ice IV, the onset temperature of unfreezing and the extrapolated end temperatures are very similar. An important note should be made here; the presence of glassy features does not necessarily place the material as being glass- or liquid-like in character as stated by Kauzmann.² This is supported by the fact that other crystalline ices, such as ice VI, which can exist in an orientational glassy state, are not amorphous or glassy materials.^{24, 25} The reversibility of the glassy feature was tested for the 25 mol% NH₄F PIA sample by heating to the maximum of the glass transition at 155 K, cooling the sample back down to 93 K and then heating the sample at 10 K min⁻¹ to run the program as performed for all the other samples (Figure 5.11(a)).

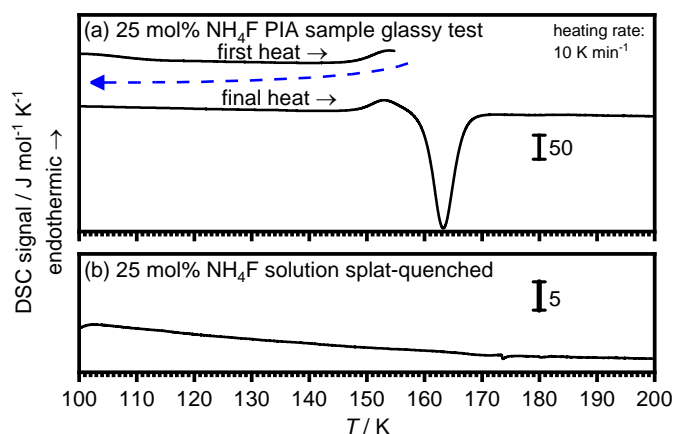


Figure 5.11: DSC thermograms associated with 25 mol% NH₄F compositions. (a) Test for reversibility of glassy character of the 25 mol% NH₄F PIA sample. (b) Splat-quenched 25 mol% NH₄F solid solution prepared at ambient pressure returned no signal. All scans were performed at 10 K min⁻¹, and the cooling scan in (a), which is not shown, was performed at 30 K min⁻¹.

It was found that the endothermic glass transition remained for the 25 mol% NH₄F PIA sample as shown in Figure 5.11(a). As the glassy character of the 25 mol% NH₄F PIA seemed to be inherent to the sample of this concentration, the effect of splat-quenching

5. Pressure-induced amorphisation of $\text{NH}_4\text{F-H}_2\text{O}$ mixtures

the starting solution at 77 K and at ambient pressure was also investigated by DSC to see if a glassy material could be obtained. Unfortunately, no meaningful features were seen (Figure 5.11(b)).

For DSCs of concentrations greater than 25 mol% NH_4F in Figure 5.10, the higher concentrations still produce a single exotherm, though these are decidedly broader and especially weak on reaching the known crystalline compositions at 75 and 100 mol% NH_4F . The reduction of intensity of these thermograms is put down to the presence of $\text{NH}_4\text{F I}$ in the sample which would not contribute at all to the signal.

5.5 Conclusions

The introduction of NH_4F to ice presents the opportunity to ‘switch off’ the influence of hydrogen disorder in the context of PIA, which is attributed to the derailment of ice IV formation, and instead results in HDA. NH_4F has been reported to form solid solutions over a large composition range^{3, 18, 26} (and this has additionally been confirmed in Chapter 3.1 of this thesis), hence the effect of positional disorder in the compressed solid solutions of the two species is likely to not suffer from the absolute hydrogen disorder of pure ice.

Heating 0 and 2.5 mol% NH_4F PIA samples showcases comparable trends, yet obvious differences are apparent in both the XRD peak maxima on heating (Figure 5.9(a)) and from the DSC data (Figure 5.10). From 6 mol% NH_4F and above, LDA-like structures are no longer apparent as far as can be determined by DSC (Figure 5.10), though from the heating XRD contour of the 9 mol% NH_4F PIA sample (Figure 5.8(b)), one could argue that, from the peak maxima data (Figure 5.9), some LDA-like character just about lingers. From the further XRD heating contour plots, LDA-like structures are absent at concentrations as low as 25 mol% NH_4F , instead a fully HDA-type (and microcrystalline-free) structure is seen. This further contradicts the supposed link between HDA and LDA having a structural relation with the proposed HDL and LDL. Surely if the two-liquid theory had some foundation, compositions as water-rich as 25 mol% NH_4F would still lead to the transformation of HDA- to LDA-type materials on heating at ambient pressure due to the expected dominant water-like character. Shephard *et al.* noted that HDA is composed of crystalline remnants of ice I after PIA;⁵ an analogous situation is seen for the product of pure $\text{NH}_4\text{F I}$ compressed solid which is composed of unconverted $\text{NH}_4\text{F I}$ (Figure 5.3(d)). The emergence of microcrystalline

5. Pressure-induced amorphisation of $\text{NH}_4\text{F-H}_2\text{O}$ mixtures

ice IV-like domains in the 35 and 50 mol% NH_4F PIA samples (Figure 5.7) also highlights that HDA must also be composed of ‘mid-converted’ ice IV structures. This further confirms that HDA is far closer in character to an ill-crystalline solid and not the supercooled liquid.

The influence of NH_4F in ice on PIA demonstrates that even in water-rich samples with concentrations as low as 35 mol% NH_4F , crystalline character begins to emerge with the derailment slowly ‘getting back on track’. This is apparent from XRD patterns collected at ~ 95 K (Figure 5.7). The crystallinity of the compressed solid solutions is fully realised by 75 mol% NH_4F and above – derailment no longer occurs.

The onset pressures determined from the initial pressure collapse traces in Figure 5.6(a) show that the pressures first drop into a basin on increasing quantities of NH_4F . On coming out of the basin at between 25 to 35 mol% NH_4F , with the onset pressures increasing, the compressed products begin to exhibit more crystallinity. Eventually the change in increase in onset pressure becomes more subtle until full crystallinity is attained.

An unexpected effect of NH_4F addition was also observed in the very prominent glass transition that occurs for the 25 mol% NH_4F structure with its associated $\Delta C_p = 28.5 \text{ J mol}^{-1} \text{ K}^{-1}$. The effect of NH_4F on the relaxation of the amorphous solid exceeds that for known crystalline ices.

Future work should investigate the short-range structure of the HDA-like structures that are formed from the NH_4F -ice solid solutions, which do not transform to an LDA-type structure on heating. This can be potentially ascertained by pair distribution functions or vibrational spectroscopy, to establish whether or not the HDA-like structures are indeed closer to high-density or low-density amorphous ice.

5.6 References

1. O. Mishima, L. D. Calvert and E. Whalley, *Nature*, 1984, **310**, 393-395.
2. J. J. Shephard and C. G. Salzmann, *J. Phys. Chem. Lett.*, 2016, **7**, 2281-2285.
3. C. G. Salzmann, *J. Chem. Phys.*, 2019, **150**, 060901.
4. G. Schubert, in *Treatise on Geophysics, 11 Volume Set (2nd Edition)*, Elsevier.
5. J. J. Shephard, S. Ling, G. C. Sosso, A. Michaelides, B. Slater and C. G. Salzmann, *J. Phys. Chem. Lett.*, 2017, **8**, 1645-1650.
6. S. Stølen, *Chemical thermodynamics of materials macroscopic and microscopic aspects / Svein Stolen, Tor Grande with a chapter on thermodynamics and materials modelling by Neil L. Allan, Hoboken, NJ : J. Wiley, Hoboken, NJ, 2004.*
7. T. Strässle, A. M. Saitta, S. Klotz and M. Braden, *Phys. Rev. Lett.*, 2004, **93**, 225901.
8. J. S. Tse, D. D. Klug, C. A. Tulk, I. Swainson, E. C. Svensson, C. K. Loong, V. Shpakov, V. R. Belosludov, R. V. Belosludov and Y. Kawazoe, *Nature*, 1999, **400**, 647-649.
9. N. Binggeli, N. R. Keskar and J. R. Chelikowsky, *Phys. Rev. B*, 1994, **49**, 3075-3081.
10. N. Choudhury and S. L. Chaplot, *Phys. Rev. B*, 2006, **73**, 11.
11. O. Mishima, *Nature*, 1996, **384**, 546-549.
12. D. Mariedahl, F. Perakis, A. Späh, H. Pathak, K. H. Kim, C. Benmore, A. Nilsson and K. Amann-Winkel, *Philos. Trans. R. Soc. A*, 2019, **377**, 20180164.
13. C. A. Tulk, J. J. Molaison, A. R. Makhlof, C. E. Manning and D. D. Klug, *Nature*, 2019, **569**, 542-545.
14. A. K. Soper, *J. Chem. Phys.*, 2019, **150**, 234503.
15. C. Bellin, A. Mafety, C. Narayana, P. Giura, G. Rousse, J.-P. Itié, A. Polian, A. M. Saitta and A. Shukla, *Phys. Rev. B*, 2017, **96**, 094110.
16. H. Engelhardt and B. Kamb, *J. Chem. Phys.*, 1981, **75**, 5887-5899.
17. A. Lawson, R. Roof, J. Jorgensen, B. Morosin and J. Schirber, *Acta Crystallogr. Sect. B: Struct. Sci.*, 1989, **45**, 212-218.
18. A. K. Lyashchenko and G. G. Malenkov, *J. Struct. Chem.*, 1969, **10**, 616-617.

5. Pressure-induced amorphisation of NH₄F-H₂O mixtures

19. W. M. Haynes, *CRC Handbook of Chemistry and Physics*, CRC Press Inc., 91st edn., 2010-2011.
20. C. G. Salzmann, E. Mayer and A. Hallbrucker, *Phys. Chem. Chem. Phys.*, 2004, **6**, 1269-1276.
21. C. G. Salzmann, P. G. Radaelli, B. Slater and J. L. Finney, *Phys. Chem. Chem. Phys.*, 2011, **13**, 18468-18480.
22. G. N. Ruiz, L. E. Bove, H. R. Corti and T. Loerting, *Phys. Chem. Chem. Phys.*, 2014, **16**, 18553-18562.
23. M. P. Longinotti, V. Fuentes-Landete, T. Loerting and H. R. Corti, *J. Chem. Phys.*, 2019, **151**, 064509.
24. A. Rosu-Finsen and C. G. Salzmann, *Chem. Sci.*, 2019, **10**, 515-523.
25. A. Rosu-Finsen, A. Amon, J. Armstrong, F. Fernandez-Alonso and C. G. Salzmann, *J. Phys. Chem. Lett.*, 2020, **11**, 1106-1111.
26. R. Brill and S. Zaromb, *Nature*, 1954, **173**, 316-317.

6 Phase behaviour of high-pressure NH_4F II and III at ambient pressure

6.1 Aims

To assess the behaviour of NH_4F II and NH_4F III when heated at ambient pressure, with a particular interest to prepare, from the heating of the high-pressure polymorphs, stacking faulted variants of NH_4F I, which have been mentioned by Nabar *et al.*¹ In Nabar and co-workers' study, it was stated that heating NH_4F II at ambient pressure led to the formation of stacking faulted NH_4F V, while the heating of NH_4F III at ambient pressure led to the formation of two successive stacking variants NH_4F VI and VII.¹

6.2 Preparation of NH_4F II and NH_4F III

The volume change plot for compression of NH_4F I at room temperature with a rate of 1 kN min^{-1} from ambient pressure up to 1.75 GPa is shown in Figure 6.1. One can appreciate the NH_4F I to NH_4F II phase transition which occurs sharply at ~ 0.4 GPa, and then the rather sluggish phase change of NH_4F II to NH_4F III at ~ 1.35 GPa.

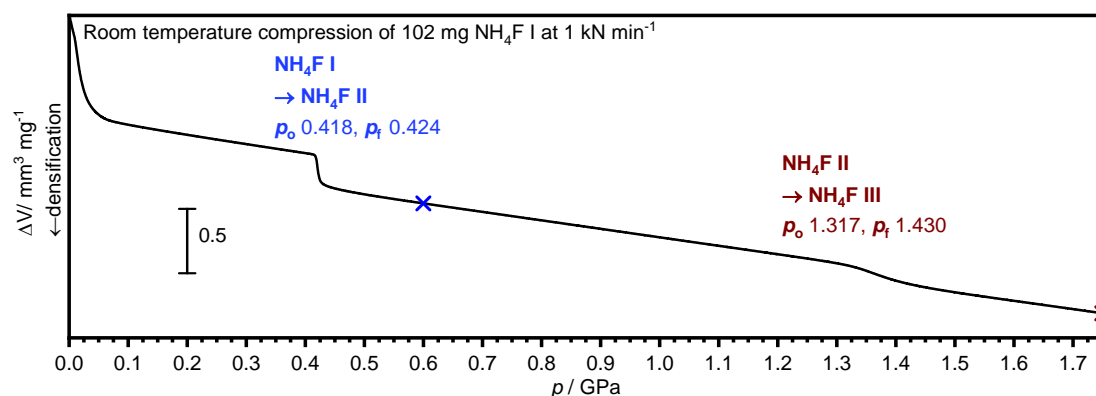


Figure 6.1: Change in volume observed on the compression of NH_4F I at room temperature up to 1.75 GPa at a rate of 1 kN min^{-1} . Onset pressures (p_o) and final pressures (p_f) of each phase transition are indicated. The phase change from NH_4F I to NH_4F II can be seen from the sharp volume drop that begins at ~ 0.41 GPa. The blue- and wine-coloured crosses show the pressures at which quenching took place for the retrieval of NH_4F II and NH_4F III respectively.

NH_4F II was prepared on the room temperature compression of NH_4F I up to 0.6 GPa, which was quenched with liquid nitrogen and then retrieved at ambient pressure. Ice IV (space group $R\bar{3}c$)² is isostructural with NH_4F II, yet it is not so easily prepared as it exists as a metastable phase amongst the many other phases of ice that also occur in the

6. Phase behaviour of high-pressure NH₄F II and III at ambient pressure

p - T region of the phase diagram.³⁻⁵ The only way it can be reproducibly prepared is *via* high-density amorphous ice which is heated at a slow rate of 0.4 K min⁻¹).^{3, 4}

Meanwhile NH₄F III was prepared from the room temperature compression of NH₄F I up to 1.75 GPa. In similarity to the NH₄F II sample, this was also quenched and then handled under liquid nitrogen.

Studies by Kuriakose *et al.* and Kaneda *et al.* discussed the preparation of the high-pressure NH₄F phases from the compression of NH₄F I at room temperature.^{6, 7} The pressures at which they observed both the NH₄F I to NH₄F II and NH₄F II to NH₄F III phase changes were at ~0.37 GPa and ~1.16 GPa respectively.⁶ The reason for the discrepancy could potentially arise from compression rates used or the particle size of the NH₄F I solid that was pressurised. Also, in this study, rates were not measured on the decompression of the compressed NH₄F sample at room temperature. Kaneda *et al.* rule out water composition as having an effect on the pressures of phase transition for both phase changes.⁷ Kasahara *et al.* also reported that on the compression of NH₄F I and the phase transition to NH₄F II, multiple elastic shocks were observed.⁸ Kuriakose *et al.* and Kaneda *et al.* did not observe such elastic shocks,^{6, 7} and neither were they observed here in this thesis.

Kaneda *et al.* investigated the effect of temperature on the phase transitions observed and concluded from compressions conducted at -25°C that the NH₄F II to NH₄F III transition was especially sluggish, so much so that in some cases it could not be visibly observed through volume changes of the sample.⁷ From Figure 6.1, it was also found that in comparison to the NH₄F I to NH₄F II transition, the NH₄F II to NH₄F III transition was particularly drawn out.

With regard to the volume changes associated with each transition, from Figure 6.1 it was determined that the volume of the sample decreases by 24% and 11% on the conversion of NH₄F I to NH₄F II and NH₄F II to NH₄F III respectively. Kaneda *et al.* observed similar volume changes of 24% and 9% for the same transitions.⁷ This represents the sample becoming increasingly dense through highly-efficient packing achieved from the interpenetration of networks of NH₄F which do not touch.^{9, 10} The 24% drop in volume is accomplished from the extremely effective restructuring mechanism called the Englehardt-Kamb collapse (which is also seen for ice *Ih* converting to ice IV^{10, 11} and discussed in more detail in Chapter 5).

6. Phase behaviour of high-pressure NH₄F II and III at ambient pressure

6.3 Observation of stacking disorder from heating NH₄F II

To investigate the stacking variant tentatively named NH₄F V by Nabar *et al.*¹ NH₄F II was heated at ambient pressure from 95 K up to 270 K at a rate of 10 K min⁻¹ and tracked with XRD (Figure 6.2). The retrieval of the particularly dense high-pressure sample involved the prising of the compressed sample from indium foils while under liquid nitrogen and proved to be quite difficult, which explains why there was some conversion back to NH₄F I. It can be seen that heating NH₄F II does indeed lead to the development of broad, asymmetric peaks, in particular in the angle range between 20° to 30° from even the lowest temperature of 100 K, which are linked to stacking disordered NH₄F I. At this temperature, the peaks at 15°, 33° and 34° are also weakly present (highlighted by the blue boxes), but are largely gone by 120 K. The stacking disordered material appears to be related to NH₄F I and will be referred to as NH₄F *Isd* from hereon. In Nabar *et al.*'s paper, it was stated that NH₄F II transformed to NH₄F V at 120 K¹ – this observation can loosely be tied with the disappearance of the peaks at 15°, 33° and 34°. Yet the appearance of stacking-disordered character from NH₄F *Isd* is undoubtedly apparent at lower temperatures.

The XRD data was analysed using MCDIFFaX to quantify the degree of cubic stacking, or cubicity (Φ_c), present at each temperature. The MCDIFFaX fits, alongside the experimental data of the heated NH₄F II from 100 K to 270 K and are shown in Figure 6.2 with their calculated cubicities. It can be seen at the lowest temperatures, the value of cubicity is at its largest at around 0.77, and heating the material leads to only a small drop in cubicity. This value of maximum cubicity is similar to what has been observed in other cubically-biased stacking disordered materials such as ice.^{12, 13} On the heating of the sample up to 200 K, the cubicity remains largely the same, centred at ~0.74. The NH₄F *Isd* persists on heating up until around 210 K where the emergence of the three trident peaks associated with the hexagonal phase appear.

6. Phase behaviour of high-pressure NH_4F II and III at ambient pressure

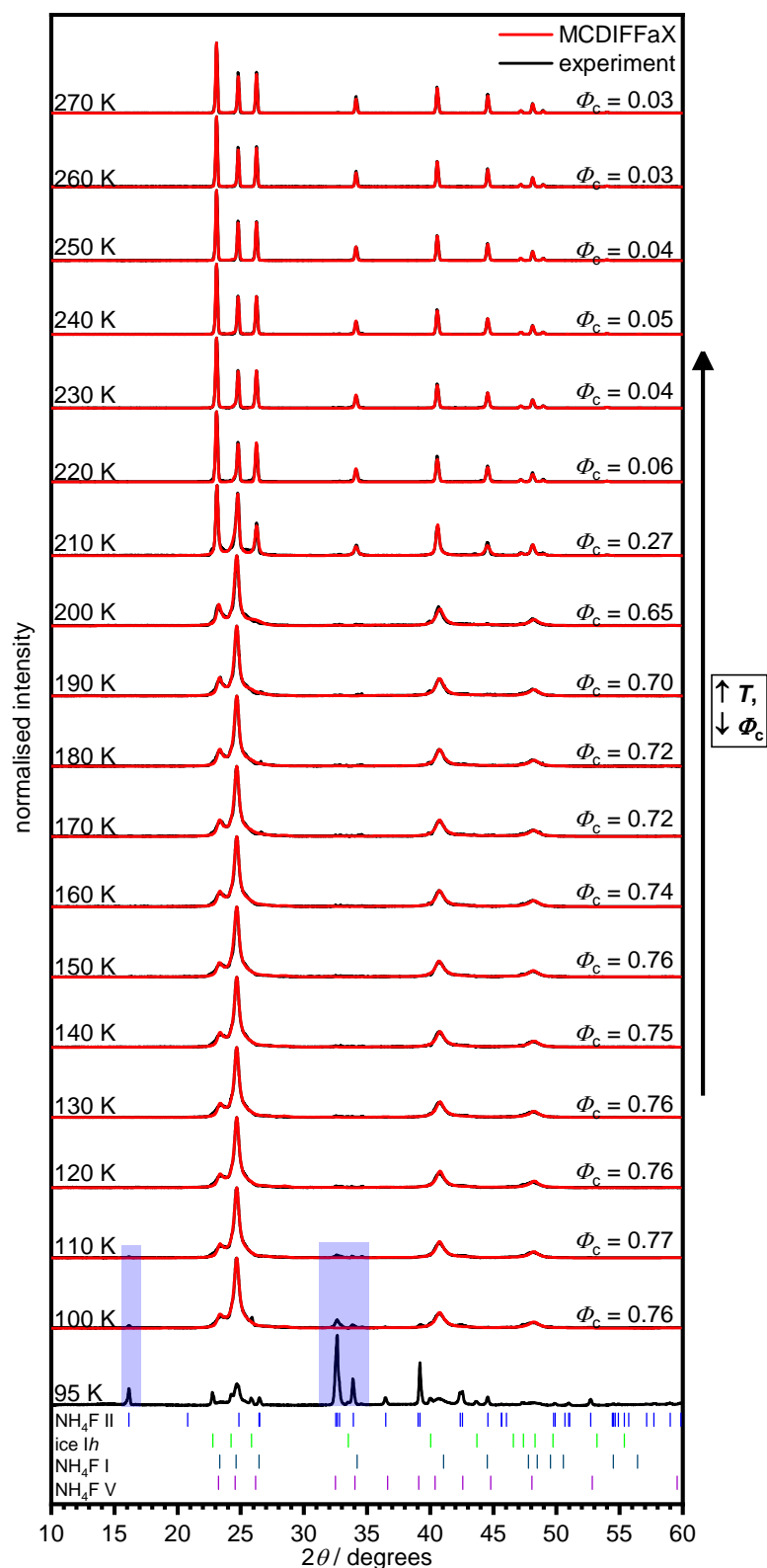


Figure 6.2: XRD patterns (black lines) and MCDIFFaX fits (red lines) of NH_4F II heated at 10 K min^{-1} at ambient pressure from 95 K to 270 K. The blue boxes highlight the characteristic NH_4F II peaks at 15° , 33° and 34° . The tickmarks of NH_4F V are those reported by Nabar and co-workers.¹ Increasing the temperature of the sample leads to the

6. Phase behaviour of high-pressure NH₄F II and III at ambient pressure

sharp drop in cubicity from 210 K and the formation of an almost entirely hexagonal sample from 220 K.

In contrast, Nabar *et al.* observe the transformation of their stacking disordered NH₄F to hexagonal NH₄F at 230 K.¹ Ice IV, the isostructural counterpart of NH₄F II, also transforms to its stacking disordered material – ice *Isd* – on heating at ambient pressure at ~140 K,⁴ before then transforming to hexagonal ice *Ih* at higher temperatures.² From 210 K to 220 K, the cubicity very sharply drops from 0.27 to 0.06 which represents near-complete hexagonal stacking, signalling the transformation to an almost fully hexagonal wurtzite structure, which is also apparent from the presence of the three ‘trident’ peaks centred at ~24.5°.

From the MCDIFFaX fits of the heated NH₄F II sample, information related to memory effects of stacking events was determined and plotted onto a stackogram (Figure 6.3). A stackogram plots Φ_{cc} against Φ_{hc} which describe the probability of a cubic stacking event followed by another cubic stacking event and the probability of a cubic stacking event after a hexagonal stacking respectively.¹² In essence, a stackogram illustrates dependencies of stacking events based on previous stacking and is characterised by four corners which describe physical mixtures; cubic NH₄F; alternating cubic and hexagonal stacking; and hexagonal NH₄F. A key feature is the black diagonal random stacking line which represents no memory effects.¹²

In Figure 6.3, starting from the lowest temperature samples up to 190 K, and in some similarity with the XRD patterns shown in Figure 6.2, there is no substantial change in values associated with the stacking probabilities, however they begin to experience a higher tendency to have hexagonal stacking followed by hexagonal stacking. From 200 K, the samples suddenly begin to resemble more of a physical mixture of cubic and hexagonal constituents, before reaching almost entirely hexagonal character, as evident from the data points sitting on the y axis. The small remaining 3% of cubic stacking prevents the highest temperature data point at 270 K from lying in the bottom left corner of the stackogram which represents a fully hexagonal NH₄F. Nevertheless, the 3% cubic stacking present in the highest temperature sample is likely within the margin of error of fully hexagonal NH₄F. The stacking probabilities reported for ices, as discussed by Malkin *et al.*, have not been seen to converge toward the physical mixture corner of the stackogram, but instead hover closer to the regions between the random stacking line and the hexagonal stacking corner.¹⁴

6. Phase behaviour of high-pressure NH_4F II and III at ambient pressure

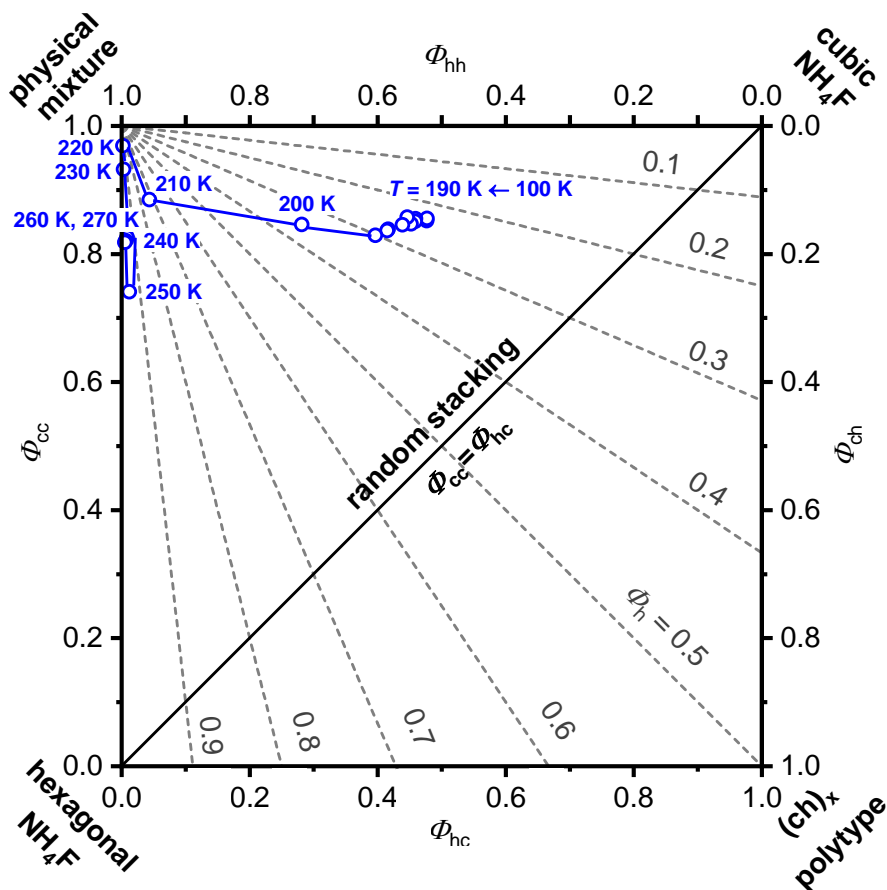


Figure 6.3: Stackogram illustrating stacking probabilities upon heating NH_4F II from 100 K to 270 K. On heating, stacking probabilities tend to have a higher tendency for hexagonal-hexagonal stacking until reaching the almost fully hexagonal product at 270 K.

Ice samples have been reported to stay in a given type of stacking sequence and not veer towards the $(\text{ch})_x$ polytype corner of the stackogram.^{11, 15} Diamond and AgI samples have also been seen to have stacking probabilities that remain above the random stacking of the stackogram.^{12, 13}

6.4 Observation of stacking disorder from heating NH_4F III

The sample of NH_4F III was also heated while observed under XRD, and similar to the heated NH_4F II, the resulting material containing NH_4F I *sd* was analysed using MCDIFFaX to ascertain the cubicities associated with the sample at each temperature, as demonstrated in Figure 6.4. The high symmetry of the NH_4F III sample at 95 K is expressed through its few peaks, as can be seen in its XRD pattern in Figure 6.4. NH_4F III is isostructural with ice VII (space group $Pn\bar{3}m$), which has an equally minimal XRD pattern. Ice VII forms from higher pressures of beyond 2 GPa at room temperature as a

6. Phase behaviour of high-pressure NH₄F II and III at ambient pressure

consequence of the extensive stability region of the less dense ice VI⁹ which does not share an NH₄F-based analogue.

From Figure 6.4, it can be seen that heating the high symmetry NH₄F III by just 5 K leads to a dramatic transformation of the structure as observed by XRD, which suddenly sees the development of peaks that are more attributable to NH₄F II – namely those at 15°, 33° and 34° (shown by the blue boxes). The presence of the peaks at 33° and 34° greatly hindered the possibility of fitting the XRD patterns with MCDIFFaX. Data that can be fit with MCDIFFaX first needs to be normalised to the characteristic stacking disordered peaks of NH₄F *Isd* centred at 24.5°, which on heating eventually mature into the hexagonal trident peaks. Nevertheless, even in the absence of MCDIFFaX fitting from 100 K to 200 K, stacking disorder is clearly present in the material, as well demonstrated by the broad asymmetric peaks centred at 24.5° which were also present for the heating of NH₄F II sample. Additionally, the material formed on heating of NH₄F III is certainly unique from the heated NH₄F II. It seems more accurate to describe the stacking disordered material obtained from the heating of NH₄F III as having: (i) NH₄F II character (seen in the blue-shaded boxes); (ii) NH₄F *Isd* similar to that seen on the heating of NH₄F II; and (iii) some more distinctive character which arises from three of lower symmetry planes centred at ~42° (highlighted by the orange box). It should be noted that the peaks in the orange-shaded region coincide with the second broad feature that is seen in LDA.¹⁶ It seems that the peaks centred at ~42° originate from the destruction of the highly intense 39° peak of the NH₄F III.

6. Phase behaviour of high-pressure NH_4F II and III at ambient pressure

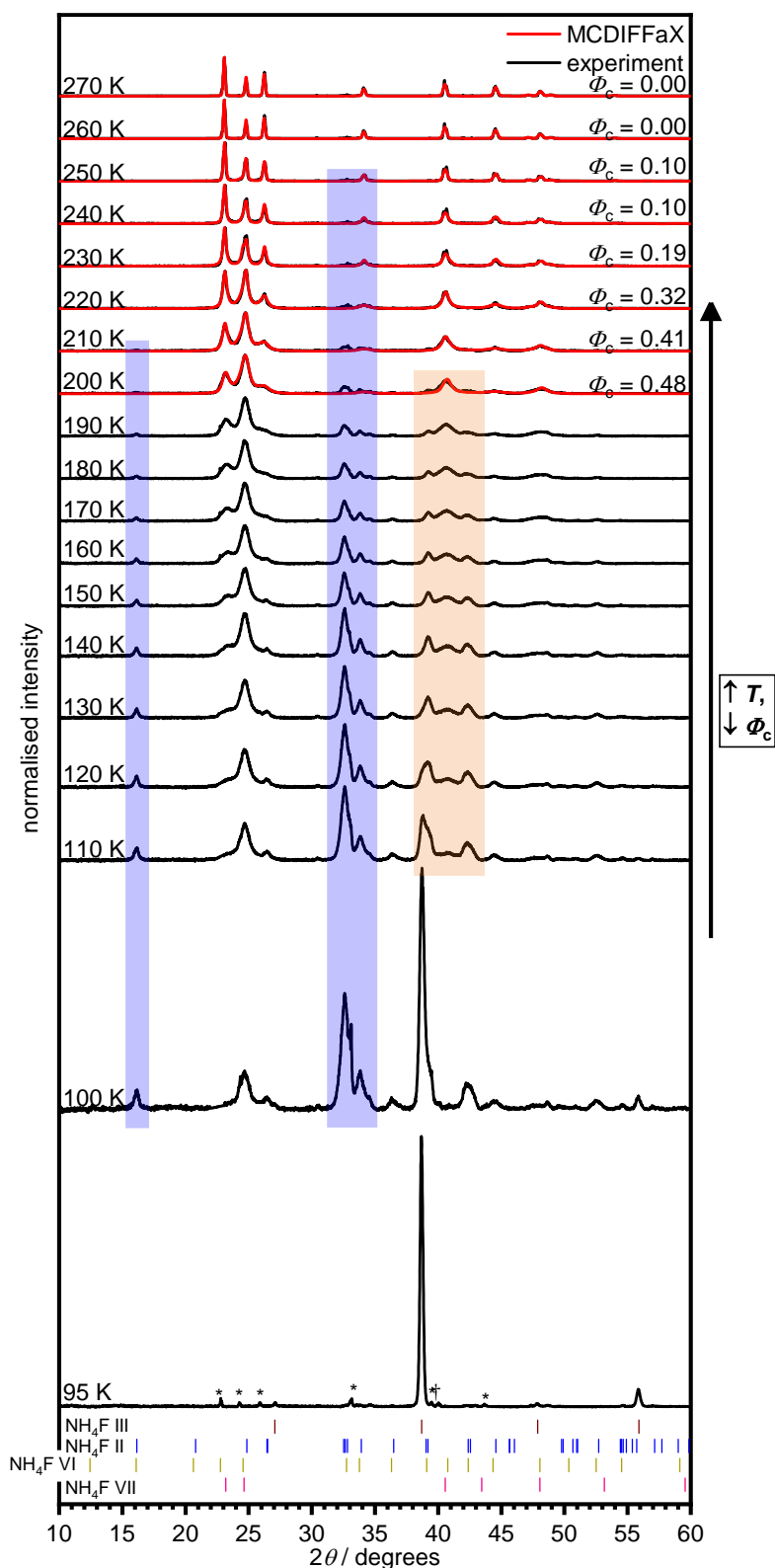


Figure 6.4: XRD patterns (black lines) and MCDIFFaX fits (red lines) of NH_4F III heated at 10 K min^{-1} at ambient pressure from 95 K to 270 K. Traces of ice Ih and NH_4F I in the pattern of NH_4F III at 95 K are shown by the asterisks and daggers respectively. The blue boxes highlight the characteristic NH_4F II peaks at 15° , 33° and 34° , and the orange box highlights the peaks centred at 42° which appear at the disappearance of the sharp NH_4F III peak at 39° . The tickmarks of NH_4F VI and NH_4F VII are those reported by Nabar and

6. Phase behaviour of high-pressure NH₄F II and III at ambient pressure

co-workers.¹ The tickmarks of NH₄F III were derived from the reduction of symmetry of an ice VII cell, as discussed in the introduction (Chapter 1.5.3). MCDIFFaX could only be performed from 200 K onwards, due to the overwhelming presence of additional peaks that were not included in the MCDIFFaX model for NH₄F Isd. Generally, increasing the temperature of the sample leads to the drop in cubicity.

Remarkably the two NH₄F II-type peaks at 33° and 34° persist with heating of the material, and are still present as traces even on reaching 270 K. Yet the FWHM of the peaks at 33° and 34° are 0.97° and 0.52° respectively, in comparison to the FWHMs of 0.50° and 0.45° for the pure NH₄F II in Figure 6.2. This implies that NH₄F II is present in some poorly crystalline form which has far larger grain or domain sizes than ‘regular’ NH₄F II. The case that arises from the heating of NH₄F III is undoubtedly more complex than that seen for the heating of NH₄F II. Nabar *et al.* stated that heating of NH₄F III led to the formation of stacking variant NH₄F VI at 120 K which transformed to NH₄F VII at 200 K before turning to hexagonal NH₄F at 230 K.¹ At a push, it could be stated that at 120 K, the XRD in Figure 6.4 sees the complete disappearance of the sharp peak at 39° associated with NH₄F III and that from 200 K the three broad peaks centred at ~42° (orange box) begin fading away. However, as is clearly apparent in Figure 6.4, the evolution of the warmed sample with increasing temperature demonstrates slow transformation processes where sharp structural transitions cannot be pinpointed. Thus, the definition of structures NH₄F VI and NH₄F VII by Nabar *et al.*¹ are seemingly redundant.

Ice VII is isostructural with NH₄F III, and on quenching to retrieve and study at ambient pressure, undergoes the transformation to its hydrogen-ordered counterpart – ice VIII – which still shares the same heavy-atom structural network of NH₄F III.^{11, 17, 18} The heating of ice VIII at ambient pressure leads to its transformation to low density amorphous ice (LDA) from ~110 K, which then transforms to ice Isd from ~140 K.¹⁶ It does appear that there could be some LDA-like character from the poorly crystalline peaks that are centred at ~42° and highlighted by the orange box, as well as in the trident region centred at 24.5°. Intriguingly Lin *et al.* recently observed that on heating of ice VIII, before the sample converted to LDA it actually could be seen to transform to HDA first.¹⁹ It is tempting to suggest that as NH₄F does not experience hydrogen disorder in the way that ice does, no amorphous features can be observed upon heating of NH₄F III.¹⁰ Indeed it has been noted that the presence of hydrogen disorder and hydrogen order in the entire H₂O system is thought to lead to its complexity.¹¹

6. Phase behaviour of high-pressure NH₄F II and III at ambient pressure

A stackogram was prepared with the stacking probability data from the heated NH₄F III, as shown in Figure 6.5.

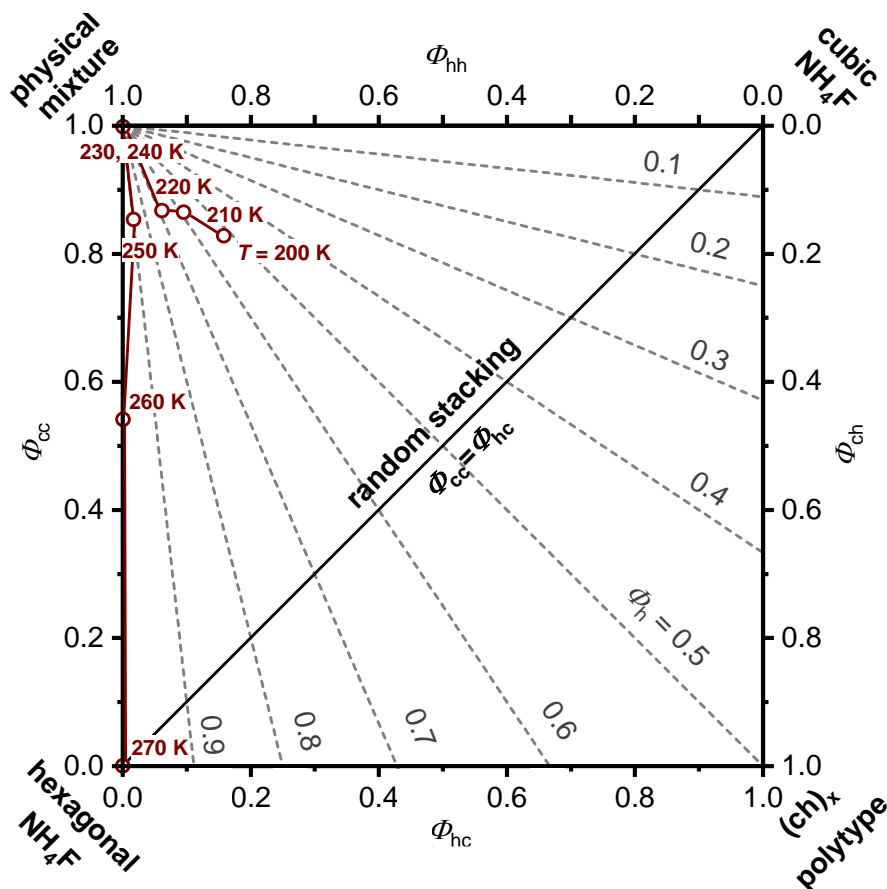


Figure 6.5: Stackogram illustrating stacking probabilities of the heated NH₄F III sample from 200 K up to 270 K. Similarly to the heated NH₄F II, heating the NH₄F III leads to a greater tendency for hexagonal-hexagonal stacking until a fully hexagonal product is achieved at 270 K.

As with the heated NH₄F II sample, all the stacking probabilities of the heated NH₄F III remain above the random stacking line. The data points all venture towards the physical mixture corner as the degree of cubic stacking begins dropping, before eventually fully transforming to hexagonal NH₄F at 270 K.

6.5 A comparison of cubicities of heated NH₄F II and NH₄F III

A summary plot of trends in cubicity of the heated high-pressure polymorphs as determined from the MCDIFFaX fits of the XRD data is shown below in Figure 6.6.

6. Phase behaviour of high-pressure NH_4F II and III at ambient pressure

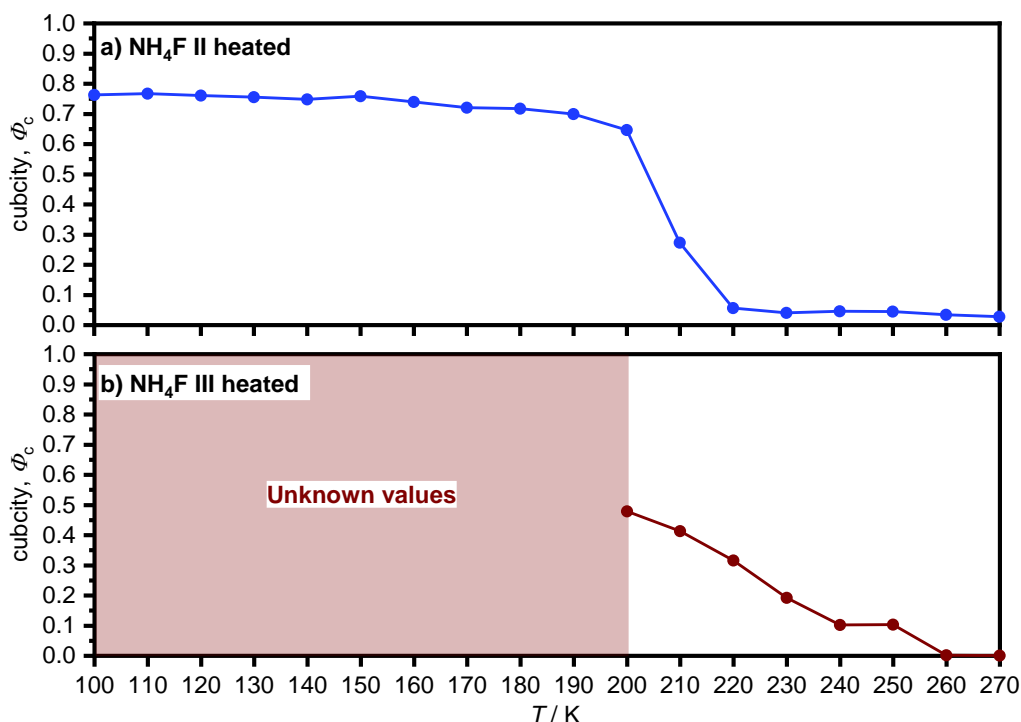


Figure 6.6: Cubicities of (a) heated NH_4F II and (b) heated NH_4F III at ambient pressure up to 270 K. For the heated NH_4F III in (b) fits could only be made from 200 K onwards, as previously discussed.

In the case of both phases, the higher the temperature of the sample the higher the tendency to have hexagonal stacking. Although there is limited data for the NH_4F III sample, an interesting observation can be made when comparing the cubicity trends of the two heated phases. For the warmed NH_4F II (Figure 6.6(a)), the transformation from the highest cubicity sample to the virtually fully hexagonal sample takes place over a 20 K temperature window. Yet in the instance of the heated NH_4F III (Figure 6.6(b)), from where the cubicity data starts at 200 K, the transformation towards the wurtzite structure is gradual and far ‘smoother’ than for the NH_4F II. It seems as though the warmed NH_4F III, which already contains NH_4F *Isd* features but has lingering NH_4F II character, needs to overcome a larger activation energy barrier to transform to hexagonal NH_4F I.

6.6 Calorimetric trends on heating the high-pressure phases of NH_4F

In order to gain some calorimetric insights into the heating of NH_4F II and III, samples were heated in the DSC with the same heating rate of 10 K min^{-1} , as is shown in Figure 6.7. In Figure 6.7(b), an isothermally compressed NH_4F sample – composed of 70 w% NH_4F II and 30 w% NH_4F I – in attempt to potentially observe pressure-induced amorphisation, as discussed in Chapter 5, is also shown for comparison.

6. Phase behaviour of high-pressure NH_4F II and III at ambient pressure

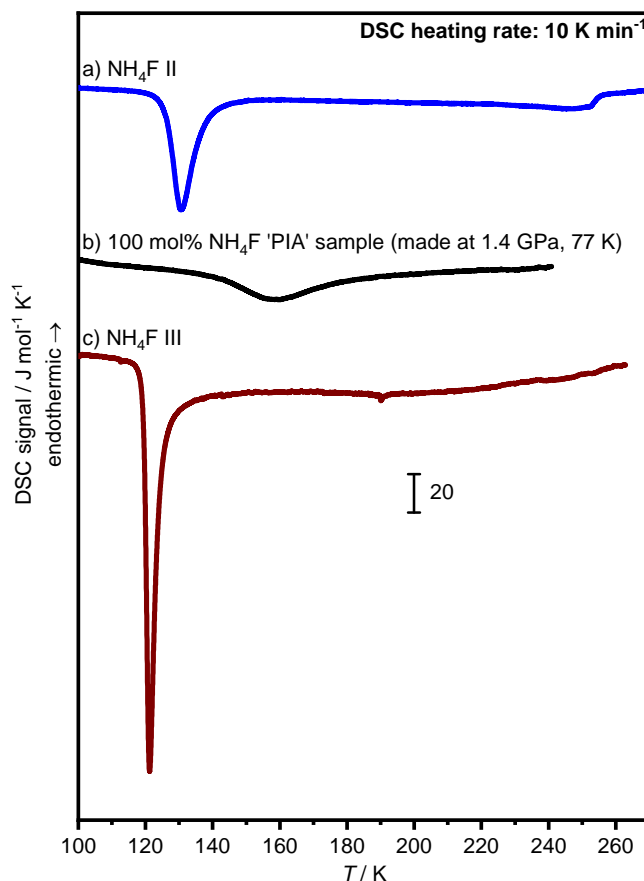


Figure 6.7: DSC scans of (a) NH_4F II made by compression to 0.6 GPa at room temperature and (b) an isothermally compressed sample of NH_4F I at 77 K to 1.4 GPa which was found to be 70 w% NH_4F II and 30 w% NH_4F I. (c) NH_4F III made by compression at room temperature to 1.75 GPa. All scans were performed at ambient pressure with a heating rate of 10 K min^{-1} .

In Figure 6.7(a), NH_4F II transforms to stacking disordered NH_4F I (NH_4F *Isd*) from an onset temperature of 125 K, and the exotherm relating to the transition was calculated as $(540.1 \pm 6.6) \text{ J mol}^{-1}$. The temperature of transition agrees with the XRD data in Figure 6.2 as this coincides with the disappearance of the peaks at 15° , 33° and 34° ; it is also in line with what Nabar *et al.*¹ observe. The next event, seen from $\sim 220 \text{ K}$ onwards, results from the NH_4F *Isd* transition to hexagonal NH_4F which can be inferred from the beginning of the downward slope which then increases at $\sim 250 \text{ K}$. Nabar *et al.*¹ stated that the conversion of NH_4F V to NH_4F I occurred at 230 K, which falls within the temperature boundaries indicated by the DSC in Figure 6.7(a), as well as the drop in cubicity seen in Figure 6.2.

Surprisingly, the sample of 70 w% NH_4F II (and 30 w% NH_4F I) that was prepared on the isothermal compression of NH_4F I at 77 K to 1.4 GPa (to demonstrate its null pressure-induced amorphisation) as shown in Figure 6.7(b), is markedly

6. Phase behaviour of high-pressure NH₄F II and III at ambient pressure

different in its appearance of a delayed exotherm which also had a smaller associated area of $(392.3 \pm 33.0) \text{ J mol}^{-1}$. The disparity between the two scans could result from the 'PIA' sample having fewer homogenous domains of NH₄F II due to Ostwald ripening which require more energy to restructure into the stacking disordered variant in a reverse EKC mechanism.

The thermogram for the warmed NH₄F III in Figure 6.7(c) has a sharp exotherm from 120 K which has an associated area of $(942.4 \pm 63.3) \text{ J mol}^{-1}$, which appears to coincide with the disappearance of the 39° peak of NH₄F III (Figure 6.4). A question remains as to what the exact nature of the transition results from, as features associated with poorly crystalline NH₄F II can be seen in the XRD patterns at temperatures until at least 200 K as evident from blue-shaded boxes in Figure 6.4. Hence, the exotherm cannot simply result from the transformation of NH₄F III to NH₄F *Isd*. Nevertheless, the ΔH associated with the NH₄F III transition is almost double the value seen for the heating of the NH₄F II to NH₄F *Isd*. Beyond the sharp exotherm at 120 K, on further heating from 130 K up to the maximum temperature, there appears to be a broad feature which is stretched out across the rest of the thermogram, which implies that slow low energy processes are taking place. This is reflected in the XRD patterns in Figure 6.4, which do not appear to have any sudden or drastic changes in their appearance from temperature step-to-temperature step, but instead see a slow evolution on heating. This must be in part due to the NH₄F II-like character (highlighted in the blue boxes in Figure 6.4), which is retained until at least 200 K. Further complexity of the processes occurring on heating is also reflected in the comparatively slow drop in cubicity for the warmed NH₄F III sample as is apparent in Figure 6.6(b), which is quite unlike the relatively abrupt transformation of the warmed NH₄F II to NH₄F *Isd* in Figure 6.6(a). This reflects the pronounced metastability in maintaining the extremely dense interpenetrating cubic networks that make up the NH₄F III structure which are also observed in ice VII/VIII.¹⁸ It should be noted that large error associated with the ΔH value of the NH₄F III likely originates from traces of indium foils also present in the DSC sample pans. This arose from the difficulty to prise all the sample from the indium foils used in the sample's preparation. The small traces of indium foils then led to the inaccurate mass determination of the DSC pans with sample.

6. Phase behaviour of high-pressure NH₄F II and III at ambient pressure

6.7 Conclusions

Consistent with the study conducted by Nabar and co-workers in 1969,¹ it has been demonstrated that NH₄F II (Figure 6.2) and NH₄F III (Figure 6.4) do convert to stacking faulted variants of NH₄F *Isd* on heating these samples at ambient pressure. In addition to reporting the appearance of stacking disordered phases of NH₄F, the cubicity and stacking probabilities associated with heating each sample is reported for the first time. It was determined that the cubicities of the NH₄F *Isd* samples never exceeded 77%, which is similar to ice *Isd*, which has been reported as having maximal cubicities of 78%.¹¹

Intriguingly, the stacking disordered forms of NH₄F I that emerge from the heating of NH₄F II (Figure 6.2) and NH₄F III (Figure 6.4) are structurally distinct as is apparent from the many additional observed peaks on heating NH₄F III, which are indicative of an especially complex structure. This is in some similarity with stacking disorder in ice, where depending on the starting material, the nature of the stacking disorder later observed can vary.²⁰ The warming of the NH₄F III sample has also provided a tantalising glimpse of what ice VII/VIII would potentially transform to on heating if it did not transform to LDA.^{16, 21}

In the case of the heated NH₄F III sample, the slow changes of the XRD pattern on heating (Figure 6.4) demonstrate especially sluggish dynamics – stacking disordered features are apparent from 100 K, yet many broad NH₄F II-type features (highlighted by the blue boxes) are also present up to at least 200 K. The transformation of NH₄F III to an NH₄F II-like sample which then finally converts to NH₄F I displays characteristics of the Ostwald step rule.²²

To complement the conclusions drawn regarding the temperatures at which NH₄F *Isd* exists, efforts should also be made to see how sensitive the observation of stacking disorder is to Raman spectroscopy. In the case of ice, stacking disorder is well observed from the width of the decoupled O–D vibrations.^{11, 20} In similarity with the situation for ice, partially deuterated high-pressure NH₄F would also be expected to be sensitive in the decoupled N–D region to stacking disorder.

Although the initial classification provided by Nabar *et al.*¹ may have been useful at the time of its publication, and indeed flagged up the presence of stacking faults in NH₄F, their research fails to illustrate the true structural nature of the stacking

6. Phase behaviour of high-pressure NH_4F II and III at ambient pressure

disorder that exists and should be replaced by the findings presented in this chapter. A shortcoming that does exist however is the lack of the assignment of some peaks that emerge on the heating of NH_4F III. The peaks observed would benefit from proper indexing, yet they are likely to derive from a combination of mixtures of NH_4F *Isd* and some poorly crystalline NH_4F II-like material. An understanding of what happens on the heating of NH_4F III may assist in appreciating the factors involved in the formation of stacking disorder in other materials which remain poorly understood.²³ It is likely that computational studies will be able to present invaluable insights into the structural reorientation dynamics that take place with respect to the phase transitions that occur on heating.

In light of the recent discovery of fully cubic ice I,^{24, 25} a question now remains as to whether a potentially fully cubic NH_4F I structure could be prepared. The preparation of cubic ice *via* the heating of ice XVII, as demonstrated by del Rosso *et al.*, was reliant upon the open structural framework it provided.²⁴ Komatsu *et al.* also have prepared ice Ic by evacuation of a hydrogen hydrate.²⁵ Considering the preparation routes developed so far for ice Ic, it appears that the potential preparation of cubic NH_4F I (NH_4F Ic) may be more tricky. This is due to the fact that NH_4F is known to inhibit clathrate hydrate formation.²⁶ Also NH_4F is restricted to only forming even-numbered rings due to its stoichiometry. However if NH_4F Ic can be prepared, it would be interesting to observe whether or not it will transform directly to its hexagonal counterpart on heating (as seen for ice)^{25, 27} or convert *via* a stacking disordered intermediate.²⁸

6. Phase behaviour of high-pressure NH₄F II and III at ambient pressure

6.8 References

1. M. A. Nabar, L. D. Calvert and E. Whalley, *J. Chem. Phys.*, 1969, **51**, 1353-1356.
2. C. G. Salzmann, P. G. Radaelli, B. Slater and J. L. Finney, *Phys. Chem. Chem. Phys.*, 2011, **13**, 18468-18480.
3. C. G. Salzmann, I. Kohl, T. Loerting, E. Mayer and A. Hallbrucker, *Can. J. Phys.*, 2003, **81**, 25-32.
4. C. G. Salzmann, E. Mayer and A. Hallbrucker, *Phys. Chem. Chem. Phys.*, 2004, **6**, 1269-1276.
5. C. Lobban, J. L. Finney and W. F. Kuhs, *Nature*, 1998, **391**, 268-270.
6. A. K. Kuriakose and E. Whalley, *J. Chem. Phys.*, 1968, **48**, 2025-2031.
7. R. Kaneda, S. Yamamoto and K. Nishibata, *Fixed points on the high-pressure scale identified by phase transitions in ammonium fluoride*, U.S. National Bureau of Standards, 1971.
8. J. Kasahara, I. Ohno and K. Iida, *J. Phys. Earth.*, 1971, **19**, 47-58.
9. N. H. Fletcher, *The Chemical Physics of Ice*, Cambridge University Press, Cambridge, 1970.
10. J. J. Shephard, S. Ling, G. C. Sosso, A. Michaelides, B. Slater and C. G. Salzmann, *J. Phys. Chem. Lett.*, 2017, **8**, 1645-1650.
11. C. G. Salzmann, *J. Chem. Phys.*, 2019, **150**, 060901.
12. C. G. Salzmann, B. J. Murray and J. J. Shephard, *Diamond Relat. Mater.*, 2015, **59**, 69-72.
13. R. L. Smith, M. Vickers, M. Rosillo-Lopez and C. G. Salzmann, *Crystal Growth & Design*, 2019, **19**, 2131-2138.
14. T. L. Malkin, B. J. Murray, C. G. Salzmann, V. Molinero, S. J. Pickering and T. F. Whale, *Phys. Chem. Chem. Phys.*, 2015, **17**, 60-76.
15. B. J. Murray, T. L. Malkin and C. G. Salzmann, *J. Atmos. Sol.-Terr. Phys.*, 2015, **127**, 78-82.
16. J. J. Shephard, S. Klotz, M. Vickers and C. G. Salzmann, *J. Chem. Phys.*, 2016, **144**, 204502.
17. C. G. Salzmann, Z. Sharif, C. L. Bull, S. T. Bramwell, A. Rosu-Finsen and N. P. Funnell, *J. Phys. Chem. C*, 2019, **123**, 16486-16492.

6. Phase behaviour of high-pressure NH₄F II and III at ambient pressure

18. W. F. Kuhs, J. L. Finney, C. Vettier and D. V. Bliss, *J. Chem. Phys.*, 1984, **81**, 3612-3623.
19. C. Lin, X. Liu, X. Yong, J. S. Tse, J. S. Smith, N. J. English, B. Wang, M. Li, W. Yang and H.-K. Mao, *Proceedings of the National Academy of Sciences*, 2020, **117**, 15437-15442.
20. T. H. G. Carr, J. J. Shephard and C. G. Salzmann, *J. Phys. Chem. Lett*, 2014, **5**, 2469-2473.
21. S. Klotz, J. M. Besson, G. Hamel, R. J. Nelmes, J. S. Loveday and W. G. Marshall, *Nature*, 1999, **398**, 681-684.
22. R. A. Van Santen, *The Journal of Physical Chemistry*, 1984, **88**, 5768-5769.
23. W. F. Kuhs, C. Sippel, A. Falenty and T. C. Hansen, *PNAS*, 2012, **109**, 21259-21264.
24. L. del Rosso, M. Celli, F. Grazzi, M. Catti, T. C. Hansen, A. D. Fortes and L. Ulivi, *Nat. Mater.*, 2020, DOI: 10.1038/s41563-020-0606-y.
25. K. Komatsu, S. Machida, F. Noritake, T. Hattori, A. Sano-Furukawa, R. Yamane, K. Yamashita and H. Kagi, *Nat. Commun.*, 2020, **11**, 464.
26. S. Park, D. Lim, Y. Seo and H. Lee, *Chem. Commun.*, 2015, **51**, 8761-8764.
27. L. Del Rosso, M. Celli and L. Ulivi, *Nat. Commun.*, 2016, **7**, 13394.
28. C. G. Salzmann and B. J. Murray, *Nat. Mater.*, 2020, **19**, 586-587.

7 HCl-doped ices

7.1 The removal of residual hydrogen disorder in ice IX

7.1.1 Introduction

Ice IX is the hydrogen-ordered counterpart of ice III and is known to exist in the pressure region between 0.2 to 0.5 GPa.¹ Ice III has an extremely small region of stability,² which means that for much of the p - T range it can exist in, ice II preferentially forms due to its comparatively lower Gibbs free energy.³ This was previously discussed in detail in introduction of Chapter 4.1. Interestingly the hydrogen-ordered/disordered pair share the same space group symmetry ($P4_12_12$) and are composed of four-fold spirals which are chiral.⁴ The silica phase – Keatite⁵⁻⁷ – is also isostructural with ices III/IX. The structure of ice III is shown below in Figure 7.1.¹

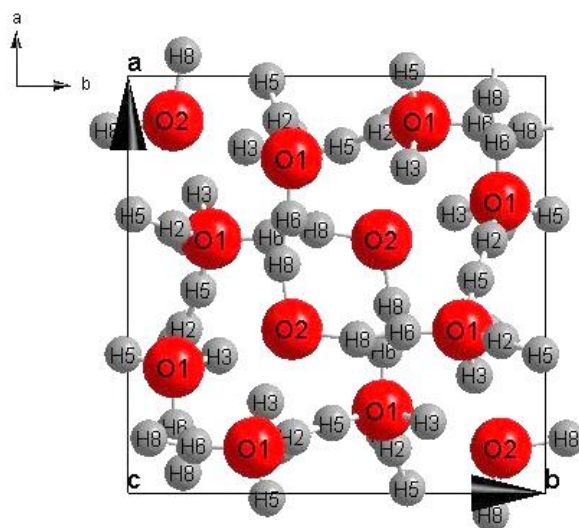


Figure 7.1: Ice III as viewed along its c-axis. Oxygen and hydrogen atoms are depicted by red and grey atoms respectively. The bonds between oxygen and hydrogen assume that the hydrogens have occupancies of 0.5 which describes a hydrogen-disordered state.

On cooling ice III under pressure, a small negative change in volume is observed when the structure transforms to ice IX; this can be identified by tracking changes in lattice parameter during neutron diffraction.⁸ However, the change is so slight that initially ice IX was also assigned as ice III as it had been deemed that no significant structural changes had taken place.⁹ Additionally, no changes in the level of hydrogen order could be elicited from infrared spectroscopy of the ice at 77 K.⁹ Eventually, ices III and IX were distinguished from each other *via* dielectric measurements¹⁰ and through the change in slope in the equilibrium line from ices I-III, at which point changes in volume

along the equilibrium line at different temperatures are minimal.⁹ This was determined from the Clausius-Clapeyron equation³ for the gradient of the phase boundary: $\frac{dp}{dT} = \frac{\Delta S}{\Delta V}$.

Following the I-III boundary from ~250 K down to ~210 K leads to a change in entropy of ~0.43 R, which is in the correct order of magnitude for a disorder-to-order transition, as dictated by Pauling's entropy of $R \ln \frac{3}{2}$.¹¹ *In-situ* neutron diffraction performed by Lobban *et al.* has subsequently confirmed that ice III is partially hydrogen-disordered in its relatively small region of stability.² Hydrogen ordering was found to vary slightly as a function of pressure and temperature.^{2, 12} For instance, Lobban *et al.* determined that at 2.5 kbar and 240 K, the ordering parameters (which have been previously discussed in detail Chapter 1.2.1) α and β were 0.35 and 0.49, while at 3.0 kbar and 250 K they were 0.36 and 0.53 respectively.²

Questions were raised about the degree of hydrogen ordering in ice IX by La Placa *et al.*¹ In his work 'On a nearly proton-ordered structure for ice IX', it was proposed that ~4% deuterium disorder was present in ice IX.¹ Based on neutron diffraction data, La Placa was able to describe the ordering within ice IX in terms of ordering parameters α and β . These are summarised in Table 7.1.

Table 7.1: Ice III fractional occupancies of atoms within the unit cell as defined by their ordering parameters. Adapted from Ref. 2

| Atom label | Occupancy | Bonded to |
|------------|--------------|-----------|
| O(1) | 1 | - |
| O(2) | 1 | - |
| D(3) | α | O(1) |
| D(4) | β | O(1) |
| D(5) | $1 - \beta$ | O(1) |
| D(6) | $1 - \alpha$ | O(1) |
| D(7) | $1 - \alpha$ | O(2) |
| D(8) | α | O(2) |

La Placa proposed four possible structural models of ice IX (structures A-D, Figure 2) which can be differentiated by their ordering parameters.¹ It was determined that structure D was the experimentally observed structure.¹

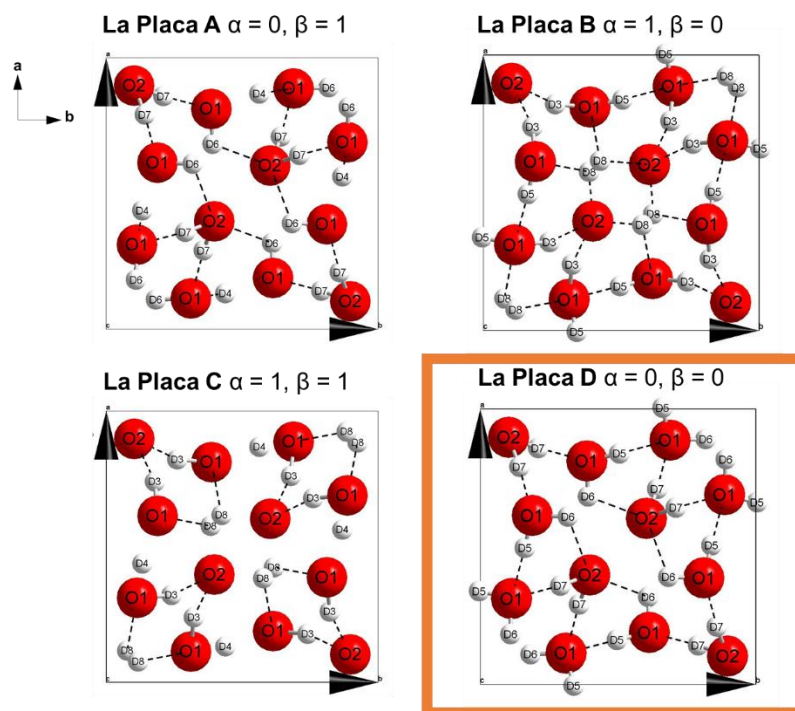


Figure 7.2: The unit cells of four ordered ice IX structures with their corresponding ordering parameters proposed by La Placa *et al.*¹ All structures belong to the $P4_212_1$ space group and are symmetry allowed with respect to hydrogen-ordering, but only structure D is observed. Full bonds are shown by the cylindrical lines, while hydrogen bonds are shown by black dashed lines. The hydrogen bonds link the previously interconnected oxygen units.

La Placa prepared the ice IX by first growing ice III crystals at 0.3 GPa and then pressure-quenching to 77 K in ~ 10 seconds. Here it was proposed that the retention of disorder could result from the quenching. Crucially, it seems that the procedure of pressure-quenching was utilised to prevent the transformation of ice III to ice II, which had proved to be a common challenge and still remains so.⁹ This is a consequence of ice IX largely existing in the stability field of ice II.^{3, 13}

The energies associated with the transformation of various high pressure phases of ice from low to higher temperatures was explored by Handa *et al.* who prepared ice IX *via* ice III that had been pressure-quenched at 0.4 GPa.¹⁴ By using both their calorimetric experimental results and theoretical calculations, they determined that the ice IX they had prepared did not possess any degree of hydrogen disorder. However, it is important to note that the ice IX sample was heated in the calorimeter at a rate of 10 K h^{-1} (1.67 K min^{-1}).¹⁴

A range of factors can determine whether ice IX is perceived as retaining hydrogen disorder or not. The characterisation method can be quite important. Diffraction is one of the best tools to assess hydrogen disorder, as it can provide the actual occupancies of the deuterium atoms which relate directly to hydrogen order.¹⁵ MacDowell *et al.* established a method to calculate configurational entropy based on the fractional occupancies of hydrogen atoms as found from diffraction.¹⁵

Meanwhile calorimetry is useful in providing information of hydrogen order with respect to enthalpies. Caution must be used here however, as heating rates will most likely influence whether or not order is seen. Recent papers have highlighted the unsuitable use of calorimetry in solely determining the presence of a phase. Primarily, work by Gasser *et al.* incorrectly stated that a new phase of ice related to ices VI/XV had been discovered on the basis of the presence of a low temperature endotherm seen in calorimetry.¹⁶ In response to this, Rosu-Finsen *et al.* highlighted the need to tread with caution if using calorimetry as the sole characterisation tool of a phase.^{17, 18} Rosu-Finsen and co-workers subsequently proved that this feature was simply a result of glass transitions occurring that related to a deep-glassy state.^{17, 18} The presence of the low temperature endotherm was found to be highly dependent on the pressure of formation, the rate of cooling of the sample while under pressure, and the rate at which the sample was heated or cooled at in the DSC at ambient pressure.¹⁷ With respect to Handa's paper,¹⁴ it is likely that as the heating rate used was comparatively slow, the signal produced was too weak to detect extremely small features. At a stretch it could also be suggested that the slow heating rate could have given the sample time to order while in the calorimeter; this may have produced a sample of ice IX which appeared more ordered than it initially was on preparation, and could have potentially given the illusion of full hydrogen order of the original ice IX sample.

Given the success of dopants in accessing hydrogen ordered phases such as ices XIII, XIV and XV,¹⁹⁻²¹ it is surprising that there has been no attempt to test their potential effect on ice IX. It seems likely that this is the case because the jury still seems to be out on whether ice IX is inherently fully hydrogen ordered or not.

7.1.2 Aims

This chapter firstly endeavours to assess levels of hydrogen order within pressure-quenched ice IX using differential scanning calorimetry. A variety of paths are explored

in an attempt to obtain full hydrogen order in the structure using both thermal control and HCl-doping. The reasoning behind the use of HCl-doping is that in many other high-pressure phases of ice which do not possess a sufficient number of intrinsic defects, HCl can provide extrinsic defects which can order phases on cooling.^{4, 19} The effect of ordering on the resulting Raman spectra of ice IX samples is also explored.

7.1.3 Calorimetric detection of hydrogen disorder

Pure H₂O ice IX prepared by isobaric heating of ice *Ih* at 0.3 GPa from 77 K to ~252 K – at which point it was quenched – was able to yield pure IX without any ice II impurity, as shown in Figure 7.3. Further details on the preparation of the ice are provided later in the chapter.

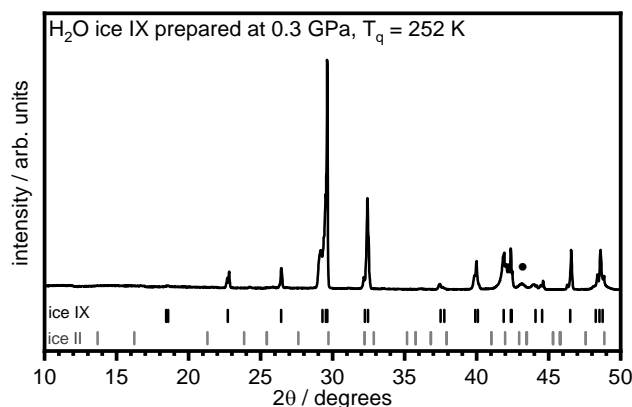


Figure 7.3: XRD of H₂O ice IX prepared at 0.3 GPa, quenched at 252 K. The pattern is phase pure and free of ice II, as shown by an absence of peaks in the known ice II peak positions. The black circle denotes a sample holder peak. The XRD was recorded at 95 K.

Heating pressure-quenched and pure H₂O ice IX at 10 K min⁻¹ from 90 K in a DSC produced features that pertain to residual disorder in ice IX. Prior to the well-documented ice IX to ice *Isd* transition ($T > \sim 150$ K), an additional exotherm with an onset temperature at ~ 120 K was also observed, as seen in scan (1a), Figure 7.4, and is highlighted by the grey shading.

To investigate the nature of this previously unreported exotherm, it was decided that samples of ice IX prepared *via* different methods – such as after thermal treatment and those prepared with dopants – should be compared. Their corresponding DSC thermograms are shown alongside that for the pure pressure-quenched H₂O ice IX in Figure 7.4.

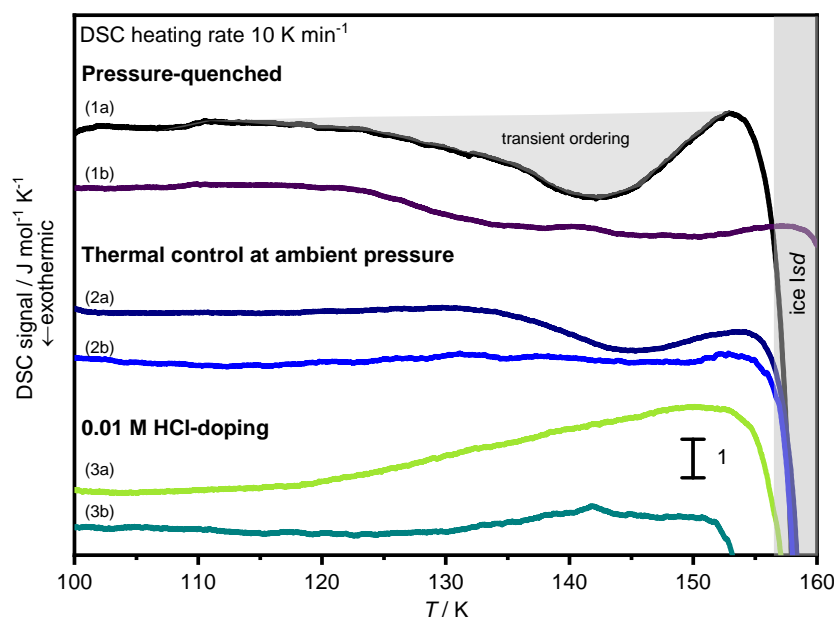


Figure 7.4: Thermograms of ice IX in the region prior to conversion to ice Isd. Thermograms in (1) show H_2O and D_2O samples that were pressure-quenched at 0.3 GPa in (1a) and (1b) respectively. Transient ordering in (1a) is highlighted by the grey-shaded region above the exotherm. Thermograms in (2) relate to H_2O pressure-quenched samples that were thermally treated while in the calorimeter. Scan (2a) comes from a sample that was heated to 145 K, before being cooled back to 90 K and then reheated. Thermal annealing was performed on (2b), where the sample was held at 120 K in the calorimeter for 90 minutes. (3) relates to 0.01 M HCl-doped ice IX samples, (3a) was from a sample prepared at 0.5 GPa, while (3b) was prepared at 0.3 GPa in a similar way to all the other samples.

The presence of the exotherm, $\Delta H = (27.9 \pm 9.8) \text{ J mol}^{-1}$, whose minimum is at ~ 145 K in scan (1a), suggests that additional ordering of the ice IX occurs on heating. Pressure-quenched D_2O ice IX in scan (1b) in Figure 7.4 unsurprisingly shows a similar exotherm on heating, albeit spread along a larger temperature range and with a lower area (as summarised in the upcoming Table 7.2). Similar transient ordering scenarios have been seen in other ices, such as in deep-glassy ice VI/XV.^{17, 22} When DCl-doped samples of ice VI/XV were prepared at 1.6 GPa and either quenched or slow-cooled, diffraction was able to show that the product was the hydrogen disordered ice VI. Intriguingly, on heating the ice VI sample it then transformed in a transient ordering process to the ordered ice XV, before disordering to ice VI on further heating.²³ The processes were also tracked by DSC which, on heating, showed an exotherm of the ice VI transiently ordering to ice XV, followed by an endotherm of ice XV disordering to ice VI.^{17, 24} The XRD pattern in Figure 7.3 of ice IX cannot attribute the product as being in a deep-glassy state. However the DSC scans (1a) and (1b) in Figure 7.4,

demonstrate transient ordering features that are characteristic of ‘deep-glassy’-like states. In a sense, the quenched H₂O and D₂O samples can be thought of as having some deep-glassy character, as on quenching under pressure, the ice exists in a metastable high free energy state, which on the heating of at ambient pressure is able to drop back down to the more favourable enthalpy provided along the dynamic equilibrium line (as discussed in Chapter 1.2.7).

Based on the high free energy of the quenched samples, it appears that H₂O (D₂O) pressure-quenched ice IX has a degree of disorder which is removed *via* transient ordering while heating in the DSC. So in scan (1a) of Figure 7.4, the sample at $T = 100$ K is more disordered than it is just before transforming to ice *Isd* at $T \sim 150$ K. Although not reported by calorimetry before, this supports what has been observed by La Placa *et al.*¹⁴ from neutron diffraction where they showed that ice IX is partially disordered.

In order to see if some additional ordering could be brought to the pressure-quenched ice IX, it would have been ideal to prepare a slow-cooled sample of ice IX. However, it is well known that unless ice III is cooled exceptionally fast while under pressure, it will always revert to the ice II structure, which has a far lower Gibbs free energy than ices III/IX for a larger temperature range.^{3, 10, 25}

7.1.4 Kinetic/thermal control of order

The next step was to test the reversibility of the transient ordering feature in scans (1a) and (1b) from Figure 7.4. The thermogram (2a) in Figure 7.4 shows a sample that was heated to 145 K (the trough of the exotherm in scan (1a)), rapidly cooled back to 90 K, and reheated past the ice *Isd* transition. To quantify the potential degree of disorder possessed by the ices in scans (1a), (1b) and (2a) in Figure 7.4, the enthalpy of each exotherm was considered and is shown in Table 7.2. The ice IX from scan (2a) Figure 7.4 was found to have a smaller area $\Delta H = (7.7 \pm 2.3) \text{ J mol}^{-1}$ than for the samples that were not thermally treated. This suggests that heating the sample to 145 K, before the usual analysis performed in scans (1a) and (1b) in Figure 7.4, led to a marginal degree of hydrogen ordering.

7. HCl-doped ices

Table 7.2: Spread of enthalpies relating to ice IX samples from scans (1a), (1b) and (2a) in Figure 7.4. Percentages of Pauling entropy are also shown bearing in mind the caveat mentioned in the text. The heating rate of the DSC in all cases was 10 K min⁻¹. The protiated ice IX appears to retain disorder on sample preparation with more ease than the other samples.

| Ice IX sample | Scan in Figure 7.4 | $\Delta H / \text{J mol}^{-1}$ | % of Pauling entropy |
|--|--------------------|--------------------------------|----------------------|
| H ₂ O ice IX | (1a) | 27.9 ± 9.8 | 6.1 ± 2.1 |
| D ₂ O ice IX | (1b) | 14.3 ± 3.6 | 3.3 ± 0.5 |
| H ₂ O ice IX \rightarrow 145 K \rightarrow 90 K | (2a) | 7.7 ± 2.3 | 1.6 ± 0.5 |

The final column of Table 7.2 also lists a fraction of the entropy of each exotherm divided by the Pauling entropy. A caveat should be placed here: given that the transient ordering feature originates from an irreversible process, the area of the transient ordering exotherm cannot strictly be defined using Pauling entropy. However, considering the transient ordering process in terms of Pauling entropy is a useful indicator to gauge the extent to which the ice IX is disordered. Fractions of Pauling entropy were determined by dividing the enthalpy²⁶ (C_p / temperature of each data point) of the area of each exotherm by the Pauling entropy ($3.38 \text{ J mol}^{-1} \text{ K}^{-1}$). With this caveat in mind, it was found that on average, there was the retention of ~6.1 and ~3.3% fraction of Pauling entropy from fully ordered protiated and deuterated ice IX respectively. Meanwhile, the sample that had been heated to 145 K, cooled and reheated (scan (2a), Figure 7.4), experienced a reduction in the exotherm area, corresponding to a 1.7% fraction of Pauling entropy. It can be seen that the thermally untreated H₂O samples of ice IX are inherently more disordered on pressure-quenching than for the D₂O samples. This is likely to be a result of kinetics usually being slower in deuterated analogues of ice due to isotopic effects.²⁷ The exotherm relating to scan (2a) in Figure 7.4 was found to have the smallest exothermic area – meaning the enthalpy associated with disorder within ice IX was the smallest of the three samples being considered.

To test whether thermal annealing would have an effect on the exotherm, another sample was annealed at ambient pressure in the DSC at 120 K for 90 minutes (scan (2b), Figure 7.4). The thermal annealing was successful in completely ordering the ice IX, as seen by the absence of an exotherm on heating the sample which altogether confirmed the exotherm to be an irreversible feature.

Hence, pressure-quenching ice III (~40 K min⁻¹) always ensures that some degree of disorder is inherent in the resultant ice IX structure. The only manner that this pure H₂O ice IX could achieve full ordering was on the ambient annealing of it for 90

minutes at 120 K. It is well known that slow-cooling ice III at slow rates while under pressure is unable to reliably yield ice IX as ice II is the more thermodynamically stable phase in much of the pressure-temperature region.⁹ Theoretically, a pressure-quenched H₂O ice IX sample held at 77 K or a similar temperature for a long time ($t \rightarrow \infty$) should exhibit full hydrogen order. More realistically, if a more sophisticated experimental setup could be used, which could selectively quench an ice III sample to 120 K, and hold the sample at this temperature isobarically, a pure ice IX sample with full hydrogen order could have potentially been isolated.

7.1.5 Acid-doping with 0.01 M HCl

In a final attempt to create a pressure-quenched sample with full order, samples of ice IX doped with 0.01 M HCl were prepared. As far as seems to be reported in the literature, it appears that ice IX with HCl-doping has not been made before. In many studies, HCl has been demonstrated as the most effective dopant at inducing hydrogen order,^{4, 19, 28} hence it was the ideal candidate for use as a hydrogen-ordering dopant. 0.01 M HCl ice IX was prepared in the identical manner to that of pure H₂O ice IX, and it produced a similar volume change plot on isobaric heating, as illustrated in Figure 7.5.

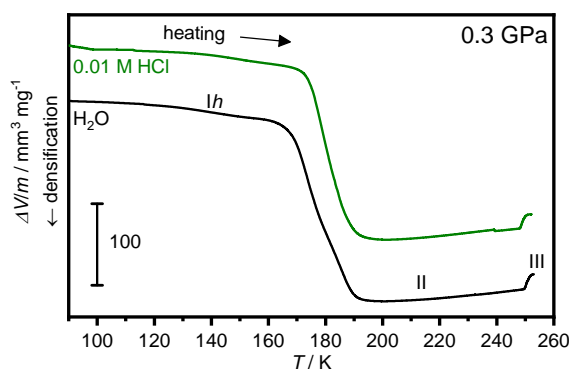


Figure 7.5: Volume change of both 0.01 M HCl (olive) and pure H₂O (black) ice heated at 0.3 GPa. The two ices share similar changes in volume with temperature. The phases known to occur for pure H₂O are demarcated above the H₂O volume-change line.

The method of preparation of pure H₂O ice IX was the isobaric heating at 0.3 GPa of ice Ih from 77 K to ~252 K. By assessing the volume change plot of sample preparation, one can appreciate the large temperature window in which ice II exists in comparison to ice III. Additionally, as ice III exists in a very narrow temperature window at which point it needs to be quenched, it becomes more likely that residual ice II could linger in the final sample.

7. HCl-doped ices

To isolate pure ice IX, a close eye had to be kept on the displacement change plot of the piston head in real-time. After the final step-wise change to ice III had occurred, and when only a linear change in displacement could be seen the sample was quenched. The ice III sample transformed to ice IX during the cooling process. This method was able to successfully yield H₂O ice IX as previously displayed in the XRD in Figure 7.3. This is replicated in Figure 7.6(a) for further comparative discussions alongside the corresponding pure H₂O ice IX thermograms shown by the black lines in Figure 7.6(d).

For the preparation of 0.01 M HCl-doped ice IX, the same logic similar to that of the pure H₂O counterpart was followed, whereby the sample was quenched only after a linear displacement of the piston head could be seen past ~250 K. This seemed rational given the similarity of the volume-change plots between pure H₂O ice being heated and HCl-doped ice being heated, as shown in Figure 7.5. Despite this, on all attempts to prepare HCl-doped ice IX at 0.3 GPa, phase-pure ice IX could not be isolated. To ensure that it was not from an unfortunate case of quenching the sample too early, the sample was made on seven separate occasions, yet this was to no avail. The presence of HCl appeared to somehow facilitate the retention of ice II. This can be seen clearly in the XRD trace (Figure 7.6(b)) and thermograms of the HCl-doped ice IX at 0.3 GPa shown in Figure 7.6(d) (olive lines). Figure 7.6(b) has additional peaks pertaining to ice II, highlighted by tickmarks, which are not seen for the pure H₂O analogue (Figure 7.6(a)) which is clearly void of ice II peaks. Furthermore, the olive thermograms in Figure 7.6(d) have additional endotherms which derive from the ice II to ice *Isd* transition (~175 K); these are not seen in the pure equivalent shown by the black line in Figure 7.6(d).

On one of many attempts to prepare ice IX with HCl-doping at 0.3 GPa, one thermogram appears to have been produced from a phase-pure region of sample (the particular pieces of ice taken must have contained only ice IX domains). The entire trace resembled that of a ‘clean’ ice IX trace (teal line, Figure 7.6(d)). No exothermic features could be seen from 120 to 140 K (this region is shown more clearly in scan (3b) of Figure 7.4), illustrating that HCl can induce full hydrogen ordering in ice IX.

Given the propensity of HCl to favour the presence of ice II at pressures of 0.3 GPa, a change of direction was taken, one that would cut ice II entirely out of the

equation (this is discussed later with respect to a volume-change plot). A different pressure regime of 0.5 GPa was adopted. Fortunately this was found to be effective in blocking ice II; the resulting XRD is shown in Figure 7.6(c) and the light green thermogram in Figure 7.6(d).

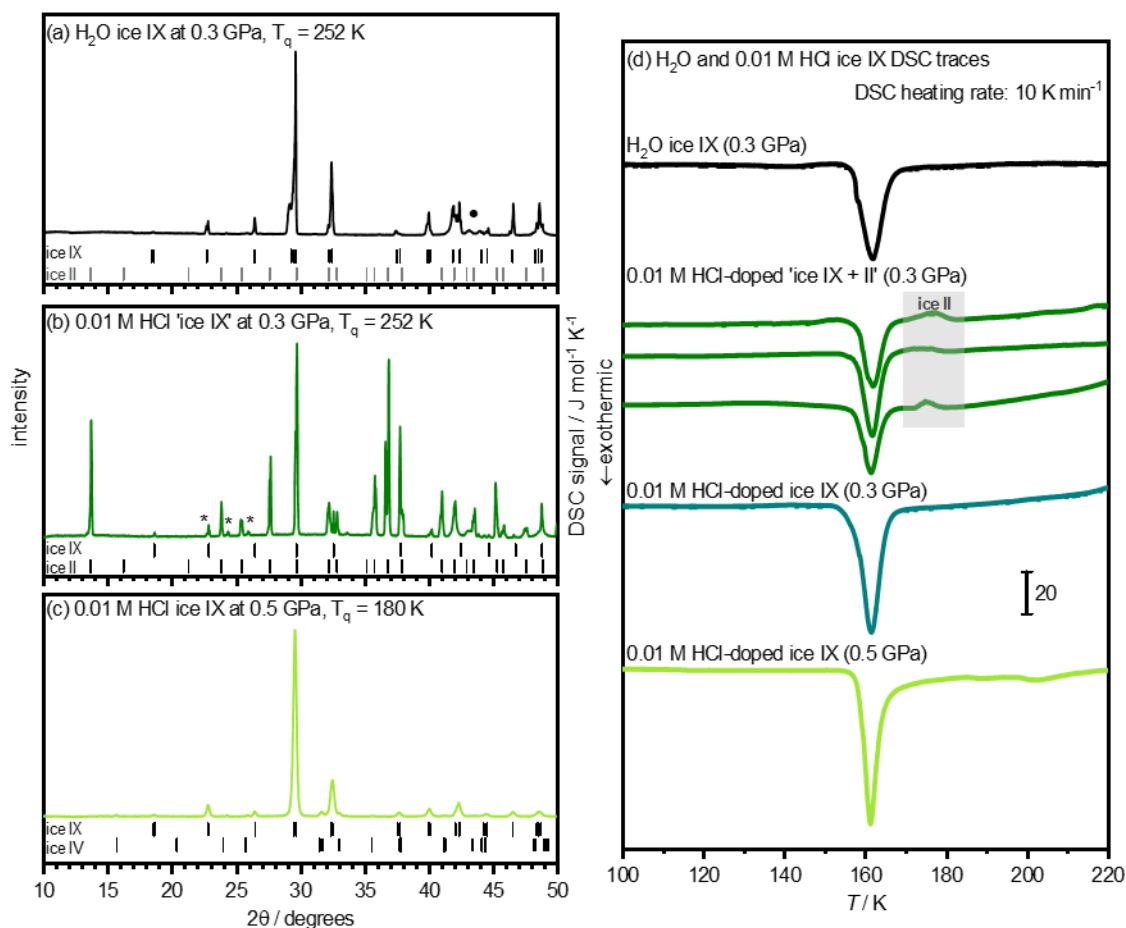


Figure 7.6: (a-c) XRDs and (d) thermograms of H_2O and HCl pressure-quenched ice IX. All XRD was carried out at 95 K at ambient pressure; all DSC was carried out at ambient pressure with a heating rate of 10 K min^{-1} . (a) shows phase-pure H_2O ice IX as demonstrated by tickmarks, the black circle denotes a sample holder peak; ice II ticks are also included as proof of its absence. (b) shows that 0.01 M HCl-doped sample prepared at 0.3 GPa which was a mixture of 84 w% ice II and 16 w% ice IX. Asterisks indicate an external ice Ih impurity. (c) shows that 0.01 M HCl ice IX prepared at 0.5 GPa could produce ice IX with a slight ice IV impurity. (d) shows corresponding thermograms. All phase-pure thermograms in (d), can be colour-matched with corresponding thermograms in Figure 7.4. The teal line shows a 'one-off' sample of 0.01 M HCl-doped ice IX sample made at 0.3 GPa which was phase pure ice as seen by the lack of an exotherm at ≈ 180 K.

At 0.5 GPa there exists a temperature region that ice III/IX can be isolated.²⁷ This region can be seen from the ΔV plot in Figure 7.7 of 0.01 M HCl ice heated isobarically at 0.5 GPa from 80 K. The ability to quench ice III/IX at 0.5 GPa was taken advantage of for a 0.01 M HCl-doped ice IX sample.

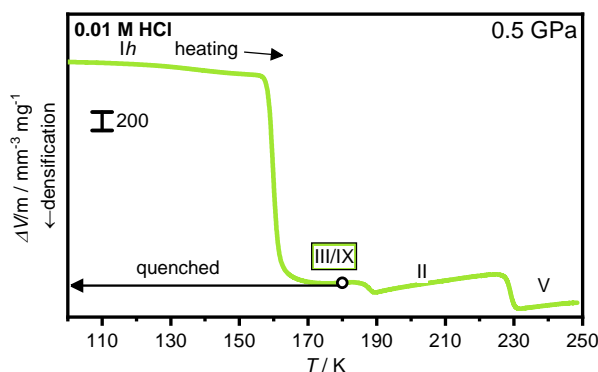


Figure 7.7: Volume change of the isobaric heating of 0.01 M HCl at 0.5 GPa. Ices III/IX, II and V are stable at various temperatures. Ice IX with HCl-doping was prepared via this route by quenching the ice at 180 K to avoid ice II being present in the sample.

The successfully produced 0.01 M HCl-doped ice IX sample made at 0.5 GPa was prepared by quenching at 180 K, as shown by the ΔV plot in Figure 7.7. XRD was performed on the sample (Figure 7.6(c)), followed by a quantitative analysis in GSAS which established that it contained ~ 4 w% ice IV. The thermogram of the HCl-doped ice IX (light green line, Figure 7.6(d)) was void of an exotherm relating to inherent partial hydrogen disorder in the region it had previously been observed from 120 to 145 K. Hence the resulting sample, as predicted, did not contain ice II as the sample was quenched before even reaching the ice II region of stability.²⁷ Regarding the presence of ice IV, it is known to be metastable in this region (as is apparent from the ice phase diagram),⁴ therefore it comes as no surprise that it was present in the 0.5 GPa sample. This quantity of ice IV is considered negligible in the thermogram. If, for some reason, it were to have an effect on the thermogram, a large glass transition would be observed at between 135 to 140 K (dependent upon heating rate)¹⁹ with a corresponding $\Delta C_p = (1.2 \pm 0.2) \text{ J mol}^{-1} \text{ K}^{-1}$.²⁹ Further heating of ice IV leads only to the formation of ice *Isd* at ~ 150 K,²⁹ and then the subsequent transition to ice *Ih*.²⁷ Thus a 0.01 M HCl-doped ice IX prepared at 0.5 GPa could be pressure-quenched while inherently possessing full hydrogen order.

Interestingly the mixed sample of 0.01 M HCl ice IX and ice II prepared at 0.3 GPa, whose thermograms are shown in Figure 7.6(d) (olive lines) are all distinct, especially in the ice II to ice *Isd* transition region, leading one to assume inhomogeneous domains are also present. This is also supported by the fact that the teal thermogram, free of ice II, is from the exact same sample prepared, yet this was free of ice II domains.

This could lead one to conclude that ice IX does not easily take in dopants or that ice II finds them very stabilising (at least in the case of HCl) in these experimental conditions. There are bound to be a range of factors which favour the formation of one phase of ice over another such as ring size, or perhaps that there are naturally already the ‘correct’ number of intrinsic defects in ice III/IX.

7.1.6 Spectroscopic consideration of inherent hydrogen disorder

Previous studies have investigated the Raman spectra of ices III/IX under pressure in their thermodynamic region of stability.^{25, 30} Minčeva-Šukarova *et al.* reported sharp shifts in frequencies on the conversion of ice IX to III at around 150 K.²⁵ In this current study, Raman spectroscopy was employed to detect the residual hydrogen disorder in ice IX, and in particular, the emphasis was to focus on the effect on the O–D decoupled stretch which is a well-known indicator for the degree of hydrogen disorder within a sample.³¹ An ice IX sample was analysed in a similar manner to the rapid heat and re-cool program (as shown in scan (2a), Figure 7.4). The sample was heated at temperatures from 78 K to 124 K in steps of 10 K at $\sim 10^{-2}$ bar before being cooled back to 78 K, at which point individual spectra were recorded. Higher temperatures were not ventured to because previous attempts to do so resulted in the sample always being transformed to ice *Isd*. This is because full temperature insulation does not exist with the current experimental setup used. Ideally, the aim was to heat the sample to 145 K – the trough of the exotherm – but, as explained above, the sample always transformed to ice *Isd* so this was not possible. Taking this into account, the sample heated to 124 K in the Raman apparatus is likely to have been almost 15 K higher than the reported temperature on the temperature sensor of the equipment.

The aim was to see if the decoupled O–D stretch became less broad to indicate potential hydrogen ordering on heating.³¹ Unfortunately, the resulting spectra did not display many differences with temperature, hence Figure 7.8 displays spectra recorded at the lowest (top line) and highest temperatures (middle line) as these would be expected to have the largest differences in peak width.

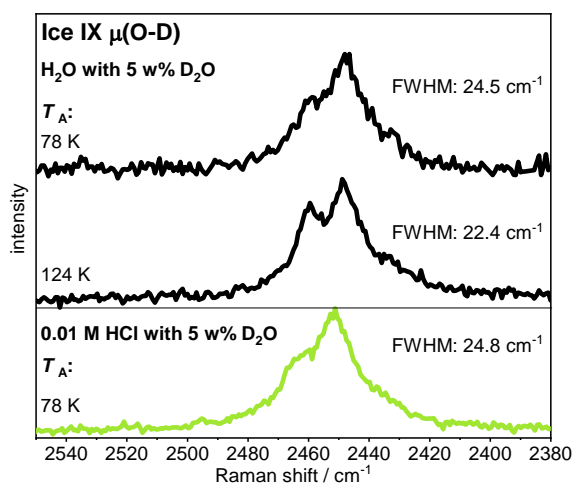


Figure 7.8: Raman spectra showing the decoupled O–D stretch of ice IX. T_A denotes the temperature the sample was annealed to; all spectra were collected at 78 K. The top and middle spectra show H_2O with 5 w% D_2O ice IX, and the bottom spectrum is of 0.01 M HCl with 5 w% D_2O ice IX (light green line). A slight reduction in FWHM can be seen between the heated sample (middle) and the unheated sample (bottom, light green line), suggesting that some transient ordering may have occurred on heating.

The black-lined spectra in Figure 7.8 are almost identical by eye, however the FWHM value of the H_2O ice IX sample at 78 K is 2 cm^{-1} greater than that of the 124 K spectrum, suggesting that some transient ordering may have occurred. If one assumes that due to the lack of temperature control in our Raman setup, the sample could have been potentially heated to $\sim 140\text{ K}$ ($= (124 + \sim 15)\text{ K}$), the Raman performed is analogous to the DSC belonging to the sample that was heated to 145 K before being rapidly cooled again (scan (2a), Figure 7.4). As shown in Table 7.2, this sample after heating had $\sim 1.7\%$ of Pauling entropy remaining *versus* the original sample which had $\sim 6.3\%$. Hence, it is likely that the spectra at the two temperatures do relate to two varying degrees of hydrogen order.

Figure 7.8 also shows a spectrum of an HCl-doped sample prepared at 0.5 GPa (light green line). This spectrum shows little visual difference with the H_2O samples prepared at 0.3 GPa. However, the FWHM value of the doped sample is almost the same as the unheated pure H_2O sample. This perhaps indicates the difficulty in using Raman to assess potential disorder given that one would have expected the FWHM of the H_2O sample at 124 K to be more similar to the HCl-doped sample.

La Placa *et al.* performed infrared spectroscopy on their ice IX sample but claimed to not see features to indicate any inherent hydrogen disorder.¹ They put their lack of observation in hydrogen disorder down to the fact that they only observed 4%

deuterium disorder, and that this minute difference would go undetected.¹ It should be noted that other authors, namely Minčeva-Šukarova *et al.*, have stressed that spectroscopic techniques are not always the best, compared to diffraction or calorimetry, to assess hydrogen disorder within ice.³²

7.1.7 Conclusions

From this chapter it seems that pressure-quenched H₂O ice IX does retain a small amount of hydrogen disorder on its formation. Although this is not the first time the notion of partial disorder within ice IX has been discussed, it is the first time that the heating rates used in calorimetry have enabled the detection of the inherent residual disorder, along with the transient ordering processes associated with the heating of pressure-quenched H₂O ice IX at ambient pressure. Yet, the inherent disorder is a property of ice IX, which has been displayed very thoroughly by neutron diffraction studies.¹ It is likely that the transient ordering which occurs reflects the fact that the pressure the ice is prepared at creates a metastable state which on heating at ambient pressure is able to drop in its enthalpy and produce the exotherm seen in similarity to characteristics seen in deep-glassy ice VI.^{4, 17, 22}

For the first time it has been demonstrated that trace quantities of HCl can be employed to assist with the complete hydrogen-ordering of pressure-quenched ice IX. But caution must be exercised with respect to the pressure used in the formation of fully hydrogen-ordered ice IX. HCl appears to stabilise ice II when samples are prepared at 0.3 GPa by influencing the kinetics of the phase transition to ice III, highlighting the competition between thermodynamic and kinetic processes. In the pressure region of 0.3 GPa, HCl somehow appears to make ices III/IX even more metastable than they already are. Nevertheless at 0.5 GPa, and by avoiding a large ice II stability region, HCl-doping does appear to be effective in ordering ice IX, as seen from the flat region of the thermograms just before ice IX transforms to ice *Isd* (scan (3a), Figure 7.4 and light green line, Figure 7.6(d)).

Ideally future work should focus on whether or not other dopants could also be used to order pressure-quenched ice IX especially at 0.3 GPa. This work also raises questions about how HCl stabilises ice II, and whether other dopants might somehow favour ice IX formation rather than forcing it to be metastable.

7. HCl-doped ices

Neutron diffraction should also be performed to determine the deuterium occupancies of pressure-quenched 0.01 M DCl-doped ice IX prepared at 0.5 GPa. In this instance, it would also be interesting to study ice III *in-situ* to see if dopants could also potentially induce full hydrogen disorder within its structure.

7.2 The metastability region of ice V/XIII at low temperatures

7.2.1 Introduction

Hydrogen-disordered ice V exists in a thermodynamic range of stability of 0.35 to 0.63 GPa and 210 to 270 K.³³ It exists with some partial hydrogen order within its region of stability.² Neutron diffraction by Lobban *et al.* highlighted that significant changes in the ordering of ice V occurs depending on the temperature and pressure ice V is held at.² Ultimately, more partial ordering in ice V can be achieved on increasing the pressure and decreasing the temperature of the sample.² No hydrogen-ordered counterpart for ice V was found for many years; heating ice V produced only a weak endotherm which could not be explicitly related to an ordering transition.^{14, 34} Also, for some time, hydrogen-ordered ice II was considered a potential ordered counterpart structure as the molar configurational entropy between the two phases was approximately that between a fully hydrogen-ordered and -disordered phase.^{3, 35, 36} In 2006, Salzmann *et al.* were able to prepare an ordered counterpart to ice V, which was named ice XIII.²⁰ Remarkably ice XIII could only be made from solutions of 0.01 M HCl, which provided the necessary number of extrinsic defects for the molecular orientation processes that occurred on ordering.²⁰

The unit cell of ice V, which contains 28 water molecules with four distinct oxygen atoms, is depicted in Figure 7.9.

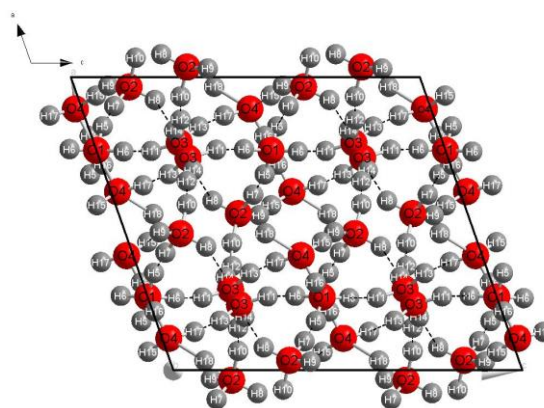


Figure 7.9. Unit cell projection along the *b* axis of monoclinic ice V. Oxygen and hydrogen are depicted by red and grey atoms respectively. Grey-cylindrical bonds represent the bonds between oxygen and hydrogen where hydrogens have occupancies equalling 0.5. The black-dotted lines show hydrogen bonds between the different molecular units.

7. HCl-doped ices

Data from neutron diffraction displayed the reduction of space group symmetry in ice V to XIII from $A2/a$ to $P2_1/a$ respectively as a result of the structure increasing in its complexity by now having seven distinct oxygen atoms.^{20, 27}

This complexity of ice V/XIII is reflected by the fact that the occupancies of the deuteriums of the ice V/XIII structure can be described using four different ordering parameters (Table 7.1). For comparison a similar structure such as ice III/IX requires only two ordering parameters to describe its five deuterium atoms.^{1, 2}

Table 7.3: Ice V fractional occupancies of atoms within the unit cell as defined by their ordering parameters.²

| Atom label | Occupancy | Bonded to |
|------------|--------------|-----------|
| O(1) | 1 | - |
| O(2) | 1 | - |
| O(3) | 1 | - |
| O(4) | 1 | - |
| D(5) | $1 - \alpha$ | O(1) |
| D(6) | α | O(1) |
| D(7) | α | O(2) |
| D(8) | β | O(2) |
| D(9) | γ | O(2) |
| D(10) | δ | O(2) |
| D(11) | $1 - \alpha$ | O(3) |
| D(12) | $1 - \delta$ | O(3) |
| D(13) | $1 - \gamma$ | O(3) |
| D(14) | $1 - \beta$ | O(3) |
| D(15) | $1 - \gamma$ | O(4) |
| D(16) | 0.5 | O(4) |
| D(17) | γ | O(4) |
| D(18) | 0.5 | O(4) |

From the refinement of fractional occupancies of deuterium sites, it was shown at 0.5 GPa that the transition temperatures were ~108 K on heating and ~117 K on cooling.³⁷ Changes in the a lattice constant were found to be an extremely sensitive indicator of the phase change from ice XIII to V and *vice versa* as shown in Figure 7.10.

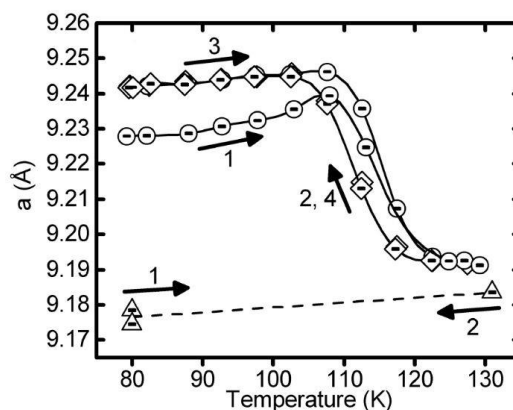


Figure 7.10: Variation in the a lattice parameter of HCl- and KOH-doped ice XIII/V samples calculated from neutron diffraction experiments undertaken at ILL and ISIS respectively. The KOH-doped samples indicated by triangles show little change in a . The numbers denote the steps carried out in order of heating (1), cooling (2) and the repeat of the sequence in (3) and (4). The circles and diamonds show heating and cooling of an HCl-doped sample. Sudden changes in the lattice constant a occur between 110 and 120 K, coinciding with the change in order detected from deuterium atom occupancies. From C. G. Salzmann, P. G. Radaelli, A. Hallbrucker, E. Mayer and J. L. Finney, *Science*, 2006, **311**, 1758.²⁰ Reprinted with permission from the American Association for the Advancement of Science.

Figure 7.10 shows that a changes in a reversible fashion on the heating and cooling of an HCl-doped ice XIII/V sample. It is also very clear that the phase transition occurs between 110 and 120 K as the lattice parameter experiences a sharp change as the sample dis/orders.²⁰

Retrieved samples of ice XIII studied at ambient pressure using DSC have also provided a wealth of information on the nature of hydrogen ordering of ice V/XIII samples. Heating ice XIII samples showed that an endotherm appeared at ~ 110 K on the transformation to ice V (the maximum value of the area associated with this was 217 J mol^{-1}), which on cooling produced an exotherm on the conversion back to ice XIII.²⁷ At the time of its discovery this was a significant finding given that other high-pressure phases of ice heated at ambient pressure (without annealing) always transformed to stacking disordered ice.^{14, 27} On the transition of ice XIII to ice V, it was calculated that there was a maximal change in configurational entropy of 66% in the most hydrogen-ordered sample of ice XIII.²⁷ Earlier neutron diffraction studies by Lobban *et al.* had elucidated that ice V displays a degree of partial order, a statement that is supported by the 66% entropy change, given that on cooling at ambient pressure ice XIII assumes full hydrogen order.² Another surprising finding was that ice XIII

which had been prepared by slow-cooling at ambient pressure in the DSC was more ordered than ice XIII that was prepared by slow-cooling under pressure.²⁷

On slow-heating and slow-cooling samples in the DSC (at rates at and below 5 K min⁻¹), two distinct features could be observed on the transition. It is thought that these separate features derive processes at two different hydrogen bonds,^{20, 27, 28, 37} however, specific details of this cannot be verified until a neutron diffraction study can take place whereby the occupancies of the deuteriums within a sample are properly examined on heat cycling.

Raman spectroscopy elegantly detected changes in hydrogen ordering on the heating and cooling of ice XIII prepared from solutions of 0.01 M HCl with 5 w% D₂O-doping. It was shown in three different spectral regions that tangible changes were apparent on the heating and cooling cycling of ice XIII. The region associated with the O–D decoupled frequencies centred around ~2450 cm⁻¹, showed a noticeable sharpening of peaks on cooling, which on heating to ice V amassed into a broad peak³⁸ representative of the many environments that would be expected in a hydrogen-disordered structure.

There have been keen efforts to examine the effects of other dopants in ordering ice V. In fact, prior to the discovery of HCl-doping in producing a hydrogen-ordered structure, attempts at KOH-doping were also made.³⁴ The logic behind this was that KOH-doping had proven to be successful in ordering ice Ih to form ice XI.³⁹ An endothermic feature was seen on heating of KOH-doped ice V, which was similar to, but more pronounced than what is seen on heating pure undoped ice V.³⁴ Unfortunately though, this feature observed on the heating of ice V was not a result of a complete hydrogen-ordering process.⁴⁰ Partial ordering was also detected in Raman spectroscopy on the cooling of KOH-doped ice V, but this also could not be fully accredited to complete hydrogen ordering.³²

Extensive calorimetric studies have been performed on ice V with hydrogen halide-doping and inorganic acid-doping.^{27, 28} The efficacy of each dopant was put down to several factors. In the case of acid dopants, factors which dictate their effectiveness are (a) their solubility in ice and (b) ability to dissociate in ice and create a mobile H₃O⁺ defect. For basic dopants a similar importance of solubility of dopants within the ice is also a key factor. However, a lack of quantitative information on

solubilities of these species in ice has made it difficult to draw strong conclusions regarding this.²⁸

The dopants which were found to be able to order ice V were HCl, HF and LiOH, whereas HClO₄, HBr, NaOH and KOH were found to be ineffective.²⁸ Initial work which focussed solely on HCl-, HF- and KOH-doped ice V to form ice XIII rationalised the superiority of the HCl dopant to KOH to the fact that the acid produced H₃O⁺ defects, while KOH was only able to form OH⁻ defects. HCl was determined to be more effective than HF and this was justified due to the higher acid strength of HCl.²⁷ Subsequent work by the same author has delved deeper into the reasons behind what dopants are effective or not by considering the entire family of dopants mentioned at the beginning of the paragraph.²⁸ Unexpectedly, LiOH was found to be an effective dopant, slightly turning the notion of OH⁻ defects being ineffective on its head. The case of HBr-doping also turned out to be almost bizarre; it could order ice VI, despite not being able to order ice V.²⁸

The relatively larger ionic radii of the species that did not order ice V are thought to have prevented them from solubilising within the ice.²⁸ This in particular explains why NaOH and KOH were found to be inadequate ordering agents compared to LiOH – the radii of the cations being 1.16, 1.52 and 0.88 Å respectively.²⁸ Overall, studies have firmly placed the best ordering agent of ice XIII to be HCl, which is found to be the most efficient at a molarity of 0.01 M, with HF and LiOH having similar abilities in being the next best dopants.^{27, 28} Ice V/XIII is currently the only known phase of ice to order with both acids and bases.²⁸

It is clear from this that a delicate interplay of different variables can tip the scales in favour of whether a dopant has the ability to hydrogen order or not. Nevertheless, further conclusions can only truly have a foundation in their claims if further computational studies are performed that assess defect mobility; additionally further experimental work needs to consider the solubilities of different bases in water and ice phases.^{27, 28}

A potential triple point of ices XIII, V and II was proposed on the basis of the extrapolation of calorimetric data of the ice XIII to ice V transition and by extending the phase boundary of ices V and II.²⁷ The triple point was estimated to occur at ~112 K at 1.3 GPa, and it is assumed that at pressures above this, ice XIII must be more stable

than ice II.²⁷ However so far this has not been tested experimentally, and no studies appear to shed light on the potential extended p - T regions ice XIII could exist at.

7.2.2 Aims

In this chapter the extended metastability region of ice XIII is considered. Firstly, the metastable region of ice V/XIII at low temperature is mapped up to elevated pressures of 1.6 GPa by measuring volume changes on the isobaric heating of ice V/XIII to VI/XV. Following this, metastable ice XIII prepared from solutions of 0.01 M HCl is studied by calorimetry to see the effects of (a) the pressure of ice preparation, and (b) the cooling rate of the sample while under pressure, on the resultant ordering in ice XIII. HCl is used as the dopant in this instance, given its superior ordering abilities over other acid and base dopants in literature.²⁸

7.2.3 Determining the low-temperature metastability region of ice V/XIII

The region of metastability of ice V/XIII remains uncharted territory. In order to inform the rest of the study, the region that ice V/XIII could exist in metastably needed to be explored. Volume-change (ΔV) plots in Figure 7.11 demonstrate how firstly (a) ice XIII was prepared at 0.5 GPa on the cooling of ice V at 250 K and secondly (b) how at set pressures the ice XIII was further compressed and heated until the volume change to ice VI/XV was observed. Figure 7.11(c) shows the resulting metastable ice V/XIII phase diagram determined from the ΔV plots in Figure 7.11(b).

In Figure 7.11(a), the well-known sequence of phase transitions on the isobaric heating of HCl-doped ice is shown.²⁷ Here, ice *I_h* transforms to ices III/IX, then ice II and finally ice V. The quenching of the ice V from 250 K to 77 K led to the formation of ice XIII. The low temperatures allow for a reduction in the entropy, which, with the presence of the HCl-dopant to catalyse molecular reorientation, leads to the hydrogen ordering of the ice.

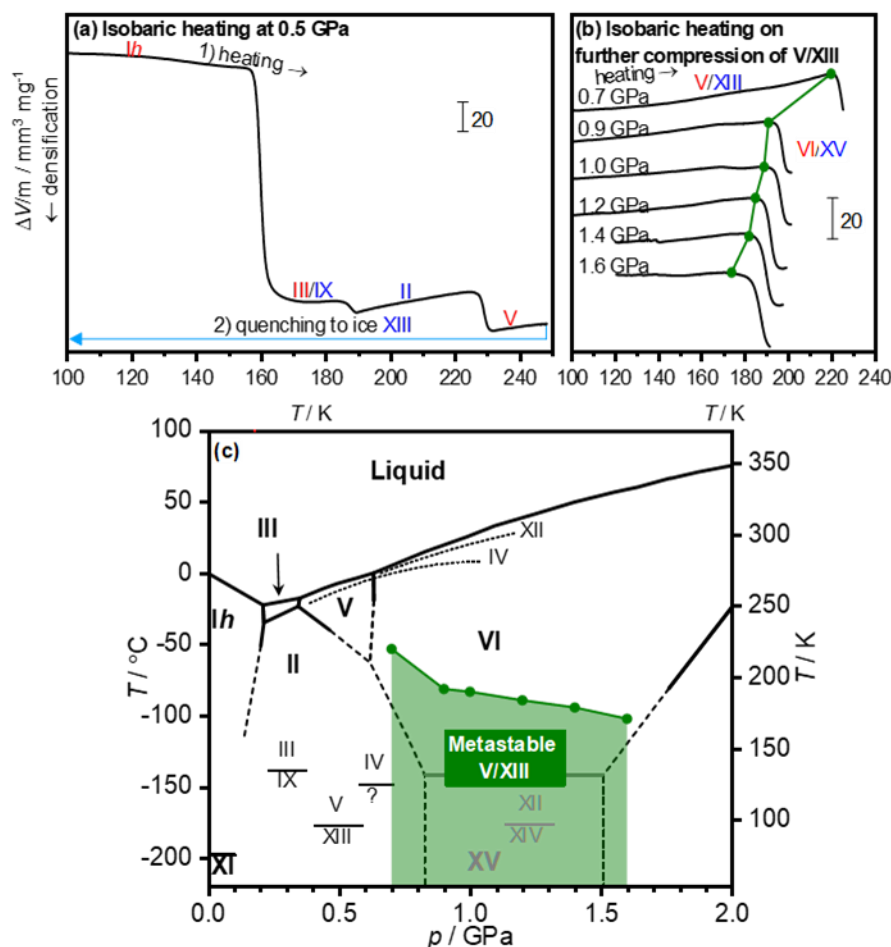


Figure 7.11: Procedure in mapping the metastability region of ice V/XIII. Changes in volume during the formation of (a) ice XIII from the quenching of ice V at 0.5 GPa, and (b) the volume changes on the heating of the ice XIII samples that had been further compressed. The olive line demarcates the V/XIII to VI/XV transition. (c) shows the ice phase diagram with the temperatures of phase transition between ice V/XIII to ice VI/XV overlaid as olive dots.

After the ice XIII was formed, it was further compressed and heated isobarically, as seen in the ΔV plots in Figure 7.11(b). Sharp volume drops occurred on the phase transition to ice VI/XV; it is from when the volume change began to decrease that the phase transition temperatures were taken – these are shown in the olive points on the ΔV plot. From the volume-change plots, a phase diagram to include the low temperature region of ice V/XIII was prepared and is shown in Figure 7.11(c). It includes the metastable phase boundary from pressures of 0.7 to 1.6 GPa, as determined from the plots in Figure 7.11(b).

From the ΔV plots shown in Figure 7.11(b), the change in volume of the sample on the heating of the ice XIII sample appears constant, implying that no potential phase change to ice V occurs. This is further confirmed by considering the first derivative of

the changes in volume, as shown in Figure 7.12, which shows data relating to the isobaric heating of ice XIII at 1.2 GPa.

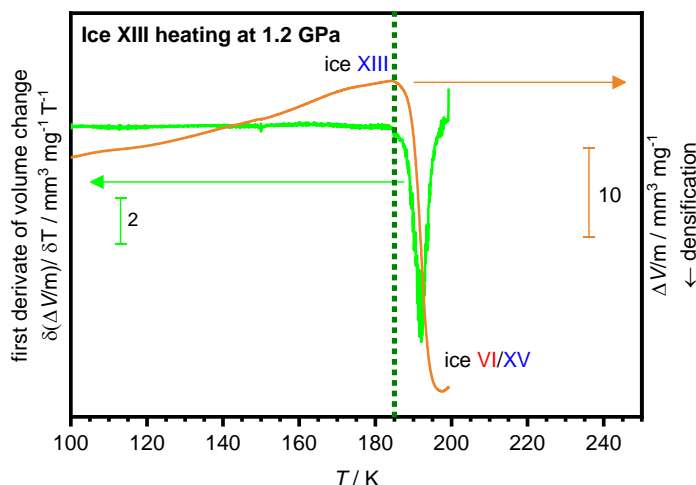


Figure 7.12: The first derivate of change in volume (green line) alongside its corresponding change in volume (orange line) of a metastable ice XIII sample during isobaric heating at an elevated pressure of 1.2 GPa. The dotted olive line indicates the phase change from ice XIII to ice VI/XV.

The first derivate (green line) remains close to horizontal until the sample transforms to ice VI/XV; this can also be well correlated to the orange line which shows the volume change of the sample. The confirmation of this was crucial to ensure that further analysis that was to have taken place would indeed be of an ice XIII, and not an ice VI, sample.

Following the mapping of the region, at select elevated pressures, samples of ice XIII were prepared in a similar manner to the route used to determine the p - T region of the metastable ice. The pressures and temperatures that these samples were cooled from varied depending on the pressure and the temperature of the determined phase boundary as shown in the phase diagram in Figure 7.11. Ices produced at pressures 0.7, 1.0 and 1.6 GPa were cooled from temperatures 200, 160 and 160 K respectively. The samples were prepared by cooling at both 2.5 K min^{-1} and $\sim 40 \text{ K min}^{-1}$ – referred to as slow-cooling and quenching – while still under pressure. It should also be noted that samples of ‘regular’ ice XIII were also prepared by slow-cooling and quenching ice V at 250 K while still at 0.5 GPa.

The aim of preparing samples with different cooling rates was to see how cooling rate would affect the subsequent hydrogen ordering within the samples and to also see how this was potentially affected by pressure.

However, to firstly verify that ice XIII was indeed being prepared *via* this experimental route, XRD was used to confirm the phase purity of the product (Figure 7.13).

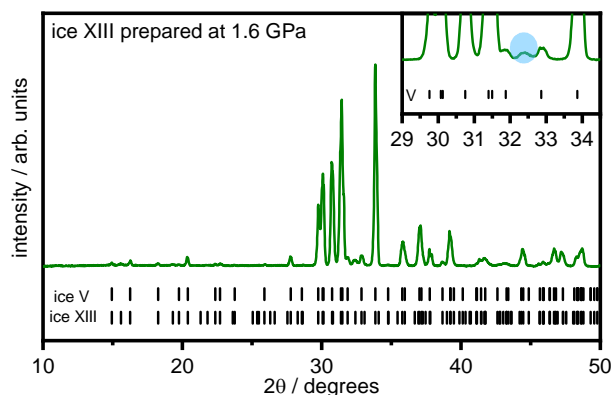


Figure 7.13: XRD of an ice XIII sample prepared at 1.6 GPa which was confirmed to possess hydrogen order due to the existence of an additional peak at $\sim 32.5^\circ$, as highlighted in the inset in the top right corner. The XRD was collected at 95 K.

The additional peak shown in the inset of Figure 7.13 results from a new reflection with Miller indices $31\bar{2}$, which was also displayed in the neutron diffraction study by Salzmann *et al.*²⁰

7.2.4 The effect of pressure and cooling rate on sample preparation

From previous calorimetric studies, it has been shown that the slow-cooling of ice V samples in a calorimeter at ambient pressure produced samples that were more hydrogen ordered than samples slow-cooled under pressure.²⁷

To assess the degree of hydrogen order in the samples made under the conditions described above which were based around the mapping of the phase boundaries, DSC was carried out where samples were heated from 93 K at 10 K min^{-1} to beyond the transition to stacking-disordered ice. The resulting thermograms are shown in Figure 7.14.

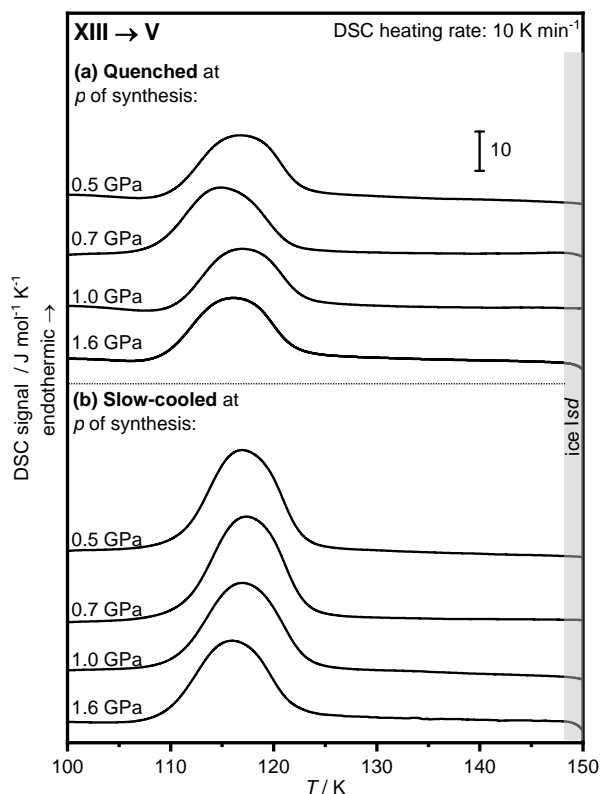


Figure 7.14: Thermograms of ice XIII transforming to ice V on heating. (a) shows samples that were prepared under pressure by slow-cooling, while (b) shows samples that were prepared by quenching while under pressure. The grey-shaded region shows where ice V irreversibly transforms to stacking-disordered ice. The scale bar applies to both plots. All DSCs were performed at a heating rate of 10 K min^{-1} .

As would be expected, all the endotherms in Figure 7.14, which indicate the disordering of ice XIII to ice V, have their maximum at $\sim 115 \text{ K}$ in line with the literature.²⁷ For some reason, the sample prepared by pressure quenching at 0.7 GPa in Figure 7.14(a) has its endothermic maximum a few degrees lower, however this temperature is still within error of the other samples. Close inspection of the region before the endotherms of the scans in Figure 7.14(a) highlights that the signal is not completely flat, but in fact possesses slight exothermic dips – this is particularly pronounced for the 1.0 and 1.6 GPa samples. The exotherms most likely derive from transient ordering processes which have been seen in several other high pressure ices on heating.¹⁷ This implies that the pressure-quenched samples retain a degree of disorder which exist with a high Gibbs free energy, which on heating rapidly revert to a more ordered form, which translates to an exotherm in these scans. The further heating leads to the disordering process to ice V. Given the irreversibility and kinetic nature of the transient ordering features, caution needs to be exercised when considering them. In 0.01 M HCl -doped ice VI/XV, features pertaining to transient ordering from deep-glassy states were found to appear

and disappear depending on a range of factors, such as the cooling rate and pressure of formation and the heating rate of the sample in the DSC.^{17, 22}

The amount of hydrogen order in the samples was quantified from the thermograms by considering the areas, and hence enthalpies, of transition of ice XIII to ice V. The resulting enthalpies are shown in Figure 7.15(a). Given the known favouring of ice XIII to order more at ambient pressure rather than while under pressure, a sample made at 1.0 GPa was annealed in the DSC at 90 K at a range of times before the XIII to V transition to see the potential effect (Figure 7.15(b)).

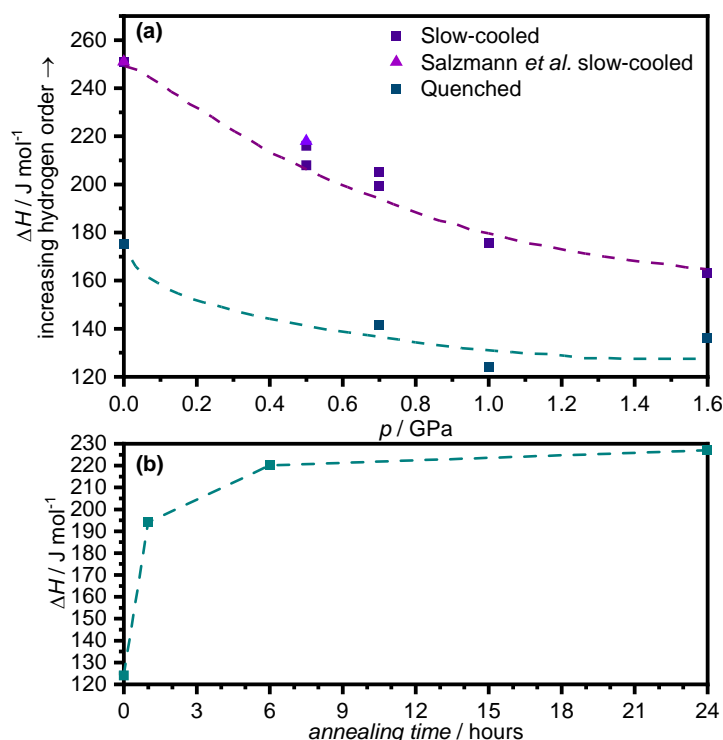


Figure 7.15: (a) Enthalpies of transition of ice XIII to ice V upon heating as function of pressure of preparation. The top purple points belong to slow-cooled samples, while the lower cyan points are from quenched samples. Squares denote data from this study, while triangles are from Salzmann *et al.*²⁷ The dotted lines are eye-guides. (b) shows the effect of annealing a sample prepared at 1.0 GPa for 1, 6 and 24 hours at 93 K. All DSCs were performed at a heating rate of 10 K min^{-1} .

Figure 7.15(a) demonstrates results in line with what would be expected based on previous literature, in that increased pressures reduce the amount of hydrogen order in ice XIII while slow cooling increases the amount of hydrogen order for a given pressure. Exerting higher pressures on ice XIII samples restricts reorientation in the ordering transition of ice V to XIII, making it less energetically demanding to transform back to ice V when disordering on heating. The trend appears to be more marked for

the slow-cooled samples as these samples have more time to reorient structurally to reach a higher level of hydrogen order. This is further exemplified by Figure 7.15(b), where the effect of annealing in the calorimeter (*i.e.* increasing ordering time) is able to induce more ordering in a disordered sample prepared by quenching at 1.0 GPa. The effect of annealing at ambient pressure is very similar to that seen in samples of deep-glassy ice VI, which were found to become increasingly relaxed with increased annealing times.¹⁷ This suggests that highly compressed ice XIII displays characteristics similar to that of deep-glassy states. However, the effect of annealing appears to taper off at times greater than 6 hours. Considering that Loerting *et al.* showed that annealing samples of ice XIV at 77 K is able to induce order over a 40 month period,⁴¹ and that here (as shown in Figure 7.15(b)), a marked increase in ordering is seen after annealing at 93 K, it would be interesting to see the potential effect of annealing ice XIII samples at just a few degrees before the XIII to V transition.

Having observed exotherms relating to transient ordering in Figure 7.14, samples treated with varying pressures and cooling rates of formation, as well as different heating rates used in calorimetry were varied to test whether transient ordering would either be encouraged or thwarted. Previous work by Salzmann *et al.* looking at deep-glassy states of ice VI demonstrated that transient ordering could be brought about by preparing samples at increased pressures as it facilitated the formation of metastable states with high Gibbs free energies.¹⁷ As cooling rates under pressure had a substantial effect on the degree of ordering, consideration was given to heating rates of samples of ice XIII to V at ambient pressure. The most ordered and most disordered ice XIII samples were prepared and heated at different rates in the DSC (Figure 7.16).

Salzmann *et al.* noted that the dis/ordering of ice V/XIII was formed as a result of two overlapping processes which they observed in the two features of their endotherms (and exotherms) when they used heating (and cooling) rates lesser than and including 5 K min⁻¹. The lower thermograms in Figure 7.16(a) and Figure 7.16(b) also very visibly displayed this characteristic, with a degree of asymmetry visible in the 5 K min⁻¹ thermograms. Another significant feature in the thermograms in Figure 7.16(b) are exotherms which occur before the endothermic transition of XIII to V.

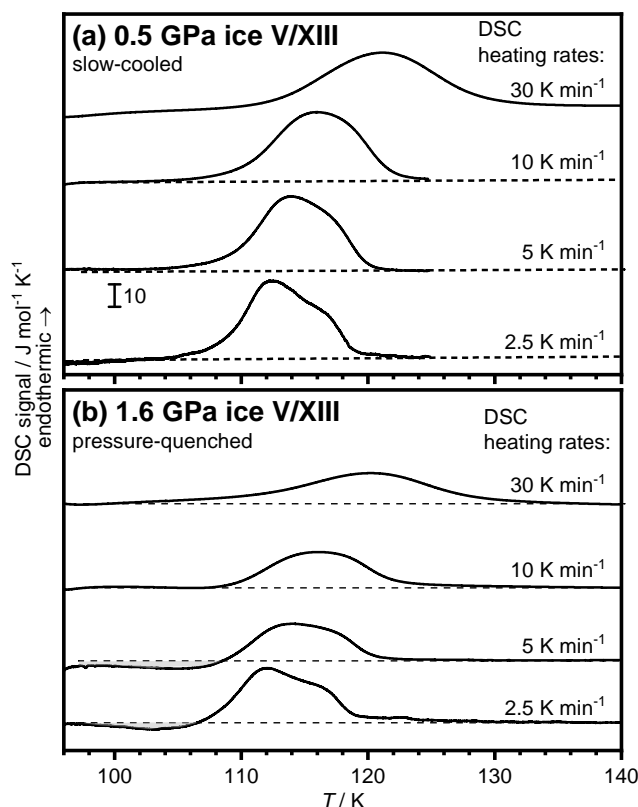


Figure 7.16: The most ordered ice XIII (a) and the most disordered ice XIII (b) heated at different rates in the calorimeter. The dotted lines provide a baseline and highlight exothermic dips prior to the XIII to V transition in the highly disordered sample in plot (b) which are attributed to transient ordering. The scale bar applies to both plots.

Transient ordering can be observed in states that have slight deep-glassy characteristics. In a true glassy state, the heating of a sample at ambient pressure leads to exotherms before the disordering endotherm. This represents the point on heating from which the sample passes the glass transition and is then able to ‘fall back’ to the equilibrium line between static and dynamic states, thereby lowering its Gibbs free energy, resulting in the presence of an exotherm in calorimetry. This process is demonstrated in the schematic in the introduction where different enthalpic pathways are introduced (Chapter 1.2.7.). A qualitative way to consider the order within the sample on heating is as follows: ‘highly’ partially disordered ice XIII \rightarrow partially disordered ice XIII \rightarrow disordered ice V. More relaxed deep-glassy states can be seen on the slow-heating of the sample at ambient pressure.^{17, 22} The transient ordering exotherm is particularly pronounced for the sample heated at the slowest rate at 2.5 K min^{-1} . No such transient ordering features are apparent in Figure 7.16(a); this is because the slow-cooling of the sample has provided the ice sufficient time to reorient into an ordered configuration, allowing for the formation of a highly-ordered sample. Chapter 7.1 also demonstrated

transient ordering to occur in pure H₂O-ice IX. Full substantiation of the conclusions made here would be possible if a neutron diffraction study to examine the transient ordering as translated into the occupancies of deuterium atoms was performed.

Raman spectroscopy was also performed on several samples of ice XIII prepared from samples of 0.01 M HCl with 5 w% D₂O (Figure 7.17). Salzmann *et al.* showed that ice XIII produced a spectrum at 80 K which could quite easily be differentiated from ice V formed from the heating of the initial ice XIII to 120 K, especially in the decoupled O–D region centred at $\sim 2450\text{ cm}^{-1}$. They reported decoupled O–D frequencies at 2501, 2496, 2490, 2460, 2440 and 2430 cm^{-1} for their ordered ice XIII.³⁸ Meanwhile in the O–H region, three small peaks were seen at 3413, 3360, 3297 cm^{-1} and a major peak could be seen at 3190 cm^{-1} .

Figure 7.17(a) and (b) show the coupled O–H and decoupled O–D regions of ice XIII respectively. Spectra (1), (2), and (3) can be attributed to ice XIII prepared by slow cooling from 1.6 GPa, quenching at 1.6 GPa and quenching at 0.5 GPa.

Figure 7.17 shows that the pressure of formation of ice XIII has a greater effect on the amount of hydrogen ordering in the sample given the variation in the sharpness of the O–D features. The spectra in Figure 7.17(a) are all very alike, all having three features at ~ 3190 , 3303 and 3429 cm^{-1} , though arguably the weakest peak is hard to assign properly. The FWHM of the most prominent peak of each spectrum was taken; for spectra (1), (2) and (3) the widths found were 57, 61 and 58 cm^{-1} respectively. Given that less-ordered environments are expected to have broader peaks, which represent a larger number of states possible, it would appear that spectrum (1) from the slow-cooled sample made at 1.6 GPa is the most ordered.

Spectrum (1) of Figure 7.17(b) also has features that demonstrate that the sample slow-cooled from 1.6 GPa is the most ordered sample being considered. The higher degree of ordering compared to the two quenched samples is apparent from the six distinct sharper regions which morph into two regions in the quenched samples. In spectrum (1) of Figure 7.17(b), which represents the most ordered ice XIII prepared, a set of six peaks were also seen with frequencies at 2504, 2496, 2490, 2460, 2443 and 2431 cm^{-1} , in similarity to the study performed by Salzmann and co-workers.³⁸

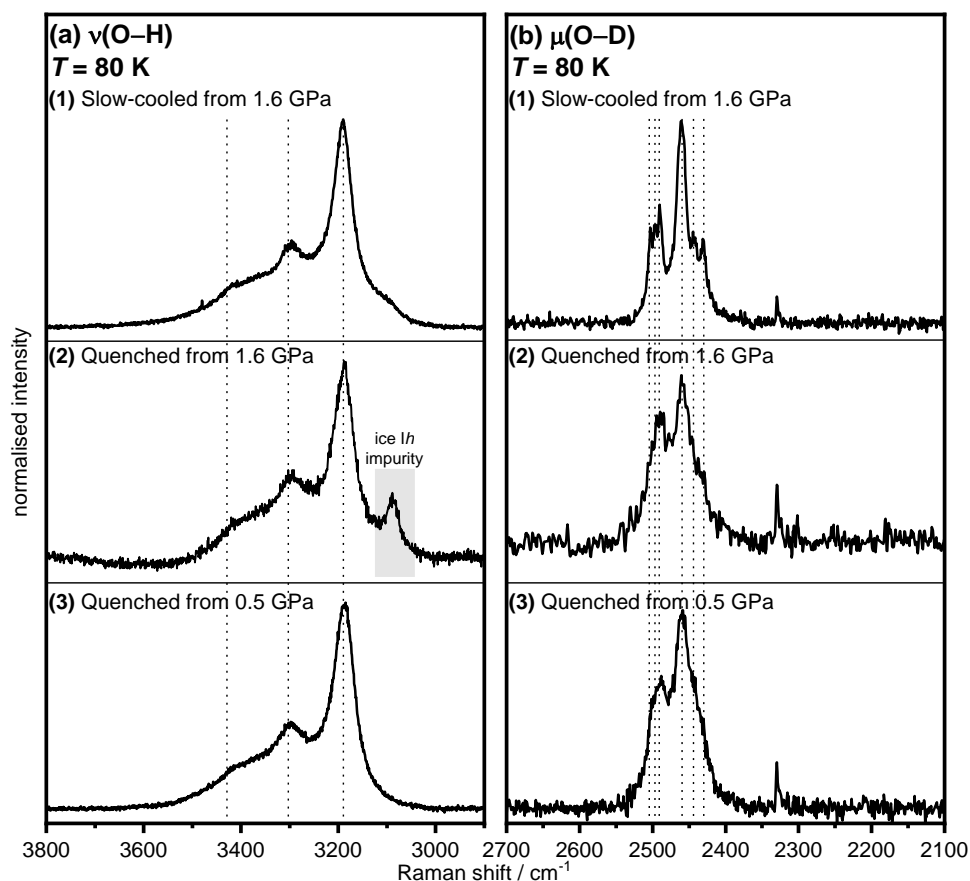


Figure 7.17: Normalised Raman spectra showing (a) the coupled O–H stretches and (b) decoupled O–D region of ice XIII prepared at varying pressures and cooling rates. (1) belongs to a slow-cooled sample prepared at 1.6 GPa, while (2) and (3) are from quenched samples prepared at pressures of 1.6 GPa and 0.5 GPa respectively. In (b), a noticeable difference can be seen between the slow-cooled and quenched samples prepared at the same pressure, while little difference is apparent between quenched samples prepared at different pressures. (a) is less indicative of the degree of order in each sample as all spectra look very similar. Dotted lines indicated literature values of intensities from Salzmann *et al.*³⁸ An external ice Ih impurity is highlighted in spectrum 2 of (a).

It appears that the two quenched samples have two bands, which from the sample at 0.5 GPa have frequencies at 2489 and 2458 cm^{-1} . In some ways the spectra of the quenched samples are in-between the appearance of ice V and ice XIII, as shown in Salzmann *et al.*'s spectroscopic work on ice XIII, which have one and six bands respectively.³⁸

If the samples shown in Figure 7.17 are correlated to their corresponding enthalpies of transition of ice XIII to V shown in Figure 7.15(a), which provide a more direct marker of the degree of hydrogen disorder they possess, the trends seen in the spectra corroborate this. In Figure 7.15(a), the enthalpies of transition of the two quenched samples at different pressures are both $\sim 150 \text{ J mol}^{-1}$, whereas the sample

slow-cooled at 1.6 GPa has an enthalpy of transition $\sim 170 \text{ J mol}^{-1}$, meaning that it is more ordered. This is well reflected by the well-defined spectral frequencies it has in the spectra (1) in Figure 7.17(a) and (b).

7.2.5 Conclusions

In this chapter, the metastability region at low temperatures boundary for ice V/XIII is reported for the first time up to pressures of 1.6 GPa. Through both calorimetry and spectroscopy, the effect of pressure of formation of ice XIII and cooling rate on the formation of ice XIII are shown to vary hydrogen order to different extents. Having said this, it may be difficult to draw absolute conclusions regarding how much slow-cooling and pressure of formation affects the degree of ordering due to the similarity of some features that have been observed here to characteristics seen in deep-glassy states. However, on the preparation of the samples, it does seem safe to say that slow cooling of ice V/XIII has a larger impact on the amount of hydrogen ordering present in the final sample than the pressure of formation. This greater influence of slow-cooling is seen in the plateauing of enthalpies of transition with respect to pressure (Figure 7.15(a)). Nevertheless, there does still exist a pressure-dependence on enthalpies of transition. The application of higher pressures on sample preparation appears to have created states with deep-glassy characteristics; this is seen especially well in the DSCs of pressure-quenched ice XIII prepared at 1.6 GPa (Figure 7.16(b)), which have exotherms that are particularly pronounced with slow-heating rates. Overall, this indicates a positive activation volume of the hydrogen-ordering process. Although HCl-doping is able to facilitate hydrogen ordering, this work confirms that full hydrogen ordering of ice XIII only remains possible on the cooling of a sample at ambient pressure,²⁷ and that, in fact, the presence of the dopant at elevated pressures may be unlocking deep-glassy qualities within the ice.¹⁷

7.3 References

1. S. J. La Placa, W. C. Hamilton, B. Kamb and A. Prakash, *J. Chem. Phys.*, 1973, **58**, 567-580.
2. C. Lobban, J. L. Finney and W. F. Kuhs, *J. Chem. Phys.*, 2000, **112**, 7169-7180.
3. V. F. Petrenko and R. W. Whitworth, *Physics of Ice*, OUP Oxford, 1999.
4. C. G. Salzmann, *J. Chem. Phys.*, 2019, **150**, 060901.
5. I. G. Polyakova, in *4. The Main Silica Phases and Some of Their Properties*, De Gruyter, 2014, DOI: <https://doi.org/10.1515/9783110298581.197>, p. 197.
6. P. P. Keat, *Science*, 1954, **120**, 328-330.
7. J. Shropshire, P. Keat Paul and A. Vaughan Philip, *Z. Kristallogr.*, 1959, **112**, 409.
8. J. D. Londono, W. F. Kuhs and J. L. Finney, *J. Chem. Phys.*, 1993, **98**, 4878-4888.
9. E. Whalley, J. B. R. Heath and D. W. Davidson, *J. Chem. Phys.*, 1968, **48**, 2362-2370.
10. K. Nishibata and E. Whalley, *J. Chem. Phys.*, 1974, **60**, 3189-3194.
11. E. Whalley and D. W. Davidson, *J. Chem. Phys.*, 1965, **43**, 2148-2149.
12. S. J. Singer and C. Knight, in *Adv. Chem. Phys.*, John Wiley & Sons, Inc., 2011, DOI: 10.1002/9781118135242.ch1, pp. 1-74.
13. C. Knight and S. J. Singer, *J. Chem. Phys.*, 2006, **125**, 064506.
14. Y. P. Handa, D. D. Klug and E. Whalley, *Can. J. Chem.*, 1988, **66**, 919-924.
15. L. G. MacDowell, E. Sanz, C. Vega and J. L. F. Abascal, *J. Chem. Phys.*, 2004, **121**, 10145-10158.
16. Tobias M. Gasser, A. V. Thoeny, L. J. Plaga, K. W. Köster, M. Etter, R. Böhmer and T. Loerting, *Chem. Sci.*, 2018, **9**, 4224-4234.
17. A. Rosu-Finsen and C. G. Salzmann, *Chem. Sci.*, 2019, **10**, 515-523.
18. A. Rosu-Finsen, A. Amon, J. Armstrong, F. Fernandez-Alonso and C. G. Salzmann, *J. Phys. Chem. Lett.*, 2020, **11**, 1106-1111.
19. C. G. Salzmann, P. G. Radaelli, B. Slater and J. L. Finney, *Phys. Chem. Chem. Phys.*, 2011, **13**, 18468-18480.
20. C. G. Salzmann, P. G. Radaelli, A. Hallbrucker, E. Mayer and J. L. Finney, *Science*, 2006, **311**, 1758.

21. C. G. Salzmann, P. G. Radaelli, E. Mayer and J. L. Finney, *Phys. Rev. Lett.*, 2009, **103**, 105701.
22. A. Rosu-Finsen, A. Amon, J. Armstrong, F. Fernandez-Alonso and C. G. Salzmann, *J. Phys. Chem. Lett.*, 2020, **11**, 1106-1111.
23. C. G. Salzmann, B. Slater, P. G. Radaelli, J. L. Finney, J. J. Shephard, M. Rosillo-Lopez and J. Hindley, *J. Chem. Phys.*, 2016, **145**, 204501.
24. J. P. Bradshaw, in *eLS*, 2014, DOI: doi:10.1002/9780470015902.a0003045.pub3.
25. B. Minčeva-Šukarova, W. F. Shermann and G. R. Wilkinson, *J. Mol. Struct.*, 1984, **115**, 137-140.
26. O. Yamamuro, M. Oguni, T. Matsuo and H. Suga, *J. Phys. Chem. Solids*, 1987, **48**, 935-942.
27. C. G. Salzmann, P. G. Radaelli, J. L. Finney and E. Mayer, *Phys. Chem. Chem. Phys.*, 2008, **10**, 6313-6324.
28. A. Rosu-Finsen and C. G. Salzmann, *J. Chem. Phys.*, 2017, **148** 244507.
29. C. G. Salzmann, E. Mayer and A. Hallbrucker, *Phys. Chem. Chem. Phys.*, 2004, **6**, 1269-1276.
30. J. E. Bertie and B. F. Francis, *J. Chem. Phys.*, 1980, **72**, 2213-2221.
31. T. H. G. Carr, J. J. Shephard and C. G. Salzmann, *J. Phys. Chem. Lett*, 2014, **5**, 2469-2473.
32. B. Mincěva-Šukarova, G. E. Slark and W. F. Sherman, *J. Mol. Struct.*, 1986, **143**, 87-90.
33. B. Kamb, A. Prakash and C. Knobler, *Acta Crystallogr.*, 1967, **22**, 706-715.
34. Y. P. Handa, D. D. Klug and E. Whalley, *J. Phys.*, 1987, **48**, 435-440.
35. G. A. Tribello, PhD thesis, University College London, 2007.
36. N. H. Fletcher, *The Chemical Physics of Ice*, Cambridge University Press, Cambridge, 1970.
37. W. F. Kuhs, W. Kuhs and R. S. o. Chemistry, *Physics and Chemistry of Ice*, RSC Publishing, 2007.
38. C. G. Salzmann, A. Hallbrucker, J. L. Finney and E. Mayer, *Phys. Chem. Chem. Phys.*, 2006, **8**, 3088-3093.
39. S. Kawada, *J. Phys. Soc. Jpn.*, 1972, **32**, 1442-1442.
40. K. W. Köster, A. Raidt, V. Fuentes Landete, C. Gainaru, T. Loerting and R. Böhmer, *Physical Review B*, 2016, **94**, 184306.

41. V. Fuentes-Landete, K. W. Koster, R. Bohmer and T. Loerting, *Phys. Chem. Chem. Phys.*, 2018, **20**, 21607-21616.

8 Final conclusions and outlook

This thesis aimed to investigate the phase diagram of ice by disturbing it with one of its most soluble species – ammonium fluoride. NH_4F is an ideal material to incorporate into ice, as a result of its shared geometry and strong hydrogen bonding.^{1, 2} Studying doped ice has provided a truly remarkable standpoint from which to assess the thermodynamic landscape of ice and its compressed NH_4F -ice solid solutions.

Overall, it can be concluded that two factors of NH_4F in ice are able to disrupt its properties, namely: (i) the fact that NH_4F does not experience hydrogen disorder in the manner that ice does, and (ii) the increase in density of its solid solutions compared to pure ice.

The increased density of NH_4F -ice solid solutions, compared to that of pure ice, shifts the thermodynamic stability of phases – this has been well demonstrated by increasing the NH_4F content in NH_4F -ice solid solutions at 0.5 GPa, which causes a reordering of the stability of phases in the known p - T stability region of ice V. The emergence of ice XII-type structures from above 12 mol% NH_4F -ice is the undoubted result of the increased density of the rings that form which find it energetically futile to form structures with interpenetrating features.

Additionally, the mapping of the 2.5 mol% NH_4F -ice phase diagram up to 1.7 GPa confirmed further shifts from the balance of states as seen for pure ice. As first reported by Shephard *et al.*, ice II is still unable to form,³ and the phases that do form in other regions of the 2.5 mol% NH_4F -ice phase diagram differ in their stability compared to the analogous pure ice phases observed in the same p - T regions. For instance, in the presence of 2.5 mol% NH_4F , ice IV is still obtained at pressures of 1.7 GPa, whereas for pure ice the same polymorph is not seen past 0.8 GPa.⁴⁻⁶ Furthermore, ice XII gains a wide region of stability and can even be prepared in a phase-pure manner simply by quenching from 190 K at 1.1 GPa.

The ability to obtain ice XII and ice XII-like structures simply from quenching a compressed crystalline solid has been unheard of up until now. Ice XII can only be formed in a reproducible manner on quenching and releasing to ambient pressure if prepared *via* an HDA precursor.⁵⁻⁷ Yet the increased density provided by the presence

8. Final conclusions and outlook

of NH_4F in ice, as established in this thesis and discussed by Lyashchenko *et al.*,¹ has made it more energetically favourable to form ice XII-type structures.

Extremely valuable insights have also been gained from the isothermal ‘pressure-induced amorphisation’ of solid solutions of NH_4F -ice across the entire solubility range at 77 K to 1.4 GPa. The addition of NH_4F to ice has allowed us to detect the crossover of amorphisation to recrystallisation as facilitated by the ‘switching off’ of the hydrogen disorder in ice by the NH_4F . Unexpectedly, in water-rich solid solutions of concentrations as low as 35 mol% NH_4F -ice, crystalline character begins to emerge in the compressed sample, indicating that this is when the thermodynamic formation of ice IV begins to get ‘back on track’ from the former derailment⁸ seen at lower concentrations of NH_4F in ice. This divergence from water-like character at water-rich concentrations has put into question the structural link between HDA and LDA with their hypothetical water analogues HDL and LDL which would be expected to exist until at least 50 mol% NH_4F .

Stacking disorder in NH_4F has also been quantified for the first time, as observed from the heating of NH_4F II and NH_4F III at ambient pressure from 95 K to 270 K. The stacking disordered materials formed from the heating of the different polymorphs led to the development of structurally distinct stacking disordered materials which were undoubtedly more complex when derived from NH_4F III. Intriguingly the material obtained from the warming of NH_4F III appeared to contain broad ill-crystalline features related to an NH_4F II-type structure, as well as some broad peaks known to coincide with the second broad feature of LDA seen in XRD. This suggests that the ill-crystalline stacking disordered material formed from heating NH_4F III shares a structural link with LDA. The highest observed cubicity of stacking disordered NH_4F was 77% and the tendency to grow in hexagonal character on heating was observed – as is seen for ice.⁹

The final chapter of this thesis demonstrated factors influencing the hydrogen ordering in ices doped with 0.01 M HCl, which was first employed by Salzmann *et al.* to prepare hydrogen-ordered counterparts to ices V, VI and XII.^{10, 11} In ice IX, it was found that the addition of the HCl dopant was able to remove residual hydrogen disorder that is retained from the act of quenching ice III in its formation. In the case of 0.01 M HCl-doped ice V/XIII, it was determined that the preparation of ice XIII at

8. Final conclusions and outlook

higher pressures and with faster cooling rates while under pressure led to the formation of samples holding on to more hydrogen disorder. In both HCl-doped ices, ‘deep-glassy’-like characteristics were observed from exotherms in calorimetry.

Overall, taking into account all the work conducted over the course of this thesis, many valuable insights have been gained which are likely to have far reaching implications of our understanding of water. Particularly, the results obtained from the pressure-induced amorphisation of NH_4F -ice solid solutions should help make a strong contribution towards the ongoing two-liquid water debate.^{8, 12-14}

To build on the conclusions that have been drawn in the thesis, the use of further characterisation techniques would be beneficial. Computational techniques may also be able to help us understand the molecular environments of NH_4F -ice solid solutions at ambient pressure and at elevated pressures. This hopefully will be able to provide complementary evidence which explains the preferential formation of ice phases which for pure ice are metastable – in particular ice XII. As is still up for debate with the more traditional acid and base dopants,^{15, 16} it would be interesting to gain an appreciation of the positions of NH_4^+ and F^- species, when incorporated into the solid solution. For instance, with respect to the PIA of NH_4F -ice solid solutions, it would be constructive to obtain pair distribution functions of the different products and see their similarity to supercooled water. Additionally, if computational techniques have the capacity and capability to, it would be interesting to see what structures are predicted at different points along the experimental pathway – *e.g.* before compression and on the heating of the compressed products. Also, preparation (or perhaps existence) of the elusive monohydrate of NH_4F remains unresolved. A characterisation technique sensitive to different atomic compositions should be employed to isolate the monohydrate of ammonium fluoride.

8.1 References

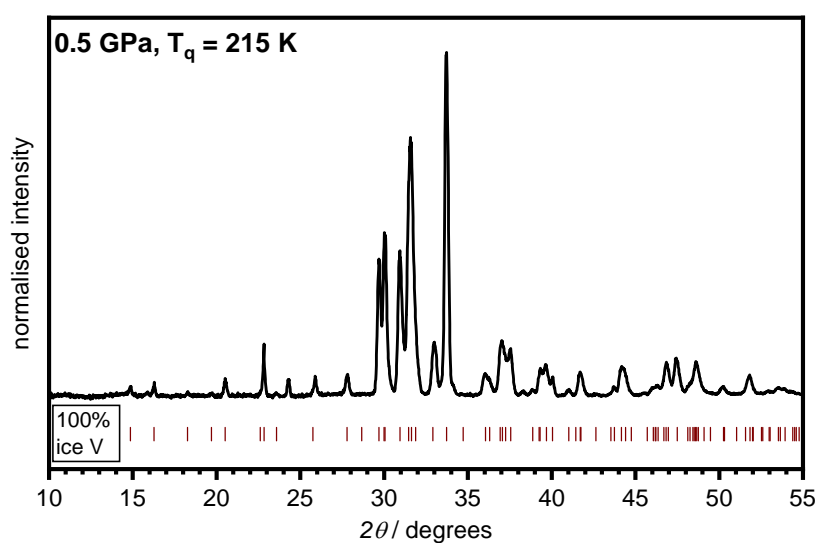
1. A. K. Lyashchenko and G. G. Malenkov, *J. Struct. Chem.*, 1969, **10**, 616-617.
2. C. G. V. Beek, J. Overeem, J. R. Ruble and B. M. Craven, *Can. J. Chem.*, 1996, **74**, 943-950.
3. J. J. Shephard, B. Slater, P. Harvey, M. Hart, C. L. Bull, S. T. Bramwell and C. G. Salzmann, *Nat. Phys.*, 2018, **14**, 569-572.
4. H. Engelhardt and B. Kamb, *J. Chem. Phys.*, 1981, **75**, 5887-5899.
5. C. G. Salzmann, I. Kohl, T. Loerting, E. Mayer and A. Hallbrucker, *Can. J. Phys.*, 2003, **81**, 25-32.
6. C. G. Salzmann, E. Mayer and A. Hallbrucker, *Phys. Chem. Chem. Phys.*, 2004, **6**, 1269-1276.
7. J. Stern and T. Loerting, *Sci. Rep.*, 2017, **7**, 3995.
8. J. J. Shephard, S. Ling, G. C. Sosso, A. Michaelides, B. Slater and C. G. Salzmann, *J. Phys. Chem. Lett.*, 2017, **8**, 1645-1650.
9. T. L. Malkin, B. J. Murray, C. G. Salzmann, V. Molinero, S. J. Pickering and T. F. Whale, *Phys. Chem. Chem. Phys.*, 2015, **17**, 60-76.
10. C. G. Salzmann, P. G. Radaelli, A. Hallbrucker, E. Mayer and J. L. Finney, *Science*, 2006, **311**, 1758.
11. C. G. Salzmann, P. G. Radaelli, E. Mayer and J. L. Finney, *Phys. Rev. Lett.*, 2009, **103**, 105701.
12. A. K. Soper, *J. Chem. Phys.*, 2019, **150**, 234503.
13. J. S. Tse, D. D. Klug, C. A. Tulk, I. Swainson, E. C. Svensson, C. K. Loong, V. Shpakov, V. R. Belosludov, R. V. Belosludov and Y. Kawazoe, *Nature*, 1999, **400**, 647-649.
14. C. A. Tulk, J. J. Molaison, A. R. Makhluf, C. E. Manning and D. D. Klug, *Nature*, 2019, **569**, 542-545.
15. V. F. Petrenko and R. W. Whitworth, *Physics of Ice*, OUP Oxford, 1999.
16. C. G. Salzmann, P. G. Radaelli, B. Slater and J. L. Finney, *Phys. Chem. Chem. Phys.*, 2011, **13**, 18468-18480.

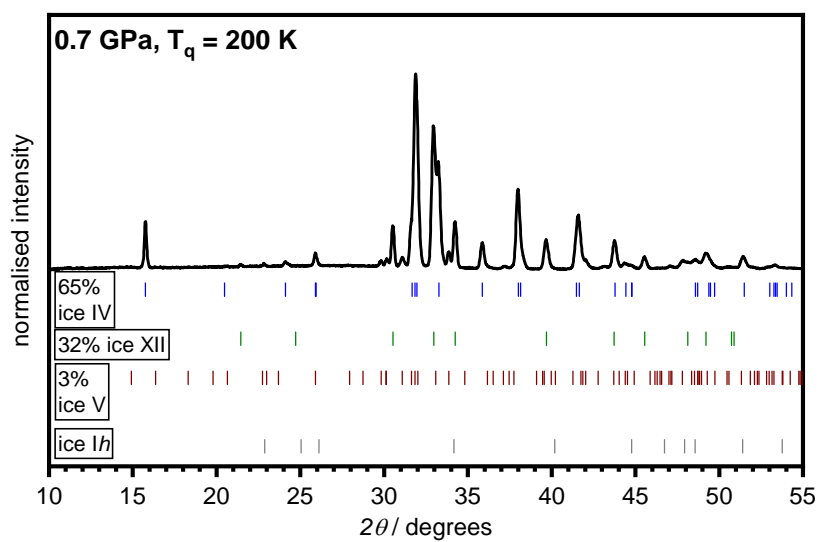
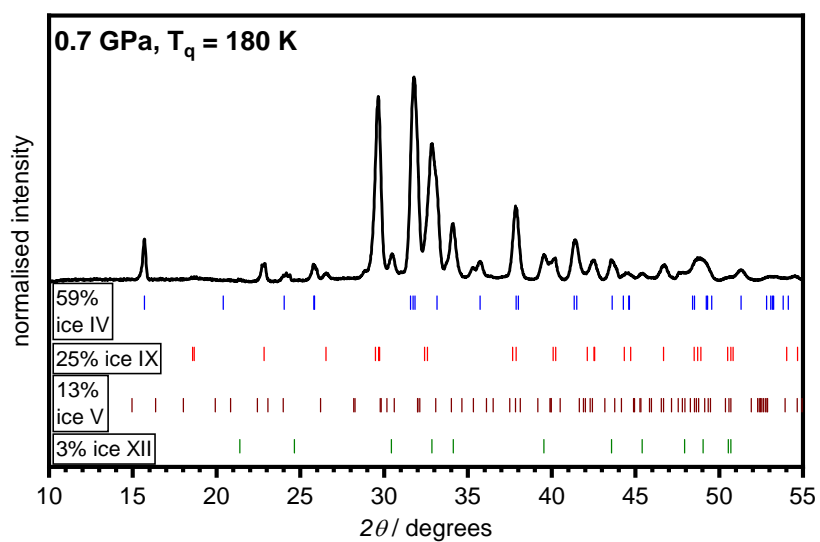
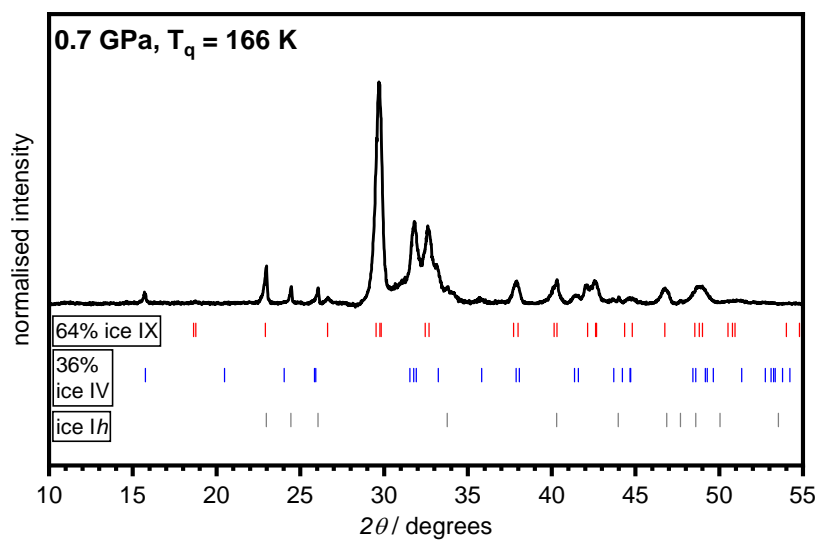
Appendix

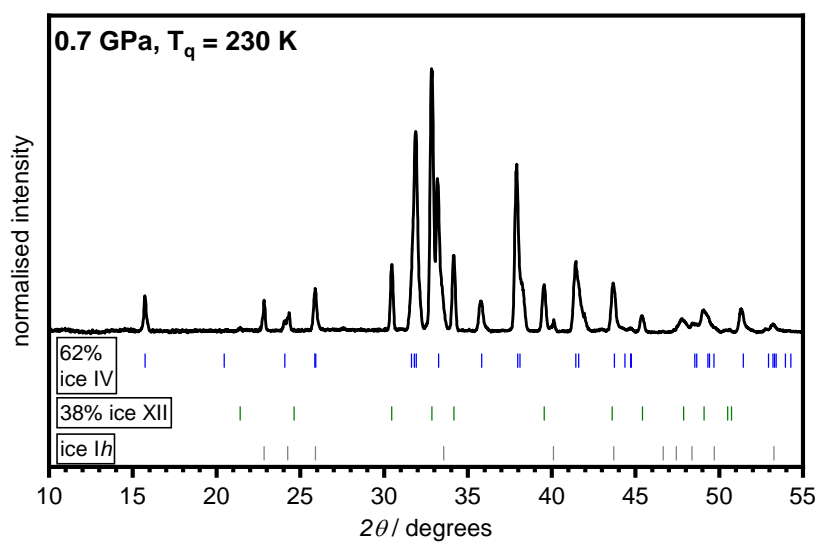
The XRD patterns shown relate to Figure 4.6 in Chapter 4.3 (Volume-change mapping of the 2.5 mol% NH_4F -ice phase diagram up to 1.7 GPa)

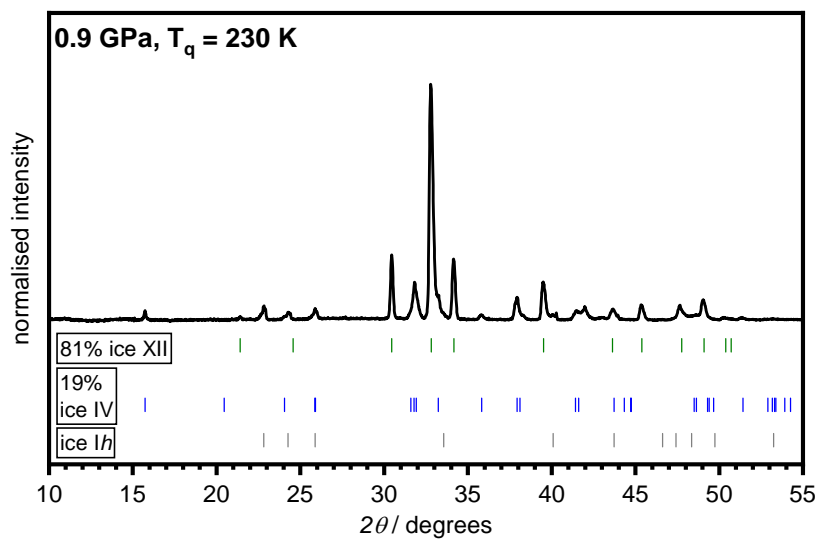
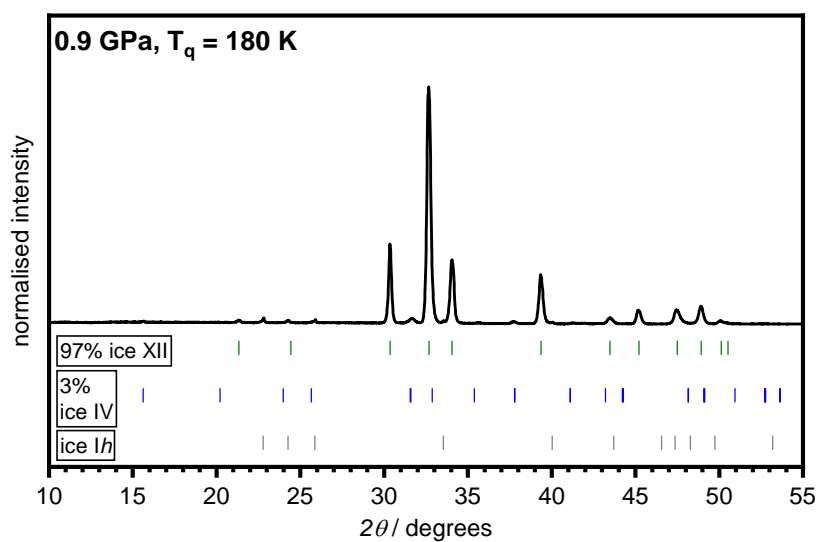
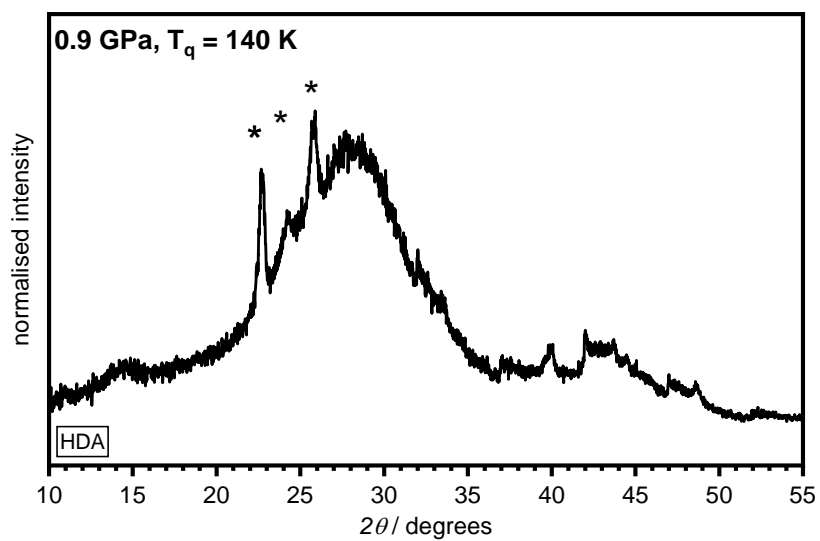
All XRD patterns are of 2.5 mol% NH_4F -ices quenched at a series of temperatures and pressures (from 0.5 to 1.7 GPa). The samples were quenched from temperatures, T_q . All patterns were collected at ~ 95 K at ambient pressure. External ice *Ih* impurities are denoted by asterisks or shown with the other tickmarks.

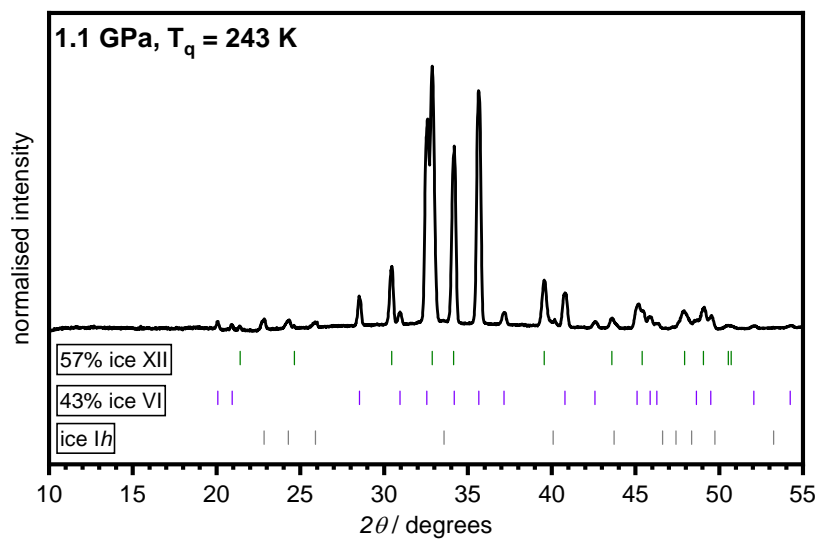
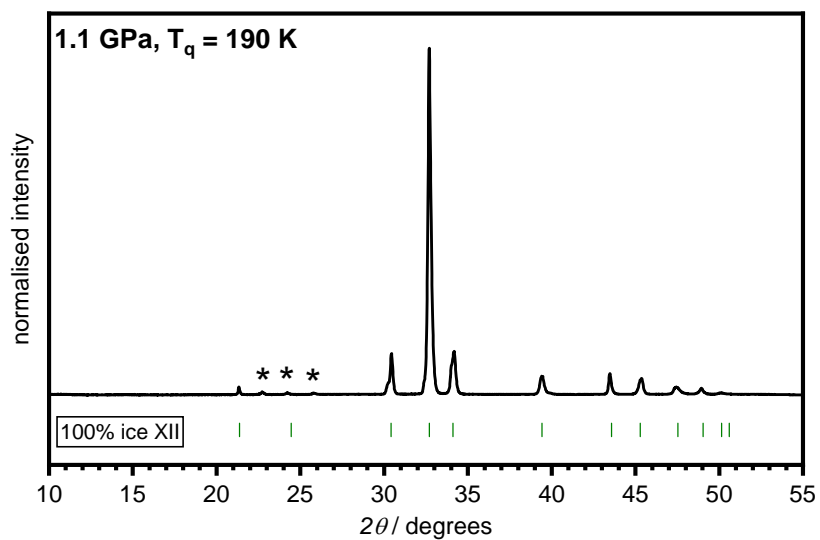
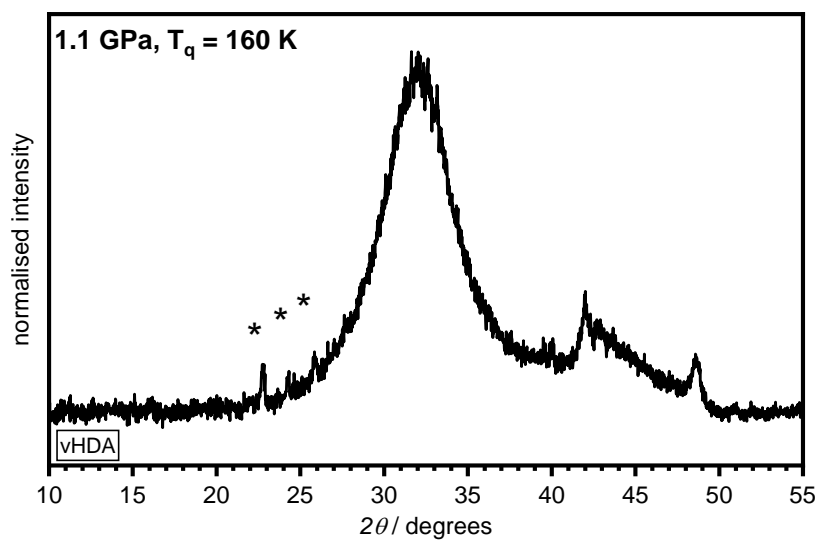
2.5 mol% NH_4F -ice at 0.5 GPa



2.5 mol% NH₄F-ice at 0.7 GPa



2.5 mol% NH_4F -ice at 0.9 GPa

2.5 mol% NH_4F -ice at 1.1 GPa

2.5 mol% NH₄F-ice between 1.3 to 1.7 GPa